UNIVERSIDADE DE LISBOA

INSTITUTO SUPERIOR TÉCNICO

Ex-Vivo Culture of Neural Stem Cells in Nanofiber Scaffolds: Cellular Organization and Dynamic Systems

Miriam Calado Amores de Sousa

Supervisor: Doctor Frederico Castelo Alves Ferreira

Thesis approved in public session to obtain the PhD in Biotechnology and Biosciences

Jury final classification: Pass with Distinction

2018

TÉCNICO LISBOA

UNIVERSIDADE DE LISBOA

INSTITUTO SUPERIOR TÉCNICO

Ex-Vivo Culture of Neural Stem Cells in Nanofiber Scaffolds: Cellular Organization and Dynamic Systems

Miriam Calado Amores de Sousa

Supervisor: Doctor Frederico Castelo Alves Ferreira

Thesis approved in public session to obtain the PhD in Biotechnology and Biosciences

Jury final classification: Pass with Distinction

Jury

Chairperson: **Doctor** Joaquim Manuel Sampaio Cabral, Instituto Superior Técnico, Universidade de Lisboa

Members of the Committee:

Doctor Joaquim Manuel Sampaio Cabral, Instituto Superior Técnico, Universidade de Lisboa

Doctor Geoffrey Robert Mitchell, Centro para o Desenvolvimento Rápido e Sustentado de Produto, Instituto Politécnico de Leiria

Doctor Alessandro Filippo Pellegata, Great Ormond Street Institute of Child Health, Faculty of Population Health Sciences, University College London, UK

Doctor Frederico Castelo Alves Ferreira, Instituto Superior Técnico, Universidade de Lisboa

Doctor Carlos André Vitorino Rodrigues, Instituto de Bioengenharia e Biociências, Instituto Superior Técnico, Universidade de Lisboa

Funding Institution: **Fundação para a Ciência e a Tecnologia**

2018

Abstract

Stem cells (SCs) hold the potential to be applied into several regenerative therapies. The majority of SCs are anchorage dependent, requiring surface areas with appropriate topology for cultivation in clinically relevant numbers. A strategy for mimicking the natural SCs niche is the use of electrospun fibers, with dimensions (200-500nm in diameter) at the scale of the fibrous proteins present in the niche, providing high contact areas required for cellular adhesion. The use of scaffolds of aligned nanofibers is particularly interesting envisaging the regeneration of neural tissue, applied to neural stem cells (NSC), providing anisotropy to stem cell organization. Nanofibers of poly-ε-caprolactone (PCL) were produced by electrospinning, subjected to aminolysis to introduce amine groups for chemical anchorage and functionalized with extracellular matrix (ECM) protein motifs: laminin (PCL-LN) and RGD sequences (PCL-RGD). The morphology and distribution of a mouse NSC (CGR8-NS) were evaluated by scanning electron microscopy (SEM) and fluorescence microscopy after immunostaining. Higher cellular alignment and neuron differentiation with longer neurite elongation was found in the PCL-LN aligned fibers. These results can potentially impact positively the quality of neurons obtained from in-situ differentiation of NSCs. A novel stirred “plate&frame” bioreactor able to accommodate nanofiber scaffolds, for the potential production of neural tissue constructs, was designed as a scalable dynamic culture system for NSC expansion and differentiation. Computational fluid dynamics (CFD) analysis suggested that allowing fluid recirculation above scaffolds frames and agitation rates above 45 rpm promote efficient mixing. A human NSC line (ReNcell VM) was effectively expanded and successfully differentiated into neurons and glial cells, in dynamic conditions, supported by aligned biofunctionalized polycaprolactone nanofibers. These results are promising for scaled up production of aligned cells for stem cell biology research, regenerative medicine or other biomedical applications.

Key words: Scaffolds, Nanofibers, Neural Stem Cells, Bioreactor, Electrospinning

Resumo

As terapias celulares com aplicação de células estaminais (CE) são de elevado potencial clínico em medicina regenerativa. A maioria dos tipos de CE para sobreviver necessita de uma superfície de adesão. Como estratégia, a utilização de biomateriais estruturados em nanofibras permite a criação de um meio artificial, actuando como substrato de adesão celular, permitindo a sua sobrevivência e expansão, mimetizando a matriz extracelular (ME).

A aplicação de nanofibras em cultura, apresenta diversas vantagens, como a aplicação de fibras de diâmetro na ordem dos 200-500 nm, à escala da composição fibrosa proteica natural da ME e, a elevada superfície de contacto e porosidade permite maior área livre para a adesão celular e uma difusão eficaz do meio de cultura.

A electrofiação é uma técnica estabelecida de processamento de materiais, em que diferentes tipos de disposição de fibra podem ser produzidos, dos quais, as fibras alinhadas, de especial interesse quando aplicadas a células estaminais neurais (CEN). Neste contexto, a geometria e organização do meio celular são relevantes para a organização geral da população de células mas também como estímulo director do alinhamento e alongamento celular. Estas condições são relevantes para a diferenciação de neurónios e geral organização celular em cultura de tecido neural.

Neste trabalho foram produzidas nanofibras de policaprolactona, funcionalizadas com motivos de adesão específicos, a laminina e a sequência de aminoácidos GRGDSP. A morfologia e distribuição de dois sistemas de CEN foram avaliadas por microscopia electrónica e microscopia de fluorescência. Verificou-se um impacto positivo em termos de alongamento celular, em nanofibras alinhadas, especialmente favorável na diferenciação neuronal.

Desenvolveu-se também um bioreactor protótipo, capaz de acomodar suportes de nanofibras, para aplicação na expansão e diferenciação de CEN. O sistema foi caracterizado na sua hidrodinâmica e transferência de massa e, por CFD. O cultivo de CEN em nanofibras e a sua diferenciação em condições dinâmicas, revelou-se promissor, em termos de diferenciação neuronal e de células da glia.

Palavras-chave: Matrizes de Suporte para Cultura de Células, Nanofibras, Células Estaminais Neurais, Bioreactor, Electrofiação

Acknowledgments

Professor Joaquim Cabral, thank you for the opportunity to develop my PhD work at the SCBL-RM lab facilities, and to integrate the group at Taguspark campus.

Frederico Ferreira, thank you for being my supervisor (again), for all the help, guidance, positive criticism, patience, patience and above all, for the patience.

Inês Ferreira and Luca Bronzato, thank you for the good contribution you gave to my work with your collaboration as Master students.

Ermelinda Maçôas, thank you for the all the help, advice and supervision with the multiphoton confocal microscope.

Inês Mariz and Sandra Pinto, thank you for helping me while Ermelinda was not around.

Prof. Vítor Geraldes, thank you for the support and advice on the CFD and bioreactor characterization.

Carina Rodrigues, thank you for all your help with Luca with the limiting current experiments.

Carlos Rodrigues, thank you for all your help during the cell culture experiments and sharing with me your cells (from the mouse) and your thoughts about Eros Ramazzotti.

Isabel Nogueira, thank you for being always helpful and available at SEM MicroLab.

Tiago Dias, thank you for being a reasonable friend person.

Sara Badenes, Claudia Miranda, Irina Simões, Maria João Sebastião, Tânia Portela, Alice Baltazar, Beatriz Monteiro, Marta Costa, Raphael Cañadas, Zé Restolho, Carla Moura, Ana Pires Soares, Amâncio Diogo Pinto, and probably I forgot someone, thank you all.

To my friends and family.

List of Contents

List of Figures

List of Tables

Abbreviations and Acronyms

2D	Two-Dimensional
3D	Three-Dimensional
CAMs	Cell Adhesion Molecules
CNS	Central Nervous System
DCM	Dichloromethane
DMEM	Dulbecco's Modified Eagle's Medium
DMF	N,N-dimethylformamide
DMSO	Dimethyl Sulfoxide
ECM	Extracellular Matrix
ESC	Embryonic Stem Cells
EGF	Epidermal Growth Factor
FDA	Food and Drug Administration
FGF2	Fibroblast Growth Factor 2
FN	Fibronectin
GA	Glutaraldehyde
GAG	Glycosaminoglycans
GFAP	Glial Fibrillary Acidic Protein
HDA	1,6-Hexanediamine
HFP	1,1,1,3,3,3-Hexafluoro-2-propanol
iPSC	Induced Pluripotent Stem Cells
LN	Laminin
MAP2	Microtubule Associated Protein 2
MMPs	Matrix Metalloproteinases
NEP	Neuroepithelial Progenitors
NSC	Neural Stem Cells
PAM	Polyacrylamide
PBS	Phosphate Buffer Solution
PCL	Poly(epslon-caprolactone)
PCL-NH_2	Poly(epslon-caprolactone) after Aminolysis
PCL-FN	Poly(epslon-caprolactone) after Fibronectin Immobilization
PCL-LN	Poly(epslon-caprolactone) after Laminin Immobilization
PCL-RGD	Poly(epslon-caprolactone) after RGD motif Immobilization
PDMS	Polydimethyl Siloxane
PEG	Poly(ethylene glycol)
PFA	Paraformaldehyde
PHB	Polyhydroxybutyrate
PLCL	Poly(lactide-co-prolactone)
PLGA	Poly(lactide-co-glycolide)
PLLA	Poly(L-lactide)
PNS	Peripheral Nervous System
PS	Polystyrene
PSA	Poly(sialic acid)
PU	Polyurethane
RG	Radial Glia
RGD	Arginine – Glycine – Aspartic Acid
R-NSC	Rosette-like Structures
RT	Room Temperature
SCI	Spinal Cord Injury
SD	Standard Deviation
SEM	Scanning Electron Microscopy
SE	Standard Error
TIMPs	Tissue Inhibitors Metalloproteinases

Chapter I

Introduction

Chapter I – Introduction

This introductory chapter is organized in four sections. Section one and two provide a general introduction regarding the main context of this work, namely the cell based therapies as a tissue engineering strategy and the potential applications of biomaterial-cell based strategies to CNS regeneration. The third section presents the motivations and the specific aims of this work and the fourth section describes the overall organization of this manuscript, outlined with a short summary of the contents of each chapter.

I.1 – Tissue Engineering and Regenerative Medicine

The field of tissue engineering is defined as the combination of cells and stem cells, biocompatible materials, as a scaffold or matrix, and appropriate biochemical and physical cues to produce new functional tissue structures, in order to repair, upon transplantation, part of an injured tissue or whole organ, restoring its function. Additionally to regenerating purposes, tissue engineering techniques combined with stem cell models are also useful to explore fundamental biological processes for the design of specific tissue structure units with potential applications for disease modeling, drug, diagnostic and toxicology screening platforms, tissue development and morphogenesis studies (Berthiaume et al. 2011; Liu et al. 2013; Merkle and Eggan 2013; Lancaster and Knoblich 2014).

Regenerative medicine comprises the tissue engineering field additionally to a set of multidisciplinary areas such as bioengineering, medicine, nanotechnology, cell biology, biomechanics and materials engineering, and strategies such as gene and cell based therapies and immunomodulation (Salgado et al. 2013). The regenerative medicine emerged from the promising application of stem cells and transplantation techniques combined with biomaterials engineering, with the aim to produce biological equivalent tissue constructs, able to repair at the cellular level and to provide the conditions for the new implantable cells to survive, promoting tissue healing (Langer and Vacanti 1993; Vacanti and Vacanti 2000).

I.1.1 Therapeutic Potential of Stem Cells

Cell based therapies as a regenerative medicine approach, take viable autologous or allogeneic cellular material (tissue specific mature cells or stem cells) to be administered into the patient, injected or transplanted into the injury site, alone or in combination with biomolecules or biomaterials. Another approach is the administration of products (drugs or biological factors) specific for the stimulation of the endogenous stem cells and inducing the activation of the patient immune system and auto regenerative processes. With the continuous developments of stem cell research, stem cell products are emerging with the potential to be applied alone or combined with established therapies to treat a number of diverse conditions, from genetic, degenerative, traumatic or oncologic (Lindvall et al. 2004; Mimeault and Batra 2006). The therapeutic role of the stem cells can be directly regenerative, when integrated into the damaged tissue, or supportive when used as vehicles to deliver biological molecules acting indirectly without integrating into the tissue. (Daley and Scadden 2008; Salgado et al. 2013; Mao and Mooney 2015).

Some concerns need to be taken into account in the application of such cell products. When the donor is distinct from the patient (allogeneic) there is the risk of immunologic reactions such as graft-versus-host disease (GVHD), rejection of the graft, hemolysis and transmission of infectious agents and limited availability of compatible sources. When the cells or tissues derive from non-human animals (xenogeneic), graft rejection and contamination of infectious agents are always major concerns, as these biological materials are usually prepared with animal derived products (fetal bovine serum for example) and those can be a source of contamination (prions). Additionally therapeutic products based on stem cells, specifically from human embryonic origin (ESCs) raises ethical concerns since it depends on a source of human embryos and their destruction. But, the development of induced pluripotent stem cells (iPSCs), and accessibility to placental and umbilical stem cells and adult stem cells are important alternative and reasonable sources. Nevertheless, in vitro ESC derived cell lines are high risk tumorigenic (teratoma formation), and these products demand a high quality assessment in order to ensure the absence of pluripotent cells in the final product. (Berthiaume et al. 2011; Weinberg 2013)

Current FDA approved and licensed standard cell therapy procedures include hematopoietic stem cell transplantation (HSCT) for bone marrow reconstitution using HPC (hematopoietic progenitor cells)

products and epithelial stem cells applied to burn treatments and corneal tissue replacements, HPC products derived from umbilical cord blood for allogeneic HSCT, cartilage repair by autologous cultured chondrocytes, nasolabial folds improvement with autologous fibroblasts, autologous cellular immunotherapy for prostate cancer (Weinberg 2013).

Bone marrow transplantation, for engraftment of hematopoietic stem cells (HSC) to address various hematologic disorders, such as lymphoma and leukemia are known established cell therapies (Siena et al. 2000; Daley and Scadden 2008; Weinberg 2013). The maintenance and homing of the hematopoietic microenvironment is held by the mesenchymal stem cells (MSCs), and a number of clinical studies (osteoarthritis, multiple sclerosis (MS), amyotrophic lateral sclerosis (ALS), GVHD, Crohn's disease, nervous system, cancer, cardiovascular) have shown evidence of MSCs immunomodulatory, angiogenic and anti inflammatory properties, with reduction of apoptosis and fibrosis. Regeneration based on MSCs relies instead on the activity in paracrine and endocrine functions by secretion of trophic factors (cytokines) without MSC differentiation and direct engraftment. Some MSC therapeutic products are approved and available for clinical application, such as Cartistem®, an allogeneic umbilical cord blood-derived mesenchymal stem cell drug for osteoarthritis, or Cupistem®, autologous adipose-derived mesenchymal stem cells for Crohn's fistula. A major challenge in application of MSCs in patients is the low availability of cells, and a high number for infusion is required (cell dose must be around 4-5 million cells/kg body weight) (Siena et al. 2000; Trounson and McDonald 2015; Gao et al. 2016).

Other examples of cell based products are available in the market that provide significant regenerative results, such as Carticel™ that includes harvesting of autologous chondrocytes, ex vivo expansion and implant on the injury site, for the treatment of focal articular cartilage defects from acute or repetitive trauma; laViv™ consists of injections of autologous fibroblasts for improved appearance of nasolabial wrinkles; Epicel® cultured epidermal autografts consists on the application of autologous keratinocytes for regeneration from severe burn hounds; Apligraf® and GINTUIT™ provide allogeneic sources of keratinocytes and fibroblasts (cultured in bovine collagen) for application in mucogengival conditions and in legs and diabetic foot ulcers; Celution® is a medical device product for the extraction of adipose stem cells from liposuction adipose tissue. (Berthiaume et al. 2011; Mao and Mooney 2015)

A recent developed immunotherapy (Kymriah®) based on genetically modified T cell to treat some types of lymphoma and leukaemia that express the CD19 specific marker was approved in August 2017. The artificial receptor, CAR (chimeric antigen receptor) T cell, recognizes specifically cancer cells expressing that marker (Blumenthal and Pazdur 2018 Jan 31).

I.1.1.1 – Challenges in Cell Based Therapies

Several clinical and pre clinical trials have been performed applying autologous stem/progenitor cells to address cardiovascular diseases based on the underlying potential of myocardial regeneration using bone marrow cells. New stem cell therapies have been rapidly translated to clinical practice but important challenges remain such as the knowledge of the mechanism of action, long term niche engraftment, optimal cell types and number of cells isolation, dosage and route of administration. Also manufacture of the cell products such as clinical expansion and maintenance of stemness quality of the cell products are still to be resolved. (Sanganalmath and Bolli 2013; Bartel 2015)

Therefore, the development of manufacture technologies of cell products is necessary, such as the design of bioreactors and processes for stem cell expansion in a systematic, safe, robust and cost-effective way, complying with the established regulation guidelines.

Large scale bioreactors for mammalian cell culture have been developed and implemented for the production of recombinant proteins or monoclonal antibodies, nonetheless the design of the culture device systems and respective bioprocesses for stem cells manufacture must take into account the balanced microenvironment found in in vivo as the final product has to maintain the quality and exact characteristics of the initial cellular sample or expected end product (identity or specific ratio, potency, viability, sterility and purity). Whether the therapeutic strategy is autologous or allogeneic, the manufacture system presents different challenges from a large-scale production perspective. For example with autologous products each batch is unique and patient specific presenting additional process challenges, and the cell product is not readily available as it needs to be produced on demand only after sample collection; in the manufacture of allogeneic products, besides the inherent donor-recipient risks, with one sample from a donor several patients could be treated which simplifies the production process, but in order to have readily available products, extensive culture and long period cryopreservation are needed increasing the risk of cellular modification due to excessive manipulation

additionally to the harvest processing steps necessary after cell culture. In spite of the challenges a leading autologous cell therapy product, Ixmyelocel-T, is under phase II clinical trials, it consists of a selective multicellular expansion of a sample of 50 mL of bone marrow cultured in an automated, fully closed cell-processing system capable of expanding the number of cells up to 300 times than those found in the starting material. The results suggest high potential for long term engraftment to treat dilated cardiomyopathy or critical limb ischemia. (Kirouac and Zandstra 2008; Bartel 2015; Patel et al. 2016)

I.1.2 – Biomaterials in Cell Based Products

Whereas, the use of cell systems alone, i.e. without a biomaterial support, is a valid strategy for many therapies and disease model systems, many applications require and benefit of using cells in combination with scaffolds. Such artificial cell supporting structures offer mechanical support and have important effects such as to increase the rate of cell survival or minimize injected cell loss at the lesion site, as well as to improve graft integration with vascularization and innervation, or activation of host immunomodulation. The use of scaffolds resembling the natural extracellular matrix (ECM) provides important 3D support for cell-cell contact, cell organization within the tissue helping cell attachment and migration, biomechanical properties, and integrates the transmission and diffusion of biological, chemical and physical cues in an adequate porous environment. (Berthiaume et al. 2011; Mao and Mooney 2015)

Some examples of biomaterial based products for regenerative applications are available such as Dermagraft® human fibroblast-derived dermal substitutes as 3D polymer scaffolds for venous ulcers application; DermaPure® provides decellularized dermal allographs from human cadaveric skin; CryoLife® provides decellularized cardiac and vascular tissue. An injectable material designed to meet specific qualities of porosity and reabsorption rates, PuraMatrix™, is composed of small oligopeptide fragments that self assemble into nanofibers resembling the natural ECM. Other biopharmaceuticals based on local delivery of growth factors coupled with a biomaterial such as Regranex® a recombinant platelet-derived growth factor (PDGF) therapy for diabetic neuropathic ulcers, GEM 21S® growth-factor enhanced matrix for dental therapy containing PDGF with an osteoconductive matrix of ß-TCP,

Infuse™ Bone Graft is a natural matrix enriched with the growth factor BMP (bone morphogenic proteins) for dental bone grafting. (Berthiaume et al. 2011; Mao and Mooney 2015)

An important component of the ECM is the fibrous proteins that provide tridimensional structure for cell support. In the very particular case of the neural cell systems, neurons make anisotropic structures to promote orientated neural tissue growth, which can be supported by tailored made biomaterial structures. A brief overview on the use of biomaterials and importance of cell based therapies for neural diseases are provided below.

I.2 – Biomaterial-Cell Based Strategies for CNS Regeneration

The use of stem cell (SC) bioengineering coupled with biomaterials engineering has been an emergent approach with high potential impact on the study the central nervous systems (CNS) injuries and the development of cell based therapies (Shoffstall et al. 2012; Roger Y Tam et al. 2014). This combinatory approach potential relies on the possibility to merge two interesting features:

- SC are appealing for tissue regeneration therapies, since SC are undifferentiated cells with unlimited capacity of self-renewal (and thus it is possible to obtain large amounts of cells from a relative low number) and able to differentiate into fully mature specialized cells (NIH 2001) (to restore or regenerate damaged or non-functional tissue) and,
- the possibility to recreate and model the *in vivo* cell microenvironment by engineering biocompatible and biodegradable materials, where the role of the biomaterial scaffold includes shaping the mechanical and physicochemical properties to the new tissue over its *in-vivo* development and maturation, but also contribute to tissue organization (including anisotropy when required); importantly the scaffold contributes to cell homing, avoiding losses of infused stem cell, adequate surface topology for cell adhesion and shaping and supporting efficient cell migration, proliferation, and ultimately the differentiation and geometrical organization of a mature specialized and fully functional regenerated tissue (Kim et al. 2012).

Examples of interesting studies for neural regeneration include the development of implanted materials, able to stimulate the growth of neurons to be used as nerve grafts in the repair damaged neural tissue. On such studies, natural or engineered synthetic materials had been engineered into

porous scaffolds to stimulate neurite extension and axonal guidance. The combination of such scaffolds with injectable hydrogels allows to build systems for delivering drugs and trophic factors locally (Shoffstall et al. 2012; Roger Y Tam et al. 2014).

Another challenge in neural tissue repair concerns the glial scar formation during astrogliolisis, which it is triggered by subtle or traumatic CNS hounds and inhibits nerve regeneration due to the activation of natural inhibitors such as neurite outgrowth inhibitor and myelin-associated glycoprotein (Sofroniew 2009). In this study a engineered biomaterial was designed to address these biological phenomena smoothing healing process and mitigating scar formation, moreover this particular case application to the patient is possible using minimum invasion techniques (Shoffstall et al. 2012).

The natural cell niche and primary structure, the extracellular matrix (ECM), is a complex environment composed by proteins and polysaccharides, as well as a pool of soluble growth factors and molecules involved in signaling pathways. The ECM is crucial to provide a physical support of adherent cells, as well as to mediate biological and mechanical stimuli that will determine cell fate. The use of biomaterials to reproduce the properties of the ECM providing a support and organization of the NSC culture can actually contribute to the regeneration therapies regarding the CNS. Namely, recreation of the *in-vivo* microenvironment using materials that display adequate specific mechanical, structural and geometric properties, while providing natural stimuli for cell adhesion and soluble or immobilized signals to direct cell fate, is at center of current trends of strategies that combine biomaterials and stem cells to engineering regeneration of neural tissue.

I.2.1 – Overview on CNS Injuries and Available Therapeutic Strategies

Central nervous system (CNS) injuries can be caused by infection, ischemia, trauma or neurodegenerative diseases and represent an important concern in present society due to the economic and social burden associated with care of the affected individuals (WHO | Neurological Disorders 2006; Lunn et al. 2011; WHO | International perspectives on spinal cord injury 2013). Cell based therapies applications to traumatic injury or neurodegenerative diseases are gaining attention, since they have the potential to promote neural tissue regeneration and thus provide therapeutic solutions in cases where there is no available effective treatment solutions (Sloane et al. 2002; Lunn et al. 2011).

The death of neurons, glia cells and oligodendrocytes in the brain, spinal cord and retina results in the general degeneration of the sensory, motor and cognitive functions (Roger Y. Tam et al. 2014). Such loss of those specialized cells affects abilities such as emotional behavior, memory, learning and communication, among others, which is a direct consequence of the destruction of the extracellular matrix structure in the lesion site, lack of axon-growth factors and presence of neuron regeneration inhibitors driven from the scaring process (Roger Y. Tam et al. 2014).

To develop potential therapies, it is crucial to access the relevant cell populations. The use of endogenous SC, multipotent neural stem cells (NSC), able of high proliferations in *in-vitro* cultures and to differentiate into the main cell types of the CNS, neurons, astrocytes and oligodendrocytes has a great potential in cell replacement and tissue regeneration (Aboody et al. 2011; Roger Y. Tam et al. 2014). Endogenous NSC can be found in fetal brain or in specific adult CNS regions where neurogenesis is active. The use of drugs, neurotrophic factors and cytokines, without requiring cell transplantation, for stimulation *in situ* on the damaged region to promote regeneration is a therapeutic possibility (Aboody et al. 2011; Roger Y. Tam et al. 2014). Exogeneous transplantation of NSC on the injury site allows replacing lost cells, repairing damaged cells by remyelination or stimulating the environment for regeneration by providing trophic support (Kim et al. 2012). Sourcing fetal cells carries on ethical issues and the isolation of adult cells in relevant amounts is challenging and carries risk to the patient. Pluripotent embryonic stem cells (ESC) and induced pluripotent stem cells (iPSC) are, thus additional alternative sources of NSC.

The emergence of bioengineering approaches, merging the fields of biology, materials and engineering allowed to develop further technologies and tools able to support further studies for understanding the basic nature of neural disorders and to develop and implement cell based therapies. The current thesis aims to contribute to such effort. Cell replacement therapies addressing neurological disorders have been developed as potential clinical applications and brief examples of therapeutic needs for neurological related diseases are listed below (Table I.1).

Table I.1 – Brief overview of neurological related diseases and examples of therapeutic strategies.

Problem	*Cause and Prevalence*	*Strategies*	*Challenges*	*References*
Spinal cord injury	• Traumatic compression of the spinal cord; loss of motor and sensory functions below the lesion site; • 15 – 40 cases per million per year worldwide.	• Neural cell replacement for neuroprotection and axon regeneration; • PhaseI/II clinical trial with transplantation of NSPCs.	• Ethical problems; autologous cells not available.	(Ackery et al. 2004; Tewarie et al. 2009; Willerth 2011; Mothe and Tator 2012)
Parkinson's disease	• Gradual loss of midbrain dopamine neurons; loss of motor function (resting tremor, rigidity, hypokinesia); • Most prevalent neurodegenerative disease, affects 2% of individuals above 65 years worldwide.	• Mesencephalic fetal tissue transplants rich in dopaminergic neurons into the striatum brain of patients.	• Ethical problems, availability limitations, sample variability.	(Lindvall and Björklund 2004; Arenas 2010; Lindvall and Kokaia 2010)
Alzheimer's disease	• Protein plaques deposition leading to loss of neurons and neuron communication (loss of memory, dementia, cognitive decline; • 26.6 million elderly affected worldwide, and expected to quadruplicate by 2050.	• Administration of stem cells for growth factor release to stimulate endogenous regeneration; • PhaseI/II clinical trial to delivery of nerve growth factor (NGS) to prevent cell death and stimulate cell function.		(Tuszynski et al. 2005; Brookmeyer et al. 2007; Kim and de Vellis 2009; Lindvall and Kokaia 2010)
Ischemic stroke	• Vascular obstruction in the brain: 80 – 85% by thromboembolism, 15 – 20% hypertension or vessel hemorrhage (tissue necrosis, loss of neurons and glia); • One in every six elderly individuals affected worldwide	• Transplantation of stem cell grafts and endogenous stimulation with promising results; • Stimulation of neurogenesis with hepatocyte growth factor as a potential strategy.	• Very small endogenous recovery;	(Kelly et al. 2004; Pollock et al. 2006; Lindvall and Kokaia 2010; Shang et al. 2011; Kalladka and Muir 2014)
Huntington's disease	• Autosomal dominant neurodegenerative disease with degeneration of neurons (progressive motor dysfunction, cognitive decline, psychiatric disturbances); • 4 – 10 individuals per 100000, are affected in western countries.	• Replacement of embryonic/fetal grafts relieves motor and cognitive dysfunctions (animal models and clinical trials); • Replacement of endogenous cells, delivery of neurotrophic factors and stimulation of neurogenesis.	• Ethical concerns with embryonic/fetal grafts	(Curtis et al. 2003; Song et al. 2007; Clelland et al. 2008; Ross and Tabrizi 2011; Maucksch et al. 2013)
Amyotrophic lateral sclerosis	• Rare incurable disease with the progressive degeneration of the motor system with total loss of motor neurons in CNS; • 1.5 to 2.5 individuals are affected in 100000 per year.	• Trophic support to control neuron degeneration by stem cell transplantation; • Phase I clinical trial: lumbar intraspinal of neural stem cells with promising improvement on endogenous neurons survival and motor recovery; • Phase I clinical trial with MSCs transplant into the spinal cord for the stimulation of immunomodulatory effects.		(Cizkova et al. 2007; Logroscino et al. 2008; Henkel et al. 2009; Lindvall and Kokaia 2010; Mazzini et al. 2010; Glass et al. 2012)
Multiple sclerosis	• Inflammatory autoimmune CNS disease; axon myelin destruction and formation of plaques with destruction of neurons; sensory and motor disturbance of limbs, visual loss; • 1.1 – 1.2 million cases with twice the prevalence in women.	• Clinical trials using autologous transplanted MSCs or iPSCs with promising neuroprotective effects.	• The transplanted cells can be destroyed due to the inflammatory reaction.	(Stüve and Oksenberg 1993; Pugliatti et al. 2002; Pugliatti et al. 2006; Lassmann et al. 2007; Aharonowiz et al. 2008; Yamout et al. 2010; Connick et al. 2012; Douvaras et al. 2014)

I.3 - Thesis Motivation, Aim and Challenges

This project is focused on engineering biomaterials, using the electrospinning technique to build functional nanofiber based scaffolds and apply them to *ex-vivo* neural stem cells (NSC) culture. The overall aim of this thesis is to establish a scalable platform that contributes to the study and therapy of CNS related diseases using neural stem cells cultured under dynamic conditions supported by anisotropic scaffolds.

This thesis addresses the following three challenges:

- Development of scaffolds that allow in situ expansion and differentiation of NSCs. It is important that such scaffolds are biodegradable, able to promote cell adhesion, align and elongate cells and provide geometrical cues for cell differentiation.
- Design a new device able to support stem cultivation in electrospun fibers under dynamic conditions. This device should allow a homogenous mixing for several electrospun fiber meshes at once, to control mixing for optimal mass transfer of nutrients and inhibitory compounds with minimal negative effects of shear stress on cells. Moreover the device should be easy to manipulate, to sterilize and fitting commercial available cell culture incubators.
- Provide a positive example, testing the hypothesis that NSCs culture benefit from appropriate conjugation of scaffold geometry, proper adhesion cues and dynamic conditions.

The first challenge addressed in this work is to establish a platform of scaffolds for in situ expansion and differentiation of NSCs envisaged for the culture of tissue constructs, suitable to be transplanted for CNS injuries applications, or for research applications. The features identified as key for the development of such scaffold were:

(i) Biodegradability, for erosion when implanted in-vivo, but not during ex-vivo stage,

(ii) Anisotropy, for guiding and organization of neural tissue

(iii) Fibrous structure with diameters adequate to mimic ECM structure and adequate cell sensing of surface (at hundred-nano/deci-micro scale dimensions)

(iv) Surface modification with biological motifs that promote adequate cell adhesion and organization along scaffold structure, such material functionalization is required to promote a specific cell response or function, such as tissue organization or cell differentiation prior to transplantation.

The NSC fate, self-renewal and differentiation, is evaluated according to the stimulus provided by the structural and physicochemical properties of the scaffold.

The second challenge to be addressed is to perform the culture of neural stem cells, supported in the nanofibers, under dynamic conditions. The production of a tissue construct requires a stage of ex-vivo cell cultivation. This stage aims at ex-vivo cell seeding, proliferation and, depending of the strategy followed, differentiation of cells in the scaffold. The obtained construct is desired to be robust for potential applications as an implant suitable for in vivo maturation or to be applied as a disease model platform. Culture of SC within nanofiber scaffolds is usually performed in static systems, overlooking the effects of shear stress. To address this factor the following actions were carried out:

(i) A bioreactor able to accommodate a scaffold platform was designed and constructed specifically for neural stem cells cultivation in electrospun fibers.

(ii) The bioreactor was characterized through investigation of the flow dynamic profile and wall shear stress by computational fluid dynamics (CFD), complemented by mass transfer data obtained by a hydrodynamic voltammetry technique.

The third challenge to be addressed is the development of a scalable system, suitable to perform ex-vivo culture of NSC in the nanofiber scaffolds. Scalability is required for a systematic production of tissue transplants, or tissue engineered platforms. In that context:

(i) The novel nanofiber-bioreactor system was designed as a stirred “plate and frame” vessel, providing a dynamic scalable system

(ii) Such system was assessed for neural stem cell (NSC) expansion and differentiation within the scaffolds.

The projected system is envisaged for further development in order to meet certain criteria namely it’s applicability to biological needs, suitable to comply with regulation requirements,

and general conditions such as scalability (scale up, scale out), reproducibility, robustness, automation (sterilization, manipulation, scaffold insertion, media replacement), mixing control and monitoring (homogeneity, shear stress).

I.4 - Thesis Outline

This thesis is organized into six chapters. Chapter I introduces the context of this work, main aims and motivation. Chapter II provides a relevant literature review to support the studies developed in this thesis. Chapters III, IV and V correspond to the presentation of the most important results obtained throughout the course of this thesis and respective discussion. Each of these chapters is organized in sub sections, that include: an *Abstract,* with the summary of the chapter contents; a brief *Introduction* to the specific topic addressed; the *Materials and Methods* with the description of the experimental methods and techniques used; the *Results and Discussion*, where the obtained results are presented and discussed against the literature; the *Conclusions* that summarize the overall main conclusions of the chapter. Finally, in Chapter VI the general thesis conclusions are reviewed along with remarks on future work perspectives. Briefly a short description of the following chapters:

Chapter II - Literature Review

A concise literature review of the most relevant subjects within the context of this thesis is presented, including the definition of stem cells, their properties, sources, culture and regulation of cell fate. An overview on the use of materials to mimic the extracellular matrix, including the description of the electrospinning technique and approaches for functionalization of scaffolds, and description of relevant biological, topological and mechanic cues is provided. Current literature concerning bioreactors development for cell culture in scaffolds is mentioned at the end of the chapter.

Chapter III - Neural Stem Cell Culture in Functionalized Nanofibers: Cell Morphology and Organization

This chapter describes the experimental results obtained for NSCs cultured on aligned and randomly distributed poly-epsilon-caprolactone (PCL) nanofibers prepared by electrospinning and functionalized with ECM motifs for cell adhesion such as laminin and GRGDSP. The aligned topology of the nanofibers and presence of adhesion factors was evaluated regarding NSC alignment and elongation after cell expansion, and neuron elongation and alignment after differentiation.

Chapter IV - Design and Characterization of a Stirred Bioreactor Enclosing Nanofibers

A novel bioreactor was designed and a prototype was constructed. This concept was designed as a stirred vessel able to accommodate six units of nanofiber scaffolds. The prototype was characterized relative to mixing effectiveness and CFD for evaluation of the fluid velocity and shear stress. Calculated values were complemented with data obtained from limiting current experiments from which mass transfer coefficients were estimated.

Chapter V - Dynamic Culture of Neural Stem Cells Supported in Nanofiber Scaffolds

An evaluation on the NSC organization and distribution in nanofiber matrices was performed in dynamic culture conditions. NSCs proliferation was first assessed in PCL nanofiber scaffolds at different hydrodynamic conditions. NSC were cultured, in RGD and laminin functionalized aligned PCL nanofibers in different velocity mixing conditions.

Chapter VI - General Conclusions and Future Perspective

The main conclusions and general comments are presented, regarding the main outcomes from the previous chapters, and future work approaches are suggested.

All experimental work was performed at the SCERG (Stem Cell Engineering Research Group) group facilities, from the Bioengineering Department in Instituto Superior Técnico, located in Taguspark campus in Oeiras. SEM and confocal microscopy analysis were performed at Instituto Superior Técnico in Alameda campus, in Microlab Electron Microscopy Laboratory from ICEMS (Institute of Materials and Surfaces Sciences and Engineering) and in CQFM (Centro de Química Física Molecular) facilities, respectively.

References

Aboody K, Capela A, Niazi N, Stern JH, Temple S. 2011. Translating stem cell studies to the clinic for CNS repair: current state of the art and the need for a Rosetta stone. Neuron. 70(4):597–613. doi:10.1016/j.neuron.2011.05.007.

Ackery A, Tator C, Krassioukov A. 2004. A Global Perspective on Spinal Cord Injury Epidemiology. J Neurotrauma. 21(10):1355–1370. doi:10.1089/neu.2004.21.1355.

Aharonowiz M, Einstein O, Fainstein N, Lassmann H, Reubinoff B, Ben-Hur T. 2008. Neuroprotective Effect of Transplanted Human Embryonic Stem Cell-Derived Neural Precursors in an Animal Model of Multiple Sclerosis. Aboody KS, editor. PLoS ONE. 3(9):e3145. doi:10.1371/journal.pone.0003145.

Arenas E. 2010. Towards stem cell replacement therapies for Parkinson's disease. Biochem Biophys Res Commun. 396(1):152–156. doi:10.1016/j.bbrc.2010.04.037.

Bartel RL. 2015. Chapter 8 - Stem Cells and Cell Therapy: Autologous Cell Manufacturing. In: Translational Regenerative Medicine. Boston: Academic Press. p. 107–112. [accessed 2018 Jun 2]. https://www.sciencedirect.com/science/article/pii/B9780124103962000086.

Berthiaume F, Maguire TJ, Yarmush ML. 2011. Tissue Engineering and Regenerative Medicine: History, Progress, and Challenges. Annu Rev Chem Biomol Eng. 2(1):403–430. doi:10.1146/annurev-chembioeng-061010-114257.

Blumenthal GM, Pazdur R. 2018 Jan 31. Approvals in 2017: gene therapies and site-agnostic indications. Nat Rev Clin Oncol. doi:10.1038/nrclinonc.2018.11. [accessed 2018 May 31]. https://www.nature.com/articles/nrclinonc.2018.11.

Brookmeyer R, Johnson E, Ziegler-Graham K, Arrighi HM. 2007. Forecasting the global burden of Alzheimer's disease. Alzheimers Dement. 3(3):186–191. doi:10.1016/j.jalz.2007.04.381.

Cizkova D, Kakinohana O, Kucharova K, Marsala S, Johe K, Hazel T, Hefferan MP, Marsala M. 2007. Functional recovery in rats with ischemic paraplegia after spinal grafting of human spinal stem cells. Neuroscience. 147(2):546–560. doi:10.1016/j.neuroscience.2007.02.065.

Clelland CD, Barker RA, Watts C. 2008. Cell therapy in Huntington disease. Neurosurg Focus. 24(3–4):E9. doi:10.3171/FOC/2008/24/3-4/E8.

Connick P, Kolappan M, Crawley C, Webber DJ, Patani R, Michell AW, Du M-Q, Luan S-L, Altmann DR, Thompson AJ, et al. 2012. Autologous mesenchymal stem cells for the treatment of secondary progressive multiple sclerosis: an open-label phase 2a proof-of-concept study. Lancet Neurol. 11(2):150–156. doi:10.1016/S1474-4422(11)70305-2.

Curtis MA, Penney EB, Pearson AG, Roon-Mom WMC van, Butterworth NJ, Dragunow M, Connor B, Faull RLM. 2003. Increased cell proliferation and neurogenesis in the adult human Huntington's disease brain. Proc Natl Acad Sci. 100(15):9023–9027. doi:10.1073/pnas.1532244100.

Daley GQ, Scadden DT. 2008. Prospects for stem cell-based therapy. Cell. 132(4):544–548. doi:10.1016/j.cell.2008.02.009.

Douvaras P, Wang J, Zimmer M, Hanchuk S, O'Bara MA, Sadiq S, Sim FJ, Goldman J, Fossati V. 2014. Efficient Generation of Myelinating Oligodendrocytes from Primary

Progressive Multiple Sclerosis Patients by Induced Pluripotent Stem Cells. Stem Cell Rep. 3(2):250–259. doi:10.1016/j.stemcr.2014.06.012.

Gao F, Chiu SM, Motan DAL, Zhang Z, Chen L, Ji H-L, Tse H-F, Fu Q-L, Lian Q. 2016. Mesenchymal stem cells and immunomodulation: current status and future prospects. Cell Death Dis. 7(1):e2062. doi:10.1038/cddis.2015.327.

Glass JD, Boulis NM, Johe K, Rutkove SB, Federici T, Polak M, Kelly C, Feldman EL. 2012. Lumbar Intraspinal Injection of Neural Stem Cells in Patients with Amyotrophic Lateral Sclerosis: Results of a Phase I Trial in 12 Patients. STEM CELLS. 30(6):1144–1151. doi:10.1002/stem.1079.

Harman D. 2006. Alzheimer's Disease Pathogenesis. Ann N Y Acad Sci. 1067(1):454–460. doi:10.1196/annals.1354.065.

Henkel JS, Beers DR, Zhao W, Appel SH. 2009. Microglia in ALS: the good, the bad, and the resting. J Neuroimmune Pharmacol Off J Soc NeuroImmune Pharmacol. 4(4):389–398. doi:10.1007/s11481-009-9171-5.

Kalladka D, Muir KW. 2014. Brain repair: cell therapy in stroke. Stem Cells Cloning Adv Appl. 7:31–44. doi:10.2147/SCCAA.S38003.

Kelly S, Bliss TM, Shah AK, Sun GH, Ma M, Foo WC, Masel J, Yenari MA, Weissman IL, Uchida N, et al. 2004. Transplanted human fetal neural stem cells survive, migrate, and differentiate in ischemic rat cerebral cortex. Proc Natl Acad Sci U S A. 101(32):11839–11844. doi:10.1073/pnas.0404474101.

Kim H, Cooke MJ, Shoichet MS. 2012. Creating permissive microenvironments for stem cell transplantation into the central nervous system. Trends Biotechnol. 30(1):55–63. doi:10.1016/j.tibtech.2011.07.002.

Kim SU, de Vellis J. 2009. Stem cell-based cell therapy in neurological diseases: A review. J Neurosci Res. 87(10):2183–2200. doi:10.1002/jnr.22054.

Kirouac DC, Zandstra PW. 2008. The systematic production of cells for cell therapies. Cell Stem Cell. 3(4):369–381. doi:10.1016/j.stem.2008.09.001.

Lancaster MA, Knoblich JA. 2014. Organogenesis in a dish: Modeling development and disease using organoid technologies. Science. 345(6194):1247125. doi:10.1126/science.1247125.

Langer R, Vacanti JP. 1993. Tissue engineering. Science. 260(5110):920–926.

Lassmann H, Brück W, Lucchinetti CF. 2007. The Immunopathology of Multiple Sclerosis: An Overview. Brain Pathol. 17(2):210–218. doi:10.1111/j.1750-3639.2007.00064.x.

Lindvall O, Björklund A. 2004. Cell Therapy in Parkinson's Disease. NeuroRX. 1(4):382–393. doi:10.1602/neurorx.1.4.382.

Lindvall O, Kokaia Z. 2010. Stem cells in human neurodegenerative disorders — time for clinical translation? J Clin Invest. 120(1):29–40. doi:10.1172/JCI40543.

Lindvall O, Kokaia Z, Martinez-Serrano A. 2004. Stem cell therapy for human neurodegenerative disorders - how to make it work. Nat Med. 10(7):S42–S50. doi:10.1038/nm1064.

Liu W, Deng Y, Liu Y, Gong W, Deng W. 2013. Stem cell models for drug discovery and toxicology studies. J Biochem Mol Toxicol. 27(1):17–27. doi:10.1002/jbt.21470.

Logroscino G, Traynor BJ, Hardiman O, Chio' A, Couratier P, Mitchell JD, Swingler RJ, Beghi E, Eurals F. 2008. Descriptive epidemiology of amyotrophic lateral sclerosis: new evidence and unsolved issues. J Neurol Neurosurg Psychiatry. 79(1):6–11. doi:10.1136/jnnp.2006.104828.

Lunn JS, Sakowski SA, Hur J, Feldman EL. 2011. Stem Cell Technology for Neurodegenerative Diseases. Ann Neurol. 70(3):353–361. doi:10.1002/ana.22487.

Mao AS, Mooney DJ. 2015. Regenerative medicine: Current therapies and future directions. Proc Natl Acad Sci. 112(47):14452–14459. doi:10.1073/pnas.1508520112.

Maucksch C, Vazey EM, Gordon RJ, Connor B. 2013. Stem cell-based therapy for Huntington's disease. J Cell Biochem. 114(4):754–763. doi:10.1002/jcb.24432.

Mazzini L, Ferrero I, Luparello V, Rustichelli D, Gunetti M, Mareschi K, Testa L, Stecco A, Tarletti R, Miglioretti M, et al. 2010. Mesenchymal stem cell transplantation in amyotrophic lateral sclerosis: A Phase I clinical trial. Exp Neurol. 223(1):229–237. doi:10.1016/j.expneurol.2009.08.007.

Merkle FT, Eggan K. 2013. Modeling Human Disease with Pluripotent Stem Cells: from Genome Association to Function. Cell Stem Cell. 12(6):656–668. doi:10.1016/j.stem.2013.05.016.

Miljan EA, Sinden JD. 2009. Stem cell treatment of ischemic brain injury. Curr Opin Mol Ther. 11(4):394–403.

Mimeault M, Batra SK. 2006. Concise Review: Recent Advances on the Significance of Stem Cells in Tissue Regeneration and Cancer Therapies. STEM CELLS. 24(11):2319–2345. doi:10.1634/stemcells.2006-0066.

Mothe AJ, Tator CH. 2012. Advances in stem cell therapy for spinal cord injury. J Clin Invest. 122(11):3824–3834. doi:10.1172/JCI64124.

NIH. 2001. Stem Cells: Scientific Progress and Future Research Directions [Stem Cell Information]. [accessed 2015 Nov 2]. http://stemcells.nih.gov/info/2001report/pages/2001report.aspx.

Patel AN, Henry TD, Quyyumi AA, Schaer GL, Anderson RD, Toma C, East C, Remmers AE, Goodrich J, Desai AS, et al. 2016. Ixmyelocel-T for patients with ischaemic heart failure: a prospective randomised double-blind trial. The Lancet. 387(10036):2412–2421. doi:10.1016/S0140-6736(16)30137-4.

Pollock K, Stroemer P, Patel S, Stevanato L, Hope A, Miljan E, Dong Z, Hodges H, Price J, Sinden JD. 2006. A conditionally immortal clonal stem cell line from human cortical neuroepithelium for the treatment of ischemic stroke. Exp Neurol. 199(1):143–155. doi:10.1016/j.expneurol.2005.12.011.

Pugliatti M, Rosati G, Carton H, Riise T, Drulovic J, Vécsei L, Milanov I. 2006. The epidemiology of multiple sclerosis in Europe. Eur J Neurol. 13(7):700–722. doi:10.1111/j.1468-1331.2006.01342.x.

Pugliatti M, Sotgiu S, Rosati G. 2002. The worldwide prevalence of multiple sclerosis. Clin Neurol Neurosurg. 104(3):182–191. doi:10.1016/S0303-8467(02)00036-7.

Ross CA, Tabrizi SJ. 2011. Huntington's disease: from molecular pathogenesis to clinical treatment. Lancet Neurol. 10(1):83–98. doi:10.1016/S1474-4422(10)70245-3.

Salgado AJ, Oliveira JM, Martins A, Teixeira FG, Silva NA, Neves NM, Sousa N, Reis RL. 2013. Tissue engineering and regenerative medicine: past, present, and future. Int Rev Neurobiol. 108:1–33. doi:10.1016/B978-0-12-410499-0.00001-0.

Sanganalmath SK, Bolli R. 2013. Cell Therapy for Heart Failure: A Comprehensive Overview of Experimental and Clinical Studies, Current Challenges, and Future Directions. Circ Res. 113(6):810–834. doi:10.1161/CIRCRESAHA.113.300219.

Shang J, Deguchi K, Ohta Y, Liu N, Zhang X, Tian F, Yamashita T, Ikeda Y, Matsuura T, Funakoshi H, et al. 2011. Strong neurogenesis, angiogenesis, synaptogenesis, and antifibrosis of hepatocyte growth factor in rats brain after transient middle cerebral artery occlusion. J Neurosci Res. 89(1):86–95. doi:10.1002/jnr.22524.

Shoffstall AJ, Taylor DM, Lavik EB. 2012. Engineering therapies in the CNS: what works and what can be translated. Neurosci Lett. 519(2):147–154. doi:10.1016/j.neulet.2012.01.058.

Siena S, Schiavo R, Pedrazzoli P, Carlo-Stella C. 2000. Therapeutic relevance of CD34 cell dose in blood cell transplantation for cancer therapy. J Clin Oncol Off J Am Soc Clin Oncol. 18(6):1360–1377.

Sloane PD, Zimmerman S, Suchindran C, Reed P, Wang L, Boustani M, Sudha S. 2002. The Public Health Impact of Alzheimer's Disease, 2000–2050: Potential Implication of Treatment Advances. Annu Rev Public Health. 23(1):213–231. doi:10.1146/annurev.publhealth.23.100901.140525.

Sofroniew MV. 2009. Molecular dissection of reactive astrogliosis and glial scar formation. Trends Neurosci. 32(12):638–647. doi:10.1016/j.tins.2009.08.002.

Song J, Lee S-T, Kang W, Park J-E, Chu K, Lee S, Hwang T, Chung H, Kim M. 2007. Human embryonic stem cell-derived neural precursor transplants attenuate apomorphine-induced rotational behavior in rats with unilateral quinolinic acid lesions. Neurosci Lett. 423(1):58–61. doi:10.1016/j.neulet.2007.05.066.

Stüve O, Oksenberg J. 1993. Multiple Sclerosis Overview. In: Pagon RA, Adam MP, Ardinger HH, Wallace SE, Amemiya A, Bean LJ, Bird TD, Fong C-T, Mefford HC, Smith RJ, et al., editors. GeneReviews(®). Seattle (WA): University of Washington, Seattle. [accessed 2015 Nov 1]. http://www.ncbi.nlm.nih.gov/books/NBK1316/.

Tam Roger Y, Fuehrmann T, Mitrousis N, Shoichet MS. 2014. Regenerative Therapies for Central Nervous System Diseases: a Biomaterials Approach. Neuropsychopharmacology. 39(1):169–188. doi:10.1038/npp.2013.237.

Tam Roger Y., Fuehrmann T, Mitrousis N, Shoichet MS. 2014. Regenerative Therapies for Central Nervous System Diseases: a Biomaterials Approach. Neuropsychopharmacology. 39(1):169–188. doi:10.1038/npp.2013.237.

Tewarie RSN, Hurtado A, Bartels RH, Grotenhuis A, Oudega M. 2009. Stem Cell–Based Therapies for Spinal Cord Injury. J Spinal Cord Med. 32(2):105–114.

Trounson A, McDonald C. 2015. Stem Cell Therapies in Clinical Trials: Progress and Challenges. Cell Stem Cell. 17(1):11–22. doi:10.1016/j.stem.2015.06.007.

Tuszynski MH, Thal L, Pay M, Salmon DP, U HS, Bakay R, Patel P, Blesch A, Vahlsing HL, Ho G, et al. 2005. A phase 1 clinical trial of nerve growth factor gene therapy for Alzheimer disease. Nat Med. 11(5):551–555. doi:10.1038/nm1239.

Vacanti JP, Vacanti CA. 2000. CHAPTER 1 - THE HISTORY AND SCOPE OF TISSUE ENGINEERING. In: Vacanti RPLL, editor. Principles of Tissue Engineering (Second Edition). San Diego: Academic Press. (Tissue Engineering Intelligence Unit). p. 3–7. [accessed 2015 Nov 2]. http://www.sciencedirect.com/science/article/pii/B9780124366305500052.

Weinberg RS. 2013. Chapter 81 - Overview of Cellular Therapy. In: Shaz BH, Hillyer CD, Roshal M, Abrams CS, editors. Transfusion Medicine and Hemostasis (Second Edition). San Diego: Elsevier. p. 533–540. [accessed 2018 May 23]. https://www.sciencedirect.com/science/article/pii/B9780123971647000811.

WHO | International perspectives on spinal cord injury. 2013. WHO. [accessed 2015 Oct 31]. http://www.who.int/disabilities/policies/spinal_cord_injury/en/.

WHO | Neurological Disorders: Public Health Challenges. 2006. WHO. [accessed 2015 Oct 31]. http://www.who.int/mental_health/neurology/neurodiso/en/.

Willerth SM. 2011. Neural tissue engineering using embryonic and induced pluripotent stem cells. Stem Cell Res Ther. 2(2):17. doi:10.1186/scrt58.

Yamout B, Hourani R, Salti H, Barada W, El-Hajj T, Al-Kutoubi A, Herlopian A, Baz EK, Mahfouz R, Khalil-Hamdan R, et al. 2010. Bone marrow mesenchymal stem cell transplantation in patients with multiple sclerosis: A pilot study. J Neuroimmunol. 227(1–2):185–189. doi:10.1016/j.jneuroim.2010.07.013.

Chapter II

State of The Art

Chapter II – State of The Art

Since the emerging of tissue engineering, in the last 20 years, a variety of different approaches have been proposed to develop scaffolds of different levels of geometries and complexities. Regardless the complexity of the natural tissues, the design of scaffolds can be extremely simplified to provide 3 key features which are identified as crucial on giving initial cues to the NSC to organize themselves and produce tissue of high quality: i) promotion of cell adhesion, ii) topologies and geometries able to provide cell orientation and alignment, iii) biological, physical and chemical cues to direct cell fate (self renewal and differentiation).

This literature review includes two sections focus in the cells: Embryonic and Adult Stem Cell (II.1), Neural Stem Cells (II.2); a section focus on the biomaterials, (II.3), with a particular emphasis to nanofiber scaffolds and a final section concerning bioreactors for stem cells (II.4).

The first two subsections II.1 and II.2 provide context embryonic stem cells and neural stem cells and elaborate on neural stem cells. In light of this background, ethical issues, difficulties to harvest human neural stem cells, reproducibility issues and targeting cell-material interface systems, it was decided to use two NSC cell models to develop the work on this thesis, CGR8-NS and ReNcell; details on each of the models are presented in Chapter III and V respectively. NSC isolation and culture, concerning media and supplemented grow factors are discussed in chapter II.

In this thesis production of nanofibers by electrospinning was selected as a simpler technique to prepare scaffolds with interesting features to support NSC culture. Chapter II.3 discusses biomaterials aspects. The several materials previously used for NSC culture are discussed in section II.3.1. In the current work it was decided to use polycaprolactone, due to its biocompatibility, slow biodegradation, cost effectiveness and easy to be functionalized (II.3.6). NSC adhesion is favored by the use of specific adhesion proteins and motifs as revised in section II.3.2, it was decided to explore PCL functionalization with laminin and GRGDSP. NSC culture fate is dependent on scaffold topology and stiffness as discussed in section II.3.3. Bearing in mind the information retrieved from this sections it was decided to

manufacture fiber scaffolds using electrospinning, which provide interesting topologies and aligned geometries. Section II.3.5 describes the electrospinning method and section II.3.6 describes the PCL fibers functionalization. The decisions considering the use of PCL, electrospinning and adhesion motifs, as well as comparison with previous work done, is further discussed in chapter III. Briefly, electrospun nanofibers have been reported to be successful to support NCS expansion and differentiation. The information collected from such studies allowed to make a rational design of our scaffold using aligned nanofibers with thicknesses around 300 – 750 nm of a biodegradable material polycaprolactone covalently functionalized with laminin and GRGDSP adhesion factor, rather than use non-biodegradable materials coated or blended with natural materials. Importantly this study privileges the use of adhesion factor rather than the use of cues for self renewal/differentiation (as those can easily be added to the culture over time) and provides a comparison with the use of non functionalized material. Further discussion of the rational taken considering the state of the art can be found in section II.3.4.

Chapter II.4 Describes bioreactors systems for stem cell culture starting with an overview on bioreactor systems and the main features controlled by those, followed by an highlight of specific works that design bioreactors for cell culture in electrospun fibers. The previous reported work is focused on the use of perfusion systems, rotary wall vessel bioreactor or adapted spinner flasks. While perfusion systems using pumps are prompted to contamination, scaffolds in rotating wall vessels and spinner flasks are interesting configurations of dynamic culture to be used in laboratory but non scalable. Considering the scarcity of works in this field, a main contribution of this thesis is the development of a scalable system for dynamic culture of NSC in electrospun nanofiber meshes which allows for liquid perfusion without the use of pumps but instead promoting fluid movement with stirring. This system was built to allow easy sterilization and to facilitate its stand alone use in commercial available cell culture incubators.

II.1 - Embryonic and Adult Stem Cells

Stem cells are characterized by the indefinite self-renewal capacity, producing identical progeny, and under specific physiological conditions are able to differentiate into mature cells with specific tissue function (for example skin, neurons, cardiomyocytes, blood cells) (NIH 2001). As illustrated in Figure II.1 stem cells may be defined, according to the capacity of generating specialized cells in: totipotent, which is the capacity to originate an entire organism, as is the case of the fertilized egg; pluripotent, corresponding to the ability to generate the three primary germ layers (ectoderm, mesoderm, endoderm) related to the different types of tissue of the organism, which is the case of the inner cell mass of the blastocyst; multipotent, as the capacity of generating multiple, but limited cell types within a tissue type (NIH 2001).

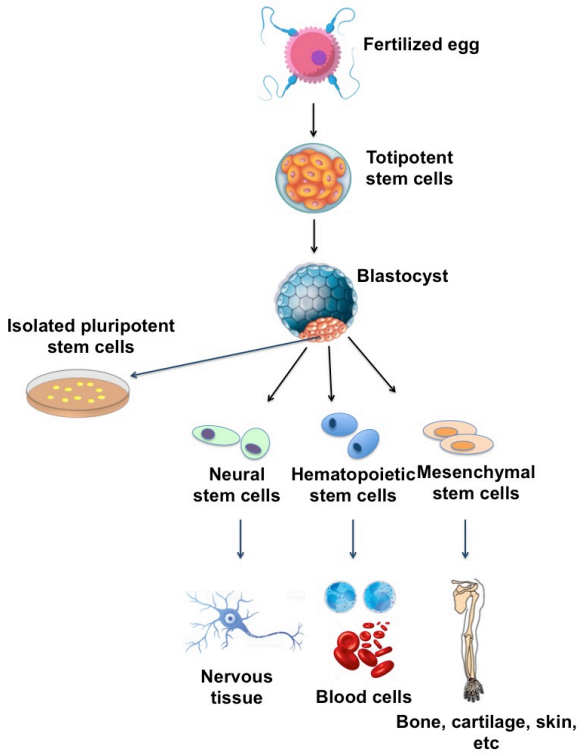

Figure II.1 – Stem cell types derived from the pluripotent stem cells of the blastocyst.

Sources of stem cells are found in embryonic and adult tissues. Pluripotent embryonic stem (ES) cells are isolated from the blastocyst, and can be expanded in *in vitro* cultures. The expansion of ES cells, derived from mouse and human embryos, was accomplished for the

first time as described by Evans and Kaufman (Evans and Kaufman 1981) and Thomson (Thomson et al. 1998), respectively.

A discovery of a new source of pluripotent SC was accomplished by Takahashi and Yamanaka (Takahashi and Yamanaka 2006; Takahashi et al. 2007; Yu et al. 2007), by successfully reprograming adult mature cells (fibroblasts) back into a primitive pluripotent state, so nominated as induced pluripotent stem (iPS) cells. A new reprograming strategy was developed where the pluripotent state is bypassed, meaning that differentiated neurons, designated as induced neurons (iN), were generated directly in one step from adult fibroblasts, from mouse (Vierbuchen et al. 2010) and human models (Pang et al. 2011).

Adult stem cells are found in low amounts in several adult tissues such as in the bone marrow, skin, peripheral blood or gut, for example. These multipotent cells are able to self renew and to differentiate into the specific tissue according to the organ where they reside, and function essentially to maintain the basal regeneration process due to natural cell death (NIH 2001).

There are various types of adult stem/progenitor cell populations associated with the various specialized tissues and organs of the body, for example epithelial progenitor cells located in the lining of the digestive tract. With some relevance, the bone marrow (BM) lodges the adult hematopoietic stem cells (HSC), which are responsible for the renewal of blood, and the adult mesenchymal stem cells (MSC), involved in the generation of bone, cartilage and fat cells. These cell systems, cooperate reciprocally leading to the formation of different BM and blood-stream cell lineages, have been widely used in medicine and tissue engineering applications. The BM is an organized tissue located at the centre of the large bones, composed of the basic elements from the stroma (mesenchymal) and hematopoietic systems (NIH 2001).

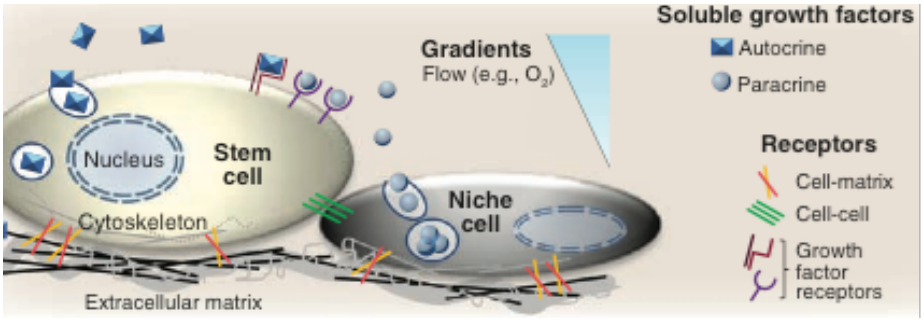

Figure II.2 – Various stimuli present in the stem cell niche. Adapted from (Discher et al. 2009).

After embryonic development, the adult stem cells are accommodated in the stem cell niche, defined for the first time by Schofield (Schofield 1978), represented in Figure II.2. The stem cell niche is characterized by a complex microenvironment, specific to each type of organ or tissue, defined by regulatory paracrine and endocrine signaling molecules, biophysical and chemical cues, cell-extracellular matrix and cell-cell interactions, providing support for cell survival and maintenance, regulating cell function and fate (Scadden 2006).

II.2 - Neural Stem Cells

Neural stem cells are adult multipotent cells that are able to generate the three main cell types of the CNS, neurons, astrocytes and oligodendrocytes (NIH 2001). NSCs exist in specific areas of the CNS, demonstrating that neurogenesis takes place in the adult organism, which was identified to occur in precise regions of the brain, represented in Figure II.3: in the subventricular zone (SVZ) surrounding the lateral ventricles, the subgranular zone (SGZ) of the hippocampus, the olfactory bulb and the subcallosal zone underlying the corpus callosum (De Filippis and Binda 2012). This evidence is very promising, with the possibility for the activation of endogenous stem cells that can be induced to maturate into specific neuronal populations, supporting localized neurogenesis acting as a possible repair for neurodegenerative disorders (De Filippis and Binda 2012; Kim et al. 2012).

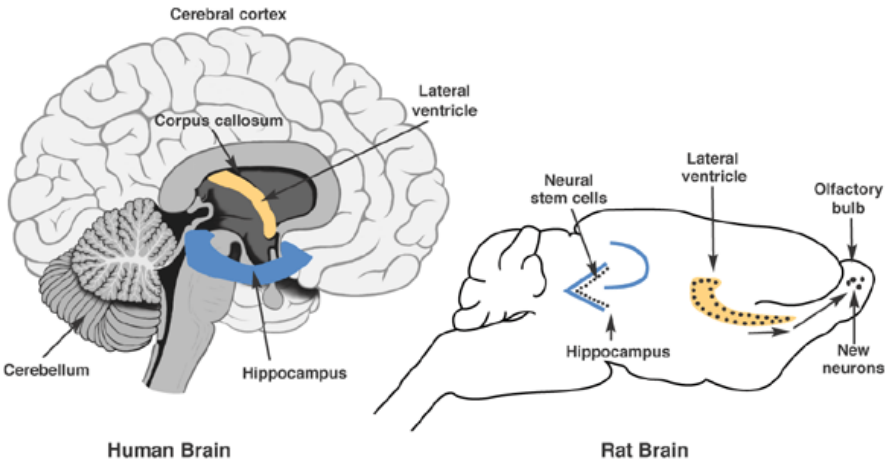

Figure II.3 – Active zones of adult neurogenesis in human and rodent brain. Adapted from (NIH 2004).

Neurogenesis in the embryonic development in mammals starts with the formation of the neuroectoderm, which forms the neural plate evolving through the formation of the neural tube (Conti and Cattaneo 2010). The neuroepithelial progenitors (NEP), are responsible for the starting of neurogenesis in the neural tube, giving rise to basal progenitors and radial glia (RG). In the subventricular zone the main cell population is composed by basal progenitors (or neurogenic precursors) that are responsible for the temporary amplification of the neuronal cells in specific time frames (Conti and Cattaneo 2010). Another important short-term population is the RG which is predominant in the initial stages of the neurogenesis, and is characterized by a bipolar morphology and has the crucial function of providing physical support to the development of the new neurons and also function as neural progenitors (Pollard and Conti 2007).

II.2.1 - Neural Stem Niche

Looking in particular to the rodent and the human adult brains, the identified neurogenesis sites, the sub-ependymal zone (SEZ)) and subgranular zone (SGZ) correspond effectively to the specific locations of the housing of the NSCs. The differences between the two models lay essentially on the lowest number of developing cells (proliferation and maturation into neurons) in the human SVZ. That is due to the presence of a cellular gap that separates the active SVZ astrocytes from the ependyma (ependymal cells) and also due to the absence of ependymal cells on the human SGZ. In comparison to the rodent model this results in a restricted self renewal process. The sequence of the niche cell maturation involves the ependymal cells regulation of the SVZ population proliferation with the maturation of the astrocytes that by asymmetric division (transit population of cells) originate transitory progenitor cells, which proliferate to neuroblasts that ultimately maturate into neuronal cells (Kazanis et al. 2008). Figure II.4 illustrates both rodent and human niches differences.

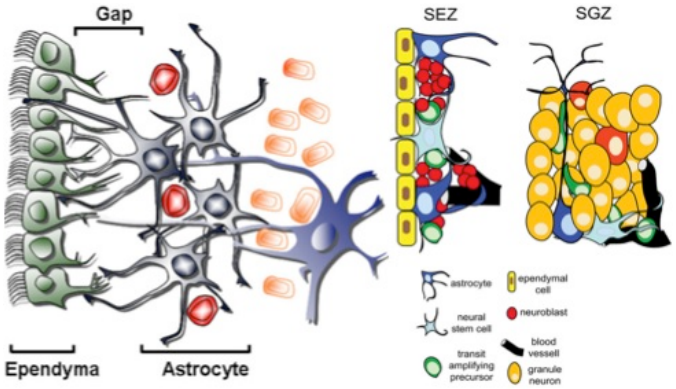

Figure II.4 – Representation of the germinal regions in the stem cell niche: adult human SVZ (left) and adult rodent SVZ (or SEZ) and SGZ (right). Adapted from (Arias-Carrión 2008; Kazanis et al. 2008).

II.2.2 - Regulation of Cell Fate

Numerous complex processes heavily regulate the cellular developments occurring in the niche. Essentially these are based in direct interaction of the NSCs (and neural progenitors) with the ECM constituents and via signaling transduction. The ECM structure provides the niche all the vital conditions for its maintenance (cell fate regulation, homeostasis), namely physical structure (mechanical properties, elasticity/rigidity, tensile stress, porosity), biochemical cues and signaling molecules (growth factors). For example cell adhesion molecules (CAMs) present at the surface of the cells recognize specific peptide sequences of complex ECM adhesion proteins. The CAMs include complex molecules of integrins, immunoglobulins, selectins and cadherins that recognize ECM proteins such as for example laminin, fibronectin, collagen, proteoglycans and glycoproteins. Signaling molecules include for example growth factors such as fibroblast growth factor -2 (FGF-2), epidermal growth factor (EGF), pigment epithelium derived factor (PEDF), vascular endothelial growth factor (VEGF) provided by the vascular net, supportive cells (fibroblasts) and cerebrospinal fluid. (Chan and Leong 2008; Kazanis et al. 2008; Bian 2013)

II.2.3 - NSC Culture

NSCs can be obtained from the fetal brain and adult brain and spinal cord, as *in vivo* sources, or derived *in vitro* from ESC or from iPSCs (Conti and Cattaneo 2010). Due to the limitation sources and ethical constraints on the use of fetal tissue (human), ESCs or iPSCs are more promising alternative cell sources, nevertheless research is needed to determine stable cell sources and protocol optimization for cellular proliferation (De Filippis and Binda 2012). NSC in vitro proliferation protocols have been developed under floating aggregates (neurospheres) or in adherent monolayer conditions in the presence of growth factors (Conti and Cattaneo 2010). There are limitations associated with the cellular proliferation under neurospheres, most importantly higher potential formation of heterogeneous cell populations specially in the core of the aggregates, where an increased limitation on diffusion properties is more likely to occur leading to decrease cell viability, restriction to nutrients, oxygen and toxic metabolites/ by products accumulation, leading to divergent cellular fate.

On the other hand under adherent monolayer culture, in the presence of EGF and FGF growth factors, the limitative problems associated with reduced media diffusion can be circumvented. The cells in monolayer culture originate a homogeneous population, are capable of maintaining the cellular integrity with expression of specific markers typical of radial glia: Nestin, (sex determining region Y)-box 2 (Sox2), (sex determining region Y)-box 1 (Sox1); and maintain the differentiation capacity into the specific neural lineages. (Pollard, Conti, et al. 2006; Conti and Cattaneo 2010; Carlos A. V. Rodrigues, Diogo, et al. 2011; De Filippis and Binda 2012)

NSC proliferation cultures are desirable to provide homogenous cell populations with high cell numbers and with retention of the multipotent capacity aiming NSCs applications. With the culture advantage under monolayer conditions, however a strategy to increase the cell output of expansion cultures is the increase of the flat surface area available for the adherent culture. For example the application of microcarriers under suspension culture provides a solution to improve the efficiency of the expansion providing higher cell numbers cultured in adherent monolayers. (Conti and Cattaneo 2010; Carlos A. V. Rodrigues, Diogo, et al. 2011)

The in vitro differentiation of NSC is based on different optimized protocols (Pollard, Benchoua, et al. 2006) and depending on the cell lines, is based fundamentally on not providing mitogens FGF-2 and EGF to the culture medium.

II.3 - Mimicking the ECM and Effects of the Material

II.3.1 – Materials Used for Scaffold Production

A variety of materials have been developed and explored processed as scaffolds with promising improvements in NSC migration, proliferation and differentiation *in vitro* and *in vivo* (Little et al. 2008; Cui et al. 2011; Kim et al. 2012). Natural polymers or polysaccharides, such as alginate, gelatin, collagen, chitosan, fibrin, cellulose, hyaluronic acid, dextran, silk, starch, chondroitin sulphate, and heparin, among others have the required cell recognition structural motifs (as amino acid sequences), providing cues for stem cells or reactive chemical side groups (as amine or carboxyl groups) that allow further functionalization with biological motifs. These materials are often biocompatible and biodegradable (Little et al. 2008; Beachley and Wen 2009; Subramanian et al. 2009). On the other hand natural materials might present some limitations such as the loss of biological activity during processing, difficulty to be processed in 3D structures to adjust the mechanical properties, batch-to-batch variations, and production scale-up problems due to low reproducibility (Little et al. 2008).

Synthetic materials (polymers, or ceramics) with specific chemical composition are advantageous of being prone to be processed with very precise qualities, such as hydrophobicity, degradation time and mechanical properties, or used as vehicles for the release of biochemical molecules (cues), where processing reproducibility and efficient scale-up synthesis is possible (Little et al. 2008; Cui et al. 2011; Liu et al. 2012). Some disadvantages are expected such as inflammatory reactions due to some degree of toxicity of the degradation by-products from the contact of the material with the surrounding cellular environment, and intrinsic degradation rate (Cui et al. 2011).

Examples of synthetic polymers, are poly(epsilon)caprolactone (PCL), polydimethylsiloxane (PDMS), polystyrene (PE), polyacrylamide (PolyA), poly(D,L-lactide) (PLA), polydopamine (PD), poly(ethylene glycol) (PEG), polyhydroxybutyrate (PHB), poly(D,L-lactic-co-glycolic acid) (PLGA), polyurethane (PU), poly(L-lactide) (PLLA). Some of these polymers, depending of their nature, can be processed in the form of hydrogels, self-assembled protein constructs, electrospun fibrous matrices, among others, working as substrates for NSC culture applications (Agarwal et al. 2008; Little et al. 2008; Cui et al. 2011; Liu et al. 2012).

The standard tissue culture plates provide a very specific substrate for cell culture without any resemblance to the ECM in vivo conditions (flat, rigid, bidimensional). With that it is desirable that a scaffold biomaterial to present enhanced and more interesting properties accommodating the cells in a more enriched environment, namely for example to provide a tridimensional structure (topography, mechanical properties), high biocompatibility (specific adhesion proteins and biological cues) and biodegradability (or not, depending on the application), suitable porosity to allow tissue vascularization, cellular migration and good nutrient and oxygen diffusion. (Little et al. 2008; Guilak et al. 2009; Subramanian et al. 2009; Delcroix et al. 2010)

II.3.2 - Biological Cues

A number of strategies can be applied in order to increase the cytocompatibility and biological characteristics of synthetic materials, namely by the creation and increase of cell recognition active sites at the surface of the material based on adsorption or covalent biding of molecules or factors (Liu et al. 2012). Laminin (LN), fibronectin (FN), heparin, retinoic acid, hyaluronic acid and growth factors are some examples of biomolecules used to functionalize polymeric substrates. Following is a brief detail of few examples.

Laminin is an important adhesion ligand for NSC growth and survival and specifically for neurite elongation on differentiated neurons. This protein is one of the ECM components of the basement membrane presented in complex structures of sheets formed by associated LN molecules. LN protein has a typical “T”-shaped mosaic structure (400 – 900 kDa) and contains specific amino acid sequences such as arginine-glycine-aspartic acid (RGD),

isoleucine-lysine-valine-alanine-valine (IKVAV) and tyrosine-isoleucine-glycine-serine-arginine (YIGSR) described to be fundamental to guide cell adhesion and enhanced neurite outgrowth (Venstrom and Reichardt 1993; Little et al. 2008).

Zander et al. demonstrated that neuron like PC-12 cells showed enhanced adhesion and neurite outgrowth, in laminin aligned functionalized PCL nanofibers. Also neurite orientation seemed highly aligned with fiber axis, in both covalently and adsorbed laminin substrates (Zander et al. 2010).

The arginine-glycine-aspartic acid (RGD) motif is a specific polypeptide sequence highly conserved in nature and is found in most of ECM proteins (laminin, collagen, vitronectin, fibronectin); this sequence is highly recognizable by the cell integrins family providing high binding specificity. It is a motif widely applied in scaffold functionalization specially to enhance cellular adhesion to the substrate (Venstrom and Reichardt 1993; Little et al. 2008; Delcroix et al. 2010; Gloria et al. 2012). RGD is often used with flanking amino acids glycine and serine (GRGDS), Bockelmann and co workers, immobilized GRGDS peptide in aligned electrospun fibers of PCL using a blend with star-shaped NCO-poly(ethylene glycol)-stat-poly(propylene glycol) (PCL/sPEG) as a covalent linker for the peptide. It was observed that the Schwann cells migrate faster and sensory axons followed exhibit higher grow in the direction of GRGDS functionalized fibers (Bockelmann et al. 2011).

Transmembrane αβ heterodimers complexes characterize the integrin proteins families. The specific aminoacid sequences of the ECM protein are recognized by receptors at the cells membrane surface. The binding process is characterized by a series of conformational changes both at the integrin side and at the ECM protein side, resulting in successive signals transmitted. In the presence of growth factors the cell self-renewal is regulated in a synergistic way which is characterized by the signaling pathway of the mitogen activated protein kinases (MAPK) (Flanagan et al. 2006).

Another example of a RGD containing sequence protein is fibronectin (450 kDa), present in the neural ECM, participating both in cell surface and ECM proteins interactions (Venstrom and Reichardt 1993; Delcroix et al. 2010). Fibronectin and GRGDS peptide functionalized

fibers of PCL/sPEG promoted increased cell migration and axonal outgrowth, in dorsal root ganglia explants, as demonstrated by Klinkhammer et al. (Klinkhammer et al. 2010).

The role of growth factors, as the EGF and the FGF-2, in culture (both added directly to the culture or secreted by the cells in culture) is essential for the regulation of intracellular chemical signaling hence for the regulation of the transcription of genes related to the processes of self renewal and maintenance of the differentiation capacity in in vitro culture of NSCs. These chemical factors are very specific cell dependent and also depend on cell maturation level and concentration in the culture media. (Tarasenko et al. 2004; Discher et al. 2009; Conti and Cattaneo 2010)

Hackett et al. developed a system of PCL-collagen nanofiber scaffolds in order to deliver *in vivo* growth factors, FGF-2 and nerve growth factor (NGF), to promote the proliferation of endogenous neural stem cells (Hackett et al. 2010). The controlled delivery of encapsulated retinoic conjugated with aligned PCL nanofibers shown to enhance MSC neural commitment evidenced by up-regulation of neural markers Tuj-1, MAP2, GalC and RIP, when compared with standard tissue cultures in polystyrene, as demonstrated by Jiang et al. (Jiang et al. 2012). Another study by Cho et al. compares the effect of chemically attached and adsorbed NGF from poly(ethylene glycol) (PEG) - PCL aligned nanofibers in neuronal differentiation of MSCs, where the expression of neural markers was notably higher for culture in aligned nanofibers conjugated with NGF than for cultures where NGF was only physically adsorbed and without specific topographic cues (Cho et al. 2010).

II.3.3 - Topographic and Mechanical Cues

Aligned nanofibers as scaffolds applied to NSC culture are advantageous in terms of the specific topography that supports cellular elongation and alignment with the direction of the fiber axis, which is desirable as one of the main characteristic features of CNS differentiated cells (specially neurons) are the ramified and extended cellular processes(Gertz et al. 2010). Cooper et al. demonstrated that the topography of chitosan-PCL fibers influenced nerve cell organization and function. It was observed that Schwann cells grown on aligned fibers shown

a bipolar morphology oriented along the direction of the fiber, compared with the multipolar morphology observed on randomly fibers. Also, aligned fibers promoted PC-12 cells growth, improved unidirectional neurite extension along fiber direction with higher expression of beta-tubulin specific neuron marker, than those on randomly oriented fibers (Cooper et al. 2011).

The fluorescence images in Figure II.5 are a clear example of the effect of functionalized PCL laminin nanofibers topography on directing and promoting neurite outgrowth. Neurite elongation and orientation are clear in images A and B, for cultures on aligned and randomly oriented nanofibers, respectively, where neurite extension is enhanced in aligned fibers. The elongation and organization of the cells are clearly well defined along fiber direction and neurite extension is enhanced in aligned fibers.

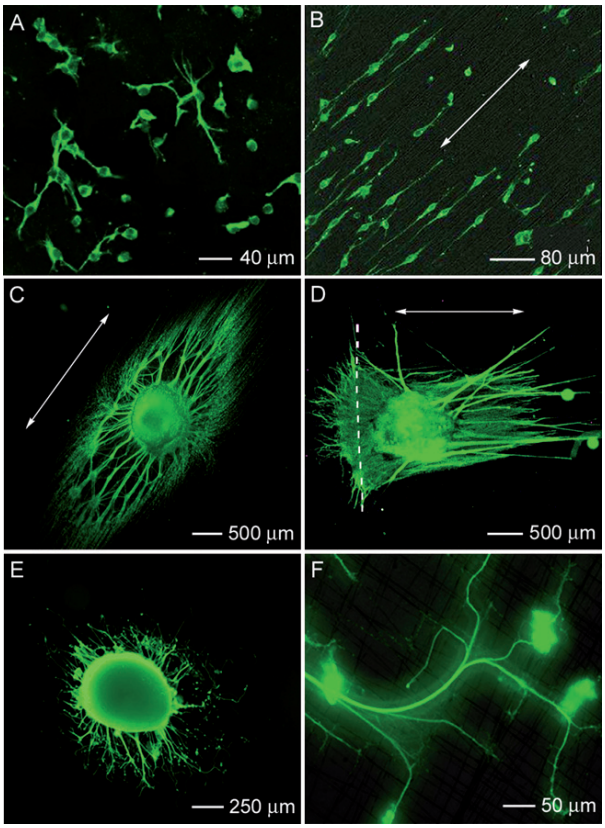

Figure II.5 - Fluorescence images of immunostained neurofilament in neural stem cells cultured in PCL-LN nanofibers: (A) on random fibers, (B) on aligned fibers, (C) neurite projection from dorsal root ganglia on aligned fibers, (D) neurite projection from dorsal root ganglia at a border between random and aligned fibers, (E, F) neurite field projected from dorsal root ganglia on a mat of perpendicular fibers. Adapted from (Xie et al. 2009).

Similarly, in image C, dorsal root ganglia (DRG) neurite extension is clearly aligned with nanofiber orientation. Interestingly, in image D is shown the neurite outgrowth in a nanofiber matrix that is simultaneously random and aligned, where DRG cultured on the boundary of the two topographies exhibit respectively aligned and random neurite fields as stimulated by the underlying topography. Images E and F correspond to perpendicular oriented layers of nanofibers, which actually influenced in both directions the neurite extension in DRG. What is observed in both images is the effect of the density (perpendicular layers) of the substrate, where neurites show a biaxial orientation (Xie et al. 2010).

The diameter of the nanofibers is also important in NSC development, as studied by Wang et al. that determined that diameter does not influence cell function, however show some effect on neurite outgrowth and Schwan cell migration when DRG explants were cultured on aligned fibers with diameters ranging from 1325 to 293 nm. The results pointed to larger nanofiber diameters lead to longer neurite extensions from DRG, and on lowest diameter condition DRG evidenced perpendicular outgrowth between the fibers (Wang et al. 2010). Mahairaki et al. studied the effect of cultured neural progenitors (NP) in laminin coated PCL aligned and randomly oriented nano and microfibers, where it was evidenced that fiber diameter (and alignment) influenced NP viability only in the presence of mitogens (FGF-2 and EGF) (Mahairaki et al. 2011).

The mechanical properties of the ECM namely the stiffness, elasticity and contractile/compression forces play an important role on cell-ECM signaling, and thus the importance of the mechanical characteristics of the scaffold substrate, that can have a direct impact on cell fate (migration, proliferation, differentiation, cell death) (Guilak et al. 2009). In Figure II.6 is exemplified the characteristic mechanical stiffness of some specific tissues, spanning from a wide range of elastic modulus, namely soft tissues as found in the brain (E'~ 1kPa), contrasting to harder tissues such as cartilage and bone (E ~ 10^9 - 10^{10} Pa) (Discher et al. 2009).

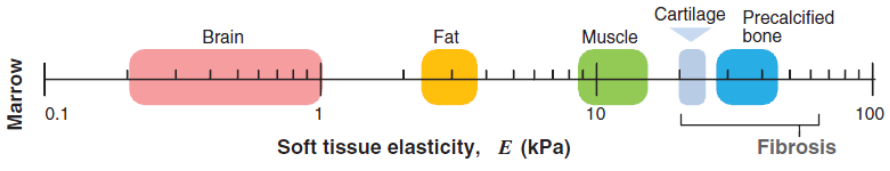

Figure II.6 - Range of stiffness, in elastic modulus, of different tissues. Adapted from (Discher et al. 2009).

Some examples of the influence of the stiffness of the adhesion substrate include the direction of MSC differentiation into two distinct cell lineages, where soft materials directed to neural type of cells, and with progressive increase of the stiffness muscle cells (myogenic stimulation) and further bone cells (osteogenic stimulation) were obtained. (Engler et al. 2006). Regarding NSCs under culture in substrates of synthetic hydrogels showed that softer conditions (~10 Pa) failed to promote cellular development while increasing stiffness, around 500 Pa, favored the cell culture specially on cell proliferation and posterior neuronal differentiation, although the glial lineage is improved in even stiffer substrates (E~1-10 kPa) (Saha et al. 2008).

II.3.4 – Rational for the Design of the Scaffolds

There are several complex scaffold systems for neural tissue, while hydrogels systems are better on providing soft highly hydrated matrices, typically they lack the ability to organize the cells providing structure and organization that can contribute for effective neural differentiation. The use of nanofibrous scaffolds allows to mimic the ECM collagen fibers responsible for structure and organization of the tissue. A robust and easy way to produce nanofibers is the use of the electrospinning, which can confer to the scaffold different topologies and fiber alignments according with the conditions used. Still, in the context of NSC culture such scaffolds should be tailored to promote cell adhesion, provide cell orientation and alignment and biological, physical and chemical cues able to direct cell fate (self renewal and differentiation). With respect to those features several report on the literature should be considered on the design of the simplest possible electrospun nanofiber scaffold, namely:

- Planar substrates, random or aligned fibers have been used in NSC culture. Aligned PLLA nanofibers promoted the NSC alignment and neurite extension according to fiber direction (Yang et al. 2005); the fibrous geometry of PCL nanofibers on rat NSCs determined oligodendrocytes specific lineage differentiation when compared to a planar substrate (Nisbet et al. 2008); higher proliferation of Schwann cells and human NPs was found in aligned fibers of PCL-PLGA (Subramanian et al. 2012), and

in PCL nanofibers (Mahairaki et al. 2011), respectively. However, an interesting research question is whether those materials are able to promote effective neural stem cell adhesion alone or require the use of biological/natural materials.

- Cell proliferation or tissue formation was higher when natural materials were blended with synthetically polymers, examples include neural progenitor cells (NPs) in aligned collagen nanofibers (Wang et al. 2011), mouse NSCs in PCL/collagen nanofibers (Hackett et al. 2010), mouse CGR8-NS in PLGA/matrigel fibers (Massumi et al. 2012) and Schwann cells in PCL-chitosan nanofibers (Cooper et al. 2011); laminin coated PCL aligned nanofibers promote neurite extension along the fiber alignment axis of adult rat NSCs with accentuated cellular alignment, and also higher number of differentiated Tuj1 cells (Lim et al. 2010); on the other hand no statistical significant differences between aligned and random matrices as with PC-12 cells in PCL functionalized or coated with laminin and collagen (Zander et al. 2010). However, systems where biological materials are coated or blended are imprecise and lack long term robustness, therefore this thesis privileges the use synthetic materials (PCL) covalently functionalized with biological factors, rather than mixtures or coating with biological materials.
- Interesting works that functionalized PCL fibers with biological factors using growth factors include human NSC derived from ESC cultured in EGF functionalized aligned fibers, resulting higher expression of glial and neuron markers and axon extensions (Lam et al. 2010); culture of neural stem/progenitor cells in GDNF functionalized PCL fibrous scaffolds (Wang et al. 2012) resulting in increased cell viability, proliferation and neurite outgrowth upon transplantation; and the use of PCL fibers functionalized with BDNF to promote cell differentiation with cortical NSCs in PCL-BDNF nanofibers (Horne et al. 2010) resulting on higher proliferation with preferential differentiation into oligodendrocytes and neurons. Different growth factors are required at different stages of cell expansion and differentiation; therefore the deliver of those growth factors through immobilization will increase scaffold complexity while they are easily supplemented in the culture medium at different time points. Therefore this thesis is focused on the immobilization of adhesion factors.

- The fiber diameter of laminin coated PES fibers (non biodegradable material) directed the proliferation and differentiation of rat adult NSCs, from which oligodendrocytes and neurons were preferentially differentiated in 283 and 749 nm, respectively (Christopherson et al. 2009); therefore this thesis scaffolds fibers (PCL a biodegradable material) are targeted to be in this range. Other studies in non biodegradable materials, LN coated PS aligned nanofibers, show NSCs have a more polarized and elongated morphology with higher neuronal lineage differentiation (Bakhru et al. 2011).
- A few studies functionalized PCL with laminin and adhesion motifs. Examples of these studies are for instance, mouse ESC in aligned and functionalized fibers with YIGSR, a derived peptide from laminin, increased the expression of neural markers, neuron-specific Tuj1 and neurite extensions when compared to random and non functionalized fibers (Smith Callahan et al. 2013); neural precursors, derived from hESC, on aligned LN coated PCL fibers show a more accentuated polar morphology, and increased neuronal differentiation and neurite extension, along the fiber alignment direction (Mahairaki et al. 2011).

II.3.5 - Electrospinning to Produce Nanofiber Scaffolds

A variety of different designs and strategies of scaffold substrates for neural regeneration are available ranging from nanofibers, polymeric membranes or films, guidance grooves, for example. The selection of nanofibers as scaffolds for NSC applications resides in the considerable advantages of this substrate, namely: distinct topographies provide distinct physic guidance, 3D geometry at the cells length scale, display high porosity as well as high surface to volume ratio and considerable permeability, all important for efficient utrient and oxygen diffusion and also cellular lodging, migration and cellular organization. (Agarwal et al. 2008; Saha et al. 2008; Beachley and Wen 2009; Gertz et al. 2010; Wang et al. 2012)

The nanofiber scaffolds can be produced by different methods such as phase separation, template synthesis, self-assembly, drawing, and electrospinning (Teo and Ramakrishna 2006; Gloria et al. 2012). The electrospinning technique is a simple, reproducible, cost effective

method for the production of nanofibers with virtually few limitation of processing materials, where the materials used can be polymers, composites, semiconductors, and ceramics (Teo and Ramakrishna 2006). Briefly, the electrospinning components include a syringe with a needle, a syringe pump, a high power voltage supply and a conductive collector, as represented in Figure II.7 (Sahay et al. 2011). The electrospinning process is based on the application of an electrical field on the polymer solution, forcing it through the needle to a conductive collector. When the repulsive electrostatic force exceeds the surface tension of the polymer solution at the tip of the needle (and needle walls) the solution is pulled towards the conductive collector as a result of the applied electrostatic force, by a continuous jet characteristically marked by the formation of the Taylor cone at the tip of the needle at a specific potential applied.

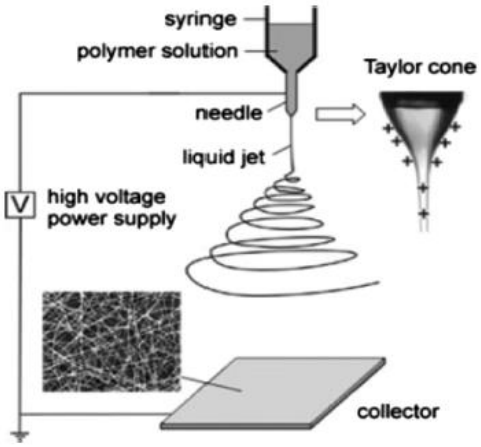

Figure II.7 – Representation of the components of the electrospinning. Adapted from (Garg and Bowlin 2011).

The continuous solution spinning jet emerges from the Taylor cone, with a bending shape directed towards the collector. The solvent of the polymer solution is able to evaporate (partially) and the formed fibers (nano or microfibers) are deposited on the grounded collector (Garg and Bowlin 2011). Several parameters influence the process that must be adjusted according to the desired type of fiber mesh produced. These parameters are the intrinsic solution properties (viscosity, conductivity, elasticity, and surface tension), the electrospinning conditions (applied electric potential, solution flow rate, needle tip diameter, and distance between the tip to the collector) and room temperature and humidity (Teo and Ramakrishna 2006; Garg and Bowlin 2011).

Some strategic conditions are desirable in order to produce a stable polymer solution jet able to produce fibers, namely: the solvent of the mixture must be able to evaporate during the spinning process (or at least most of the solvent), so that the fibers are able to harden by the time they reach the collector, which is essential to obtain homogenous defect free fibers; consequently it is desirable that the viscosity of the solution is not too high obstructing the jet formation, or too low being difficult to control the jet direction; the applied electric potential should be high enough to pull the solution with a force higher than the surface tension of the polymer solution; the distance between the needle and the grounded collector should be small enough to allow the formation of a stable electrical field between the electrodes and simultaneously large enough to allow solvent evaporation and formation of uniform fibers. With the adjustment of the processing parameters, it is possible to control the cross-sectional shape, as well as promoting fiber alignment and the formation of a variety of nanofiber morphologies and topography configurations (Teo and Ramakrishna 2006; Garg and Bowlin 2011). Diverse styles of fiber assemblies, such as the ones represented in Figure II.8, such as non-woven, aligned or patterned fiber meshes and random 3D structures can be produced by controlling the electrical field or by using dynamic collector devices (Sahay et al. 2011).

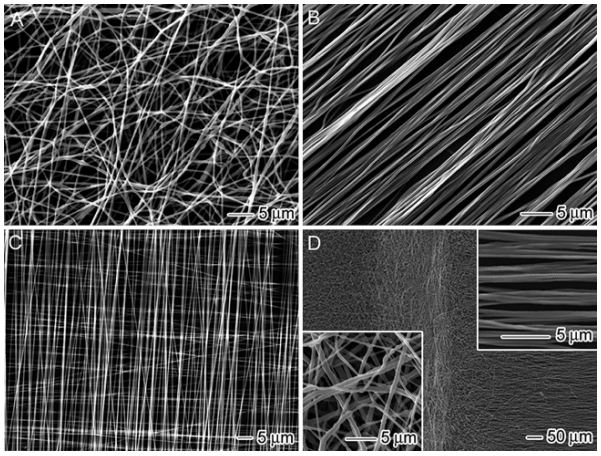

Figure II.8 - SEM images of diverse morphologies of electrospun nanofibers: (A) randomly oriented PCL nanofibers, (B) uniaxial aligned PCL nanofibers, (C) perpendicularly stacked array of PCL nanofibers, (D) a mat containing both random (left side) and aligned (right side) PCL nanofibers. Adapted from (Xie et al. 2009).

A variety of collectors are available, such as flat copper plates, rotating drums, rotating cylinder collectors or parallel bars as examples (Sahay et al. 2011). As example using a flat-grounded collector plate the collected fiber mesh obtained is comprised by randomly oriented

fibers, while using two parallel plates separated by an air-gap it is possible to collect a mesh of aligned fibers. However the parallel bar target is limited when high lengths or thicker layers deposited are desirable, still it shows to be a good option to prepare highly aligned and homogeneous fiber meshes (Teo and Ramakrishna 2006; Sahay et al. 2011).

II.3.6 - Functionalization of Material Surface

Poly-epsilon-caprolactone (PCL) (Figure II.9) is an aliphatic synthetic polyester, and is an established material used in a number of biomedical applications (FDA/EMEA), such as scaffolds for cell culture applications or tissue engineering, as examples. This polymer is very cost effective, biodegradable and biocompatible also easy processed in different configurations (nanofibers, films, membranes) (Woodruff and Hutmacher 2010; Gloria et al. 2012).

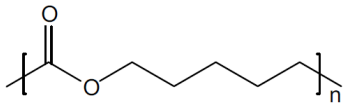

Figure II.9 – Chemical structure of polycaprolactone, charactherized by the presence of ester groups (–COO–).

Due to the low reactivity of the PCL polymer surface, and in order to increase the biocompatibility of the material, surface modification techniques such as partial cleavage of the PCL chain (plasma, gamma or ozone oxidization and alkaline hydrolysis) or end-grafting, and *in situ* polymerization can be applied in order to create labile and reactive groups at the surface of the polymer allowing further functionalization, by adsorption or covalent bonding (by carbodiimide or glutaraldehyde based reactions), with more complex components (biological molecules for example) (Ghasemi-Mobarakeh et al. 2010; Woodruff and Hutmacher 2010; Gloria et al. 2012; Zhu et al. 2012).

II.4 - Bioreactors for SC Culture

II.4.1 - Brief Overview of Bioreactors for Stem Cell Culture

Therapeutic strategies based on cell therapies are attractive for different biomedical applications, and usually such therapeutic approaches require large cell numbers. However, only a small number of cells can be obtained from donors, and therefore, to overcome such limitation, it is required the production of cells in a scaled-up process *in vitro*, complying with the regulatory guidelines in a cost effective manner. The use of bioreactors provides an efficient strategy for scale-up of cell expansion technologies able to increase the number of cells or systematic ex-vivo seeding and culture of cells in scaffolds for preparation of tissue constructs, prior to its implantation.

Important physicochemical parameters controlled in a bioreactor setting include pH, oxygen solubility, temperature, nutrient, metabolites and growth factors concentrations.

- Oxygen tension has an significant influence on stem cell self-renewal, maintenance and differentiation, and studies show that hypoxia conditions leads to increase cell viability, higher cell proliferation, without affecting the potency capacity of neural stem cells (Carlos A. V. Rodrigues, Fernandes, et al. 2011).
- The transfer of energy from the impeller to the culture medium originating areas of turbulence characterizes the hydrodynamic shear stress, resulting from the fluid stirring agitation, or sparging gas bubbles for aeration. These phenomena may lead to cell damage or low cell viability or eventually stimulate different cell responses such as cell differentiation (Carlos A. V. Rodrigues, Fernandes, et al. 2011).
- The determination and control of the suitable concentrations of growth factors in culture is crucial, since they have a major role, which translates into the interactions between the culture environment and the intracellular signaling, being critical to provide a balance for cell survival, proliferation and differentiation.
- Additionally it is important to control and determine nutrient and metabolite concentrations, according to the consuming rate of substrates (glucose or glutamine)

or the production rate of metabolic by-products (lactate) (Carlos A. V. Rodrigues, Fernandes, et al. 2011).

Several types of bioreactors are used for stem cell expansion. The most basic configurations at the laboratory scale are the tissue culture flasks (T-flasks), well plates or gas-permeable blood bags, which are static cell culture systems. These systems present some restraints regarding the expansion of higher amounts of cells, as well as limitations in oxygen, nutrient and metabolite diffusion, due to lack of agitation leading to the formation of concentration gradients. Dynamic and more robust perfusion and stirred bioreactor systems, as exemplified in Figure II.10, are used for the production of large numbers of cell, where limitations in terms of mass transfer and diffusional problems are minimized (Carlos A. V. Rodrigues, Fernandes, et al. 2011); this study reports a cell fold increase of 35 over 6 days of culture from seeding densities of 9.3 and 37 thousand cells per cm^2, for microcarrier system with 54 and 216 cm^2, respectively, implying final cell densities of 325 and 1295 thousand cells per cm^2 respectively. Roller bottles bioreactors are widely used in the production of recombinant proteins and monoclonal antibodies, and stirred-suspension bioreactors (SBs) are used in large-scale production of stem cells, in single cells culture or in aggregates using microcarriers. Rotating wall vessels are used to minimize shear stress in cell culture, as represented in Figure II.11 by the slow turning lateral vessel configuration (STLV). The wave bioreactor was developed to provide agitation to a disposal vessel for easy compliance with regulatory GMP guidelines and it is essentially used for clinical applications (Carlos A. V. Rodrigues, Fernandes, et al. 2011). Perfusion systems such as hollow fiber, fix and fluidized bed and parallel plate bioreactors, work with a continuous change of media where mass transfer is increased compared to stirred systems (Carlos A. V. Rodrigues, Fernandes, et al. 2011).

The combination of a system of bioreactors to allow the systematic expansion of cells within a scaffold is usually performed in static systems or with scaffolds placed in spinner flasks, often neglecting the scalability of those seeding systems, scaffold-tissue platforms, for the systematic production of transplants.

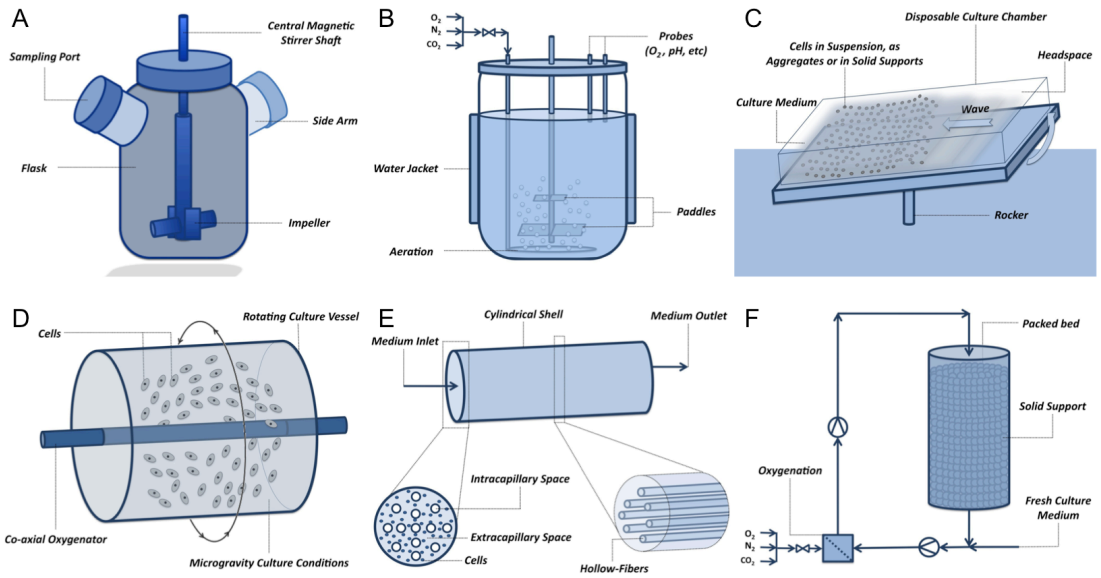

Figure II.10 – Bioreactor configurations for stem cell culture: A) Spinner flask, B) Stirred suspension bioreactor, C) Wave bioreactor, D) Rotating wall vessel - slow turning lateral vessel (STLV), E) Hollow-fiber bioreactor, F) Packed-bed bioreactor. Adapted from (Carlos A. V. Rodrigues, Fernandes, et al. 2011).

In literature it is possible to find different strategies for stem cells expansion in dynamic conditions described by stirred suspension systems, combined with different culture approaches, such as microcarriers (C.A.V. Rodrigues et al. 2011), cell aggregates (Gilbertson et al. 2006) and encapsulation of cells (Serra et al. 2009).

II.4.2 - Bioreactor Systems Integrated with Nanofiber Scaffolds

Hosseinkhani et al. coupled a hybrid poly(glycolic acid) (PGA) nanofiber scaffold with a perfusion culture bioreactor to enhance osteogenic differentiation of MSC (Hosseinkhani et al. 2006). Chu et al. developed a multi-layer radial-flow perfusion bioreactor based on galactosylated chitosan nanofiber scaffolds to work as a support for hepatic failure patients. Cell adhesion and function of hepatocytes was enhanced when compared with the same bioreactor without nanofibers (Chu et al. 2009). An approach to expand neural stem cells was developed by Liu et al. that stimulated neural differentiation of murine embryonic stem cells in polyethylene terephthalate (PET) microfibrous matrices adapted in a spinner flask, which lead to higher percentage of nestin positive cells when compared to static cultures (Liu et al.

2013). Valmikinathan, et al. show a promising approach using a rotating wall vessel where spiral shaped PCL nanofibers (aligned or random) scaffolds were cultured, showing increased cell rate proliferation when compared to static cultures (Valmikinathan et al. 2011). In another study, Li et al. cultured in a rotary wall vessel bioreactor cell-nanofiber composites (CNCs) encapsulated with chondrocytes, and demonstrated that the composites cultured in dynamic conditions revealed higher cartilage tissue weight than those culture in static conditions (Li et al. 2008).

Scaffold systems coupled with a bioreactor is a promising approach to enhance the system response into a specific effect such as for example to enhance a specific cell function or direct cell differentiation, by providing improved culture conditions closer to that found *in vivo*. The examples provided above illustrate the research awareness for the need of cultivation of cells in scaffolds under dynamic conditions. However few of the referred developed systems are designed to be scalable. The work of Valmikinathan, et al. presents itself as the more promising scalable approach, for the production of grafts for peripheral nerve regeneration. Considering the several strategies under research and development and their current limitations, one can recognize the need to develop a nanofiber-bioreactor for the systematic production of tissue grafts as a challenge that deserves to be further explored.

Regardless the approaches taken for neural tissue regeneration, the use of scaffolds is often advantageous. The scaffold supports the new tissue formation, accommodating and retaining the cells in the proper location, sustaining tissue renewal. The use of electrospun fibers (aligned or random matrices) has been proposed in the literature, as suitable scaffolds providing a highly porous network of fibers resembling the ECM (Agarwal et al. 2008; Discher et al. 2009; Gertz et al. 2010) being suggested as potential cellular supports for applications in neural therapies (Little et al. 2008; Gertz et al. 2010; Wang et al. 2012). The ex-vivo expansion of stem cells usually is required before its application in therapy, due to the small numbers of cells extracted from biological sources. The NSCs have the advantage to be able to proliferate with relatively high rates (Sen et al. 2001; Kallos et al. 2003; Conti et al. 2005; Baghbaderani et al. 2008; Baghbaderani et al. 2010; Conti and Cattaneo 2010; Carlos A. V. Rodrigues, Diogo, et al. 2011) and therefore systems that allow providing high number of NSCs in supportive scaffolds is a promising technology, for the potential application in

regenerative neural therapies. The ability to obtain an adequate amount of cells for cellular therapies is still, however, an issue of debate representing a limitation in the field of tissue regeneration (Nanou and Azzouz 2009). The current project is focused on the application of adherent NSCs, seeded and expanded in electrospun scaffolds and differentiated into specific cell types. Considering the existing literature very few works report the use of bioreactors or other systems able to support NSC cultivation on nanofibers under dynamic conditions.

References

Agarwal S, Wendorff JH, Greiner A. 2008. Use of electrospinning technique for biomedical applications. Polymer. 49(26):5603–5621. doi:10.1016/j.polymer.2008.09.014.

Arias-Carrión O. 2008. Basic mechanisms of rTMS: Implications in Parkinson's disease. Int Arch Med. 1(1):2. doi:10.1186/1755-7682-1-2.

Baghbaderani BA, Behie LA, Sen A, Mukhida K, Hong M, Mendez I. 2008. Expansion of human neural precursor cells in large-scale bioreactors for the treatment of neurodegenerative disorders. Biotechnol Prog. 24(4):859–870. doi:10.1021/bp070324s.

Baghbaderani BA, Mukhida K, Sen A, Kallos MS, Hong M, Mendez I, Behie LA. 2010. Bioreactor expansion of human neural precursor cells in serum-free media retains neurogenic potential. Biotechnol Bioeng. 105(4):823–833. doi:10.1002/bit.22590.

Bakhru S, Nain AS, Highley C, Wang J, Campbell P, Amon C, Zappe S. 2011. Direct and cell signaling-based, geometry-induced neuronal differentiation of neural stem cells. Integr Biol Quant Biosci Nano Macro. 3(12):1207–1214. doi:10.1039/c1ib00098e.

Beachley V, Wen X. 2009. Fabrication of Nanofiber Reinforced Protein Structures For Tissue Engineering. Mater Sci Eng C Mater Biol Appl. 29(8):2448–2453. doi:10.1016/j.msec.2009.07.008.

Bian S. 2013. Cell Adhesion Molecules in Neural Stem Cell and Stem Cell- Based Therapy for Neural Disorders. In: Bonfanti L, editor. Neural Stem Cells - New Perspectives. InTech. [accessed 2015 Nov 3]. http://www.intechopen.com/books/neural-stem-cells-new-perspectives/cell-adhesion-molecules-in-neural-stem-cell-and-stem-cell-based-therapy-for-neural-disorders.

Bockelmann J, Klinkhammer K, von Holst A, Seiler N, Faissner A, Brook GA, Klee D, Mey J. 2011. Functionalization of electrospun poly(ε-caprolactone) fibers with the extracellular matrix-derived peptide GRGDS improves guidance of schwann cell migration and axonal growth. Tissue Eng Part A. 17(3–4):475–486. doi:10.1089/ten.TEA.2010.0369.

Chan BP, Leong KW. 2008. Scaffolding in tissue engineering: general approaches and tissue-specific considerations. Eur Spine J. 17(Suppl 4):467–479. doi:10.1007/s00586-008-0745-3.

Cho YI, Choi JS, Jeong SY, Yoo HS. 2010. Nerve growth factor (NGF)-conjugated electrospun nanostructures with topographical cues for neuronal differentiation of mesenchymal stem cells. Acta Biomater. 6(12):4725–4733. doi:10.1016/j.actbio.2010.06.019.

Christopherson GT, Song H, Mao H-Q. 2009. The influence of fiber diameter of electrospun substrates on neural stem cell differentiation and proliferation. Biomaterials. 30(4):556–564. doi:10.1016/j.biomaterials.2008.10.004.

Chu X-H, Shi X-L, Feng Z-Q, Gu J-Y, Xu H-Y, Zhang Y, Gu Z-Z, Ding Y-T. 2009. In vitro evaluation of a multi-layer radial-flow bioreactor based on galactosylated chitosan nanofiber scaffolds. Biomaterials. 30(27):4533–4538. doi:10.1016/j.biomaterials.2009.05.020.

Conti L, Cattaneo E. 2010. Neural stem cell systems: physiological players or in vitro entities? Nat Rev Neurosci. 11(3):176–187. doi:10.1038/nrn2761.

Conti L, Pollard SM, Gorba T, Reitano E, Toselli M, Biella G, Sun Y, Sanzone S, Ying Q-L, Cattaneo E, et al. 2005. Niche-independent symmetrical self-renewal of a mammalian tissue stem cell. PLoS Biol. 3(9):e283. doi:10.1371/journal.pbio.0030283.

Cooper A, Bhattarai N, Zhang M. 2011. Fabrication and cellular compatibility of aligned chitosan-PCL fibers for nerve tissue regeneration. Carbohydr Polym. 85(1):149–156. doi:10.1016/j.carbpol.2011.02.008.

Cui F-Z, Deng H, Fang C-F, Wei Y-T, Shen X-C. 2011. A Mini Review on Interactions Between Neural Stem Cells and Biomaterials. Recent Pat Regen Med. 1(1):19–29. doi:10.2174/2210296511101010019.

De Filippis L, Binda E. 2012. Concise review: self-renewal in the central nervous system: neural stem cells from embryo to adult. Stem Cells Transl Med. 1(4):298–308. doi:10.5966/sctm.2011-0045.

Delcroix GJ-R, Schiller PC, Benoit J-P, Montero-Menei CN. 2010. Adult cell therapy for brain neuronal damages and the role of tissue engineering. Biomaterials. 31(8):2105–2120. doi:10.1016/j.biomaterials.2009.11.084.

Discher DE, Mooney DJ, Zandstra PW. 2009. Growth Factors, Matrices, and Forces Combine and Control Stem Cells. Science. 324(5935):1673–1677. doi:10.1126/science.1171643.

Engler AJ, Sen S, Sweeney HL, Discher DE. 2006. Matrix elasticity directs stem cell lineage specification. Cell. 126(4):677–689. doi:10.1016/j.cell.2006.06.044.

Evans MJ, Kaufman MH. 1981. Establishment in culture of pluripotential cells from mouse embryos. Nature. 292(5819):154–156.

Flanagan LA, Rebaza LM, Derzic S, Schwartz PH, Monuki ES. 2006. Regulation of human neural precursor cells by laminin and integrins. J Neurosci Res. 83(5):845–856. doi:10.1002/jnr.20778.

Garg K, Bowlin GL. 2011. Electrospinning jets and nanofibrous structures. Biomicrofluidics. 5(1):13403. doi:10.1063/1.3567097.

Gertz CC, Leach MK, Birrell LK, Martin DC, Feldman EL, Corey JM. 2010. Accelerated neuritogenesis and maturation of primary spinal motor neurons in response to nanofibers. Dev Neurobiol. 70(8):589–603. doi:10.1002/dneu.20792.

Ghasemi-Mobarakeh L, Prabhakaran MP, Morshed M, Nasr-Esfahani MH, Ramakrishna S. 2010. Bio-functionalized PCL nanofibrous scaffolds for nerve tissue engineering. Mater Sci Eng C. 30(8):1129–1136. doi:10.1016/j.msec.2010.06.004.

Gilbertson JA, Sen A, Behie LA, Kallos MS. 2006. Scaled-up production of mammalian neural precursor cell aggregates in computer-controlled suspension bioreactors. Biotechnol Bioeng. 94(4):783–792. doi:10.1002/bit.20900.

Gloria A, Causa F, Russo T, Battista E, Della Moglie R, Zeppetelli S, De Santis R, Netti PA, Ambrosio L. 2012. Three-dimensional poly(ε-caprolactone) bioactive scaffolds with controlled structural and surface properties. Biomacromolecules. 13(11):3510–3521. doi:10.1021/bm300818y.

Guilak F, Cohen DM, Estes BT, Gimble JM, Liedtke W, Chen CS. 2009. Control of Stem Cell Fate by Physical Interactions with the Extracellular Matrix. Cell Stem Cell. 5(1):17–26. doi:10.1016/j.stem.2009.06.016.

Hackett JM, Dang TT, Tsai EC, Cao X. 2010. Electrospun Biocomposite Polycaprolactone/Collagen Tubes as Scaffolds for Neural Stem Cell Differentiation. Materials. 3(6):3714–3728. doi:10.3390/ma3063714.

Horne MK, Nisbet DR, Forsythe JS, Parish CL. 2010. Three-dimensional nanofibrous scaffolds incorporating immobilized BDNF promote proliferation and differentiation of cortical neural stem cells. Stem Cells Dev. 19(6):843–852. doi:10.1089/scd.2009.0158.

Hosseinkhani H, Hosseinkhani M, Tian F, Kobayashi H, Tabata Y. 2006. Ectopic bone formation in collagen sponge self-assembled peptide-amphiphile nanofibers hybrid scaffold in a perfusion culture bioreactor. Biomaterials. 27(29):5089–5098. doi:10.1016/j.biomaterials.2006.05.050.

Jiang X, Cao HQ, Shi LY, Ng SY, Stanton LW, Chew SY. 2012. Nanofiber topography and sustained biochemical signaling enhance human mesenchymal stem cell neural commitment. Acta Biomater. 8(3):1290–1302. doi:10.1016/j.actbio.2011.11.019.

Kallos MS, Sen A, Behie LA. 2003. Large-scale expansion of mammalian neural stem cells: a review. Med Biol Eng Comput. 41(3):271–282.

Kazanis I, Lathia J, Moss L, ffrench-Constant C. 2008. The neural stem cell microenvironment. In: StemBook. Cambridge (MA): Harvard Stem Cell Institute. [accessed 2015 Nov 3]. http://www.ncbi.nlm.nih.gov/books/NBK27023/.

Kim H, Cooke MJ, Shoichet MS. 2012. Creating permissive microenvironments for stem cell transplantation into the central nervous system. Trends Biotechnol. 30(1):55–63. doi:10.1016/j.tibtech.2011.07.002.

Klinkhammer K, Bockelmann J, Simitzis C, Brook GA, Grafahrend D, Groll J, Möller M, Mey J, Klee D. 2010. Functionalization of electrospun fibers of poly(epsilon-caprolactone) with star shaped NCO-poly(ethylene glycol)-stat-poly(propylene glycol) for neuronal cell guidance. J Mater Sci Mater Med. 21(9):2637–2651. doi:10.1007/s10856-010-4112-7.

Lam HJ, Patel S, Wang A, Chu J, Li S. 2010. In vitro regulation of neural differentiation and axon growth by growth factors and bioactive nanofibers. Tissue Eng Part A. 16(8):2641–2648. doi:10.1089/ten.TEA.2009.0414.

Li W-J, Jiang YJ, Tuan RS. 2008. Cell-nanofiber-based cartilage tissue engineering using improved cell seeding, growth factor, and bioreactor technologies. Tissue Eng Part A. 14(5):639–648. doi:10.1089/tea.2007.0136.

Lim SH, Liu XY, Song H, Yarema KJ, Mao H-Q. 2010. The effect of nanofiber-guided cell alignment on the preferential differentiation of neural stem cells. Biomaterials. 31(34):9031–9039. doi:10.1016/j.biomaterials.2010.08.021.

Little L, Healy KE, Schaffer D. 2008. Engineering biomaterials for synthetic neural stem cell microenvironments. Chem Rev. 108(5):1787–1796. doi:10.1021/cr078228t.

Liu N, Ouyang A, Li Y, Yang S-T. 2013. Three-dimensional neural differentiation of embryonic stem cells with ACM induction in microfibrous matrices in bioreactors. Biotechnol Prog. 29(4):1013–1022. doi:10.1002/btpr.1742.

Liu X, Holzwarth JM, Ma PX. 2012. Functionalized synthetic biodegradable polymer scaffolds for tissue engineering. Macromol Biosci. 12(7):911–919. doi:10.1002/mabi.201100466.

Mahairaki V, Lim SH, Christopherson GT, Xu L, Nasonkin I, Yu C, Mao H-Q, Koliatsos VE. 2011. Nanofiber matrices promote the neuronal differentiation of human embryonic stem cell-derived neural precursors in vitro. Tissue Eng Part A. 17(5–6):855–863. doi:10.1089/ten.TEA.2010.0377.

Massumi M, Abasi M, Babaloo H, Terraf P, Safi M, Saeed M, Barzin J, Zandi M, Soleimani M. 2012. The effect of topography on differentiation fates of matrigel-coated mouse embryonic stem cells cultured on PLGA nanofibrous scaffolds. Tissue Eng Part A. 18(5–6):609–620. doi:10.1089/ten.TEA.2011.0368.

Migneault I, Dartiguenave C, Bertrand MJ, Waldron KC. 2004. Glutaraldehyde: behavior in aqueous solution, reaction with proteins, and application to enzyme crosslinking. BioTechniques. 37(5):790–796, 798–802.

Nanou A, Azzouz M. 2009. Gene therapy for neurodegenerative diseases based on lentiviral vectors. Prog Brain Res. 175:187–200. doi:10.1016/S0079-6123(09)17513-1.

NIH. 2001. Stem Cells: Scientific Progress and Future Research Directions [Stem Cell Information]. [accessed 2015 Nov 2]. http://stemcells.nih.gov/info/2001report/pages/2001report.aspx.

NIH. 2004. Alcohol, Neural Stem Cells, and Adult Neurogenesis. [accessed 2015 Nov 4]. http://pubs.niaaa.nih.gov/publications/arh27-2/197-204.htm.

Nisbet DR, Yu LMY, Zahir T, Forsythe JS, Shoichet MS. 2008. Characterization of neural stem cells on electrospun poly(ε-caprolactone) submicron scaffolds: evaluating their potential in neural tissue engineering. J Biomater Sci Polym Ed. 19(5):623–634. doi:10.1163/156856208784089652.

Pang ZP, Yang N, Vierbuchen T, Ostermeier A, Fuentes DR, Yang TQ, Citri A, Sebastiano V, Marro S, Südhof TC, et al. 2011. Induction of human neuronal cells by defined transcription factors. Nature. 476(7359):220–223. doi:10.1038/nature10202.

Pollard SM, Benchoua A, Lowell S. 2006. Neural stem cells, neurons, and glia. Methods Enzymol. 418:151–169. doi:10.1016/S0076-6879(06)18010-6.

Pollard SM, Conti L. 2007. Investigating radial glia in vitro. Prog Neurobiol. 83(1):53–67. doi:10.1016/j.pneurobio.2007.02.008.

Pollard SM, Conti L, Sun Y, Goffredo D, Smith A. 2006. Adherent neural stem (NS) cells from fetal and adult forebrain. Cereb Cortex N Y N 1991. 16 Suppl 1:i112-120. doi:10.1093/cercor/bhj167.

Rodrigues C.A.V., Diogo MM, Lobato da Silva C, Cabral JMS. 2011. Design and operation of bioreactor systems for the expansion of pluripotent stem cell-derived neural stem cells. In: Bioengineering (ENBENG), 2011. ENBENG 2011. 1st Portuguese Meeting in. p. 1–3.

Rodrigues Carlos A. V., Diogo MM, da Silva CL, Cabral JMS. 2011. Microcarrier expansion of mouse embryonic stem cell-derived neural stem cells in stirred bioreactors. Biotechnol Appl Biochem. 58(4):231–242. doi:10.1002/bab.37.

Rodrigues Carlos A. V., Fernandes TG, Diogo MM, da Silva CL, Cabral JMS. 2011. Stem cell cultivation in bioreactors. Biotechnol Adv. 29(6):815–829. doi:10.1016/j.biotechadv.2011.06.009.

Saha K, Keung AJ, Irwin EF, Li Y, Little L, Schaffer DV, Healy KE. 2008. Substrate modulus directs neural stem cell behavior. Biophys J. 95(9):4426–4438. doi:10.1529/biophysj.108.132217.

Sahay R, Thavasi V, Ramakrishna S, Sahay R, Thavasi V, Ramakrishna S. 2011. Design Modifications in Electrospinning Setup for Advanced Applications, Design Modifications in Electrospinning Setup for Advanced Applications. J Nanomater J Nanomater. 2011, 2011:e317673. doi:10.1155/2011/317673, 10.1155/2011/317673.

Scadden DT. 2006. The stem-cell niche as an entity of action. Nature. 441(7097):1075–1079. doi:10.1038/nature04957.

Schofield R. 1978. The relationship between the spleen colony-forming cell and the haemopoietic stem cell. Blood Cells. 4(1–2):7–25.

Sen A, Kallos MS, Behie LA. 2001. Effects of Hydrodynamics on Cultures of Mammalian Neural Stem Cell Aggregates in Suspension Bioreactors. Ind Eng Chem Res. 40(23):5350–5357. doi:10.1021/ie001107y.

Serra M, Brito C, Costa EM, Sousa MF, Alves PM. 2009. Integrating human stem cell expansion and neuronal differentiation in bioreactors. BMC Biotechnol. 9(1):82. doi:10.1186/1472-6750-9-82.

Smith Callahan LA, Xie S, Barker IA, Zheng J, Reneker DH, Dove AP, Becker ML. 2013. Directed differentiation and neurite extension of mouse embryonic stem cell on aligned poly(lactide) nanofibers functionalized with YIGSR peptide. Biomaterials. 34(36):9089–9095. doi:10.1016/j.biomaterials.2013.08.028.

Subramanian A, Krishnan UM, Sethuraman S. 2009. Development of biomaterial scaffold for nerve tissue engineering: Biomaterial mediated neural regeneration. J Biomed Sci. 16:108. doi:10.1186/1423-0127-16-108.

Subramanian A, Krishnan UM, Sethuraman S. 2012. Fabrication, characterization and in vitro evaluation of aligned PLGA-PCL nanofibers for neural regeneration. Ann Biomed Eng. 40(10):2098–2110. doi:10.1007/s10439-012-0592-6.

Takahashi K, Tanabe K, Ohnuki M, Narita M, Ichisaka T, Tomoda K, Yamanaka S. 2007. Induction of pluripotent stem cells from adult human fibroblasts by defined factors. Cell. 131(5):861–872. doi:10.1016/j.cell.2007.11.019.

Takahashi K, Yamanaka S. 2006. Induction of pluripotent stem cells from mouse embryonic and adult fibroblast cultures by defined factors. Cell. 126(4):663–676. doi:10.1016/j.cell.2006.07.024.

Tarasenko YI, Yu Y, Jordan PM, Bottenstein J, Wu P. 2004. Effect of growth factors on proliferation and phenotypic differentiation of human fetal neural stem cells. J Neurosci Res. 78(5):625–636. doi:10.1002/jnr.20316.

Teo WE, Ramakrishna S. 2006. A review on electrospinning design and nanofibre assemblies. Nanotechnology. 17(14):R89. doi:10.1088/0957-4484/17/14/R01.

Thomson JA, Itskovitz-Eldor J, Shapiro SS, Waknitz MA, Swiergiel JJ, Marshall VS, Jones JM. 1998. Embryonic stem cell lines derived from human blastocysts. Science. 282(5391):1145–1147.

Valmikinathan CM, Hoffman J, Yu X. 2011. Impact of Scaffold Micro and Macro Architecture on Schwann Cell Proliferation under Dynamic Conditions in a Rotating Wall Vessel Bioreactor. Mater Sci Eng C Mater Biol Appl. 31(1):22–29. doi:10.1016/j.msec.2010.04.001.

Venstrom KA, Reichardt LF. 1993. Extracellular matrix. 2: Role of extracellular matrix molecules and their receptors in the nervous system. FASEB J Off Publ Fed Am Soc Exp Biol. 7(11):996–1003.

Vierbuchen T, Ostermeier A, Pang ZP, Kokubu Y, Südhof TC, Wernig M. 2010. Direct conversion of fibroblasts to functional neurons by defined factors. Nature. 463(7284):1035–1041. doi:10.1038/nature08797.

Wang HB, Mullins ME, Cregg JM, McCarthy CW, Gilbert RJ. 2010. Varying the diameter of aligned electrospun fibers alters neurite outgrowth and Schwann cell migration. Acta Biomater. 6(8):2970–2978. doi:10.1016/j.actbio.2010.02.020.

Wang T-Y, Forsythe JS, Nisbet DR, Parish CL. 2012. Promoting engraftment of transplanted neural stem cells/progenitors using biofunctionalised electrospun scaffolds. Biomaterials. 33(36):9188–9197. doi:10.1016/j.biomaterials.2012.09.013.

Wang Y, Yao M, Zhou J, Zheng W, Zhou C, Dong D, Liu Y, Teng Z, Jiang Y, Wei G, et al. 2011. The promotion of neural progenitor cells proliferation by aligned and randomly oriented collagen nanofibers through β1 integrin/MAPK signaling pathway. Biomaterials. 32(28):6737–6744. doi:10.1016/j.biomaterials.2011.05.075.

Woodruff MA, Hutmacher DW. 2010. The return of a forgotten polymer—Polycaprolactone in the 21st century. Prog Polym Sci. 35(10):1217–1256. doi:10.1016/j.progpolymsci.2010.04.002.

Xie J, MacEwan MR, Li X, Sakiyama-Elbert SE, Xia Y. 2009. Neurite outgrowth on nanofiber scaffolds with different orders, structures, and surface properties. ACS Nano. 3(5):1151–1159. doi:10.1021/nn900070z.

Xie J, MacEwan MR, Schwartz AG, Xia Y. 2010. Electrospun nanofibers for neural tissue engineering. Nanoscale. 2(1):35–44. doi:10.1039/B9NR00243J.

Yang F, Murugan R, Wang S, Ramakrishna S. 2005. Electrospinning of nano/micro scale poly(l-lactic acid) aligned fibers and their potential in neural tissue engineering. Biomaterials. 26(15):2603–2610. doi:10.1016/j.biomaterials.2004.06.051.

Yu J, Vodyanik MA, Smuga-Otto K, Antosiewicz-Bourget J, Frane JL, Tian S, Nie J, Jonsdottir GA, Ruotti V, Stewart R, et al. 2007. Induced Pluripotent Stem Cell Lines Derived from Human Somatic Cells. Science. 318(5858):1917–1920. doi:10.1126/science.1151526.

Zander NE, Orlicki JA, Rawlett AM, Beebe TP. 2010. Surface-modified nanofibrous biomaterial bridge for the enhancement and control of neurite outgrowth. Biointerphases. 5(4):149–158. doi:10.1116/1.3526140.

Zhu Y, Mao Z, Shi H, Gao C. 2012. In-depth study on aminolysis of poly(ε-caprolactone): Back to the fundamentals. Sci China Chem. 55(11):2419–2427. doi:10.1007/s11426-012-4540-y.

Chapter III

Neural Stem Cell Culture in Functionalized Nanofibers: Cell Morphology and Organization

Chapter III - Neural Stem Cell Culture in Functionalized Nanofibers: Cell Morphology and Organization

III.1 - Abstract

This chapter discusses the importance of including biological adhesion motifs on the surface of aligned electrospun poly-ε-caprolactone (PCL) nanofiber scaffolds to support and direct the differentiation of neural stem cells (NSCs), using CGR8-NS as cell model.
A five rank scale for fiber density was suggested and a 3.5 - 4 level, corresponding to 70 - 80% fiber density, was selected as adequate for NSC ex-vivo culture.

In general, aligned nanofibers directed NSC elongation and distribution, especially in the presence of LN and GRGDSP motif. In situ differentiation resulted in relative higher cells expressing Tuj1 in aligned fibers in the presence of LN, pointing that the scaffold topology and ECM motifs increased the neuron elongation and alignment.

Aligned PCL functionalized with Laminin (PCL-LN) and GRGDSP (PCL-RGD) motif promotes higher NSC elongation with average eccentricities of 0.90 ± 0.02 and 0.86 ± 0.01, respectively, and with 0.64 ± 0.02 or 0.67 ± 0.01 for non-functionalized PCL aligned fibers or PCL-RGD random fibers, respectively. Alignment of differentiated neurons (Tuj1) with fibers direction was also improved with functionalization. Aligned PCL-LN promotes significantly longer neurite development (41.1 ± 1.0 μm) than PCL-RGD (32.0 ± 1.0 μm), pristine PCL (25.1 ± 1.2 μm) or PCL-RGD random fibers (26.5 ± 1.4 μm), showing the need for the LN specificity to obtain high quality neurons. The highest astrocyte percentage was obtained for cultures on PCL-RGD random fibers.

III.2 - Introduction

The Neural Stem Cells (NSCs) are multipotent cells with the capacity to differentiate into neurons and glial cells (astrocytes and oligodendrocytes), and able to proliferate while retaining the multipotent capacity in the presence of the growth factors EGF and FGF-2 (Pollard, Conti, et al. 2006; Conti and Cattaneo 2010). The use of such cells combined with engineered biomaterials have the potential to provide therapeutic routes, or disease models platforms, envisaging the regeneration of the central nervous system (CNS) when impaired by traumatic injuries or neurodegenerative diseases (spinal cord injury, brain ischemia, Alzheimer's or Parkinson's diseases) (Cao et al. 2002).

The NSC niche is a complex structure, defined by a specific extracellular matrix (ECM), able to support NSC maintenance and differentiation in-vivo. The biochemical composition of the extracellular environment interacts with cells through cellular surface receptors, mainly integrin activation, which act determining the cellular behavior and function through intracellular signaling pathways, affecting specific gene expression (Flanagan et al. 2006; Y. Wang et al. 2011).

Culture substrates processed from natural and synthetic materials have been developed to replace the role of the ECM on the support of NSCs (Ciardelli et al. 2005; Kim and Park 2006; Hiraoka et al. 2009; Ananthanarayanan et al. 2010; Hackett et al. 2010; Cooper et al. 2011; Nakaji-Hirabayashi et al. 2012). Among the later, polyesters such as polycaprolactone (PCL), polylactic acid, polyglycolic acid and their co-polymers are of particular interest to be used in regenerative medicine as cell scaffolds. Such polymers are biocompatible and biodegradable and have been approved by the regulatory entities for medical applications. Still, these polymers do not present specific biological motifs for cell adhesion. The functionalization of synthetic biomaterials may be essential for cellular compatibility, and several studies suggested the use of peptide fragments of ECM proteins or specific bioactive short peptide motifs recognizable by the cellular integrin-mediated receptors to promote cell adhesion. The use of recombinant proteins or synthetic peptides with adhesion motifs for the cells can be used for biomaterial functionalization while avoiding the issues raised by the use of natural

polymers or materials from animal sources (batch to batch variability, pathogen and immunogenic contamination) (Hersel et al. 2003; Hall et al. 2008; Ananthanarayanan et al. 2010).

The use of material approaches to mimic the ECM for supporting NSCs culture must provide adequate biochemical and biomechanical stimuli, and importantly resemble the native tissue architecture. Nanofiber matrices are promising structured substrates for NSCs culture applications, where the nanofiber configuration can provide specific geometries at the cell scale, being easily produced by electrospinning. The nanofiber mesh, depending on the pore size and hydrophilicity, provides high surface to volume ratio, which is important to cell adhesion, offering high porosity and permeability allowing suitable nutrient, metabolite and gases diffusion. In ex-vivo culture, the substrate topography and the presence of specific biochemical signals (adhesion molecules and growth factors) is critical to control the cellular fate, affecting primarily cellular adhesion and morphology (elongation, spreading) (Beachley and Wen 2009; Ghasemi-Mobarakeh et al. 2010; Hackett et al. 2010; Gloria et al. 2012). Extensive studies have shown the importance of using electrospun fibers to promote tissue organization applied to different cell systems (Kim and Park 2006; G. Wang et al. 2011; Massumi et al. 2012; Smith Callahan et al. 2013). To improve cell/material interface natural biological and synthetic constituents have been combined into biodegradable materials (Hackett et al. 2010; Lam et al. 2010; Mahairaki et al. 2011) or, aiming at higher reproducibility and manufacture standardization, different peptides or biological motifs into synthetic biodegradable materials are combined (Yang et al. 2005; Nisbet et al. 2008; Horne et al. 2010; Lam et al. 2010; Lim et al. 2010; T.Y. Wang et al. 2012). Other applications, where material erosion is insignificant, include the use of non-biodegradable materials (Christopherson et al. 2009; Bakhru et al. 2011).

Examples of these studies are for instance, mouse ESC in aligned and functionalized fibers with YIGSR, a derived peptide from laminin, increased the expression of neural markers, neuron-specific Tuj1 and neurite extensions when compared to random and non functionalized fibers (Smith Callahan et al. 2013); neural precursors, derived from hESC, on aligned LN coated PCL fibers show a more accentuated polar morphology, and increased neuronal differentiation and neurite extension, along the fiber alignment direction (Mahairaki

et al. 2011); higher expression of glial and neuron markers and axon extensions in human NSC derived from ESC, was higher in EGF functionalized aligned fibers (Lam et al. 2010); aligned PLLA nanofibers promoted the NSC alignment and neurite extension according to fiber direction (Yang et al. 2005); laminin coated PCL aligned nanofibers promote neurite extension along the fiber alignment axis of adult rat NSCs with accentuated cellular alignment, and also higher number of differentiated Tuj1 cells (Lim et al. 2010); the fibrous geometry of PCL nanofibers on rat NSCs determined oligodendrocytes specific lineage differentiation when compared to a planar substrate (Nisbet et al. 2008); cortical NSCs have higher proliferation and preferentially differentiate into oligodendrocytes and neurons in aligned and random BDNF functionalized PCL nanofibers (Horne et al. 2010); Neural stem/progenitor cells showed increased cell viability, proliferation and neurite outgrowth, upon transplantation in GDNF functionalized PCL fibrous scaffolds (T.Y. Wang et al. 2012); the fiber diameter of laminin coated PES fibers directed the proliferation and differentiation of rat adult NSCs, from which oligodendrocytes and neurons were preferentially differentiated in 283 and 749 nm, respectively (Christopherson et al. 2009); NSCs show a more polarized and elongated morphology in LN coated PS aligned nanofibers and high neuronal lineage differentiation (Bakhru et al. 2011).

In this work, a comparative study is presented using PCL nanofibers of different topologies functionalized with synthetic GRGDSP motif and LN to determine the importance of combining fibers organization and the selected biological motifs on the NSC proliferation, morphology and differentiation, focusing the analysis on the quantification of NSC differentiation, morphology and organization. The GRGDSP peptide is one of the most active RGD containing sequences for recognition by cell adhesion molecules (Hautanen et al. 1989; Hersel et al. 2003). The RGD sequence is a small peptide fragment, which is conserved in nature, present in many ECM proteins, including Laminin (LN) and fibronectin, which activates cellular engagement by β1 integrin (Hersel et al. 2003; Causa et al. 2010; Gloria et al. 2012) and LN is an ECM protein found in the basement membrane described to support NCS adhesion, migration and differentiation (Hall et al. 2008; Koh et al. 2008; Hiraoka et al. 2009; Klinkhammer et al. 2010).

Medical approved PCL was selected due to its slow biodegradability (in the range of 1 – 2 years), which ensures support of cells during slow tissue regeneration in in vivo applications. The CGR8-NS cell line, derived from the mouse embryonic cell line CGR8, was selected as NSC model. This NSC model expresses the specific attributes of the radial glia (Conti et al. 2005; Pollard, Benchoua, et al. 2006) and proliferates in adherent monolayer to physical supports (Rodrigues et al. 2010; Rodrigues et al. 2011), which is of particular interest to easily assess the effect of electrospun fibers with different topologies towards cell morphology.

III.3 - Materials and Methods

III.3.1 - PCL Nanofibers Preparation by Electrospinning

Aligned and randomly distributed PCL nanofibers were prepared using an electrospinner, as described elsewhere (Canadas et al. 2014). The equipment setup is shown in Figure III.1 – A and it was assembled inside a fumehood for extraction of any organic solvent vapor and using a dehumidifier for humidity control.

The device was composed of a high voltage power supply (Model PS/EL40P0, Series EL 1, Glassman High Voltage Inc., High Bridge, NJ, USA), a syringe pump (Model KDS Legato 210, KDS Scientific, Holliston, MA, USA) and a tube connecting a syringe (Henke Sass Wolf, Germany) to a needle (Needle Valve Dispense Tip Kit, EFD International Inc., UK) with an inner diameter of 0.84 mm.

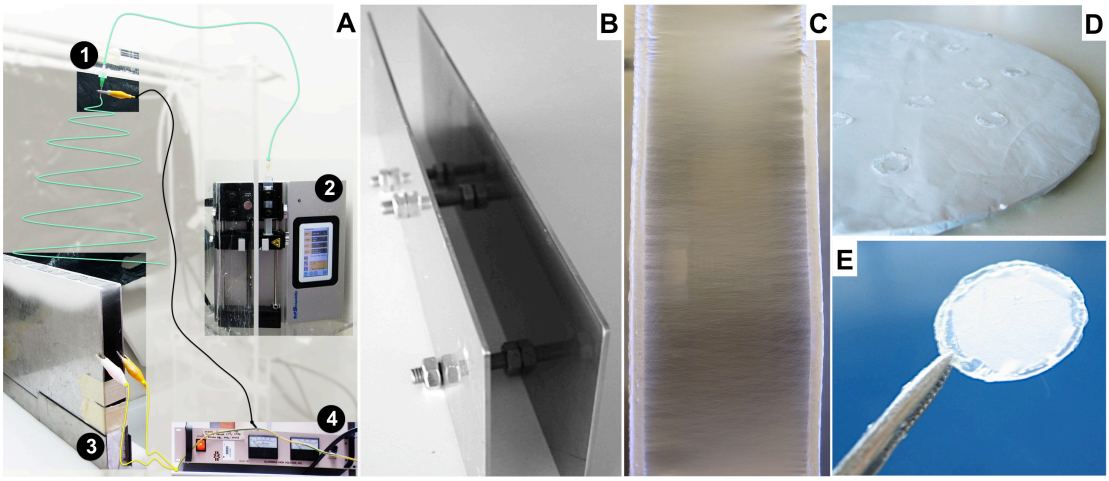

Figure III.1 – Nanofiber preparation and assembly: (A) Adapted view of the electrospinner apparatus: 1 – needle, 2 – syringe pump, 3 – parallel plate collector, 4 – power source; (B) Parallel plates used as a collector for aligned nanofibers; (C) Detailed view of deposited aligned nanofibers oriented perpendicular to the edges of the plates; (D) Round flat collector covered with a random fiber mesh; (E) Nanofiber sample fixed on a glass slide.

The nanofibers were prepared with 6% w/w solution of PCL (70,000-90,000 MW, Sigma-Aldrich, St. Louis, MO, USA,) in 1,1,1,3,3,3-hexafluoro-2-propanol (HFP, Sigma-Aldrich) at a flow rate of 1 $mL.h^{-1}$, with an applied electrical potential and working distance (tip of the

needle to the nanofiber deposition target) of 26 kV and 20 cm or 30 kV and 35 cm to produce aligned (using a two parallel steel plates with 2 cm gap collector, (Figure III.1 – B, C) or randomly distributed nanofibers (using a flat cooper plate collector, Figure III.1 – D).
The polymer solution contained in the syringe is loaded at a constant flow by the pump (2) along a tube (green line) to the needle (1) positioned above and perpendicular to the grounded collector (3). The power source equipment (4) provides the electric potential to charge the polymer solution, wired to the stainless steel tip of the needle by the black cable, while allowing grounding the collector connected by the yellow wires (Figure III.1 – A).

Two types of collectors were used (Figure III.1 - B, D), parallel plates and a flat plate, positioned below and perpendicular to the needle. Aligned nanofibers were deposited in the gap (2 cm) between the two parallel steel plates (Figure III.1 - C), and random fibers deposited on the surface of the flat copper plate (Figure III.1 – D). Both methodologies with different deposition targets are reported extensively in the literature (Li et al. 2003; Teo and Ramakrishna 2006; Beachley and Wen 2009).

The fibers were carefully collected from the supports and fixed onto glass slides (13 mm diameter, VWR, Radnor, PA, USA) with medical grade biocompatible silicone glue (Silastic Medical Adhesive Silicone type A, Dow Corning, Midland, MI, USA) ensuring that the mesh maintained structure integrity throughout the experiments (Figure III.1 - E). The average humidity and temperature working conditions was 30 – 40% and 22-25 ºC, respectively.

III.3.2 - Functionalization of the PCL Nanofibers

III.3.2.1 - Aminolysis Treatment

The nanofibers were washed with 50% v/v ethanol (ThermoFisher Scientific, Waltham, MA, USA) solution in water for 1 hour and rinsed with deionized water under gentle agitation at room temperature. The aminolysis reaction took place immersing the samples in 10% w/v solution of 1,6-hexanediamine (HDA, Fluka, Germany) in isopropanol (ThermoFisher Scientific) for 40 minutes at 37°C, as described in the literature (Zhu et al. 2002). After aminolysis, the nanofibers were abundantly rinsed with deionized water.

III.3.2.2 - Protein Immobilization

Solutions of 20 $\mu g.mL^{-1}$ of laminin (LN, Sigma-Aldrich) and of 50 $\mu g.mL^{-1}$ of peptide motif Glycine – Arginine – Glycine - Aspartic acid – Serine - Proline (GRGDSP, Sigma-Aldrich) were prepared in phosphate buffer (PBS, Life Technologies, Waltham, MA, USA). Protein and peptide crosslink to the amine group (previously introduced in the PCL fibers) was performed by reaction over 24 hours with glutaraldehyde (Migneault et al. 2004) atmosphere, using a solution of 2.5% v/v glutaraldehyde (GA, Sigma-Aldrich). Following, the samples were washed with PBS and immersed in 100 $mg.mL^{-1}$ of glycine (Sigma-Aldrich) solution in PBS for 1 hour at room temperature, in order to react with free aldehyde groups, and washed again with PBS at room temperature.

III.3.2.3 – Quantification of Immobilized Protein

Protein and peptides covalently attached to the scaffold surface were estimated by quantification of the total amine groups using the colorimetric ninhydrin assay (Zhu et al. 2002; Friedman 2004). This method is based on the reaction of the amino groups with ninhydrin with the formation of a blue compound measurable by absorbance spectroscopy. Nanofiber samples of equivalent dimensions (nanofiber mesh covering approximately 0.8 cm^2 of surface area) were removed from the glass slides and immersed in 0.5 mL of 1.0 $mol.L^{-1}$ of ninhydrin (Merck, Germany) solution in ethanol for 1 minute at room temperature and heated at 80°C for 20 minutes, until ethanol evaporation. In order to dissolve the sample of PCL mesh 0.5 mL of 1,4-dioxane (ThermoFisher Scientific) were added, followed by 0.5 mL of isopropanol, in order to stabilize the blue compound formed. Pristine PCL fibers, without any chemical treatment, were used as control for any non-specific residual chromophore response and, PCL fibers submitted to aminolysis but without protein functionalization, were used as an additional control. The absorbance of the reaction product was measured at 538 nm using a microplate reader (Infinite M200 Pro, Tecan, Switzerland). A reference calibration curve was obtained measuring the absorbance of ninhydrin–NH_2 product as a function of graded concentrations of HDA in 1:1 v/v of 1,4-dioxane/isopropanol solutions (Figure IIIA.3 in Appendix).

III.3.3 - NSC Culture

The cell model used was the NSC line CGR8-NS, derived from the mouse ESC line CGR8 (Conti et al. 2005), provided by the laboratory of Professor Austin Smith (Welcome Trust Centre for Stem Cell Research, Cambridge, United Kingdom).

III.3.3.1 – CGR8-NS Culture in Standard Polystyrene Surface

The NSC culture was performed according to previously described (Conti et al. 2005). Cryopreserved CGR8-NS cells, upon thawing, were expanded on uncoated tissue culture T-flasks or 24-well plates (Falcon, BD Biosciences, San Jose, CA, USA), in serum free culture medium composed with DMEM/F12 + GlutamaxTM (Life Technologies) supplemented with 1% v/v N2 (Life Technologies), 20 $ng.mL^{-1}$ of both FGF-2 and EGF (PeproTech, Rocky Hill, NJ, USA), 0.1% v/v B27 (Life Technologies), 1% v/v penicillin-streptomycin (10000 UmL^{-1}, Life Technologies), 1.6 $g.L^{-1}$ glucose (Sigma-Aldrich) and 20 $mg.L^{-1}$ insulin (Sigma-Aldrich). The cells were cultured at 37°C under 5% CO_2 humidified atmosphere, and maintained at passages between 45 and 54. Each passage was performed at 80-90% confluence. Cells were harvested using Accutase (Life Technologies) and cell viability was evaluated using the trypan blue (Life Technologies) exclusion method (Strober 2001) by direct counting of viable cells in a hemacytometer, under an optical microscope (Olympus, Germany). Cell viability remained above 90%.

III.3.3.2 – CGR8-NS Culture on the PCL Nanofibers

The nanofibers were placed in sterile 24-well ultralow attachment cell culture plates (Corning, NY, USA), and sterilized with antibiotic-antimicotic (Life Technologies) solution over night. After sterilization, the nanofibers were washed with sterile PBS and rinsed with culture medium before cell seeding. A suspension of 100 µL with approximately 2.0×10^5 CGR8-NS cells in fresh supplemented medium was deposited carefully on top of each nanofiber, and incubated for 1 - 2 hours to promote initial cell deposition and adhesion to the material.

The seeding density was defined considering an optimal initial cell density of 1.0×10^4 cells.cm^{-2}, in normoxia conditions (Rodrigues et al. 2010), and also the surface available for cells to adhere on the nanofibers as being at least 3 times higher than the flat surface of the well of the tissue culture plate. Reporting to section III.4.2 ahead, a ratio 6:1 of fibers per flat surface was estimated, so the cell density was increased for cells to adhere on the available greater surface and also to overcome any cell death in the beginning of the culture, as the optimal initial cell density is reported to cultures in standard tissue culture plates. Fresh supplemented culture medium was added to final 0.5 mL of culture volume after cell adhesion to the nanofiber. In order to control the cells quality, CGR8-NS cells (2.5×10^4 cells.cm^{-2}) were cultured in standard uncoated 24-well tissue culture plates (in Appendix Figure IIIA.4).

III.3.3.3 - Evaluation of Cell Growth

Viability and estimation of CGR8-NS cell number was monitored indirectly over time using Alamar Blue® (Life Technologies) according to the manufacturer instructions and through a calibration curve (in Appendix, Figure IIIA.1) relating the fluorescence intensity with the number of CGR8-NS cells (estimated by the trypan blue exclusion test from cultures in standard 24-well tissue culture plates). Fluorescence was measured using a microplate reader at excitation and emission wavelengths of 560 nm and 590 nm, respectively.

III.3.3.4 – CGR8-NS Differentiation

After 11 days of NSC expansion on the nanofibers, a differentiation protocol towards neuronal conversion was adapted (Pollard, Benchoua, et al. 2006) and performed in situ. Fresh DMEM/F12 + GlutamaxTM, supplemented as previously described, with 10 ng.mL^{-1} each EGF and FGF-2 was exchanged at day 1 of the differentiation. On the next day fresh medium was replaced, this time without EGF, and with FGF-2 at 5 ng.mL^{-1} and 2% v/v B27. Half the medium was replaced after 4 days. At day 9, culture medium was replaced to DMEM/F12 + GlutamaxTM with Neurobasal medium (1x) (Life Technologies) (1:1) without EGF or FGF-2 and with 2% v/v B27. Half the medium was replaced after 4 days, and the culture was

maintained until day 15 of differentiation. The following scheme (Figure III.2) summarizes the applied protocol.

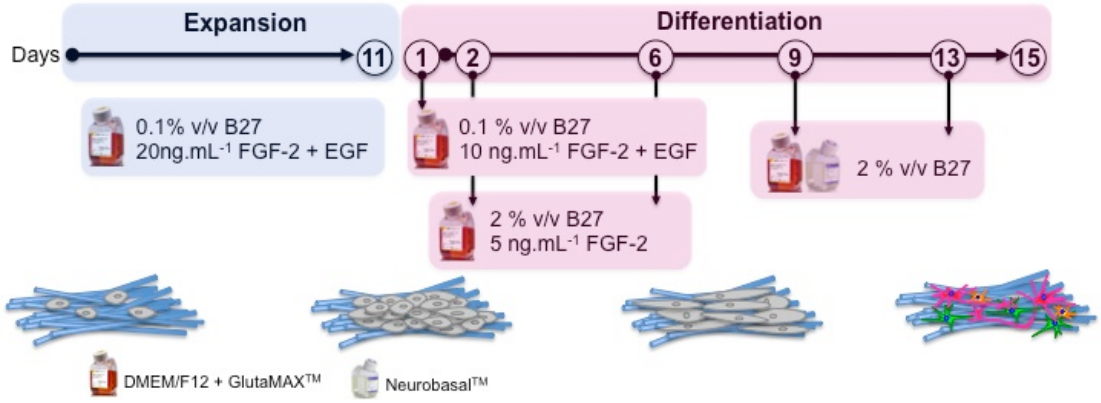

Figure III.2 – Differentiation protocol applied to the NSCs after 11 days of expansion on the nanofiber scaffolds.

III.3.4 – Cell Staining and Immunocytochemistry

The spatial distribution and morphology of CGR8-NS cells on the nanofibers was qualitatively assessed by labeling the nuclei with 4',6-diamino-2-phenylindole (DAPI, Sigma-Aldrich) and f-actin filaments with fluorescent dye phalloidin-tetramethylrhodamine B isothiocynate (TRITC) (Invitrogen) to show nuclear integrity and for cytoskeleton evidence, respectively. CGR8-NS cells were fixed with 4% paraformaldehyde (PFA, Sigma-Aldrich) for 10 minutes at room temperature, washed once with PBS and permeabilized with 0.1% v/v Triton-X-100 (Sigma-Aldrich) and 5% v/v Normal Goat Serum (NGS, Sigma-Aldrich) in PBS for 15 minutes. The cells were stained with 300 µL of phalloidin-rhodamine probe (0.2 µg.mL^{-1} in PBS) for 45 minutes at room temperature. Following one washing with PBS, the cells incubated in 300 µL of DAPI (1.5 µg.mL^{-1} in PBS) for 5 minutes at 37°C under a 5% CO_2 humidified atmosphere. Finally, the cells were washed two times in PBS and kept in PBS protected from light. Blue-stained nuclei and red-stained cytoskeleton were visualized under a fluorescence optical microscope (DMI 3000B, Leica, Germany). Digital images were taken with a digital camera (DXM 1200F, Nikon, Japan).

Immunophenotype analysis was performed for Sox2, Nestin, Tuj1, and GFAP antibodies. The cells were fixed in 4% PFA for 10 minutes at room temperature, washed once with PBS and

permeabilized with 0.1% v/v Triton-X-100 and 10% v/v NGS in PBS for 1 hour at room temperature. Primary antibodies were incubated overnight at 4°C in 0.1% v/v Triton-X-100 and 5% v/v NGS in PBS. The following primary antibodies were used: anti-Sox2 (1:100, R&D Systems, MN, USA), anti-Nestin mouse monoclonal antibody (1:200, Millipore, Germany), anti-βIII-tubulin (1:2000, Tuj1, Covance, Princeton, NJ, USA), and anti-Glial Fibrillary Acidic Protein GFAP (1:100, GFAP, Millipore). After primary antibody incubation, the cells were washed once with PBS and incubated with the proper secondary antibody conjugated with Alexa Fluor 546 (1:500, Life Technologies) for 1 hour at room temperature, protected from light. Next, the cells were washed with PBS and nuclei stained with DAPI (1.5 $\mu g.mL^{-1}$ in PBS) for 5 minutes at room temperature. Finally, the cells were washed two times in PBS and kept in PBS protected from light to be visualized under a fluorescence optical microscope.

III.3.5 - Scanning Electron Microscopy (SEM)

The nanofibers and cell morphology were examined by scanning electron microscopy (SEM). Scaffold samples containing cells were fixed with 4% PFA for 15 minutes, washed once with PBS, and dried by immersion in graded concentrations of ethanol solutions in water (25, 50, 75 and 100% v/v). The samples were kept in an aseptic environment until complete drying. Prior to SEM visualization, the samples were coated with a 45 nm gold/palladium layer by a sputter coater (model E5100, ex-Polaron, Quorum Technologies, ON, Canada) and observed under a conventional SEM (model S2400, Hitachi, Japan) with an electron beam with 20 kV of accelerating voltage. SEM images were analyzed with image analysis software ImageJ (National Institute of Health, USA) to estimate both orientation and diameter fiber profiles. At least 50 samples were individually measured for each condition.

III.3.6 - Statistical Analysis

The results are expressed as standard error of the mean (SEM) expressed by mean ± standard error of the mean (SEM), where SEM = standard deviation / $\sqrt{n}$, where n is the number of independent events. Statistical analysis was performed with one way ANOVA with

Tukeys test for multiple comparison tests, where statistically significant results were considered for determined p values below 0.05. Regressions were calculated by the least squares method and the correlation coefficient by the Pearson product-moment.

III.4 - Results

III.4.1 - Nanofiber Alignment, Diameter and Density

The electrospinning conditions were optimized for a constant and uniform deposition of a solution of 6% PCL to produce reproducible aligned and random defect-free nanofibers with smooth surface morphology. In Figure III.3 are shown the SEM images of the prepared nanofibers with the quantification of the distribution of diameters and relative orientation angles.

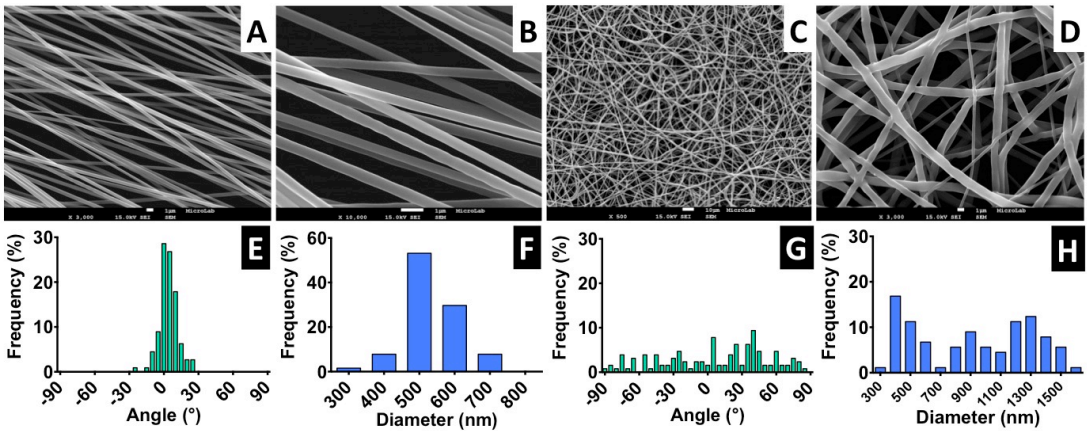

Figure III.3 – Fiber orientation and diameter: (A – D) SEM images of aligned and randomly distributed fibers; (E – H) Histograms of alignment profile and fiber diameter distribution. Scale bar: 1 µm for A, B and D and 10 µm for C. At least 100 fibers were measured in each case.

The fiber alignment was estimated by measuring the angle of each fiber relative to a horizontal reference line. The angle values were normalized, and represented in a histogram within a range of - 90° and + 90°. The estimated average diameter of the aligned nanofibers was 0.54 ± 0.08 μm, with more than 90% of the fibers oriented within a range of ± 30° angle to a reference axis, evidencing a clear uniaxial disposition (Figure III.3 – E).

The random fibers obtained present a wide dispersion, with the fiber angles relative to the reference axis (Figure III.3 - G) covering all the ± 90° angle range and with only around 35% fibers oriented within the narrower range of ± 30°; this feature is highly in contrast with the tight distribution found for the aligned fibers. Also the random fibers diameters fall in a range

of 0.32 - 1.55 μm (average 0.89 ± 0.39 μm) (Figure III.3 - H), as captured by the higher standard deviation value.

The distributions of diameters and relative orientation angles of the prepared aligned and random nanofibers, are coherent with other examples reported in literature (Wang et al. 2009; Wang et al. 2010; Cooper et al. 2011). For this particular study, heterogeneity in the random fiber meshes is desirable, as we were interested in producing a random matrix structure contrasting with the uniformity of the aligned nanofiber samples, in order to obtain two distinct types of topography with impact on NSC proliferation and differentiation (Yang et al. 2005; Nisbet et al. 2008; Christopherson et al. 2009; Hackett et al. 2010; Horne et al. 2010).

The higher average diameter obtained for random fibers compared with the aligned, can be attributed to the material and configurations of the two collectors, considering that the other conditions involved in the electrospinning process, polymer concentration/solution viscosity, flow rate and solvent (Teo and Ramakrishna 2006; Nezarati et al. 2013), were kept the same.

When the parallel plates are used, these are maintained at the same potential, with the electric field established between the needle and the edges of the two grounded plates. The application of an electrical field to this collector configuration forces the formed aligned fibers to be continuously subjected to electrical pulling forces between the two collector plates, both during deposition and post deposition, with continuous stretching of the fibers; such fiber stretching and deformation reduces differences on fiber morphologies compensating for eventual variations in solution viscosity or other system heterogeneities. Therefore, the result is thinner and elongated aligned fibers in a more homogeneous sized mesh (Li et al. 2003; Teo and Ramakrishna 2006; Beachley and Wen 2009). On the other hand random fibers are deposited in the flat-grounded copper surface, not subjected to such pulling forces, thus resulting in a more heterogeneous fiber matrices with, on average, wider diameter fibers. This was similarly reported with other types of collectors (Yang et al. 2005; Chew et al. 2008) where no pulling forces between collector regions are in place. The underlying reason for variations in fiber diameters maybe attributed to heterogeneities in solution viscosity at the tip of the syringe; when subjected to the electric potential different solution viscosities, in each moment, result on different balance between electrical force applied and polymer

solution/needle walls surface tension, which is one of the main phenomena that rules the properties of the fiber produced (Nezarati et al. 2013).

The applied electrospinning method for producing the nanofibers is non-automatic and performed manually, and in fact it is challenging to control the density of the deposited fibers mesh produced. Therefore, to ensure fiber meshes used in cell culture have similar density, it was included a post-manufacturing step of fiber mesh sorting, to which we suggest the introduction of a "Five-scale-fiber-density-ranking" method. To establish that scale, we present both optical microscopy images and higher resolution SEM images of different fibers series.

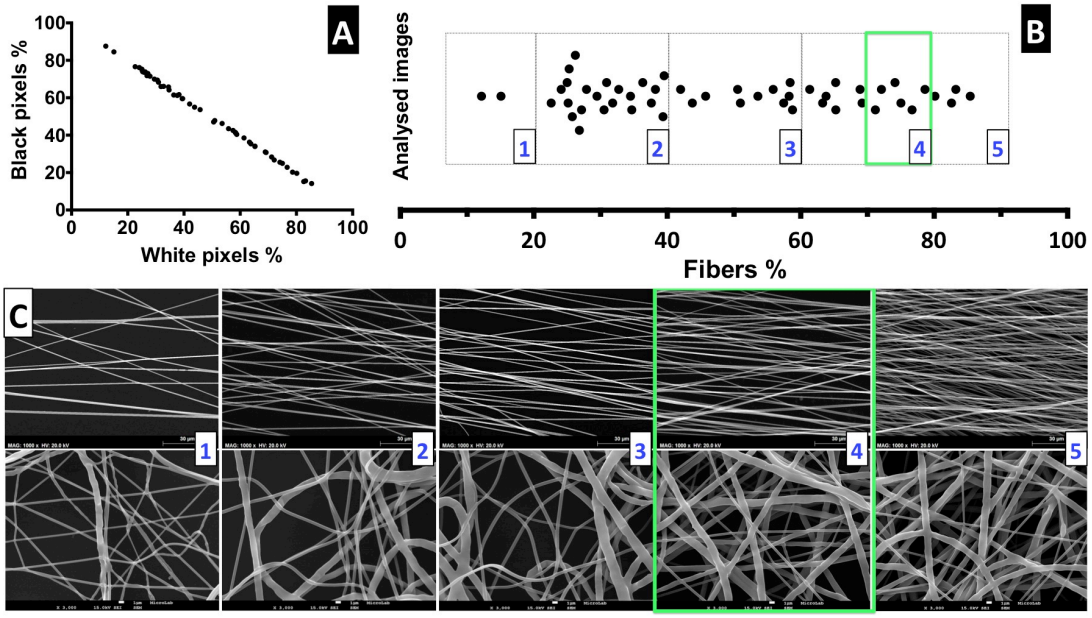

Figure III.4 – Evaluation of the PCL nanofiber mesh density: (A) Proportion of the black and white pixels that compose the bimodal images; scale bars: 30 and 1 µm for the aligned and random meshes, respectively; (B) Distribution of analyzed images with correspondent percentage of fiber mesh, divided into five degrees of density percentage; highlighted with a green square is the interval of fiber density of the samples selected for the cell culture experiments; (C) SEM images for aligned and random fibers, ordered from low to high density mesh.

Such SEM images were analyzed using ImageJ, being converted in bimodal images (with only black and white pixels) to estimate the ratio between empty space and fibers (Wang et al. 2010). In Figure III.4 - A is presented the proportion of both black and white pixels that compose the bimodal images. Figure III.4 – B presents the number of analyzed SEM images

of nanofibers distributed by the five levels of estimated fiber percentage (from approximately 10% to 90%). Examples to illustrate each level of density are shown for both aligned and random distributed fiber meshes according with fiber density level in Figure III.4 – C and the respective images obtained by optical microscopy are presented in Appendix Figure IIIA.2.

The use of scaffolds with similar fiber densities is important for the consistency of the cell culture experimental results. The fiber density should be high enough to allow cell-cell and cell-material contact, but should also provide enough porosity to ensure good culture media infiltration. High compact meshes may perform, at the cells length scale (~30μm), as a membrane or film, with less pronounced 3D structure (Stevens and George 2005; Agarwal et al. 2008). The topography provides specific mechanical input in cell to material adhesion, impacting on how the cells bind and spread. The nanoscale of the fiber structure also provides higher surface area and increased number of binding sites for cell membrane receptors (Stevens and George 2005; Agarwal et al. 2008). The fiber density should allow covering the glass surface of the slide to avoid that cells adhere to the glass, preventing inaccurate estimation of cell proliferation on the top of the nanofibers due to contribution to cell growth on the glass. Still, high-dense and compact meshes should be avoided since it makes difficult the optical characterization of cultured cells. A suitable fiber density of 70-80% was estimated to be optimal by collecting a series of nanofibers with different mesh densities and confirming which will be adequate to avoid the effects mentioned above.

The selected nanofiber samples, with a uniform dense mesh, show evidence of a highly porous structure, which is advantageous for cell culture, allowing good liquid infiltration and permeation, being suitable to accommodate the cells providing a supportive porous environment without losing the topography properties (Norman and Desai 2006; Agarwal et al. 2008; Kai et al. 2013).

For the NSC culture experiments, the nanofiber meshes used were sorted based on optical microscopy examination to fall into 3.5 to 4 level of the “Five-scale-fiber-density-ranking”. This level, highlighted in the green square of Figure III.4 - C, corresponds to a 70-80% fiber density, according with SEM images, which is appropriate to provide adequate cell growth

and visualization of the nanofibers, while avoiding cell growth on the underlying glass of the slide.

III.4.2 – Functionalization of the Nanofibers Surface

The next step for the preparation of the nanofibers for cell culture was to covalently bind LN and the GRGDSP peptide on the material surface.

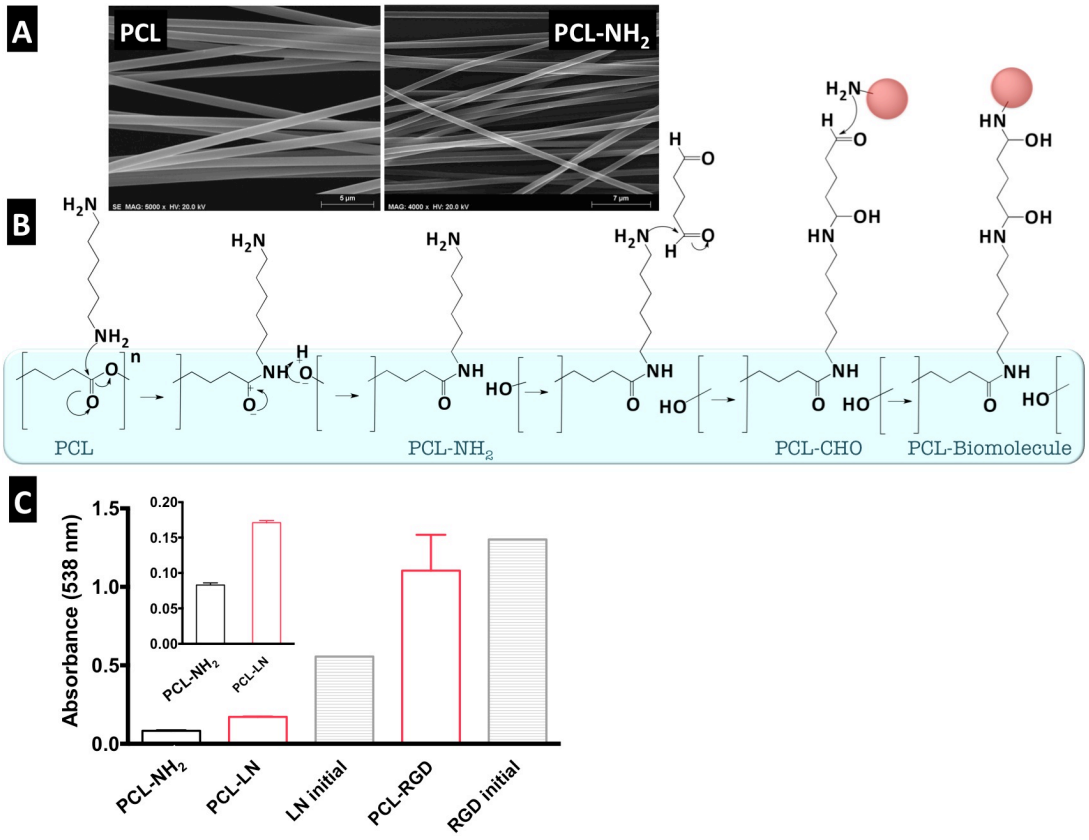

Figure III.5 - PCL nanofiber functionalization with LN and GRGDSP: (A) SEM images of PCL nanofibers before and after aminolysis treatment (scale bar: 5 (left) and 7 (right) µm); (B) Representation of the surface functionalization reaction steps to the final structure of the functionalized PCL material; (C) Absorbance at 538 nm for quantification of equivalent NH2 groups in nanofibers and initial solutions of peptide. Error bars represent SD.

The aligned PCL nanofiber meshes were identified as “PCL” for PCL pristine non-modified nanofibers, “PCL-NH_2” for aminolised PCL nanofibers and “PCL-LN” or “PCL-RGD for LN and

GRGDSP functionalized nanofibers, respectively. The random PCL fibers functionalized with GRGDSP were identified as PCL-RGDr. Examples of SEM images of the PCL nanofibers after aminolysis show structure integrity with no alteration on morphology, and the reaction scheme for the formation of the treated material PCL-NH_2 are presented in Figure III.5 – A and B, respectively.

The overall surface area of the scaffolds fiber mesh was estimated to be 5 cm^2 (considering fiber density, length and average diameter estimated from SEM images) covering 0.8 cm^2 of glass slide which corresponds to a ratio of approximately 6:1 cm^2 of fiber surface per slide. The engrafted NH_2 groups on the polymer surface and the immobilized LN and GRGDSP motif were both evaluated by the quantification of the equivalent total amine groups (Figure III.5 – C) by the ninhydrin method that quantifies free amine groups (Zhu et al. 2002; Kim and Park 2006). The amount of NH_2 groups per mesh surface area was estimated as (7.1 ± 0.8) $nmol.cm^{-2}$ for PCL-NH_2 samples, not quenched with glycine, indicating the insertion of functional amine groups onto the nanofibers (Figure III.5 – C), providing a network for further protein or peptide functionalization (calibration curve of ninhydrin – NH_2 absorbance in Figure IIIA.3 in Appendix). Estimated equivalent amine densities for the PCL-LN and PCL-RGD samples, at values of (28.1 ± 0.8) and (277.2 ± 61.2) $nmol.cm^{-2}$, respectively, were considerable higher than for PCL-NH_2 samples. In pristine PCL fibers a background misreading absorbance was estimated as (2.4 ± 0.5) $nmol.cm^{-2}$.

Comparing the ninhydrin assay results for each of the initial biomolecules solutions used in the crosslinking reaction and the respective nanofiber meshes obtained (Figure III.5 – C), an efficiency of nanofiber functionalization was determined as (22.1 ± 1.5) % and (83.8 ± 16.8) % for PCL-LN and PCL-RGD, respectively. Additionally it was estimated a number of biomolecules per functionalized area at the values of 7.2 $nmol.cm^{-2}$ and 0.60 $pmol.cm^{-2}$ for GRGDSP and LN respectively. Also for LN bonding a close distance between LN molecules of 18.2 nm was approximated (considering 8 nm for 70-90 nm sizes with a cross like structure for LN molecule). Regardless the potential inaccuracy of these approximated values, they provide an order of magnitude for the functionalization degree of fiber surface.

Covalent attachment of biological motifs has been shown to be favorable for tissue engineering applications, especially for long-term cell culture providing a more stable layer of proteins on the culture surface. Therefore, covalent immobilization of LN and GRGDSP peptide onto the nanofibers was the strategy followed in this study. However, the chemical processes may affect the active sites of the biomolecule, where partial inactivation of the immobilized biomolecules may occur (Yoo et al. 2009). Alternatively, physical adsorption of biomolecules (i.e coating of material surfaces with adhesion proteins) is a commonly applied method to improve cell adhesion to surfaces, but the weak forces between the biomolecule and the surface provide a less stable layer of adhesion molecules, and over time the molecules may be washed away (Yoo et al. 2009; Ghasemi-Mobarakeh et al. 2010; Zander et al. 2010).

For PCL nanofibers functionalization, the first step was a treatment with 1,6-hexanediamine (aminolysis) forming a covalent –CONH- bond at the fibers surface, while the second amine (PCL-NH_2) is expected to remain free allowing further immobilization of the biomolecules (Zhu et al. 2002). Glutaraldehyde was then used for covalent cross-linking between the amine groups (at the surface of the fibers previously exposed to aminolysis) and the amine groups of the LN and peptide. Glutaraldehyde has been extensively used as an effective crosslinking agent between proteins and enzymes (Migneault et al. 2004; Zhang et al. 2006), however some degree of cytotoxicity is attributed due to potential unreacted free aldehyde groups and leaching of toxic degradation residues (Zhang et al. 2006). Thus, to minimize eventual cytotoxicity in this study, the glutaraldehyde was delivered through the vapor phase, obtained from a 2.5% glutaraldehyde solution, to the PCL-NH_2 nanofibers immersed in solutions of LN or GRGDSP (Migneault et al. 2004), and in a final step, the scaffolds where immersed in a glycine solution quenching any eventual free toxic aldehyde groups with this small aminoacid.

The biological factors were immobilized successfully, with higher efficiently of immobilization and number of molecules per fiber area for the GRGDSP motif. For the estimated amine densities it is assumed an equivalent ninhydrin response for hexanediamine for both biomolecules, (in the pristine PCL the detected background absorbance could be due to chromophore possible interaction with PCL or residual absorption of the solution) however the LN and RGD include on their structures other contributions for ninhydrin response, such as

the guanidine group of arginine present in the RGD moiety and LN and several aminoacid side groups present in the LN, not only primary amines, but also the indole ring of tryptophan, the sulfhydryl group of cysteine.

The large 810 kDa multidomain glycoprotein of LN and the small 587 Da synthetic linear peptide GRGDSP, differ greatly in size and structure (Beck et al. 1990; Hersel et al. 2003). The size of GRGDSP might be advantageous in terms of reactivity (easy diffusion and chemical lability), making a more effective use of the NH_2 available at the PCL-NH_2 fiber network. In addition to the crosslink between biomolecule and amine groups in the PCL-NH_2, inter biomolecules crosslinking with glutaraldehyde could take place, implying several layers of linked biomolecules. Still, neglecting such possible effect and based on the ninhydrin assay response to pure LN and GRGDSP molecules, the higher functionalization density in PCL-RGD, assuming a homogenous functionalization monolayer of the nanofiber surface, represent for the GRGDSP the full use of the NH_2 network available.

A smaller fraction of the PCL-NH_2 amine network was used for the large LN molecule of 8 nm for 70-90 nm size with a cross like structure, however that might represent an extremely compact occupation of a large fraction of the nanofiber surface considering the small distance between LN molecules. Overall it can be said that at a micro level scale relevant for cell organization, it was possible to provide widely available binding sites for cell integrins in the biofunctionalized nanofibers.

III.4.3 - NSCs Proliferation on the Nanofiber Scaffolds

The NSC proliferation profile on the nanofiber scaffolds is represented in Figure III.6 - A. In general, over time the number of cells increased in all the conditions. Analyzing in detail the 11 days of the cell culture, an early adaptation stage is observed in the beginning of the culture at day 1. The nanofibers were seeded with 2×10^5 cells and for the number of cells in culture to reach the initial cell number it was necessary 3 days in the case of PCL-LN and PCL-RGD random, 5 days for cultures in PCL-RGD aligned and approximately 7 days for cells seeded in pristine PCL fibers.

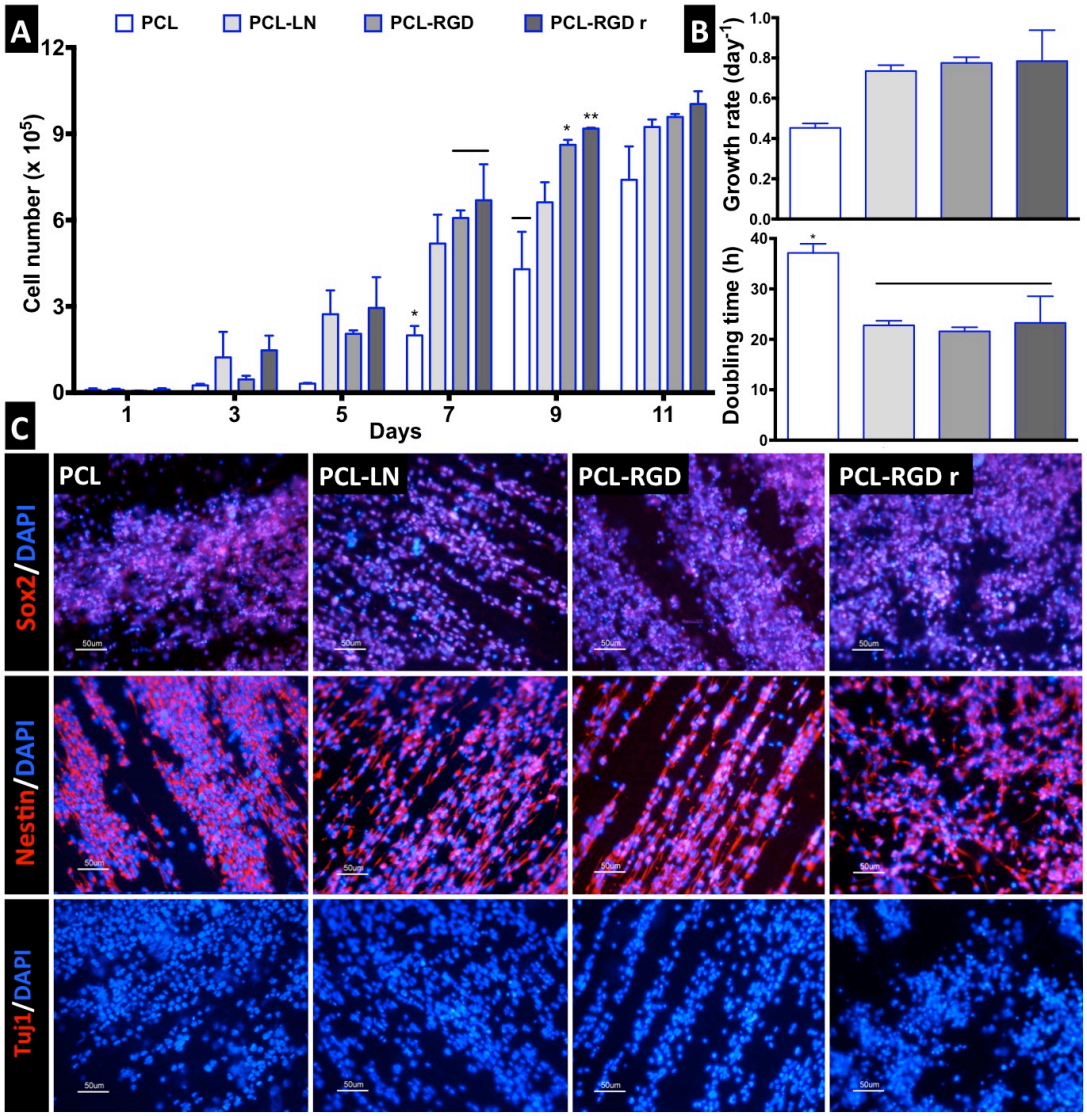

Figure III.6 - CGR8-NS growth profile on aligned PCL, PCL-LN, PCL-RGD and random PCL-RGD nanofibers: (A) Cell number variation over 11 days of culture; values correspond to initial cell seeding of 2.0 × 10^5 cells per scaffold. Mean values represented for n = 3 and error bars are SEM; * p < 0.05, ** p < 0.01; note that Alamar blue profile was carried only on expansion phase; (B) Specific growth rates (day^{-1}) and doubling times (h) for each condition, determined from the slope represented by $\ln x = \ln x_0 + mt$ and doubling time by $t_{1/2} = \ln 2/m$. (n=3, SEM); (C) Fluorescence images for the immunophenotype analysis for Nestin and Sox2 (multipotency markers, red) and Tuj1 (neuronal precursor marker, not observed) antibodies, nuclei labeled with DAPI (blue), scale bar = 50 μm.

Statistically significant different cell numbers on functionalized PCL-RGD fibers relative to pristine PCL are found at day 7 and day 9. A tendency for higher proliferation on PCL-RGD can be observed, which is more noticeable at day 9, with an increase in the meaningful differences.

From day 7 to day 9 the number of NSC in aligned PCL-LN and both PCL-RGD nanofibers was more distinct. However these differences decreased from day 9 to day 11, and turned out fairly reduced by day 11. The scaffold area is similar for all the conditions, and when its maximum capacity for cell support is used, cell proliferation becomes restricted, indicating that cell confluence may have been reached, dissipating differences between cell numbers in the functionalized scaffolds by day 11. The cell numbers at the end of the culture were (7.4 ± 1.2) × 10^5, (9.2 ± 0.3) × 10^5 and (9.6 ± 0.1) × 10^5 and (1.0 ± 0.4) × 10^6 cells for PCL, PCL-LN and aligned and random PCL-RGD, respectively.

Higher cell specific growth rate was observed in the presence of LN and GRGDSP (Figure III.6 – B). The lower specific growth rate and higher doubling time were determined for cultures on pristine PCL nanofibers (0.45 ± 0.02 day^{-1} and 37.1 ± 1.8 h). In LN (0.73 ± 0.03 day^{-1} and 22.7 ± 0.9 h) and GRGDSP (aligned 0.78 ± 0.03 day^{-1} and 21.5 ± 0.8 h; random 0.78 ± 0.15 day^{-1} and 23.2 ± 5.3 h) scaffolds an increase in the growth kinetics and faster doubling times is observed, with pristine PCL doubling time significantly higher from the remaining conditions. No major differences in terms of growth kinetics were observed between aligned and random matrices (PCL-RGD).

The cell quality after 11 days of culture on the PCL nanofiber scaffolds was evaluated by immunophenotype analysis for the expression of the specific markers Nestin, Sox2 and Tuj1 (Figure III.6 – C). It is observed form the immunostaining images that Sox2 and Nestin markers (NSC multipotency and self renewal) are positively expressed (red), whereas Tuj1 marker (neuronal maturation) is negatively expressed, in all the conditions. Moreover, the immunostaining images provide also evidence of the effect of the aligned structure of the substrate on the cellular organization on the nanofibers, where is observed that cellular distribution follows the nanofiber arrangement.

The prepared nanofiber scaffolds demonstrated to be suitable substrates for the cellular proliferation of CGR8-NS cells, in the presence of growth factors EGF and FGF-2. The NCSs kept the multipotent and self renewal capacity, with improved cell adhesion in the PCL-LN and PCL-RGD nanofibers and the cellular growth progressed more efficiently with higher growth rates and higher cell numbers attained at the end of the culture. On the other hand

NSC lower growth rate and low end cell numbers in pristine PCL nanofibers contrasts with the positive effect of the adhesion factors on improving the proliferation of the NSCs. Also the cellular proliferation was found to be equivalent in both functionalized aligned and random matrices.

Studies report variable tendencies in cell proliferation in aligned and random matrices. Increased proliferation was found in aligned nanofibers with neural progenitor cells (NPs) in collagen nanofibers (Y. Wang et al. 2011), in Schwann cells in PCL-PLGA (Subramanian et al. 2012), in human NPs in PCL nanofibers (Mahairaki et al. 2011), in mouse NSCs in PCL/collagen nanofibers (Hackett et al. 2010). Others report no statistical significant differences between aligned and random matrices as with PC-12 cells in PCL functionalized with laminin and collagen (Zander et al. 2010), with cortical NSCs in PCL-BDNF nanofibers (Horne et al. 2010), with Schwann cells in PCL-chitosan nanofibers (Cooper et al. 2011).

An enhanced cellular expansion is associated with the geometry and biochemistry of the substrate that offers more accessible contact points for cells to adhere and a degree of porosity that allows increased diffusion to a better biochemical enrichment of the substrate and cell infiltration (He et al. 2010; Y. Wang et al. 2011; Wheeldon et al. 2011). For example, the cell spreading with increased actin formation with direct impact on increased proliferation was observed in lower diameter nanofibers (Christopherson et al. 2009), while the increased NSC cellular proliferation in higher diameter nanofibers was attributed to the higher mesh size allowing better cell infiltration, indicating that cellular proliferation is influenced (but not restricted to) by fiber diameter and distance, mesh porosity and fiber organization (He et al. 2010).

The random nanofibers structure (PCL-RGDr) provided a substantial higher number of contact points, promoting the cells to efficiently adhere and thus to proliferate, even if the cells are organized in several directions lacking the unidirectional structure observed in aligned nanofibers. This could be relevant in the first 3 days of the culture where in PCL-RGDr the cell numbers were higher.

On the other hand, the surface of the non-modified aligned PCL nanofiber allowed for some cellular attachment, in the presence of the proteins supplemented in the culture media the

NCSs were able to proliferate on such surfaces, although in lower extent. The PCL has a relatively higher hydrophobic character, described by high contact angles ($\theta > 90^{o}$) on solid surfaces (Fang et al. 2011; Yuan and Lee 2013), and therefore cellular binding interactions at the PCL-cells interface are more difficult to occur. In the absence of a biochemical environment recognizable by integrin receptors, non-receptor mediated adhesion mechanisms will take place via weak chemical interactions (hydrogen bond, electrostatic, polar and ionic interactions) (Bacáková et al. 2004). Although under weak interactions with the substrate, cellular survival and proliferation has been previously reported. For example rat neural/stem progenitor cells were capable to proliferate in untreated PCL random nanofibers (Nisbet et al. 2008), and Schwann cells were found to maturate in both PCL fibers and films (Schnell et al. 2007; Chew et al. 2008). Another study showed that in the presence of -OH end groups, in a treated inert substrate in serum free culture, the adhesion and migration of NSCs was improved. Moreover it was suggested that even in the absence of exogenous ECM proteins, after a certain period of culture the cells were able to interact with the treated substrate and regulate cellular functions by endogenous secretion of ECM proteins (Yao et al. 2016).

The higher number of immobilized GRGDSP per nanofiber surface area probably had an effect on the NSC proliferation rate, as observed by the higher increase in cell number at day 9 in the PCL-RGD conditions, when compared to PCL-LN. LN has the potential to provide more specific interaction with cell integrins, but the use of a GRGDSP (linear sequence of peptides) offers a higher robustness for the immobilization protocol.

In the case of large protein complexes such as LN, losses of specificity for cell adhesion are likely to occur due to destabilization of protein structure during the crosslinking process. The unpredictable orientation of the biomolecule, might restrict the access of cellular integrins and interactions with the substrate (water affinity, topography, charge) may also interfere with the motifs accessibility to cellular receptors (Hersel et al. 2003; Nakaji-Hirabayashi et al. 2012). Moreover, protein crosslinking by glutaraldehyde reaction occurs via numerous different and simultaneous mechanisms due to the multicomponent nature of this chemical in solution, so it is expected some protein denaturation to occur (Migneault et al. 2004).

NSC multipotency and self-renewal phenotypes were maintained, by the positive expression (in red) of the Nestin and Sox2 markers and the negative expression of the class III β-tubulin (Tuj1) marker reveals that no NSC differentiation is observed, after 11 days of culture on the nanofibers, in the presence of EGF and FGF-2 growth factors. Overall the nanofiber substrates used in the culture did not affect the CGR8-NS primary properties (Conti et al. 2005).

III.4.3.1 – Evaluation of NSCs Organization and Morphology

The SEM images of the cells in culture in each of the nanofiber conditions, are shown in Figure III.7 – A, evidencing the differences of the cells morphologies. The NSCs are more spread with a more rounded shape in the PCL-RGD random nanofibers and non-functionalized PCL aligned nanofibers, while in the both aligned PCL-LN and PCL-RGD the cells are more elongated, with a more pronounced bipolar character, following the nanofibers axis orientation.

By comparative observation of the fluorescence images obtained on PCL-RGD in aligned and random nanofibers (Figure III.7 – B), the phalloidin-rhodamin stained F-actin fibers of the cellular cytoskeleton reveals an ordered distribution of the cells aligned in the direction of the aligned nanofibers, and a more dispersed and spread cellular distribution in the random nanofibers. The quantification of these differences is represented in the respective histograms (Figure III.7 – B) for the measured angles of the stained F-actin fibers with reference to the direction of the substrate nanofibers.

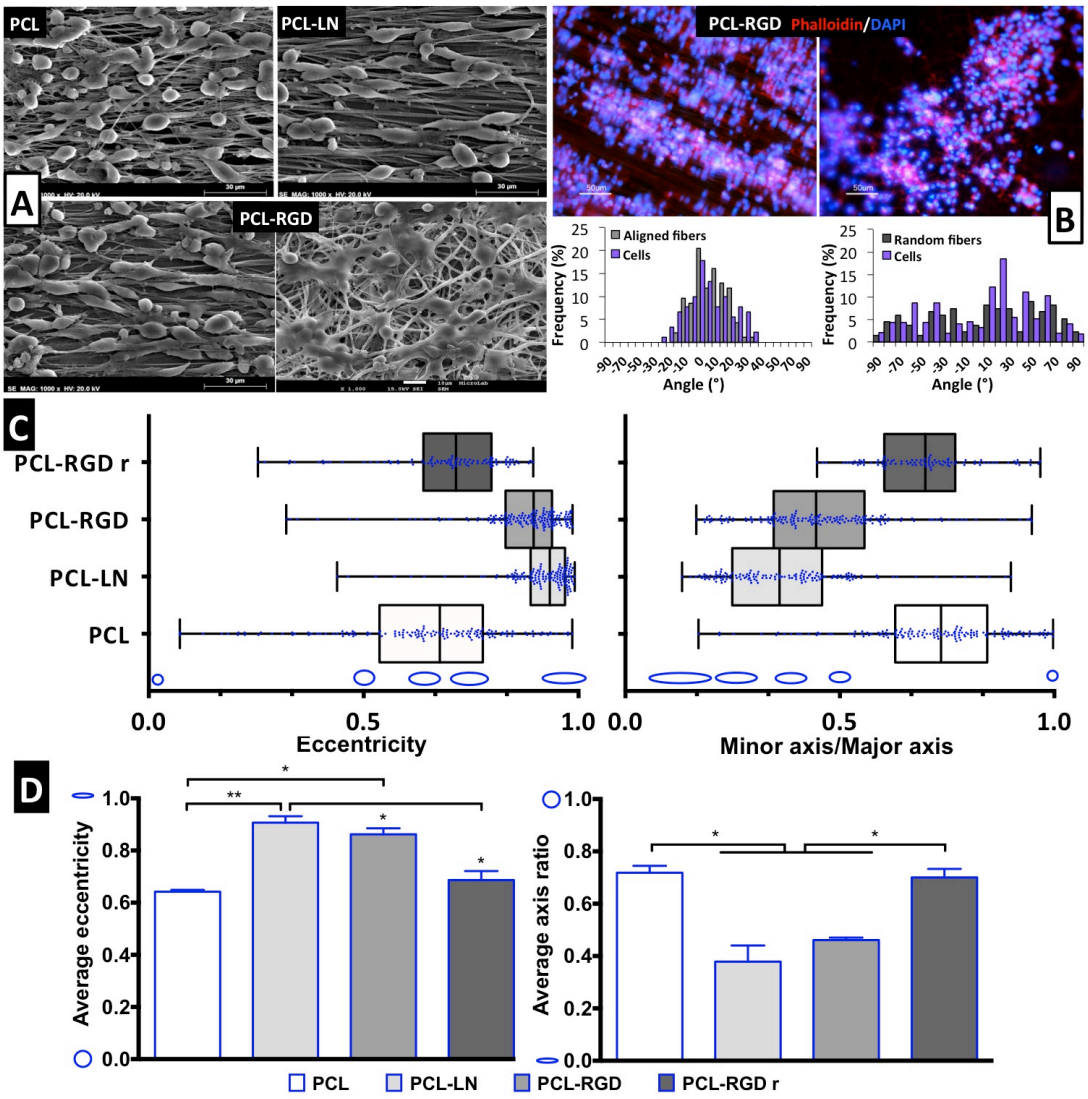

Figure III.7 - Evaluation of cell morphology and organization after CGR8-NS cells expansion on the PCL nanofibers: (A) SEM images after 3 days of expansion; scale bar 30 mm; (B) Image of cellular cytoskeleton staining with phalloidin-rhodamine in aligned and random PCL-RGD, with respective histograms of cell alignment vs fiber arrangement; scale bar 50 mm; (C) Box and whiskers plot for eccentricity (E = 0, perfect circle; E = 1, elongated shape) and aspect ratio (AR = 1, perfect circle; AR = 0, elongated shape) for cellular elongation quantification. The box boundaries represent the 25th and the 75th percentile, the straight line inside is the median (value at the 50th percentile). The points distribution is limited (whiskers) by the minimum and maximum values; a minimum of 50 cells were measured; (D) Average values for eccentricity and aspect ratio error bars represent SEM; * $p < 0.05$; ** $p < 0.01$ (n=2).

The cells in the aligned fibers are distributed across a narrower angle range of ± 30°, while in the nonaligned nanofibers the angle distribution to which cells occupy is wider over the interval of ± 90°.

The eccentricity is a parameter used to describe the cellular shape (Xie, Willerth, et al. 2009; Xie, MacEwan, et al. 2009). The NSCs bipolar shape obtained from SEM images was fitted using ImageJ to an elliptical geometric form, in order to determine the major and minor axis. The eccentricity was calculated with Equation (1),

$$Eccentricity = \frac{\sqrt{\left(a^2 - b^2\right)}}{a} \qquad (1)$$

where *a* and *b* are the semi-major and semi-minor axis of the ellipse, respectively. The ellipse has an eccentricity greater than 0 (which corresponds to a circle) but lower than 1 (in this limit closest to a line segment). Additionally, the elongation of the elliptical form measured was evaluated by the ratio between the minor and the major axis that, inversely, when equal to 1 corresponds to a perfect circle and when closest to 0 describes a shape approaching a line segment.

In the box and whiskers plots for the shape parameters (Figure III.7 – C), narrower boxes indicate a tighter population distribution within the interval of the represented values. The box and whiskers distributions profiles are identical between both parameters, where both PCL-LN and aligned PCL-RGD boxes locate towards representative values of increased elongated shape. Tighter population distributions in terms of eccentricity are found for PCL-LN and aligned PCL-RGD. For visualization purposes, the shape corresponding to discrete eccentricity and axis ratio values is illustrated on the xx-axis on Figure III.7 - C and yy-axis of Figure III.7 - D. The differences in the estimated averages of both shape parameters are also in agreement (Figure III.7 – D) for each nanofiber condition and differ identically. The average cell eccentricities in aligned PCL-LN reached a value of 0.90 ± 0.02 (very close to 1) being statistically significant different to aligned pristine PCL and random PCL-RGD fibers, with identical estimated eccentricities of 0.64 ± 0.02 and 0.67 ± 0.01, respectively. The higher differences observed (with $p < 0.01$) are according with the narrower PCL-LN distribution of eccentricity points in the box plot compared to pristine PCL. In aligned PCL-RGD scaffolds,

the NSCs show also better elongations with eccentricities of 0.86 ± 0.01, comparable to PCL-LN.

The effect of substrate topography on cellular proliferation varies with the cellular/substrate system and in fact, the cell morphology and the differentiation potential are critically susceptible to the physical substrate. In particular, NSCs, which are highly polar cells, substrate topography is often determinant (Ingber 2003; Bettinger et al. 2009; Qi et al. 2013).

Shape parameters, eccentricity and axis ratio, were in agreement, demonstrating the influence of the nanofibers topography on cell morphology and distribution. As expected, NSC cells were able to align and elongate extensively exhibiting a highly bipolar morphology especially in the presence of adhesion factors, in aligned PCL-LN and aligned PCL-RGD nanofibers. Aligned cell populations, although less elongated, were found in pristine PCL aligned fibers and cells with a more round and spread shape morphology and distribution found in randomly structured PCL-RGD nanofibers. Aligned pristine PCL and random PCL-RGD show similar cell elongation shape profiles, which is compatible with the absence of adhesion factors and effect of substrate topography, respectively.

Similar illustrative examples regarding the effect of the topography were also described with adult NSCs in PCL coated LN nanofibers (Lim et al. 2010) and with NPs after 3 days of culture in PCL poly-ornitine/LN coated nanofibers, where cells in the random substrate show a spread and less polar morphology (Mahairaki et al. 2011).

III.4.4 - NSCs in situ Differentiation

After 11 days of cell culture on the nanofiber scaffolds a neuronal differentiation protocol was applied in situ for 15 days, by removing gradually EGF and FGF-2 mitogens from the culture medium. In Figure III.8 - A the immunofluorescence images show the expression of the specific markers Tuj1 and GFAP, indicating the presence of neurons and astrocytes, respectively, in all the nanofibers conditions.

The evaluation of the number of differentiated cells in each of the nanofibers was performed based on immunofluorescence images. The values presented for differentiated cells

correspond to the analysis of subsection images for the specific Tuj1 and GFAP markers taken at day 15 of the differentiation protocol. The cells expressing positively Tuj1 or GFAP were counted and considered as positive events for differentiation at broad, with estimation of a relative percentage of neurons and astrocytes for each condition (Figure III.8 – B left). In order to give an approximate overview of the total events relative to the overall cells in culture, the number of differentiated cells (events) was normalized with the total number of DAPI stained cells (nuclei observed) in the respective images of Tuj1 and GFAP marked cells (Figure III.8 – B right). Overall a higher number of differentiated cells (total events) were counted for PCL-LN and PCL-RGD nanofibers with a lower number of differentiated cells in aligned pristine PCL nanofibers (Figure III.8 – B left). Looking at the relative percentages of neurons (values indicated in the Tuj1 bars) higher percentages were estimated in aligned non-functionalized PCL (67%) and aligned PCL-LN (59%), and similar percentages of neurons and astrocytes were estimated for aligned PCL-RGD (~50%) and an higher percentage of astrocytes was found for PCL-RGDr (59%).

In general a low percentage of differentiated cells relative to the total number of cells in culture was obtained (Figure III.8 – B right), ranging from the highest determined in PCL-LN with 7% of Tuj1 and 3% of GFAP to the lowest in pristine PCL with 3.4% of Tuj1 and 1.4% of GFAP positive cells, with the percentage of Tuj1 expressing cells higher for all the conditions.

The NSCs were able to differentiate into neurons and astrocytes, in all nanofiber scaffold conditions, after 11 days of proliferation followed by 15 days of differentiation period, however a relatively low percentage of differentiated cells was obtained (taking into reference an average of 10 - 40% differentiated neurons estimated, from the applied protocol in tissue culture plates (Pollard, Benchoua, et al. 2006)).

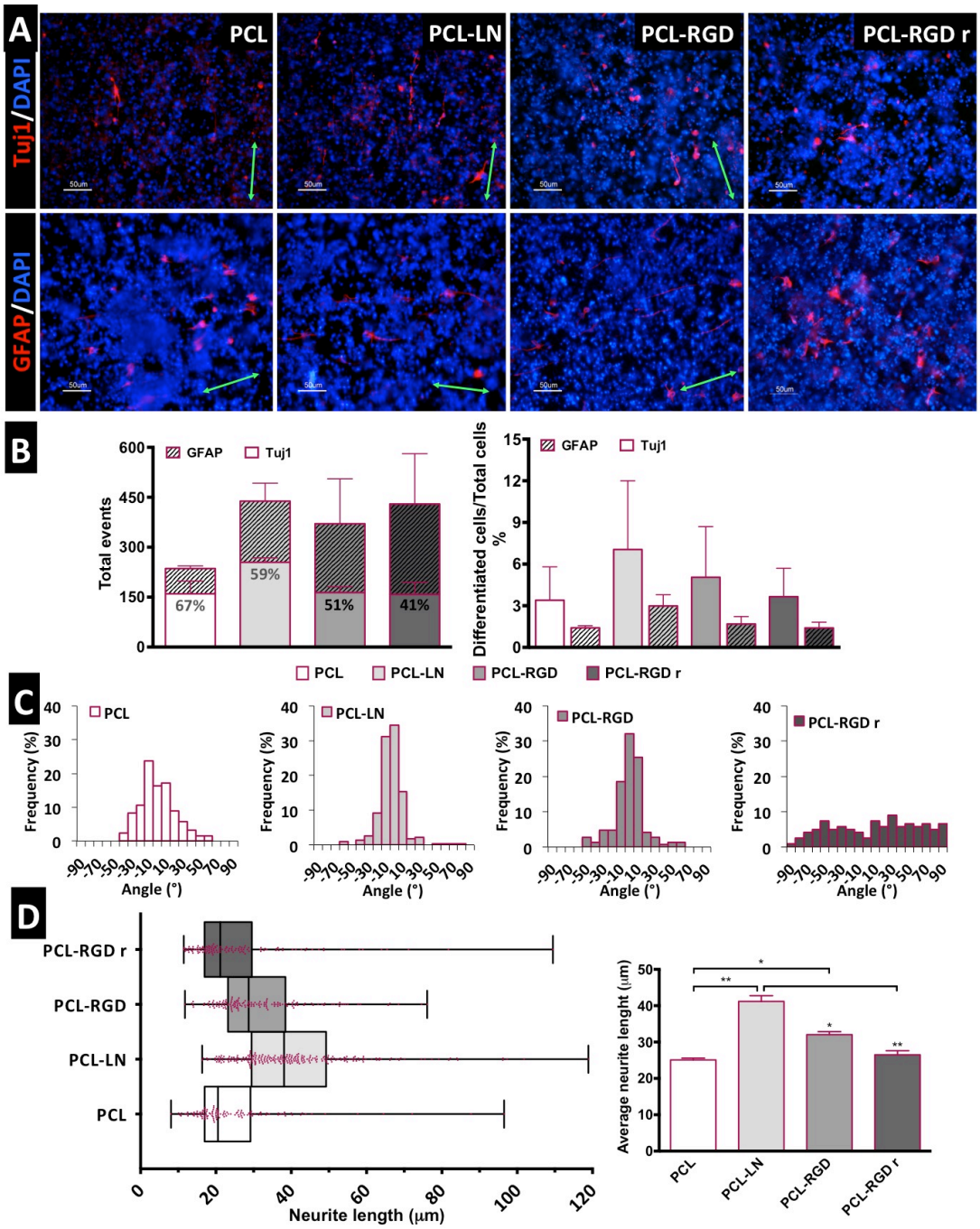

Figure III.8 - Evaluation of in-situ CGR8-NS differentiation: (A) Immunofluorescence images of the expression of the neuronal marker Tuj1 and astrocyte marker GFAP (green arrows indicate the fiber direction); (B) Total differentiated cells (events) counted (on the left), and percentage of differentiated neurons and astrocytes relative to the total cells in culture (on the right) (n=2); (C) Histograms of neuron alignment distribution; (D) Neurons elongation, by representation of the neurite lengths distribution (on the left). The box boundaries represent the 25th and the 75th percentile; the straight line inside the box represents median (50th percentile). On the right, averages of neurite lengths; a minimum of 50 cells were measured in the immunofluorescence images; * $p < 0.05$; ** $p < 0.01$ (n=2).

A number of reasons might have contributed to the low percentage, namely, the end of the differentiation at day 15 corresponds to the minimum time required for the first mature cells to start to emerge, thus a longer period of culture would be more effective; the differentiation protocol was initiated after an expansion period until almost complete confluence on the nanofibers, thus it would be expected that the total cells in culture are largely in higher number than the emerging differentiating cells; from day 14 of the differentiation protocol it is advised to supplement with BDNF to enhance and maintain to enhance and maintain neuronal differentiation for longer periods in culture, however it was intended to observe a topological response in cellular maturation without bias to neuronal cells.

However concerning the total cells in culture, the relative percentage of neurons was higher in all the conditions, but the relative percentages regarding the total events, neurons were in higher proportion in aligned pristine PCL and PCL-LN, in even percentage with astrocytes in aligned PCL-RGD and in lower percentage in PCL-RGDr.

This tendency is in agreement that alignment of the fibers seems to help neuronal differentiation, but RGD functionalization by itself would benefit differentiation towards astrocytes. Still, it is difficult to draw strong conclusions, since the overall differences (Figure III.8 – B) were found to be not statistically meaningful, and with a considerable associated error.

III.4.4.1 – Neurons Alignment and Neurite Extension

The alignment histograms (Figure III.8 – C) show the influence of the nanofiber organization (in Figure III.8 – A the green arrows indicate the fiber direction in the aligned matrices) on the differentiated neurons orientation. In non-functionalized aligned PCL matrices neurons were distributed along ± 50° orientation angle range, evidencing a well defined peak of cell alignment. Regarding PCL-LN and PCL-RGD aligned fibers sharper histogram peaks are obtained, indicating a higher percentage of the cell population following the leading fibers alignment, approximately within a narrower range of ±30° orientation angles, for both conditions. Neurons cultured in PCL-RGDr present a wide distribution of alignment angles within the broad interval of ± 90° orientation distribution, according to the randomly distributed

nanofibers, highly in contrast with the alignment peaks in the histograms determined for the aligned nanofibers conditions.

The neurite lengths profile distribution displayed in the box and whiskers plot and the corresponding average neurite lengths are represented in Figure III.8 – D left and right, respectively. Tight length distribution (narrower boxes) is observed in PCL-RGDr and in non-functionalized PCL nanofibers, where shorter neurite developed, (26.5 ± 1.4) μm and (25.09 ± 1.2) μm, respectively. A broader highest length distribution (wider box) was found in PCL-LN aligned nanofibers with the longest average cellular extensions determined, (41.07 ± 1) μm. The higher neurite lengths found in PCL-LN differ significantly with the remaining conditions, especially with pristine PCL and PCL-RGDr. The lowest neurite extensions found in pristine aligned PCL also differ significantly from PCL-RGD aligned condition.

Studies reported show that substrate dimensions and alignment exert an influence on directing Tuj1 differentiation of adult NSCs (Lim et al. 2010). It was suggested that the aligned substrate favored the survival of neural progenitors in detriment with non-neuronal progenitors and nanofiber dimension influenced cell-substrate interactions by imposing a stronger signaling cue than the intercellular signaling (Lim et al. 2010). Similarly neuronal lineage differentiation was favored in aligned nanofibers with negligible expression of astrocytes and oligodendrocytes markers (Mahairaki et al. 2011). Astrocyte differentiation predominance on flat surfaces, was also positively suppressed with greater extent of neuronal differentiation when NSCs were cultivated on fiber substrates (Bakhru et al. 2011). In the current study, the apparent prevalence of astrocytes in the random nanofibers can be explained by the physical cues provided by the random distribution of fiber diameters and fiber alignments in the PCL-RGDr. Such topology presents discrete scattered surface contact points for cell adhesion, that can promote broader spread morphology, and hence the astrocyte lineage could be favored in these conditions. In fact the astrocytes are considered as not being terminally post mitotic cells, which means that in differentiation conditions during glial maturation there is still some cellular proliferation, contrary to neuron populations which depend essentially on the capacity of maturation of NSCs and on the ability of formed neurons to survive (Flanagan et al. 2006).

On the other hand in non-functionalized PCL nanofibers, although the detected number of differentiated cells was smaller, a distinct difference was found with an increased amount of differentiated neurons. The ability of NSC survival and proliferation in non-functionalized PCL aligned nanofibers was, as suggested on previous studies, enabled by proteins driven from the culture medium that mediate some NCS adhesion to the PCL, hence migration and survival (Yao et al. 2016). Attending the fact that the aligned fibers topography acts as a force towards directing NSC lineage differentiation, the smaller number of detected differentiated cells being mostly neuronal cells could be justified by the effect of the alignment of the matrix itself.

According to Christopherson et al., neuronal lineage differentiation was improved in matrices that allowed less extensive cellular migration and lower spreading points of adhesion, hence with lower ability for NCS proliferation, supporting a neuron like elogated shape. The star-like shape of astrocytes, is in fact favored in planar substrates or random nanofibers, that allow an extensive radial spread of the NSCs actin cytoskeleton, thus correlated with higher degree of cellular proliferation (Flanagan et al. 2006; Christopherson et al. 2009). As we observed, the topography of the aligned PCL substrate eventually tends to cause some inhibition of the glial lineage differentiation due to the enhanced cellular elongation, with less contact adhesion points provided by the aligned matrix, and also absence of specific adhesion molecules, as opposed to the random nanofibers and in the presence of LN and GRGDSP.

The neurons alignment and neurite extension are in agreement with the observed previously for the multipotent NSC illustrating the effect of the functionalized material geometry in cells organization and morphology. The higher and specific cell adhesion (integrin mediated) to the nanofibers provided by the LN and GRGDSP motifs, and unidirectional organization of the substrate contributed to guide the cellular distribution and to a more extensive neuronal elongation.

A spindle like and more elongated cellular morphology are clearly enhanced by highly aligned structured substrates that influence the local formation of the cellular focal adhesion complexes, hence directing cellular morphology and elongation (Sheets et al. 2013). The shorter neurite length found in PCL-RGDr, is likely due to the disordered disposition of the

nanofibers, where the cellular morphology developed in a more spread and multidirectional fashion. The neurite extension of βIII tubulin positive neuronal cells was clearly improved by the nanofiber alignment and in the presence of adhesion factors. These observations are in agreement with other studies reported in literature (Yang et al. 2005; Zander et al. 2010; J. Wang et al. 2012; Smith Callahan et al. 2013).

III.5 - Conclusions

The prepared and characterized nanofiber scaffolds were found to be suitable for the mouse embryonic stem cell-derived CGR8-NS cells proliferation and differentiation.

CGR8-NS are able to proliferate in adherent monolayer and maintain the multipotent potential in the presence of the growth factors EGF and FGF-2, which are essential for cells to maintain the multipotent potential and symmetrical self renewal capacity. Under differentiation culture, the removal of EGF and FGF-2 suppresses NSCs symmetrical renewal and the maturation towards neuronal and glial lineages is activated. With growth factors removal the topology will play a role in NSC maturation.

The nanofibers were prepared by electrospinning resulting in nanofiber scaffolds with different degrees of fiber alignment and diameters. The protein functionalization procedure of the nanofiber scaffolds was effective, where the aminolised PCL, with a diamine, allowed to peptide crosslink via glutaraldehyde reaction.

This study shows the existence of a synergistic effect of substrate topography and specific adhesion motifs, LN and GRGDSP, on NSC fate, regarding cellular morphology, proliferation and differentiation. The functionalization with biological motifs was evidenced to be essential to promote local cellular adhesion, with the cellular proliferation of NSC also increasing in the presence of the specific adhesion motifs, LN and GRGDSP.

Non-functionalized aligned PCL nanofibers were able to promote cell alignment, but perform poorly in supporting NSC elongation and formation of cellular extensions (neurite) upon NSC differentiation. The cellular alignment in the nanofibers is further improved with narrow alignment distributions in aligned scaffolds functionalized with GRGDSP or LN, which promote specific local adhesion points according to the uniaxial matrix structure. Randomly distributed GRGDSP functionalized fibers also improve cell adhesion, but due to the lack of a single direction axis, the cellular orientation follows a distribution also in arbitrary directions. These observations are valid for undifferentiated NSCs after 11 days of proliferation and for differentiated neurons (Tuj1 positive).

In our study both functionalized aligned and random nanofibers had an equivalent effect on the cellular proliferation. Moreover, the aligned nanofibers oriented and elongated the cellular cytoskeleton with the nanofiber axis, conferring a more distinct bipolar morphology, which is advantageous to neuronal maturation under differentiation conditions. Cellular elongation is more effective when adhesion to the substrate is more efficient, requiring RGD or LN fiber functionalization. In our case the better cell elongation in aligned fibers comes from the narrower diameters and alignment in a defined orientation, as compared to the random ones. The random nanofibers with wider and dispersed diameters and angles of orientation may promote cell bridges between different fibers not contributing to better cell elongation in one single axis.

Alignment by itself favors the survival of neural progenitors in detriment of glial lineage, due to restricted cell attachment points provided by the aligned fiber architecture causing restrictions to cytoskeleton rearrangement leading to specific signaling activation, at the level of cell-cell and cell-ECM interactions.

The nanofiber topography directed neuronal lineage and neurite elongation in the aligned matrices especially in the presence of the adhesion motifs. Random GRGDSP matrices were found to be relatively preferential for astrocyte maturation. PCL-GRGDSP aligned substrate was found to promote good cellular adhesion, elongation and cellular survival, allowing neuronal lineage differentiation and elongation.

The prepared scaffold can be considered to be a good synthetic biocompatible substrate for NSC culture applications, regarding scaffolds for regeneration of CNS injuries, while the introduction of LN is more efficient on promoting elongation and higher neurite length. Moreover cellular alignment is an interesting effect that can be beneficial to tissues requiring such geometry, such as in spinal cord injury repair.

Additional improvements and scaffold development can be explored, as one of the major problems of biomaterial scaffolds is the ability to maintain cellular viability when applied on in-vivo settings. Depending on the type of CNS tissue (spinal cord or brain) a deep assessment of the in-vivo conditions is important in order to design and develop the most compatible material for in situ cellular delivery complemented with trophic factors and drugs to provide an

environment suitable for cellular survival and function. Blends of polymers to stiffness optimization, hydrogel combination to allow gradual biochemical supply or assemblies of micro and nanostructures to provide specific architecture and 3D environment, are interesting examples for future scaffold design conception.

The aligned nanofibers of PCL-GRGDSP are applied in the subsequent studies performed within the framework of this thesis. In Chapter V functionalized aligned nanofiber frames, are used as a supportive substrate applied to a human neural precursor cell line in order to evaluate NSC cell fate under dynamic conditions.

Appendix

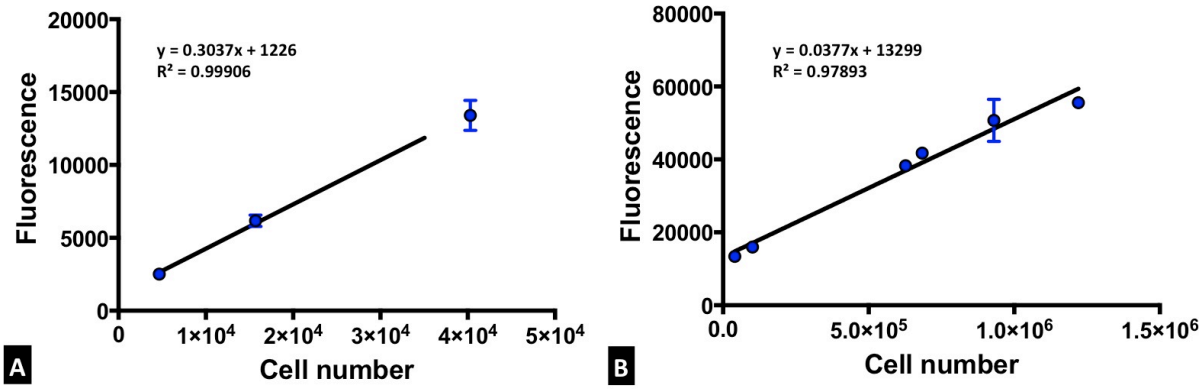

Figure IIIA.1 – Calibration lines for the fluorescence of the Alamar Blue reduced product with the CGR8-NS cell number on nanofiber scaffolds. (n=2); a) Plot for cell numbers from 5000 - 40000 and b) from 40000 - 1000000.

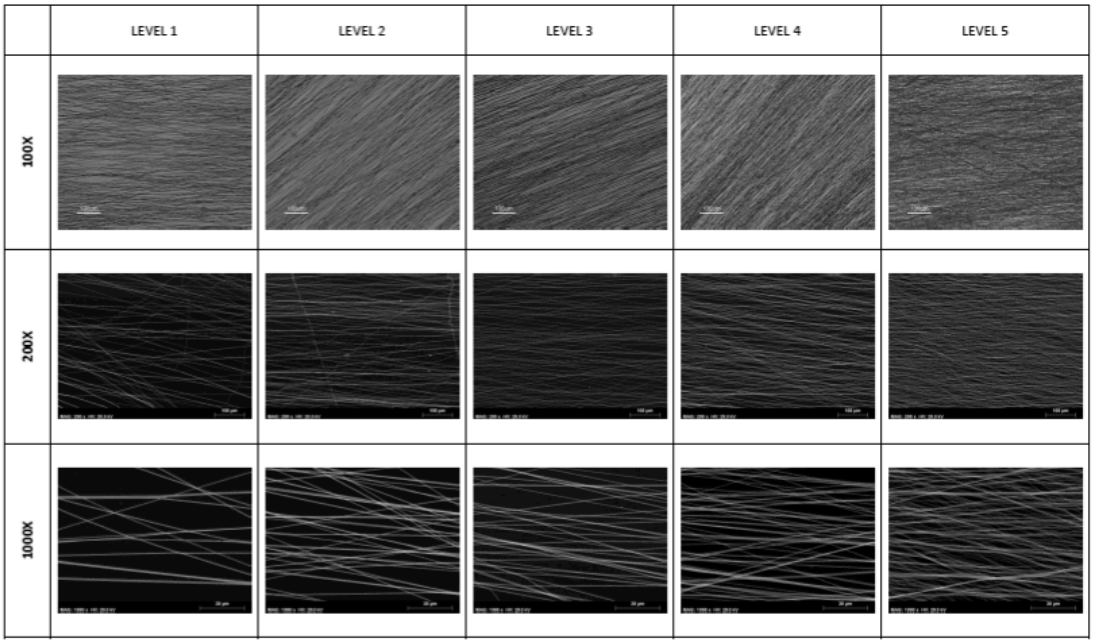

Figure IIIA.2 – SEM and optical microscope images illustrative of the nanofiber density levels considered. Scale bars are 100 µm for optical microscope images with magnifications of 100X and 200X, and 30 µm for images with magnifications of 100X.

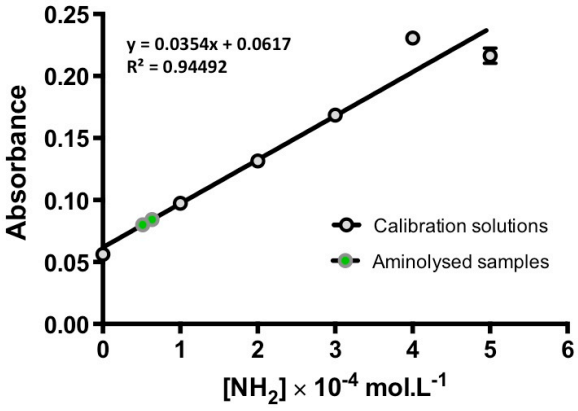

Figure IIIA.3 – Reference calibration curve of ninhydrin–NH_2 absorbance (538 nm) as a function of graded concentrations of HDA in 1:1 v/v of 1,4-dioxane/isopropanol solutions. Error bars represent SD.

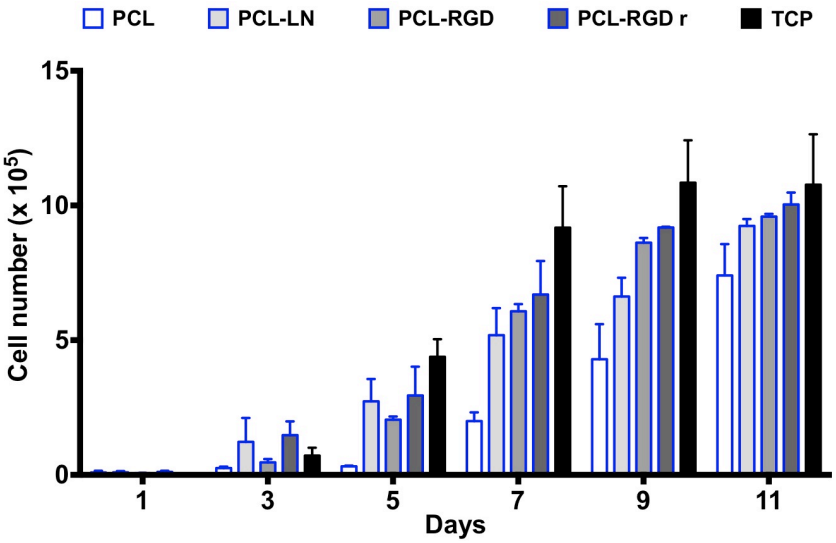

Figure IIIA.4 – Cell proliferation profile of CGR8-NS cells in PCL nanofiber scaffolds compared with the cellular growth in a 24 well polystyrene tissue culture plate (TCP).

References

Agarwal S, Wendorff JH, Greiner A. 2008. Use of electrospinning technique for biomedical applications. Polymer. 49(26):5603–5621. doi:10.1016/j.polymer.2008.09.014.

Ananthanarayanan B, Little L, Schaffer DV, Healy KE, Tirrell M. 2010. Neural stem cell adhesion and proliferation on phospholipid bilayers functionalized with RGD peptides. Biomaterials. 31(33):8706–8715. doi:10.1016/j.biomaterials.2010.07.104.

Bacáková L, Filová E, Rypácek F, Svorcík V, Starý V. 2004. Cell adhesion on artificial materials for tissue engineering. Physiol Res Acad Sci Bohemoslov. 53 Suppl 1:S35-45.

Bakhru S, Nain AS, Highley C, Wang J, Campbell P, Amon C, Zappe S. 2011. Direct and cell signaling-based, geometry-induced neuronal differentiation of neural stem cells. Integr Biol Quant Biosci Nano Macro. 3(12):1207–1214. doi:10.1039/c1ib00098e.

Beachley V, Wen X. 2009. Effect of electrospinning parameters on the nanofiber diameter and length. Mater Sci Eng C Mater Biol Appl. 29(3):663–668. doi:10.1016/j.msec.2008.10.037.

Beck K, Hunter I, Engel J. 1990. Structure and function of laminin: anatomy of a multidomain glycoprotein. FASEB J. 4(2):148–160.

Bettinger CJ, Langer R, Borenstein JT. 2009. Engineering Substrate Topography at the Micro- and Nanoscale to Control Cell Function. Angew Chem Int Ed. 48(30):5406–5415. doi:10.1002/anie.200805179.

Canadas RF, Cavalheiro JMBT, Guerreiro JDT, de Almeida MCMD, Pollet E, da Silva CL, da Fonseca MMR, Ferreira FC. 2014. Polyhydroxyalkanoates: waste glycerol upgrade into electrospun fibrous scaffolds for stem cells culture. Int J Biol Macromol. 71:131–140. doi:10.1016/j.ijbiomac.2014.05.008.

Cao Q, Benton RL, Whittemore SR. 2002. Stem cell repair of central nervous system injury. J Neurosci Res. 68(5):501–510. doi:10.1002/jnr.10240.

Causa F, Battista E, Della Moglie R, Guarnieri D, Iannone M, Netti PA. 2010. Surface investigation on biomimetic materials to control cell adhesion: the case of RGD conjugation on PCL. Langmuir ACS J Surf Colloids. 26(12):9875–9884. doi:10.1021/la100207q.

Chew SY, Mi R, Hoke A, Leong KW. 2008. The effect of the alignment of electrospun fibrous scaffolds on Schwann cell maturation. Biomaterials. 29(6):653–661. doi:10.1016/j.biomaterials.2007.10.025.

Christopherson GT, Song H, Mao H-Q. 2009. The influence of fiber diameter of electrospun substrates on neural stem cell differentiation and proliferation. Biomaterials. 30(4):556–564. doi:10.1016/j.biomaterials.2008.10.004.

Ciardelli G, Chiono V, Vozzi G, Pracella M, Ahluwalia A, Barbani N, Cristallini C, Giusti P. 2005. Blends of Poly-(ε-caprolactone) and Polysaccharides in Tissue Engineering Applications. Biomacromolecules. 6(4):1961–1976. doi:10.1021/bm0500805.

Conti L, Cattaneo E. 2010. Neural stem cell systems: physiological players or in vitro entities? Nat Rev Neurosci. 11(3):176–187. doi:10.1038/nrn2761.

Conti L, Pollard SM, Gorba T, Reitano E, Toselli M, Biella G, Sun Y, Sanzone S, Ying Q-L, Cattaneo E, et al. 2005. Niche-independent symmetrical self-renewal of a mammalian tissue stem cell. PLoS Biol. 3(9):e283. doi:10.1371/journal.pbio.0030283.

Cooper A, Bhattarai N, Zhang M. 2011. Fabrication and cellular compatibility of aligned chitosan-PCL fibers for nerve tissue regeneration. Carbohydr Polym. 85(1):149–156. doi:10.1016/j.carbpol.2011.02.008.

Fang Z, Fu W, Dong Z, Zhang X, Gao B, Guo D, He H, Wang Y. 2011. Preparation and biocompatibility of electrospun poly(l-lactide-co-ε-caprolactone)/fibrinogen blended nanofibrous scaffolds. Appl Surf Sci. 257(9):4133–4138. doi:10.1016/j.apsusc.2010.12.011.

Flanagan LA, Rebaza LM, Derzic S, Schwartz PH, Monuki ES. 2006. Regulation of human neural precursor cells by laminin and integrins. J Neurosci Res. 83(5):845–856. doi:10.1002/jnr.20778.

Friedman M. 2004. Applications of the Ninhydrin Reaction for Analysis of Amino Acids, Peptides, and Proteins to Agricultural and Biomedical Sciences. J Agric Food Chem. 52(3):385–406. doi:10.1021/jf030490p.

Ghasemi-Mobarakeh L, Prabhakaran MP, Morshed M, Nasr-Esfahani MH, Ramakrishna S. 2010. Bio-functionalized PCL nanofibrous scaffolds for nerve tissue engineering. Mater Sci Eng C. 30(8):1129–1136. doi:10.1016/j.msec.2010.06.004.

Gloria A, Causa F, Russo T, Battista E, Della Moglie R, Zeppetelli S, De Santis R, Netti PA, Ambrosio L. 2012. Three-dimensional poly(ε-caprolactone) bioactive scaffolds with controlled structural and surface properties. Biomacromolecules. 13(11):3510–3521. doi:10.1021/bm300818y.

Hackett JM, Dang TT, Tsai EC, Cao X. 2010. Electrospun Biocomposite Polycaprolactone/Collagen Tubes as Scaffolds for Neural Stem Cell Differentiation. Materials. 3(6):3714–3728. doi:10.3390/ma3063714.

Hall PE, Lathia JD, Caldwell MA, ffrench-Constant C. 2008. Laminin enhances the growth of human neural stem cells in defined culture media. BMC Neurosci. 9:71. doi:10.1186/1471-2202-9-71.

Hautanen A, Gailit J, Mann DM, Ruoslahti E. 1989. Effects of modifications of the RGD sequence and its context on recognition by the fibronectin receptor. J Biol Chem. 264(3):1437–1442.

He L, Liao S, Quan D, Ma K, Chan C, Ramakrishna S, Lu J. 2010. Synergistic effects of electrospun PLLA fiber dimension and pattern on neonatal mouse cerebellum C17.2 stem cells. Acta Biomater. 6(8):2960–2969. doi:10.1016/j.actbio.2010.02.039.

Hersel U, Dahmen C, Kessler H. 2003. RGD modified polymers: biomaterials for stimulated cell adhesion and beyond. Biomaterials. 24(24):4385–4415.

Hiraoka M, Kato K, Nakaji-Hirabayashi T, Iwata H. 2009. Enhanced survival of neural cells embedded in hydrogels composed of collagen and laminin-derived cell adhesive peptide. Bioconjug Chem. 20(5):976–983. doi:10.1021/bc9000068.

Horne MK, Nisbet DR, Forsythe JS, Parish CL. 2010. Three-dimensional nanofibrous scaffolds incorporating immobilized BDNF promote proliferation and differentiation of cortical neural stem cells. Stem Cells Dev. 19(6):843–852. doi:10.1089/scd.2009.0158.

Ingber DE. 2003. Tensegrity I. Cell structure and hierarchical systems biology. J Cell Sci. 116(Pt 7):1157–1173.

Kai D, Jin G, Prabhakaran MP, Ramakrishna S. 2013. Electrospun synthetic and natural nanofibers for regenerative medicine and stem cells. Biotechnol J. 8(1):59–72. doi:10.1002/biot.201200249.

Kim TG, Park TG. 2006. Biomimicking extracellular matrix: cell adhesive RGD peptide modified electrospun poly(D,L-lactic-co-glycolic acid) nanofiber mesh. Tissue Eng. 12(2):221–233. doi:10.1089/ten.2006.12.221.

Klinkhammer K, Bockelmann J, Simitzis C, Brook GA, Grafahrend D, Groll J, Möller M, Mey J, Klee D. 2010. Functionalization of electrospun fibers of poly(epsilon-caprolactone) with star shaped NCO-poly(ethylene glycol)-stat-poly(propylene glycol) for neuronal cell guidance. J Mater Sci Mater Med. 21(9):2637–2651. doi:10.1007/s10856-010-4112-7.

Koh HS, Yong T, Chan CK, Ramakrishna S. 2008. Enhancement of neurite outgrowth using nano-structured scaffolds coupled with laminin. Biomaterials. 29(26):3574–3582. doi:10.1016/j.biomaterials.2008.05.014.

Lam HJ, Patel S, Wang A, Chu J, Li S. 2010. In vitro regulation of neural differentiation and axon growth by growth factors and bioactive nanofibers. Tissue Eng Part A. 16(8):2641–2648. doi:10.1089/ten.TEA.2009.0414.

Li D, Wang Y, Xia Y. 2003. Electrospinning of Polymeric and Ceramic Nanofibers as Uniaxially Aligned Arrays. Nano Lett. 3(8):1167–1171. doi:10.1021/nl0344256.

Lim SH, Liu XY, Song H, Yarema KJ, Mao H-Q. 2010. The effect of nanofiber-guided cell alignment on the preferential differentiation of neural stem cells. Biomaterials. 31(34):9031–9039. doi:10.1016/j.biomaterials.2010.08.021.

Mahairaki V, Lim SH, Christopherson GT, Xu L, Nasonkin I, Yu C, Mao H-Q, Koliatsos VE. 2011. Nanofiber matrices promote the neuronal differentiation of human embryonic stem cell-derived neural precursors in vitro. Tissue Eng Part A. 17(5–6):855–863. doi:10.1089/ten.TEA.2010.0377.

Massumi M, Abasi M, Babaloo H, Terraf P, Safi M, Saeed M, Barzin J, Zandi M, Soleimani M. 2012. The effect of topography on differentiation fates of matrigel-coated mouse embryonic stem cells cultured on PLGA nanofibrous scaffolds. Tissue Eng Part A. 18(5–6):609–620. doi:10.1089/ten.TEA.2011.0368.

Migneault I, Dartiguenave C, Bertrand MJ, Waldron KC. 2004. Glutaraldehyde: behavior in aqueous solution, reaction with proteins, and application to enzyme crosslinking. BioTechniques. 37(5):790–796, 798–802.

Nakaji-Hirabayashi T, Kato K, Iwata H. 2012. Improvement of neural stem cell survival in collagen hydrogels by incorporating laminin-derived cell adhesive polypeptides. Bioconjug Chem. 23(2):212–221. doi:10.1021/bc200481v.

Nezarati RM, Eifert MB, Cosgriff-Hernandez E. 2013. Effects of humidity and solution viscosity on electrospun fiber morphology. Tissue Eng Part C Methods. 19(10):810–819. doi:10.1089/ten.TEC.2012.0671.

Nisbet DR, Yu LMY, Zahir T, Forsythe JS, Shoichet MS. 2008. Characterization of neural stem cells on electrospun poly(ε-caprolactone) submicron scaffolds: evaluating their potential in neural tissue engineering. J Biomater Sci Polym Ed. 19(5):623–634. doi:10.1163/156856208784089652.

Norman JJ, Desai TA. 2006. Methods for fabrication of nanoscale topography for tissue engineering scaffolds. Ann Biomed Eng. 34(1):89–101. doi:10.1007/s10439-005-9005-4.

Pollard SM, Benchoua A, Lowell S. 2006. Neural stem cells, neurons, and glia. Methods Enzymol. 418:151–169. doi:10.1016/S0076-6879(06)18010-6.

Pollard SM, Conti L, Sun Y, Goffredo D, Smith A. 2006. Adherent neural stem (NS) cells from fetal and adult forebrain. Cereb Cortex N Y N 1991. 16 Suppl 1:i112-120. doi:10.1093/cercor/bhj167.

Qi L, Li N, Huang R, Song Q, Wang L, Zhang Q, Su R, Kong T, Tang M, Cheng G. 2013. The Effects of Topographical Patterns and Sizes on Neural Stem Cell Behavior. PLOS ONE. 8(3):e59022. doi:10.1371/journal.pone.0059022.

Rodrigues CAV, Diogo MM, da Silva CL, Cabral JMS. 2010. Hypoxia enhances proliferation of mouse embryonic stem cell-derived neural stem cells. Biotechnol Bioeng. 106(2):260–270. doi:10.1002/bit.22648.

Rodrigues CAV, Diogo MM, da Silva CL, Cabral JMS. 2011. Microcarrier expansion of mouse embryonic stem cell-derived neural stem cells in stirred bioreactors. Biotechnol Appl Biochem. 58(4):231–242. doi:10.1002/bab.37.

Schnell E, Klinkhammer K, Balzer S, Brook G, Klee D, Dalton P, Mey J. 2007. Guidance of glial cell migration and axonal growth on electrospun nanofibers of poly-epsilon-caprolactone and a collagen/poly-epsilon-caprolactone blend. Biomaterials. 28(19):3012–3025. doi:10.1016/j.biomaterials.2007.03.009.

Sheets K, Wunsch S, Ng C, Nain AS. 2013. Shape-dependent cell migration and focal adhesion organization on suspended and aligned nanofiber scaffolds. Acta Biomater. 9(7):7169–7177. doi:10.1016/j.actbio.2013.03.042.

Smith Callahan LA, Xie S, Barker IA, Zheng J, Reneker DH, Dove AP, Becker ML. 2013. Directed differentiation and neurite extension of mouse embryonic stem cell on aligned poly(lactide) nanofibers functionalized with YIGSR peptide. Biomaterials. 34(36):9089–9095. doi:10.1016/j.biomaterials.2013.08.028.

Stevens MM, George JH. 2005. Exploring and engineering the cell surface interface. Science. 310(5751):1135–1138. doi:10.1126/science.1106587.

Strober W. 2001. Trypan blue exclusion test of cell viability. Curr Protoc Immunol Ed John E Coligan Al. Appendix 3:Appendix 3B. doi:10.1002/0471142735.ima03bs21.

Subramanian A, Krishnan UM, Sethuraman S. 2012. Fabrication, characterization and in vitro evaluation of aligned PLGA-PCL nanofibers for neural regeneration. Ann Biomed Eng. 40(10):2098–2110. doi:10.1007/s10439-012-0592-6.

Teo WE, Ramakrishna S. 2006. A review on electrospinning design and nanofibre assemblies. Nanotechnology. 17(14):R89. doi:10.1088/0957-4484/17/14/R01.

Wang G, Hu X, Lin W, Dong C, Wu H. 2011. Electrospun PLGA-silk fibroin-collagen nanofibrous scaffolds for nerve tissue engineering. In Vitro Cell Dev Biol Anim. 47(3):234–240. doi:10.1007/s11626-010-9381-4.

Wang HB, Mullins ME, Cregg JM, Hurtado A, Oudega M, Trombley MT, Gilbert RJ. 2009. Creation of highly aligned electrospun poly-L-lactic acid fibers for nerve regeneration applications. J Neural Eng. 6(1):016001. doi:10.1088/1741-2560/6/1/016001.

Wang HB, Mullins ME, Cregg JM, McCarthy CW, Gilbert RJ. 2010. Varying the diameter of aligned electrospun fibers alters neurite outgrowth and Schwann cell migration. Acta Biomater. 6(8):2970–2978. doi:10.1016/j.actbio.2010.02.020.

Wang J, Ye R, Wei Y, Wang H, Xu X, Zhang F, Qu J, Zuo B, Zhang H. 2012. The effects of electrospun TSF nanofiber diameter and alignment on neuronal differentiation of

human embryonic stem cells. J Biomed Mater Res A. 100A(3):632–645. doi:10.1002/jbm.a.33291.

Wang TY, Forsythe JS, Nisbet DR, Parish CL. 2012. Promoting engraftment of transplanted neural stem cells/progenitors using biofunctionalised electrospun scaffolds. Biomaterials. 33(36):9188–9197. doi:10.1016/j.biomaterials.2012.09.013.

Wang Y, Yao M, Zhou J, Zheng W, Zhou C, Dong D, Liu Y, Teng Z, Jiang Y, Wei G, et al. 2011. The promotion of neural progenitor cells proliferation by aligned and randomly oriented collagen nanofibers through β1 integrin/MAPK signaling pathway. Biomaterials. 32(28):6737–6744. doi:10.1016/j.biomaterials.2011.05.075.

Wheeldon I, Farhadi A, Bick AG, Jabbari E, Khademhosseini A. 2011. Nanoscale tissue engineering: spatial control over cell-materials interactions. Nanotechnology. 22(21):212001. doi:10.1088/0957-4484/22/21/212001.

Xie J, MacEwan MR, Li X, Sakiyama-Elbert SE, Xia Y. 2009. Neurite outgrowth on nanofiber scaffolds with different orders, structures, and surface properties. ACS Nano. 3(5):1151–1159. doi:10.1021/nn900070z.

Xie J, Willerth SM, Li X, Macewan MR, Rader A, Sakiyama-Elbert SE, Xia Y. 2009. The differentiation of embryonic stem cells seeded on electrospun nanofibers into neural lineages. Biomaterials. 30(3):354–362. doi:10.1016/j.biomaterials.2008.09.046.

Yang F, Murugan R, Wang S, Ramakrishna S. 2005. Electrospinning of nano/micro scale poly(l-lactic acid) aligned fibers and their potential in neural tissue engineering. Biomaterials. 26(15):2603–2610. doi:10.1016/j.biomaterials.2004.06.051.

Yao S, Liu X, He J, Wang X, Wang Y, Cui F-Z. 2016. Ordered self-assembled monolayers terminated with different chemical functional groups direct neural stem cell linage behaviours. Biomed Mater Bristol Engl. 11(1):014107. doi:10.1088/1748-6041/11/1/014107.

Yoo HS, Kim TG, Park TG. 2009. Surface-functionalized electrospun nanofibers for tissue engineering and drug delivery. Adv Drug Deliv Rev. 61(12):1033–1042. doi:10.1016/j.addr.2009.07.007.

Yuan Y, Lee TR. 2013. Contact Angle and Wetting Properties. In: Surface Science Techniques. Springer, Berlin, Heidelberg. (Springer Series in Surface Sciences). p. 3–34. [accessed 2017 Dec 8]. https://link.springer.com/chapter/10.1007/978-3-642-34243-1_1.

Zander NE, Orlicki JA, Rawlett AM, Beebe TP. 2010. Surface-modified nanofibrous biomaterial bridge for the enhancement and control of neurite outgrowth. Biointerphases. 5(4):149–158. doi:10.1116/1.3526140.

Zhang YZ, Venugopal J, Huang Z-M, Lim CT, Ramakrishna S. 2006. Crosslinking of the electrospun gelatin nanofibers. Polymer. 47(8):2911–2917. doi:10.1016/j.polymer.2006.02.046.

Zhu Y, Gao C, Liu X, Shen J. 2002. Surface Modification of Polycaprolactone Membrane via Aminolysis and Biomacromolecule Immobilization for Promoting Cytocompatibility of Human Endothelial Cells. Biomacromolecules. 3(6):1312–1319. doi:10.1021/bm020074y.

Chapter IV

Design and Characterization of a Stirred Bioreactor Enclosing Nanofibers

Chapter IV - Design and Characterization of a Stirred Bioreactor Enclosing Nanofibers

IV.1 - Abstract

A novel scalable system for culture of stem cells in nanofiber scaffolds is presented. This system is developed to allow the culture of NSCs in dynamic conditions, supported in nanofiber scaffolds. The designed prototype is composed by an ellipsoidal vessel, a magnetic stir and six frames of nanofibers, following a concept of plate and frame, where the nanofiber scaffolds are positioned as frames and the liquid is promoted to flow parallel to the scaffold surfaces. The liquid flows in the compartments between the frames that are connected by a chamber underneath, where a stirrer promotes proper mixing. The system hydrodynamics was characterized for two filling volumes in a range of speeds of the magnetic stirrer, in order to evaluate the fluid uniformity and velocity and the shear stress profiles along the vessel, in particular for regions immediately adjacent to the scaffolds, that will act to support the adherent stem cells.

The motivation for this study is to establish culture conditions that promote fluid mixings high enough to avoid local toxic by-products accumulation or substrates depletion, that can affect the cellular maintenance, and to understand if the geometry of the reactor provides a homogeneous mixing for all the scaffolds, i.e if all are exposed to the same hydrodynamics, and also to estimate the local forces, at the interfaces nanofiber/bulk solution, that can affect cellular disruption or trigger cellular responses. Such analysis followed three approaches: i) a first assessment of the mixing time using a dye and by visual observation of the blending of the fluid in solution; ii) an experimental evaluation of the effect of the liquid volume and stirring speed on mass transport using the limiting current technique, allowing to calculate Sherwood numbers and liquid film mass transfer coefficient, k, at the boundary of the frames, iii) a theoretical modeling of the stirred vessel using computing fluid dynamics (CFD) to evaluate differences in shear stress exposure and fluid velocity between the scaffolds.

The experimental approach shows that using a level of liquid higher than the top of the scaffolds (30 mL) the fluid dynamics is more regular, and the mass transfer between the scaffolds placed at the different positions in the vessel more consistent. The CFD highlights that the mixing uniformity using 30 mL of working volume creates a fluid recirculation in the regions above the scaffolds, delivering the fluid between the frames, as an effect of the fluid recirculation provided by the stirrer. Overall, it is possible to estimate the k and the thickness of stagnant liquid film layer for the different frame interfaces which can be used to calculate concentration of toxic inhibitors in this boundary layer, as well as the shear stress at which the cells will be submitted. The results obtained indicate that the stirring conditions used, while in laminar-oscillatory flow regime, provide sufficient mixing to avoid local accumulations of by-products (e.g. lactate).

IV.2 - Introduction

IV.2.1 – Background and Motivation

The most common forms of neurodegenerative diseases are Alzheimer disease (AD), Parkinson disease (PD), Huntington disease (HD), Amyotrophic lateral sclerosis (ALS) and Spinal muscular atrophy (SMA) and in the USA, approximately 7 million people are affected by one of these diseases (Lunn et al. 2011). Recently, cellular therapies have earned increased attention, for the treatment of injury and diseases using cells or tissue grafts (Lunn et al. 2011), together with gene therapies that have been shown successful in many cases, however the application of these strategies to human diseases is still challenging (Nanou and Azzouz 2009). Regarding cellular therapies two different approaches exist: cellular replacement and environmental enrichment. The first one consists in the derivation of the specific subtype of cells of interest from neural stem cells, and grafting these cells into the affected area. In the second case, neural stem cells are implanted in the damaged tissue in order to provide environmental enrichment by producing neurotrophic factors.

The main limitation to stem cells based therapies and tissue engineering strategies is the lack of a source that provides high number of stem cells, bearing in mind ethical considerations, and thus the restricted availability of new tissue for transplants (Nanou and Azzouz 2009). Consequently the development of efficient methodologies for large-scale expansion of stem cells is important. The ability to obtain an adequate amount of cells for cellular therapies is still a limiting factor in the field of tissue regeneration. This project wishes to contribute, concerning the field of neural stem cells, to the development of systems suitable to expand at a large scale neural stem cells and neural tissue constructs.

In literature it is possible to find different strategies addressing large scale stem cells expansion. The most recurring solutions are the stirred suspension systems, combined with different culture approaches, such as microcarriers (Rodrigues, Diogo, et al. 2011) cell aggregates (Gilbertson et al. 2006) and cell encapsulation (Serra et al. 2009). These systems offer attractive advantages of scalability and relative simplicity. The stirring provides a more

homogenous culture environment and allows the measurement and control of extrinsic factors such as nutrients and metabolites.

The hydrodynamic shear stress in stirred culture systems has been described with different effects (harmful or stimulating) depending on the cellular systems and culture processes (singular cell and cellular aggregates suspensions, suspensions of microcarriers), where the type of impeller configurations (and mixing velocity) is determinant for the balance of an effective mixing with an adequate shear environment (King and Miller 2007; Rodrigues, Fernandes, et al. 2011).

The friction of the fluid (in temporal and spatial variation) at the cell membrane surface triggers mechanosensing structures (protrusions, invaginations, pores, long chain molecules such as glycosaminoglycans and proteoglycans) that transduce the friction (also tension and compression) along the cytoskeleton into the activation of signaling pathways to cellular responses. A number of studies is reported regarding the effect of fluid flow shear stress in microfluidic devices emulating the flow shear in physiological conditions to adherent cells (Shemesh et al. 2015).

While in Chapter III the development of scaffolds with functionalized biological motifs able to support NSC adhesion, proliferation, organization and specific morphology, was addressed, the current chapter addresses the importance to cultivate cells in a dynamic culture, with controlled hydrodynamics, shear stress and proper mass transfer (nutrients and byproducts), envisaging the possibility to scale the system to the production of tissue grafts (i.e. scaffolds supporting a population of viable cells).

Whereas, most of the research in stem cells is made in stationary conditions in planar culture systems, proper solution media mixing, obtained in dynamic conditions, is crucial to provide a more homogenous culture environment with the measurement and control of extrinsic factors such as nutrients and metabolites. In bioreactors operating with scaffolds the mixing is often achieved by liquid perfusion for osteogenic differentiation of mesenchymal stem cells (Hosseinkhani et al. 2006) or hepatocyte cell cultures support (Chu et al. 2009). Shake flask approaches have been adopted for neural cell culture in nanofibers (N. Liu et al. 2013) and

rotary wall vessel have been used with nanofibers systems for chondrocyte (Li et al. 2008) or Schwann (Valmikinathan et al. 2011) cell culture. The stirring systems offer attractive advantages of scalability and relative simplicity, providing mixing without the need of auxiliary pumps. The innovative approach in this chapter is to evaluate the performance of a stirred vessel designed to operate with nanofiber scaffolds. The main aims are the design and manufacture of a prototype with the evaluation of the operating conditions based on the designed configuration. The working parameters, liquid volume and stirring velocity, are characterized, taking into consideration the optimal distribution of nutrients in order to guarantee a minimum concentration polarization of toxic products (lactate), and selecting shear stress forces produced during the operating process not harmful to the cells or that not affect negatively the cellular fate. Mixing times were initially established using a dye. The mass transfer coefficient and the Sherwood number were evaluated experimentally by the limiting current technique. With Computational Fluid Dynamics (CFD), the shear stress and fluid velocity profiles were established.

IV.2.2 – Theoretical Background

The hydrodynamic shear stress has a direct effect on the cellular survival with impact on the quality of the final cellular product. The shear or shearing force can be described as the force that causes a laminar deformation, as in two planar plates sliding over each other (parallel shear) or the rotational sliding of the walls in a set of cylinder tubes packed into each other (rotational shear). Depending on the medium viscosity, density and fluid motion (turbulence and eddies), and on the air dispersion (gas bubbles for medium aeration) in many bioreactor systems, the cells in culture are subjected to different levels of localized shear produced by the culture hydrodynamics. That is, the force exerted of the fluid in motion over a surface or interface (as the wall of a bioreactor or a cell membrane surface) that provides the mechanical effects responsible for the efficacy on the transport of mass and energy on the culture process. (Doran 1995)

The dissipation of the kinetic energy produced by the stirring source (in a turbulent environment provided by a stirrer or impeller) is performed by the successive formation of eddies of different sizes. The formed eddies accumulate the energy and rapidly breakdown successively into smaller and smaller eddies, dissipating progressively the kinetic energy. Gradually, the size of the eddies ultimately reaches such a small length that the viscosity of the fluid dissipates the remaining energy into the system. The kinetic energy of an agitated system is dissipated through the cells or cellular aggregates or adherent to microcarriers in suspension, or the wall surfaces of a bioreactor, and the resulting shear intensity is dependent on the eddie size interacting with the surrounding objects. A larger eddie surrounds the object and this is carried away along with the turbulent flow, thus the shear that the object is subjected to is not concentrated in a singular point. When the size of the eddie is smaller than the object that interacts with (Kolmogorov eddies, flexible rotating cylinders of fluid that with increasing agitation the length size decreases) the exerted shear is localized in specific points of the object, and depending on the intensity the effect can be detrimental to the culture system. (Cherry and Kwon 1990; Doran 1995; Sen et al. 2002)

One of the main mechanisms by which molecules, ions, or other small particles move within a solution is diffusion, where the driving force for transport is determined by gradients of concentration, driving the molecules to move from a fluid region of relatively high concentration to regions of lower concentration. The other mechanism important for mixing is convection. The liquid moves due to the natural convection phenomena with origin in density variations due to changes in temperature or local solution composition and, in forced convection due to agitation promoted by stirring or perfusion, by the use of stirrers or pumps, respectively. An additional phenomenon for mass transfer in solutions is the Nernst-Planck effect that explains the movement of charged species due to local electrical fields promoted by different ion motilities within the solution (due to effects of attraction or repulsion of charged particles). However this effect can be neglected for neutral species or in circumstances where convection and/or diffusion dominate the mass transfer within the solution (Doran 1995; Cussler 1997).

The mixing regime of the system is reported by establishing an overall Reynolds number, Re, for each stirring speed assessed. Such Re number is defined for stirred vessels, and is

dependent on the solution viscosity and density, on the stirrer geometry and speed, but not dependent on the geometry of the vessel and the frames. The Re for stirred vessels is determined with the following equation:

$$Re = \frac{\rho N D^2}{\mu} \qquad \textit{Equation IV.1}$$

where N is the stirring angular rotations per second, D is the characteristic geometric length of the stirrer, ρ and μ are, respectively, the density and viscosity of the culture media. This Re is used mainly for reporting reasons, and not for an analysis of the fluid dynamics in the designed model, as it is only dependent on the velocity of the fluid at the tip of the stirrer and thus, not reflecting the variety of velocities at the different locations of the solution, specially at the surface of the scaffolds. A better description of the mixing properties of the system is achieved by CFD analysis.

IV.2.3 – Characterization of Fluid Dynamics: Mixing Time, Limiting Current and CFD

The estimation of the mixing time and circulation time offers a rough estimate of how well mixed is the system. The mixing time, t_m, is a parameter used to evaluate the mixing efficiency in fermenters and reactors, and is generally defined, as the time required of a solution to be homogenized. Several methods developed to determine the mixing efficiency are described in literature. Those methods are based essentially on monitoring the concentration of a tracer substance (acids, bases, concentrated salt solutions, dyes) at a fixed point of the vessel, distant from the point in the solution where the tracer was applied. A number of measurement techniques have been developed based on the conductivity, pH, temperature, variation in color (colorimetric) or fluorescence, as examples (Manfredini et al. 1983; Doran 1995; Nienow et al. 1996; Karcz et al. 2005; Irene Sánchez Cervantes et al. 2006; Cabaret et al. 2007; Zhang et al. 2009; Tan et al. 2011; Bulnes-Abundis et al. 2013). The tracer concentration in the measured point will change between higher and lower values, until it converges into an intermediate value. It is considered that convergence is reached

when only low variations from 5 to 10% relative to the equilibrium final concentration in the bulk fluid are observed (Doran 1995; Zhang et al. 2009; Tan et al. 2011). The circulation time can be measured as a concentration variation period, i.e the time between two maxima (or minima) of the measured tracer concentration. The circulation time represents the time that a fluid takes to make a complete circulation within a vessel, and usually for mixing times smaller or equal to 4 circulation times, it can be considered an adequate mixing for a bioreactor.

The limiting current technique is an established electrochemical method that allows measuring the mass transfer coefficient of an electro-active component in a solution of electrolyte (Lin et al. 1951; Reiss and Hanratty 1962; Selman and Tobias 1978; Szánto et al. 2008). This technique is useful not only for the study of electrochemical systems, but also to provide correlation on fluid mechanics, heat and mass transport, essential for the rational design and operating parameters of agitated vessels or membrane based processes (Scott and Lobato 2002; Sedahmed et al. 2004; Rodrigues et al. 2012).

The general concept of a limiting current experiment, involves a solution with potassium ferricyanide (III) and potassium ferrocyanide (II) to estimate the mass transfer coefficient at the interface electrode/solution via the redox couple ferri-ferro cyanide. An electrical potential is applied, promoting the reduction of ferricyanide (III) into ferrocyanide (II) at the electrode interface:

$$Fe(CN)_6^{3-} + e^- \rightarrow Fe\ (CN)_6^{4-} \qquad \textit{Equation IV.2}$$

The reverse reaction takes place in nearby regenerating electrodes, ensuring that the concentration of the ferri-ferro redox couple is constant during the process. As the reaction takes place there is movement of ions from the bulk of the solution to the surface of the electrode. When the rate of the electrolyte transport between the solution bulk and the electrode surface becomes the limiting step in the process, it is observed the formation of a concentration gradient of electrolyte (the concentration polarization phenomena), affecting the current-potential curve. In these conditions the reaction is under complete mass transport control (diffusion controlling reaction), where the concentration of ions at the surface of the electrode becomes zero, and a plateau in the current-potential curve is observed (Lin et al. 1951).

In general, three regions can be identified in the polarization curve (Figure IV.1) that is the mixed control, the plateau and the secondary reaction regions.

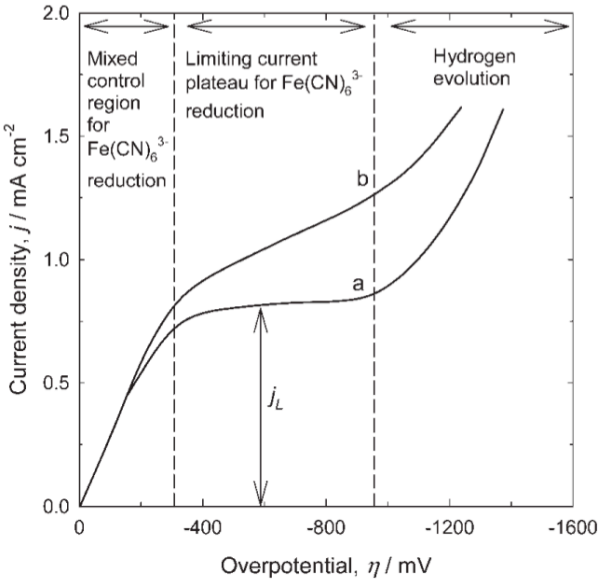

Figure IV.1 - The three regions of the polarization curve: mixed control region, limiting current plateau and hydrogen evolution. Curves a and b refer to measures using polished and unpolished electrodes, respectively. Adapted from (Szánto et al. 2008).

The mixed control region is primarily controlled by mass transport and electron transfer, in the plateau region the reaction is completely controlled by mass transport and, in the end of the curve, a secondary reaction (typically hydrogen evolution) occurs at the same time as the primarily reaction of reduction. The state of the surface of the electrodes (curves *a* and *b*) is important for the measurements and resulting polarization curve, thereby the electrodes are pretreated for the removal of oxides which is determinant for the delineation of the limiting current plateau (Szánto et al. 2008).

Determining the mass transfer coefficients for ferricyanide for a particular vessel (with certain geometry and operation conditions), can then be used as an approximation and be extrapolated to estimate the mass transfer coefficients of metabolites in solution, allowing establishing a concentration polarization at the interface scaffold/liquid bulk. Since mass transfer coefficients are estimated for each side of the frames, at each position, one can also have some insights on the system homogeneity. The estimation of the mass transfer coefficients allows for a simplified description of the transport within a liquid solution.

The Fick's law describes the diffusion phenomena alone and considering a diffusion coefficient, requires the assumption that concentration changes take place within a limited volume of the system, with fixed values at the respective boundaries. Therefore, for such cases by definition: the amount of transferred mass is proportional to the diffusion mass transfer coefficient, the concentration difference and the interfacial area:

$$\begin{pmatrix} rate\ of\ mass \\ transferred \end{pmatrix} = k \begin{pmatrix} interfacial \\ area \end{pmatrix} \begin{pmatrix} concentration \\ difference \end{pmatrix} \qquad \textit{Equation IV.3}$$

where the proportionality is summarized by the mass transfer coefficient, k. Dividing both sides of this equation by the area, it is possible to write:

$$N_i = k(c_i - c_b), \left[\frac{mol}{m^2 s}\right] = \left[\frac{m}{s}\right]\left[\frac{mol}{m^3}\right] \qquad \textit{Equation IV.4}$$

where N_i is the flux at the interface and c_i and c_b are the concentrations at the interface and in the bulk of the solution, respectively.

CFD is a mathematical framework for the theoretical calculation of the fluid dynamic, and an essential tool in the design, scale-up and performance prediction of reactor systems. This computer-based method involves the solution of complex differential equations of fluid models, for the simulation of flow patterns and velocities, and forces, applied to a case model. The model is defined in the form of a numerical grid (mesh) representing the geometric flow of the system in study. The equations applied in this method are the conservation equations of mass, energy and momentum, that fundamentally describe the motion of a fluid (fluid dynamic), with additional series of equations that define the specific case study. The Navier-Stokes equations provide a description of the fluid motion based on the conservation laws, and describe accurately the flow of a Newtonian fluid in simple geometries such as in pipes or in parallel plates. Adequate approximations and simplifications regarding complex geometries and flow types (laminar or turbulent, quantified by the Reynolds number), as examples, are applied in order to determine the most adequate solution for the case in study (Harris et al. 1996; Weyand et al. 2009; Ferziger and Peric 2012). CFD will be used for the calculation of shear stress and fluid linear velocity vectors in each point of the vessel.

The results presented in this chapter, regarding the experiments of limiting current and CFD simulations were obtained with the collaboration of an Erasmus master student, Luca Bronzato from Politecnico di Milano (Italy), to whom the constructed vessel was provided. The

results were integrated in the master thesis of Luca Bronzato under the supervision at IST of Prof. Frederico Ferreira and Prof. Vítor Geraldes, entitled “Bioreactor for Stem Cell Expansion: Theoretical Design, Modeling of Mass Transfer and Experimental Evaluation of a Stirred Vessel”.

IV.3 - Materials and Methods

IV.3.1 - Design and Construction of the Stirred Vessel

The prototype (Figure IV.2) was built in polyterafluoroethylene (PTFE), known as Teflon, the DuPont brand name of the thermoplastic fluoropolymer. The vessel consists of a single elliptical piece constructed from drilling a block of PTFE with internal dimensions, in millimeters, of 20, 45 and 40 for width, length and height, respectively (eccentricity of 0.46, approximately), with a total volume of 43 mL capacity. Twelve cylindrical slots on the inner lateral walls of the vessel (six in each wall) sustain six scaffold frames (approximately 2.3 by 1.9 cm). The slots reach from top to up to 6 mm to the bottom, allowing placing underneath a 20 mm diameter cross-shaped PTFE covered stirring bar (VWR, USA) to provide agitation when magnetically moved. With the 6 frames positioned in the slots, five compartments are defined limited between two frames, and two compartments in the extremities, limited by one frame and the vessel wall. A space at the bottom of the vessel is created (10 mL in volume), limited up to 6 mm in height where the frames are held, and the magnetic stirrer is placed allowing the flow distribution through the seven compartments above. When the vessel is filled with 25 mL of liquid, the level matches the top of the frames, limiting the liquid circulation only through the bottom chamber. Alternatively, using 30 mL of liquid, the level reaches above the top edge of the frames, allowing an additional liquid circulation through the upper region of the occupied volume above the frames.

A cap was cut from an identical block of PTFE, and was designed to not seal the vessel, working similar to a petri dish cap (Figure IV.2). In order to promote efficient air exchange the cap itself enclosures a space (approximately 16.5 mL in volume) of 30 mm in height from the end of the cap that is joined to the top border of the vessel. Thus an air chamber corresponding to 50 % in volume (from the total volume cap-vessel) is provided when using 30 mL of liquid. This compact set allows performing the cellular culture in a regular incubator chamber. In Appendix an additional drawing in SolidWorks® is presented (Figure IVA.1).

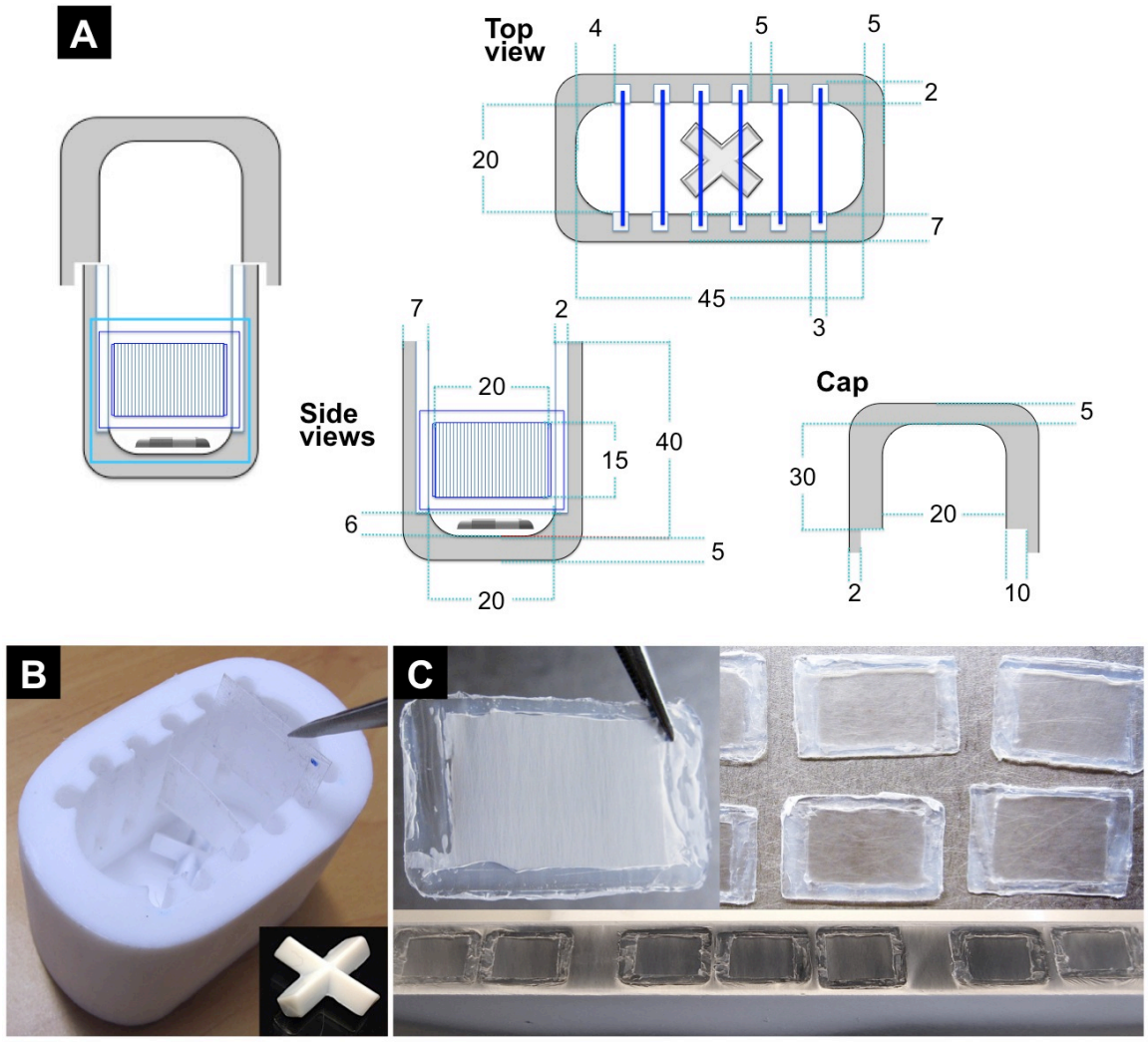

Figure IV.2 – Model of the stirred vessel: (A) Drawing of the prototype provided for construction (dimensions in millimeters); (B) Constructed prototype in PTFE and respective cross-shaped stirring bar; (C) Scaffolds of aligned polycaprolactone nanofibers assembled in PET frames.

IV.3.1.1 - Frames of Poly(ε-caprolactone) Nanofibers

Scaffolds of PCL aligned nanofibers were prepared by electrospinning as described in Chapter III. The equipment used consisted on a high voltage power supply (Model PS/EL40P0, Series EL 1, Glassman High Voltage Inc., High Bridge, NJ, USA), a syringe pump (Model KDS Legato 210, KDS Scientific, Holliston, MA, USA) and a tube that connected a syringe (Henke Sass Wolf, Germany) to a needle (Needle Valve Dispense Tip Kit, EFD International Inc., UK) with an inner diameter of 0.84 mm. Aligned nanofibers were produced using 6% w/w solution of PCL (70000-90000 MW, Sigma-Aldrich, St. Louis, MO,

USA,) in 1,1,1,3,3,3-hexafluoro-2-propanol (HFP, Sigma-Aldrich) at a flow rate of 1 mLh^{-1}, with an applied potential of 26 kV, at a working distance of 20 cm from the tip of the needle to the nanofiber deposition target (two parallel steel plates with 2 cm gap). The average humidity and temperature working conditions was 30-40% and 22-25 ºC respectively. The scaffolds were built by fixing the nanofibers to polyethylene terephthalate (PET sheet, Mylar, GoodFellow, UK) frames with biocompatible silicon glue (Sylvatic Medical Adhesive Silicone type A, Dow Corning, Midland, MI, USA).

IV.3.2 – Characterization of Dynamic Parameters: Mixing Time, Mass Transfer Coefficient, Sherwood Number, Shear Stress

The effect of the liquid volume and the stirrer rotation speed on the mass transfer and mixing efficiency, were evaluated experimentally. The system hydrodynamics was then theoretically simulated by CFD with shear stress and fluid velocity calculated in each point of the solution. The obtained experimental and theoretical results were discussed.

IV.3.2.1 – Mixing Effectiveness

A simplified colorimetric based method with image analysis was used as a first evaluation of the mixing performance and to visualize the fluid flow on the stirred vessel. A digital camera (Canon IXUS 100 IS, Japan) was used to record a video for the observation of the transition state between the application of 20 μL of tracer and the complete homogenization of the fluid. A solution of Trypan blue (Sigma) of 0.08%, prepared by 1:5 dilution of a 0.4% stock solution in water, was used as tracer to visually identify the mixing progress of the fluid. A volume of 20 μL of the tracer solution was released on one side of the vessel containing 25 mL of distilled water, enclosing six nanofiber scaffolds. The variation in color over time was estimated by analyzing individual frame images of the gradual color change during the mixing of the liquid, on three different points opposite to the tracer deposition site, at different rotation velocities. The gray scale intensity variation of the recorded image frames allows quantifying

the dissipation of the contrasting tracer solution throughout the continuous mixing of the fluid. Mixing time and circulation times were estimated.

IV.3.2.2 – Limiting Current Technique for Mass Transfer Coefficient Estimation

The vessel was centered on a magnetic stirrer plate (bioMIXdrive 1, 2mag, Germany), in a fixed position. Six electrodes were cut from nickel sheets, four with 2.85 × 1.8 cm (base × height) and two with 2.4 × 1.8 cm to fit the first and the sixth positions, modeling the scaffold frames (Figure IV.3). Three electrodes are sequentially connected to a potentiostat (Zahner PP201, Germany), in turn connected to a computer (PP201 Zahner software V6.4) for data record. The magnetic stir bar was placed inside the vessel and six flat nickel electrodes were positioned on the vessel slots made to hold the scaffold frames. The measuring current on the electrodes surface operates as a model to evaluate the mass transfer at the surface of the scaffolds for different operation conditions.

In each experiment one electrode is the recording electrode, the nearest is the regenerating electrode, and the remaining are passive in the process. For example to measure the 6^{th} electrode the regenerating electrode is the 5^{th}, while to measure the 5^{th} and 4^{th} the regenerating are the surrounding electrodes (to refer that no differences in the measured current were found when using one or two regenerating electrodes). The reduction of the ferricyanide (III) takes place at the surface of the recording electrode (cathode) where a positive faradaic current is produced, while in the regenerating electrodes (anode) a negative current is produced due to the oxidation of the ferrocyanide (II). In this way the concentration of analytes is maintained constant during the electrochemical process, where both the reduction and oxidation reactions of the couple ferri-ferro cyanide allow the movement of the analytes from the bulk of the solution to the electrode and in the opposite direction. The electrodes were thoroughly polished before every set of experiments, and painted with nail varnish for isolating the non-operating areas, leaving only accessible a rectangular area, equivalent in dimensions to the scaffold area available for cellular adhesion.

The standard solution for the electrochemical process was prepared with deionized water and is composed with 0.5 M of potassium carbonate (K_2CO_3, MerckMillipore), 0.01 M of

potassium hexacyanoferrate (II) trihydrate ($K_4Fe(CN)_6$, Sigma-Aldrich) and 0.005 M of potassium ferricyanide (III) ($K_3Fe(CN)_6$, Sigma-Aldrich). Potassium carbonate is applied in high concentration as a supportive neutral electrolyte in order to stabilize the charged species in solution, ensuring that ferricyanide (III) and ferrocyanide (II) ion migration due to ionic charge effects (attraction or repulsion) can be neglected, and that the movement of the analytes in solution is due only to diffusion and convection effects.

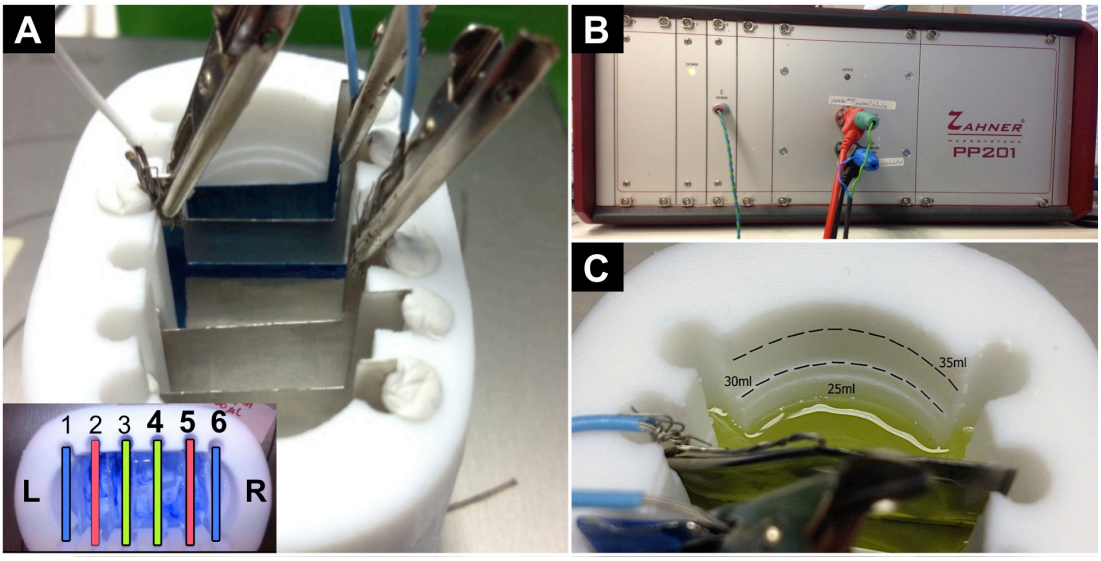

Figure IV.3 – Experimental setting for the limiting current experiments: (A) Fixed electrodes, one working electrode in between two regenerating electrodes; in the inset: identification of the location of the electrodes (1 to 6 with left (L) and right sides (R)) inside the vessel with respective color: blue – external, red – middle, green - centre; (B) potentiostat connected to the electrodes; (C) Different heights of the fluid corresponding to the respective volumes of solution.

Due to the symmetry of the vessel and for simplicity just three positions were measured: the fourth, the fifth and the sixth position (Figure IV.3 – A), for both sides of each electrode (active surfaces facing left and right). The scanning potential applied to the system was set from -1.0 V to 0 V, at a rate of 0.01 V/s for each scan. Each potential scan was performed at different velocities of agitation (0, 10, 20, 30, 40, 45, 50, 60, 90 and 120 rotations per minute) and for 25 and 30 mL of working volume.

The mass transfer coefficient is estimated considering the limiting current, I_L, value at the plateau of the current-voltage diagrams (Figure IV.1) and the equation below:

$$I_L = k_m A z F c_b \qquad \textit{Equation IV.5}$$

where k_m is the mass transfer coefficient, A is the active area of the electrode, z is the number of electrons involved in the reaction, F is the Faraday constant and c_b is the bulk concentration of the electro-active compound (Szánto et al. 2008). From this relation, it can be obtained the value of the mass transfer coefficient for ferricyanide, in the plateau area.

The physical constants of ferricyanide (III) are summarized in the following table (Eroğlu et al. 2011; Rodrigues et al. 2012):

Table IV.1 - Physical properties of ferricyanide (III) in a solution of 0.5 M of K_2CO_3.

Mass diffusivity	D_{AB}	6.8 x 10^{-10} m^2s^{-1}
Dynamic viscosity	μ	1.21 x 10^{-3} kg $m^{-1}s^{-1}$
Density	ρ	1098 kg m^{-3}
Schmidt number	Sc	1620

IV.3.2.3 - Mass Transfer Coefficient and Concentration Gradients

The limiting current technique allows estimating the mass transfer coefficient of an electrolyte such as ferricyanide. However, in the present study it is important to extrapolate such information for the estimation of the mass transfer coefficient of additional compounds, such as lactate, a toxic by-product, which is produced locally by the cells. Such approximation can be obtained by translating the mass transfer coefficient of a test component (such as ferricyanide) determined experimentally, considering the Sherwood number, Sh.

The Sherwood number is dimensionless and represents the ratio of overall convective and diffusive mass transport rates:

$$Sh = \frac{KL}{D_{AB}} = \frac{Convective\ Mass\ Transfer\ Coefficient}{Mass\ Diffusivity} \qquad \textit{Equation IV.6}$$

where L is a characteristic length in meters, D_{AB} is the mass diffusivity (or diffusion coefficient) in m^2/s and K is the convective mass transfer coefficient in m/s of ferricyanide.

The characteristic length defines the relevant geometry of the system, across which the fluid flows and from which the boundary layer is formed. This parameter is expressed by the hydraulic diameter, D_H, which provides a way to determine a diameter of non-circular conduits, defined by

$$L = D_H = \frac{4A}{P} \qquad \textit{Equation IV.7}$$

where A is the cross-sectional area for the fluid flow and P is the wetted perimeter.

An extensive number of correlations can be applied to determine the mass transfer coefficient of a specific system (such as flat plates, cylinders and spheres) based both on empirical or theoretical assumptions, and depending on the hydrodynamic conditions (laminar or turbulent). Considering a single flat plate, as the simplest relevant geometry of the system, and the average mass transfer from the plate to the fluid in a laminar regime, with forced fluid, the following dimensionless correlation was derived (Grober et al. 1961) taking into account the hydrodynamics and thus as a function of the Reynolds number, Re, and the Schmidt number, Sc:

$$Sh = 0.664 Re^{1/2} Sc^{1/3} \qquad \textit{Equation IV.8}$$

The Reynolds number, Re, is here defined as the ratio between the inertial forces and the viscous forces and is given by the following equation:

$$Re = \frac{\rho \upsilon D_H}{\mu} \qquad \textit{Equation IV.9}$$

where υ is the linear velocity of the fluid in a specific location, D_H is the characteristic geometric element responsible for shear stress, ρ and μ are, respectively the density and viscosity of the fluid.

The Schmidt number is defined by

$$Sc = \frac{\mu}{\rho . D_{AB}} \qquad \textit{Equation IV.10}$$

which relates the fluid flow due to viscosity and diffusion and convective transport processes.

The friction coefficient, C_f, is determined by

$$C_f = \frac{1.388}{\sqrt{Re}} \qquad \textit{Equation IV.11}$$

that, can be related with the shear stress, τ, and Re, by

$$C_f = \frac{\tau}{\rho \upsilon^2 /_2} = \frac{2\tau}{\rho \upsilon^2} \qquad \textit{Equation IV.12}$$

Substituting the parameters Sh, Re and Sc with the correspondent equations (6, 9, 10, 11 and 12) in equation IV.8, the mass transport coefficient, k, can be determined by

$$k = 0.46\frac{v^2}{\tau L}(\rho D_{AB})^{2/3}\mu^{1/3} \qquad \textit{Equation IV.13}$$

The following relation can be assumed, that

$$\frac{k_f \tau L}{v^2(\rho_f D_{AB_f})^{2/3}\mu_f{}^{1/3}} = 0.46 = \frac{k_{lac}\tau L}{v^2(\rho_{lac} D_{AB_{lac}})^{2/3}\mu_{lac}{}^{1/3}} \qquad \textit{Equation IV.14}$$

in order to determine the mass transfer coefficient for lactate, k_{lac} , that

$$k_{lac} = k_f \frac{(\rho_{lac} D_{AB_{lac}})^{2/3}\mu_{lac}{}^{1/3}}{(\rho_f D_{AB_f})^{2/3}\mu_f{}^{1/3}} \qquad \textit{Equation IV.15}$$

In order to predict the mixing performance of the stirred vessel, several cases can be analyzed based on an estimated specific lactate production coefficient and number of cells per scaffold. A low concentration polarization of lactate is desirable at the scaffold interface in order to avoid potential toxicity to the cells in culture. The cell culture by-products are expected to be transported into the bulk of the solution for an effective mixing regime. One of the cases that lead to higher concentration driving force for lactate is by considering the lactate concentration equal to zero in the bulk of the solution ($c_{lac\,b} = 0$). The concentration at the interface can be derived from equation IV.4:

$$c_{lac\,i} = {N_{lac}}/{k_{lac}} + c_{lac\,b} \qquad \textit{Equation IV.16}$$

in which N_{lac} is the lactate flux, $C_{lac\,i}$ the lactate concentration at the interface, $c_{lac\,b}$ the lactate concentration in the bulk of the solution and k_{lac} the mass transfer coefficient for lactate.

IV.3.2.5- Simulation by Computational Fluid Dynamic

The CFD model was performed with OpenFOAM® (Open Field Operation and Manipulation) CFD Toolbox, a free open source CFD software package based on C++ source code. OpenFOAM® includes tools for meshing, such as "SnappyHexMesh", a parallelized mesher for complex CAD geometries, for pre- and post-processing. In this study the version used is the current last release OpenFOAM 2.3.0 and computational simulations were run on an ASUS computer, model A55V with an Intel Core i7 3630QM @ 2.4GHz CPU with four physical cores and 4 GB of RAM.

For the computational simulations to be performed it is necessary to represent the structure of the vessel in a stereolithography file, a virtual mesh representing the 3D space to be simulated, the selection of the adequate governing equations, boundary conditions and solver, followed by data treatment for presentation of the results.

- ***Problem specifications***

Solution domain – The domain is a three-dimensional structure comprising the vessel, the frames and the stirrer as previously described. Additionally, to simplify the simulations and to facilitate the model convergence it was assumed round and soft edges of the magnetic stirrer (instead of sharp), the rotational axis of the stirrer is fixed parallel to y-axis (experimentally the stirrer is not totally centered), the 12 slots that hold the electrospun scaffolds were not considered in the vessel structure for simulation. A representation of the resulting domain is presented in Figure IV.4.

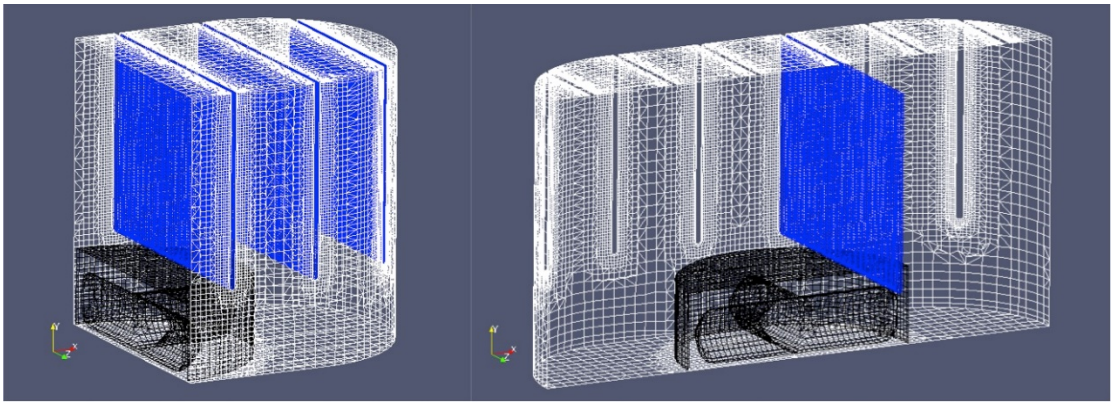

Figure IV.4 – The 3D geometry of the structure including the vessel, stirrer and scaffold frames. Example for the 25 mL case-study.

Governing Equations – The laminar and turbulence models were considered and selected according with theoretical consistence between the computed flow regime and model assumptions:

- ✓ Laminar model - The general Navier-Stokes equations are valid for incompressible and newtonian fluids; the compact vector (Equation IV.17) and continuity notations (Equation IV.18), are presented respectively:

$$\rho\left(\frac{\partial \mathbf{V}}{\partial t} + \mathbf{V}\cdot\nabla\mathbf{V}\right) = -\nabla p + \mu\nabla^2\mathbf{V} \qquad \textit{Equation IV.17}$$

$$\nabla \cdot \mathbf{V} = \frac{\partial u}{\partial x} + \frac{\partial v}{\partial y} + \frac{\partial w}{\partial z} = 0 \qquad \textit{Equation IV.18}$$

- ✓ SST k-ω Turbulence model (Menter 1993) - Shear stress transport (SST) model is a two-equation eddy-viscosity model for the simulation of a turbulent flow, that combines the k-ε formulation in the free stream and the k-ω formulation near the walls (boundary layer); the model is defined by the equations IV.19, IV.20 and IV.21 for the turbulence kinetic energy, the specific dissipation rate and the kinematic eddy viscosity, respectively:

$$\frac{\partial k}{\partial t} + \bar{u}_j \frac{\partial k}{\partial x_j} = P_k - \beta^* k\omega + \frac{\partial}{\partial x_j}\left((v + \sigma_k v_T)\frac{\partial k}{\partial x_j}\right) \qquad \textit{Equation IV.19}$$

$$\frac{\partial \omega}{\partial t} + \bar{u}_j \frac{\partial \omega}{\partial x_j} = \alpha S^2 - \beta\omega^2 + \frac{\partial}{\partial x_j}\left((v + \sigma_\omega v_T)\frac{\partial \omega}{\partial x_j}\right) + 2(1 - F_1)\sigma_{\omega 2}\frac{1}{\omega}\frac{\partial k}{\partial x_i}\frac{\partial \omega}{\partial x_i}$$

Equation IV.20

$$v_T = \frac{a_1 k}{\max(a_1\omega, b_1 F_2 S)} \qquad \textit{Equation IV.21}$$

The closure coefficients are:

$\alpha_{k1} = 0.85034$, $\alpha_{k2} = 1.0$, $\alpha_{\omega 1} = 0.5$, $\alpha_{\omega 2} = 0.85616$, $\gamma_1 = 0.5532$, $\gamma_2 = 0.04403$, $\beta_1 = 0.075$, $\beta_2 = 0.0828$, $\beta^* = 0.09$, $a_1 = 0.31$, $b_1 = 1.0$, $c_1 = 10.0$

Initial conditions - The problem was established as statistically stationary and therefore initial conditions are actually not required, still for OpenFOAM® to compute input files it is necessary to establish: *U* = 0 m/s, *p* = 0 Pa.

Boundary conditions – Slip walls on the top boundary," Moving Wall Velocity" walls on the stirrer and no-slip walls on the remaining boundaries.

Transport Properties – The following parameters were considered: density for water at 20°C of 1×10^3 kg·m^{-3}, and the dynamic viscosity of 7.2×10^{-4} Pa·s and kinematic viscosity of 7.2×10^{-7} m^{2}s^{-1} correspond to values experimentally measured for culture media at 37ºC.

Solver name - The solver used "pimpleDyMFoam", is a transient solver for incompressible flow of Newtonian fluids on a moving mesh using the PIMPLE (merged PISO-SIMPLE)

algorithm. Turbulence modeling that can be used is generic, i.e. laminar, RAS or LES may be selected.

Case name - The model was developed in the scope of Lucca Bronzato Master thesis under the supervision of Professors Vitor Geraldes and Frederico Ferreira. The model includes two variables X_1 and X_2, where X_1 is 25 or 30 mL and X_2 is 30, 45, 60, 90, 120 rpm. The other parameters were media density and viscosity, which were kept constant.

"BioReactor", located in the *$Desktop/CASES/BioReactor_X_1ml_X_2rpm* directory. OpenFOAM® directory computational case structure contains the entire set of files required to run it, which in the current case-study are:

- The "*system*" directory contains the setting parameters associated with the solution procedure itself, which are:
    - "*controlDict*" for run control parameters;
    - "*fvSchemes*" with discretization schemes used in the solution;
    - "*fvSolution*" where the equation solvers, tolerances and other algorithm controls are set for the run.
- Then other dictionaries are used, depending on the case; in this case, for example:
    - "*surfaceFeatureExtractDict*" and "*snappyHexMesh*" dictionaries were used to generate three dimensional meshes from *.stl* files;
    - "*topoSetDict*" and "*createPatchDict*" dictionaries are useful to extract the parts of interest on the scaffolds and name them;
    - "*decomposeParDict*" dictionary allows to run the case in parallel on different processors;
    - "*readFields*" make sure all the fields are loaded;
    - "*fieldAverage1*" make an average of values of some fields during the simulation.
- The "*constant*" directory contains a full description of the case mesh in a subdirectory called "*polyMesh*", files specifying physical properties and a folder with all the *.stl* files that have to be processed by "*surfaceFeatureExtractDict*".

In the time directories are stored individual file data for each particular field. The initial conditions are stored in the "*0*" directory.

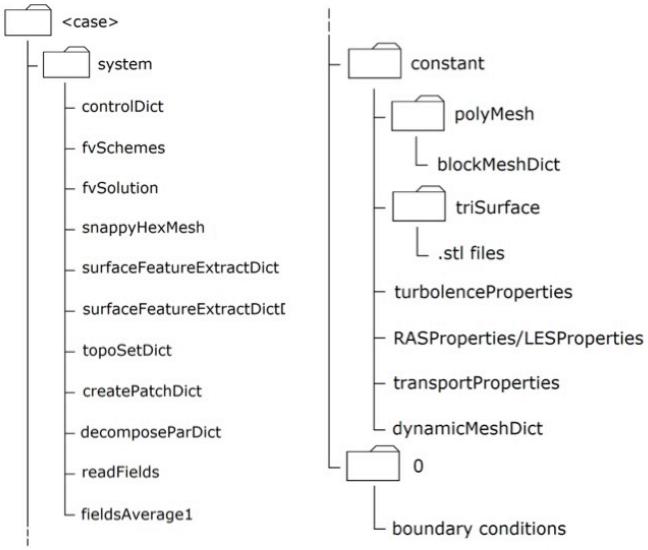

Figure IV.5 – Architectural structure of the computational fluid dynamic case.

- **Mesh generation**

A *blockMesh* dictionary was used to form two orthogonal meshes with different dimensions. A mesh of 60 × 40 × 26 blocks, with the fluid level reaching 26.5 mm from the bottom surface was built to represent the 25 mL case, while a mesh with 60 × 40 × 30 blocks, with the fluid level reaching 29 mm was built to represent the 30 mL case. Figure IV.6 illustrates part of the code.

```
vertices
(
    // Mesh
    (-0.03 0.0012 0.02)        //0
    (0.03 0.0012 0.02)         //1
    (0.03 0.0012 -0.02)        //2
    (-0.03 0.0012 -0.02)       //3
    (-0.03 0.02649 0.02)       //4
    (0.03 0.02649 0.02)        //5
    (0.03 0.02649 -0.02)       //6
    (-0.03 0.02649 -0.02)      //7
);

blocks
(
    hex (0 1 2 3 4 5 6 7) (60 40 26) simpleGrading (1 1 1)
);
```

```
vertices
(
    // Mesh
    (-0.03 0.0012 0.02)        //0
    (0.03 0.0012 0.02)         //1
    (0.03 0.0012 -0.02)        //2
    (-0.03 0.0012 -0.02)       //3
    (-0.03 0.02899 0.02)       //4
    (0.03 0.02899 0.02)        //5
    (0.03 0.02899 -0.02)       //6
    (-0.03 0.02899 -0.02)      //7
);

blocks
(
    hex (0 1 2 3 4 5 6 7) (60 40 30) simpleGrading (1 1 1)
);
```

Figure IV.6 – On the left the 25 mL case and on the right the 30 mL case blockMesh dictionary.

The stereolithography files used were built in SolidWorks®. Then *snappyHexMesh* application was used to generate 3D hexahedra (hex) and split-hexahedra (split-hex) meshes

automatically from triangulated surface geometries in *.stl* format. The *castellatedMesh* was applied to remove unused cells, the *snap* to smooth and merge faces and the *addLayers* to push the mesh away from the surface and add two layers. At the end of this process the resulting number of cells was 844.698 and 916.015 respectively for the cases of 25 mL and 30 mL.

The final resulting meshes were then improved by adjusting the dimensions of the scaffolds (exceeding in weight) and vessel (exceeding in height) to obtain a more regular mesh during the *snapping* process, as it is shown in Figure IV.7, therefore, after each structure was built the parameters of the dimensions were adjusted for each case in the *blockMesh* dictionary.

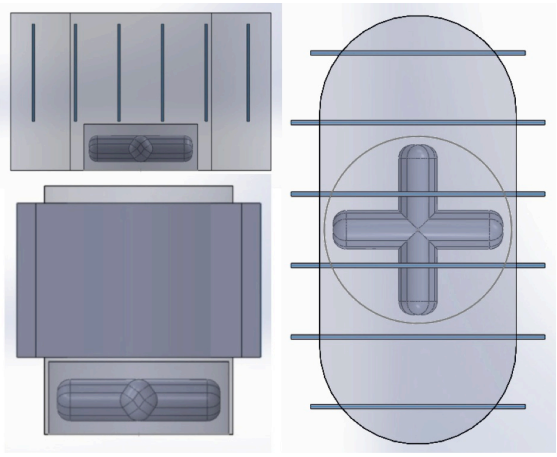

Figure IV.7 – Stereolithography files built in SolidWorks.

- **Simulation run set-up**

Considering two different fill volumes (25 and 30 mL) and 5 rotational velocities (30, 45, 60, 90, 120 rpm) ten computational cases were organized. Table IV.2 resumes the time requested, in each case, the computational time required to complete the simulation of up to six magnetic stirrer rotations, inserted in *controlDict*.

Table IV.2 - Required simulation rotation times for each computational case.

rpm	*Time/rotation (s)*	*Time/six rotations (s)*
30	2	12
45	1.33	8
60	1	6
90	0.66	4
120	0.5	3

The last complete rotation was executed by activating the function *fieldAverage* that calculates average quantities for a specified field updated during the calculation, in this case "UMean",

$$\bar{x} = \frac{1}{N}\sum_{i=0}^{N} x_i \qquad \textit{Equation IV.22}$$

and "UPrime2Mean",

$$\overline{x'^2} = \frac{1}{N}\sum_{i=0}^{N}(x_i - \bar{x})^2 \qquad \textit{Equation IV.23}$$

Then the *wallShearStress* function is calculated and for the last complete rotation is calculated for "Umean", so that an average shear stress is determined for a complete rotation.

The shear stress is calculated using the following equation:

$$Stress = R\dot{n} \qquad \textit{Equation IV.24}$$

where R is the stress tensor and n is the patch normal vector (into the domain).

Additionally in *controlDict* the *adjustTimeStep* was selected, in order to make the code automatically calculate a reasonable time step to keep the Courant number, Co, below a certain value, in this case set to 1. The formula used is:

$$Co = \frac{U\Delta t}{\Delta x} \qquad \textit{Equation IV.25}$$

where U is the characteristic velocity of the phenomenon, Δx is the characteristic mesh size and Δt is the time step.

- **Running the case and post processing**

Table IV.3 summarizes the values of Reynolds number calculated for the rotational speed, 30, 45, 60, 90 and 120 rpm, allowing to classify the type of fluid motion regime - laminar, transient or turbulent - and therefore to decide which model to apply.

Table IV.3 - Rotational velocities and Reynolds numbers of the different simulated cases.

rpm	*rps*	*rad/s*	$Re = \frac{\rho N D^2}{\mu}$
30	0.50	3.14	251
45	0.75	4.71	376
60	1.00	6.28	501
90	1.50	9.42	752
120	2.00	12.57	1003

The laminar and turbulent models were applied for stirring rotational velocities of 60, 90 and 120, for the 25 mL case. The shear stress was computed for the two models and discussed further to access which model provides better fittings for the nature of the flow hydrodynamics regime.

The utility *patchAverage* was used to extract the average values of the wall shear stress from both sides of the scaffolds in the 4th, 5th and 6th positions. The application *paraView*, provided with OpenFOAM®, was used for post processing of large data sets of results.

IV.4 - Results and Discussion

IV.4.1 – Mixing Effectiveness

A primary evaluation of the mixing time was performed using a dye and monitoring the time of full mixing in water at different rotation velocities, in three points of the vessel (*green* closer to the centre between the 4th and 5th frames, *red* between the 5th and 6th frames and *blue* on the right of the 6th frame), as indicated in Figure IV.8. The relative concentration of dye was estimated over time, which after approximately 10 seconds of mixing, the dye concentration variation becomes fairly constant at the 3 points at 40 rpm stirring speed (Figure IV.8 – (A)). Also considering at a single point (Figure IV.8 – (B)) the mixing equilibrium is reached sooner at 60 rpm (7 s) compared to 30 rpm velocity (~10 s).

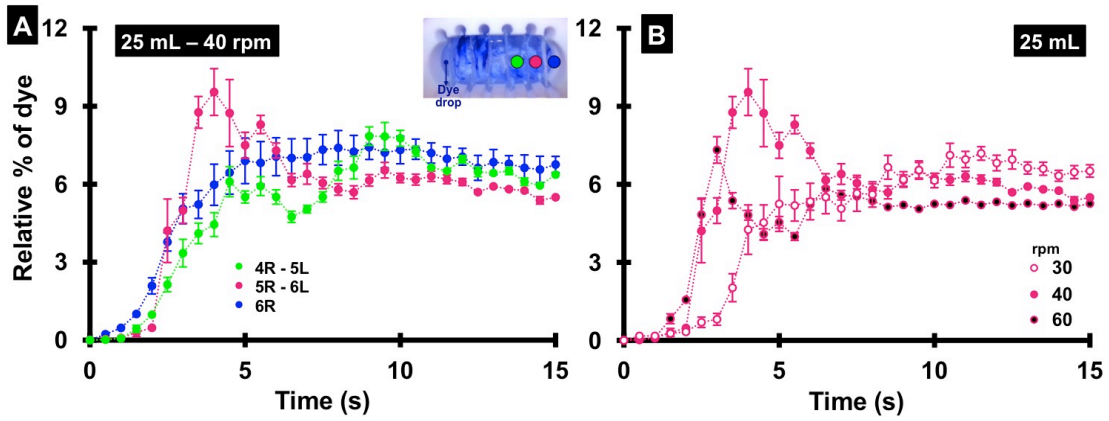

Figure IV.8 – Mixing time: (A) Relative concentration of dye over time at 40 rpm in 3 points between the nanofiber frames (on the left) and (B) relative concentration of dye over time in the region red (5R-6L) at 30, 40 and 60 rpm. Error bars represent SD.

The variation of the dye concentration at 30 rpm was less pronounced than at the faster stirring speeds, similar as observed at point C at 40 rpm.

Taking into consideration the moderate resolution of the analysed recorded images, eventually at lower speed of agitation and at a longer distance from the dye-dropping site, and due to the barrier effect of the nanofiber frames on the fluid movement, the dye variations (no dye flows contrasting with high concentration dye flows before equilibrium) become less

noticeable. A more detailed look into the mixing properties of the designed vessel follows in the next sections.

IV.4.2 – Mass Transfer Coefficient and Sherwood Number

The current intensity vs potential at different rotating velocities for the two working volume cases (25 an 30 mL) for the ferri-ferro redox couple are shown in figures IV.9 and IV.10. Current intensity values were taken from the -0.44 to -0.54 V interval, which corresponds to a steady limiting plateau segment of 100 values, as evidenced by the well defined plateaus for all the measured positions and working volumes.

In a preliminary testing experiment it was possible to establish a steady plateau for all the rotational velocities investigated, which validates the limiting current technique suitable for the estimation of mass transfer coefficients for the system in study. (Appendix IVA.3). The limiting current measurements were performed only to half of the vessel, at the 4th, 5th and the 6th positions, for left and right sides (scheme of the position of the electrodes in the vessel in Figure IV.3 – A).

The determined average value of the limiting current was used to calculate the mass transfer coefficient and the *Sh* number, both for ferricyanide, k_f, and for lactate, k_{lac}, at each stirring velocity, with the equations IV.6, IV.5 and IV.15, using as characteristic length the diameter of the stirrer, equal to 0.019 m. The parameters were estimated at the interface of the electrodes, in order to evaluate the effect of the hydrodynamics in overall nutrient and lactate distribution, that affect the device working conditions for cell culture.

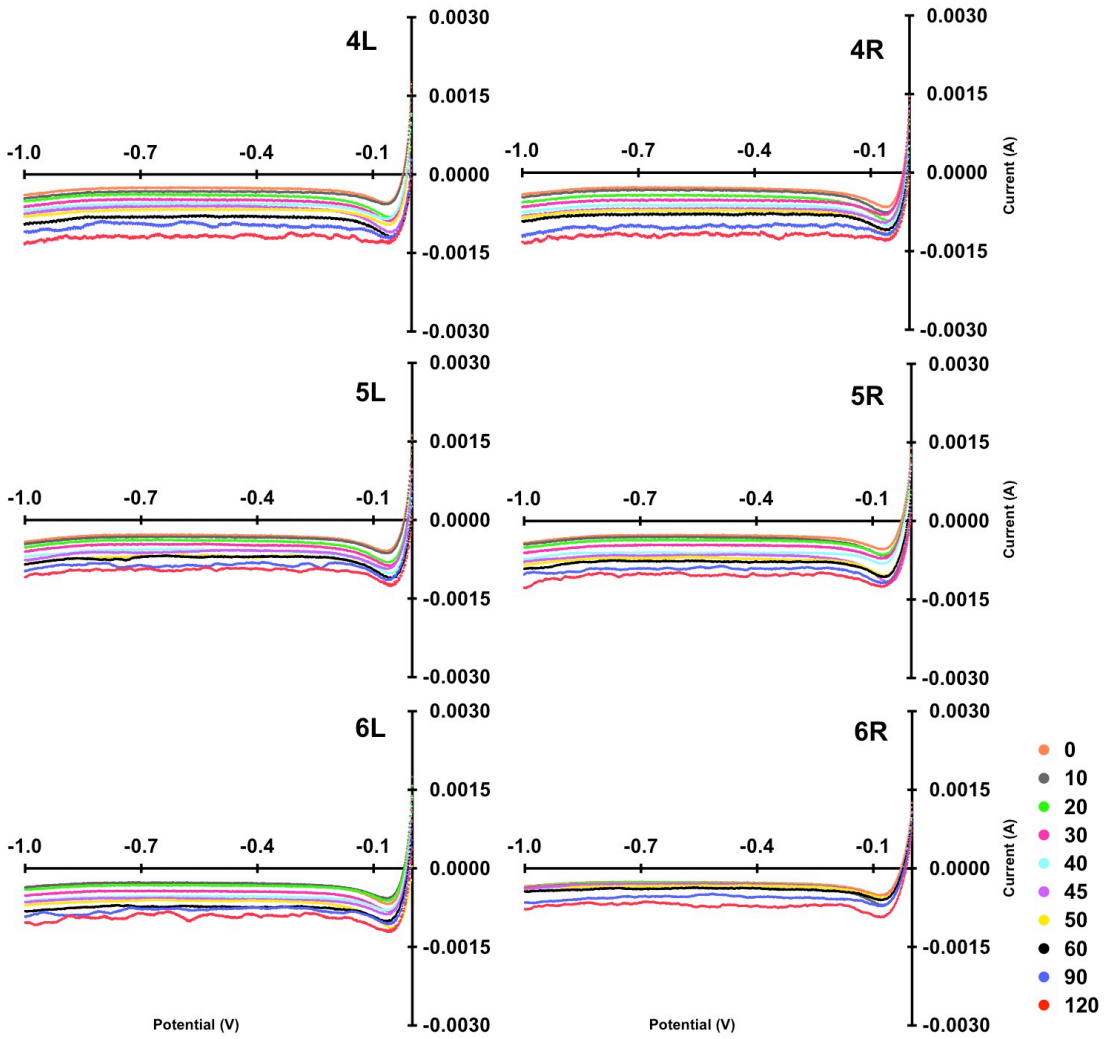

Figure IV.9 – Limiting current profiles of ferri-ferro redox couple for 25 mL of solution - Current intensity vs applied potential recorded at the 4th, 5th and 6th electrode surfaces, at left (L) and right (R) sides, with velocities of agitation from 0 to 120 rpm. Limiting current plateau considered in the range of -0.44 to -0.54 V to determine the average limiting current value. The potential applied varied from -1.0 V to 0 V, at a rate of 0.01 V/s for each scan. The dimension of the active surface of the electrodes is 0.020 × 0.014 m.

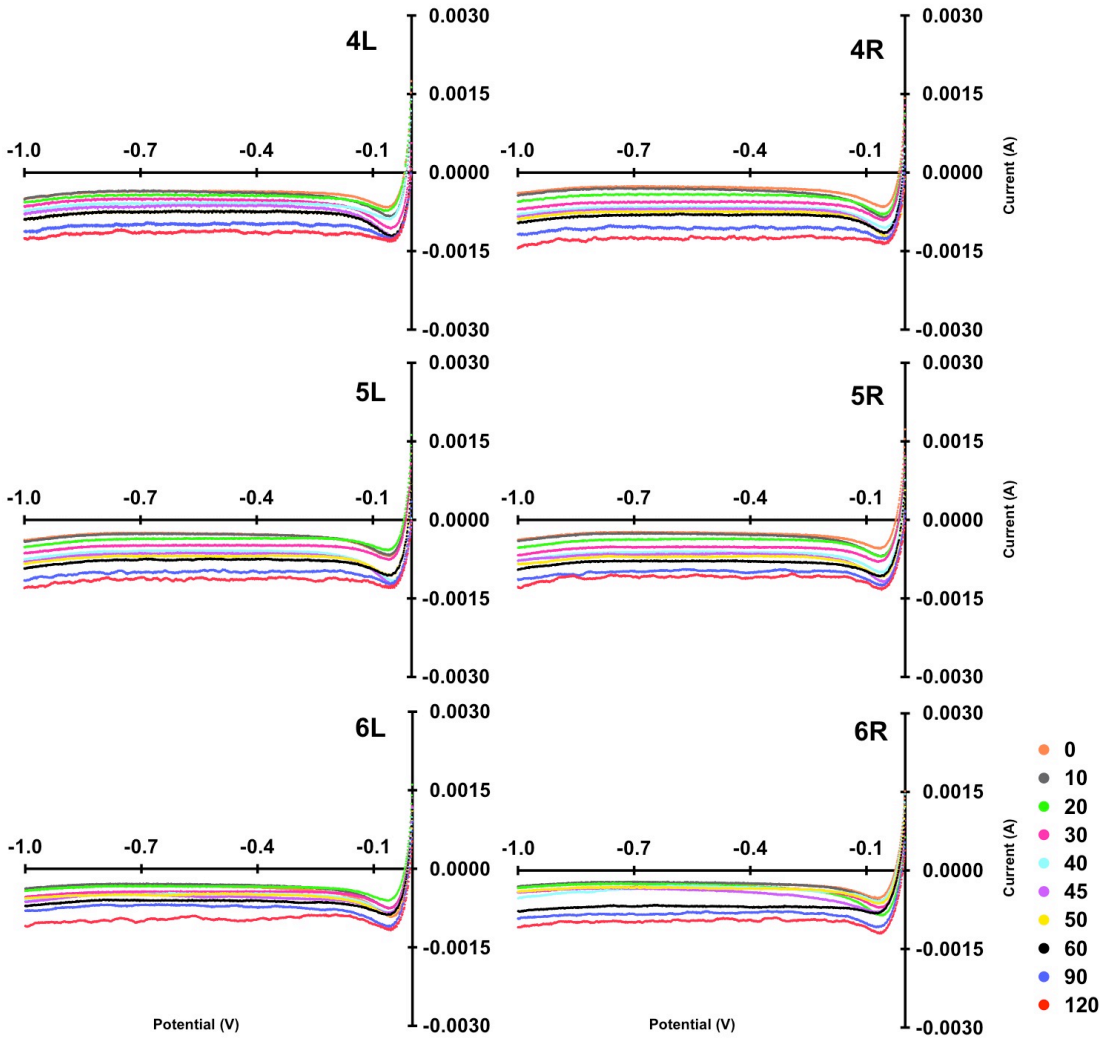

Figure IV.10 – Limiting current profiles of ferri-ferro redox couple for 30 mL of solution - Current intensity vs applied potential recorded at the 4th, 5th and 6th electrode surfaces, at left (L) and right (R) sides, with velocities of agitation from 0 to 120 rpm. Limiting current plateau considered in the range of -0.44 to -0.54 V to determine the average limiting current value. The potential applied varied from -1.0 V to 0 V, at a rate of 0.01 V/s for each scan. The dimension of the active surface of the electrodes is 0.020 × 0.014 m.

Figure IV.11 summarizes the determined parameters for both ferricyanide and lactate systems. In general the mass transport coefficient increases with the stirring rotation speed and also increases from the periphery to the centre of the device (from position 6R to 4L, with higher values at position 4 and lower values at position 6), and this difference appears to be more evident at 25 mL (Figure IV.12). The presented Re numbers are just for reference as they refer only to the velocity at the tip of the stirrer. The Re determined for lactate are lower than those for ferricyanide as this parameter (Equation IV.1) is dependent on the density and viscosity of the solute that is according to the higher viscosity and density associated to lactate. Also the estimated mass transport coefficients for lactate from the approximated relation in Equation IV.15 lead to higher mass transport coefficients and Sh (i.e. the ratio of convective to diffusive mass transport), as compared to the measured ferricyanide. Lactate is a more viscous and dense solute but also with higher diffusivity rate, and with the relation of Equation IV.15 the resulting mass transport coefficients are higher. The limiting current method was used just to derive an approximation to predict the mass transport behaviour of the lactate in solution, and not to be compared to the ferricyanide system.

The effect of the working volume on the mass transfer (and Sh), in the 30 ml case the scaffolds are completely submerged in which the fluid overtakes the height of the electrodes and is able to flow over. While, in the 25 ml case, the liquid level is slightly below the top of the electrodes, being more confined recirculating only below the electrodes; In this case a barrier is created on the circulation of the liquid, and eventually more differences may be observed in the mass transfer on the vessel regions. This can be observed from the profiles in figures IV.11 and IV.12 with more marked difference for region 6R and also with increased asymmetry in the represented values within each position in 25 mL case.

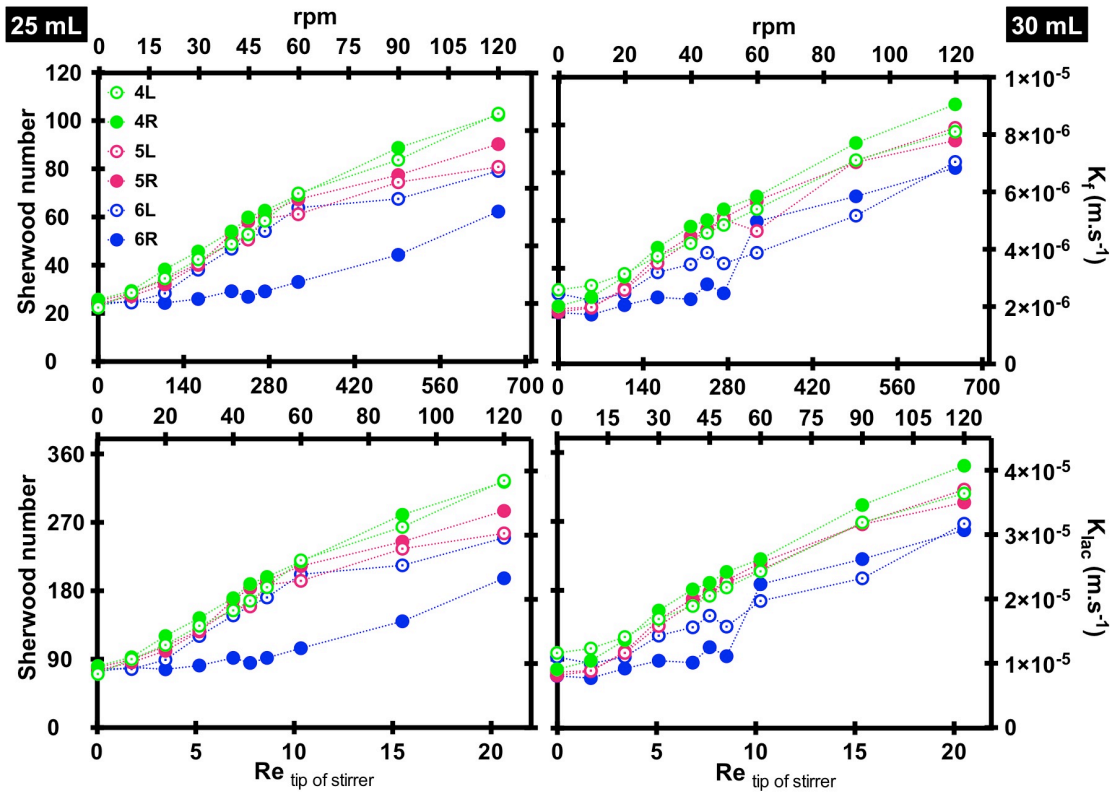

Figure IV.11 – Mass transfer coefficient and Sh variation with the velocity of mixing and position on the vessel for 25 and 30 mL of solution for ferricyanide and correlated values for lactate; the mass transfer coefficient of ferricyanide was determined from the average limiting current from each electrode surface, considering the dimensions of the active surface of 0.02 m and 0.014 m for the base and height respectively. Re values refer to the tip of the stirrer. Error bars are SD.

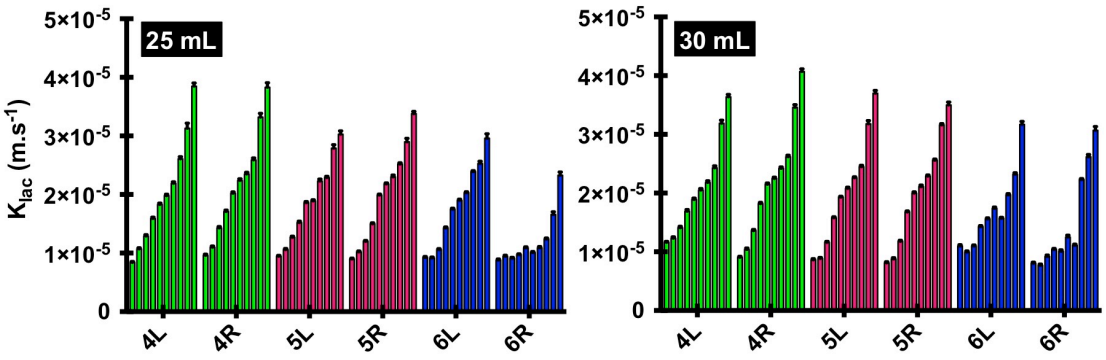

Figure IV.12 – k_{lac} profile in each position with increasing mixing velocity (from left to right in each position of the frames).

A lower mass transfer is observed at the external interface of the 6th electrode (6R), where the degree of mixing appears to be lower. On the other hand the 4th and 5th electrodes have closer values, with maximum mass transfer coefficients found at 4R side.

In the case of 30 ml on the side 6R the mass transfer increases with the agitation velocity and from rotations above 50 rpm approximating to values closer to the remaining electrodes. This is a suggestive result, indicating a uniform mixing throughout the different interface positions in the vessel.

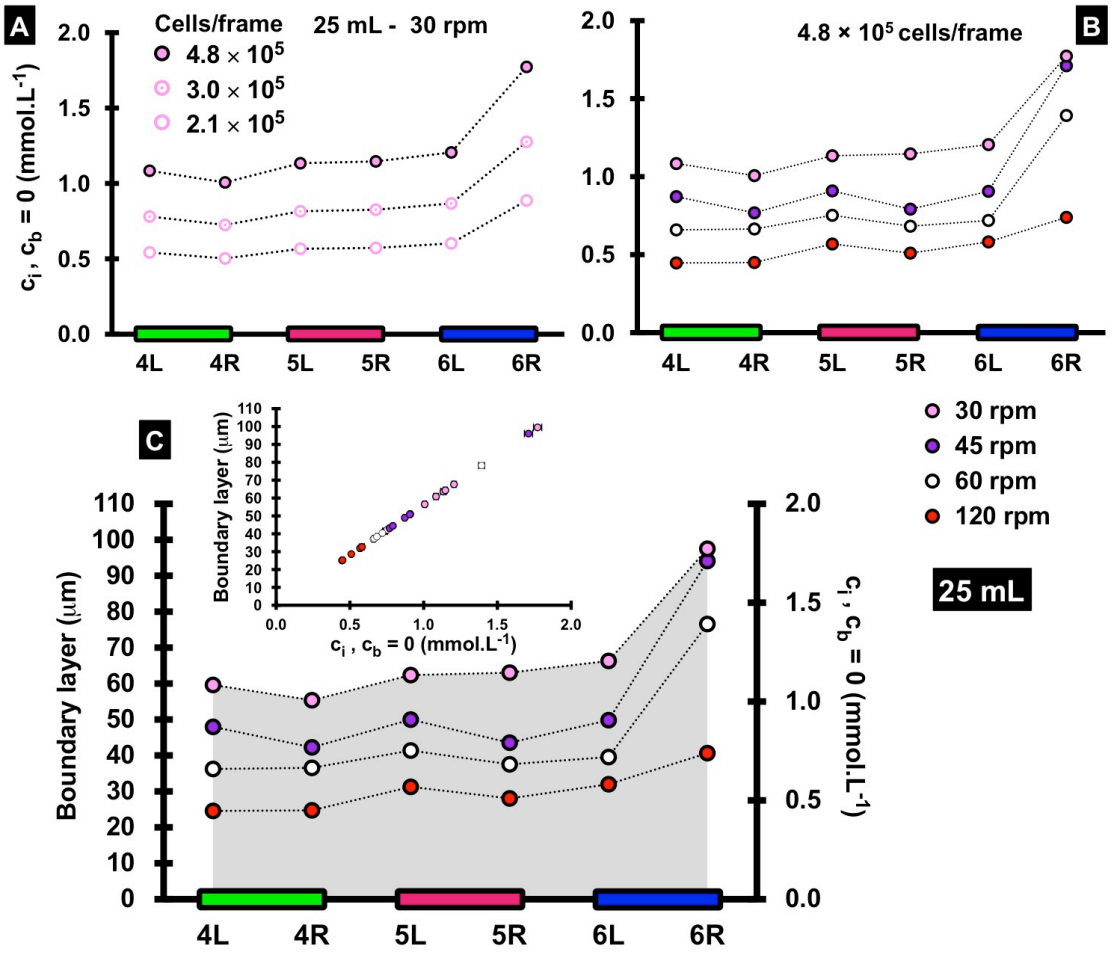

Figure IV.13 - Estimation of the minimum concentration at the interface ($c_{lac\,i}$) of lactate and boundary layer: (A) assuming 3 cell numbers per frame at each position for 30 rpm and 25 mL and (B) at a fixed cell number per frame for different mixing velocities at 25 mL, and (C) estimation of the boundary layer (diffusivity/mass transfer coefficient) according to the mixing velocity at 25 mL and position; inset graph: relation of boundary layer with $c_{lac\,i}$. Error bars are SD.

The minimum concentration of metabolite at the interface can be estimated when the bulk concentration of metabolite is zero ($c_{lac\,b} = 0$). In this situation the $c_{lac\,i}$ is just dependent on the number of cells in the frames then on the respective flux of lactate produced and on the mass transfer coefficient of the lactate, that is on the ratio between the flux and the mass transfer coefficient (Equation IV.16). In Figure IV.13 – A are represented 3 hypothetical cases for lactate concentration at the interface, assuming cell numbers per scaffold and fluxes of lactate based on cell culture experiments on the stirred device, and assuming the least efficient mixing conditions, such as low stirrer velocity of 30 rpm and 25 mL of working volume. The $c_{lac\,i}$ varies according to the mass transfer profile predicted previously, that is in the regions more centred of the vessel (4 and 5) the concentration is lower and more equivalent distributed, while closer to the periphery (region 6) the concentration increases. This is compatible with better mixing in centred regions of the vessel opposed to that on the periphery as predicted with the mass transfer coefficient profiles. The $c_{lac\,i}$ also increases with the number of cells per frame, as a consequence of the increase in the lactate production flux. Similarly, in Figure IV.13 – B, fixing a number of cells per frame, the $c_{lac\,i}$ varies with the velocity of the stirrer according to the mass transfer profile predicted, with increased mass transfer for higher stirrer rotation velocities. Again on the peripheral region (6) the mixing is less effective with a $c_{lac\,i}$ higher predicted for this region. In Figure IV.13 – C an estimate of the boundary layer at the interface of the frame and the solution is presented. The boundary layer was estimated from the relation of the diffusivity with the mass transfer coefficient, thus it is expected a similar profile to which can be associated the $c_{lac\,i}$ along the different regions on the vessel. A thinner boundary layer is expected for conditions with higher stirring velocities and consequently lower $c_{lac\,i}$ of metabolite in the boundary layer (inset graph in Figure IV.13 – C shows the proportionality between these parameters). An overall interesting theoretical prediction on the mass transfer properties of the vessel in operating conditions can be thus obtained.

The $c_{lac\,i}$ values predicted are highest for 30 rpm ranging from 0.9 – 1.8 mM and lie in the range of non-inhibitory values for cell culture taking as reference the values reported of 16 –

35 mM inhibitory for mesenchymal stem cells (Schop et al. 2009) and 14mM for a culture of NSCs in microcrriers (Rodrigues, Diogo, et al. 2011) .

The tables in Appendix (Tables IVA.2 – 5) attempt to predict the minimum value of concentration at the bulk, $c_{lac\ b}$, to which the lactate concentration at the interface can become toxic. The $c_{lac\ i}$ were determined assuming a stationary state between lactate flux production and mass transfer diffusion of lactate considering three different lactate flux production values calculated for a specific lactate production coefficient of 1.15×10^{-14} mol.m^{-1}.s^{-1} (a value estimated in chapter V and in the same range of the value 3.47×10^{-14} mol.m^{-1}.s^{-1} reported on the literature (Rodrigues, Diogo, et al. 2011), and for three scenarios concerning cell numbers per frame (208, 300, 417 thousand cells) and frame areas of 2.8 cm^2. The respective values of flux of lactate production determined are 8.61, 12.4 and 17.2 μmol.m^{-2}.s^{-1}. Note that the mass transfer coefficient of liquid films are on the range of 9.7 and 38.3 μm.s^{-1}.Therefore, recalling Equation IV.16, one can establish the value of $c_{lac\ i} - c_{lac\ b}$ as the ratio of lactate flux per liquid mass transfer coefficient, which for the cases considered lies on values below 1.77 mol.m^{-3}, posing a very low increase in lactate concentration at the interface when comparing with the one on the bulk. These results suggest that the system mixing is good enough to avoid effects of concentration polarization on cell toxicity. Note however that this is a result of a relatively low number of cells per frame.

IV.4.3 – Shear Stress and Fluid Velocity Evaluation by CFD

The CFD model of the system was built to better understand the fluid dynamic in the vessel, for both volume cases and map the overall shear stress and fluid velocity distribution profiles at the interface of the frames.

IV.4.3.1 – Shear Stress

The shear stress determined by CFD was modulated considering an incompressible flow in the system, where the density of the fluid material remains constant at each infinitesimal

volume, which circulates with a flow velocity. The wall shear stress was computed considering an area of interest of the scaffolds (effective area available for cellular adhesion) to evaluate if the designed system exceeded a threshold, in a range to influence the cell culture output.

A relation between the laminar model and the SST k-ω turbulence model (low Re turbulence model), at 25 mL, allows to verify the application of the laminar model to the system, by comparing the computed shear stress average values of both models. The laminar-oscillatory regime was considered as the model to run the different cases for each rotational velocity, taking into consideration the low rotation speed of the stirrer (low Re number). With the laminar model, the loss of energy due to turbulence is not considered, so the calculated shear stress is possibly overestimated, thus a safer approximation. Another observation (Figure IV.14) is that, in general, the same tendency of increasing shear stress with the rotation speed is observed, as well as an increase from the external to the centred locations (6th to 4th).

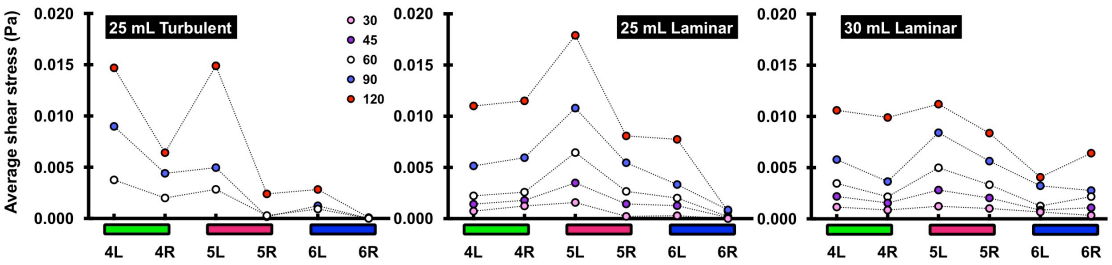

Figure IV.14 – Average shear stress profiles estimated by CFD for different rotation velocities and comparison of turbulent and laminar models.

The colorimetric maps of the distribution of the shear stress on each interface are represented in figures IV.15 and IV.16 for the 25 and 30 mL cases respectively, giving a general overview of the entire vessel. In general in the presence of 30 mL working volume the shear forces acting on the system seem better distributed, with larger and more areas among all the surfaces toned with light blue/green, meaning a more homogeneous distribution and lower shear forces, as a result of the effect of the better recirculation due to agitation. Even in the extreme right position (interface 6R) there is an increase in the shear forces, indicating increased fluid motion present in the extreme region. The tendency of increasing shear

distribution from the external region to the centre is verified, with some points of higher shear stress (red areas), specially at the interface at position 4 facing right (4R), with higher values in the order of 1.47×10^{-1} Pa at 120 rpm. Also higher minimum values are observed, indicating less stagnant regions. Interestingly (Wang et al. 2013) reported local maximum shear stress of 0.152 Pa for 75 rpm of mixing velocity for convective flow fluid in a spinner flask for adherent and suspension culture of human induced pluripotent stem cells, very similar to our case.

In the 25 mL case, also, the same overall tendency on the shear forces distribution is observed. The colour patterns show more contrasts between dark blue and red zones for the shear stress distribution. In fact higher zones of higher shear stress on the centred regions of the vessel (interfaces 4L and 4R) are observed, indicating that the liquid movement is more effective in that region, in contrast with very low forces acting when gradually moving to the periphery of the vessel (more dark blue regions observed). The higher maximum values of shear stress are in the order of 2.48×10^{-1} Pa at 120 rpm. Overall these maps of acting shear forces distribution are in agreement with the evaluation of the mass transfer done previously, where in 30 mL working case, increased mass transport is verified and as a result of an increased effect of the movement of the agitated liquid, as demonstrated by the shear forces distribution. Individually at each position it is possible to visualize in detail the shear-stress distribution in each interface, figures IV.17 and IV.18, taking for example two distinct rotational velocities, 45 and 120 rpm, respectively. In each interface there is a diverse distribution of acting shear forces, possible to distinguish the maximum and minimum by adjusting the scale to each interface observed. In general the difference between the shear forces distribution, between 25 an 30 mL, is more noticeable at 45 rpm, while at higher velocity, as 120 rpm the differences seem to decrease. The higher values observed are for the 45 rpm 25 mL case in the order of 5.06×10^{-2} Pa in the more centred interface facing the right side (4R), and in the order of 2.48×10^{-1} Pa for 120 rpm 25 mL case for the interface facing the centre (4L). Overall adding 5 mL of volume to the operating device improves mixing uniformity and homogeneity in the shear stress distribution.

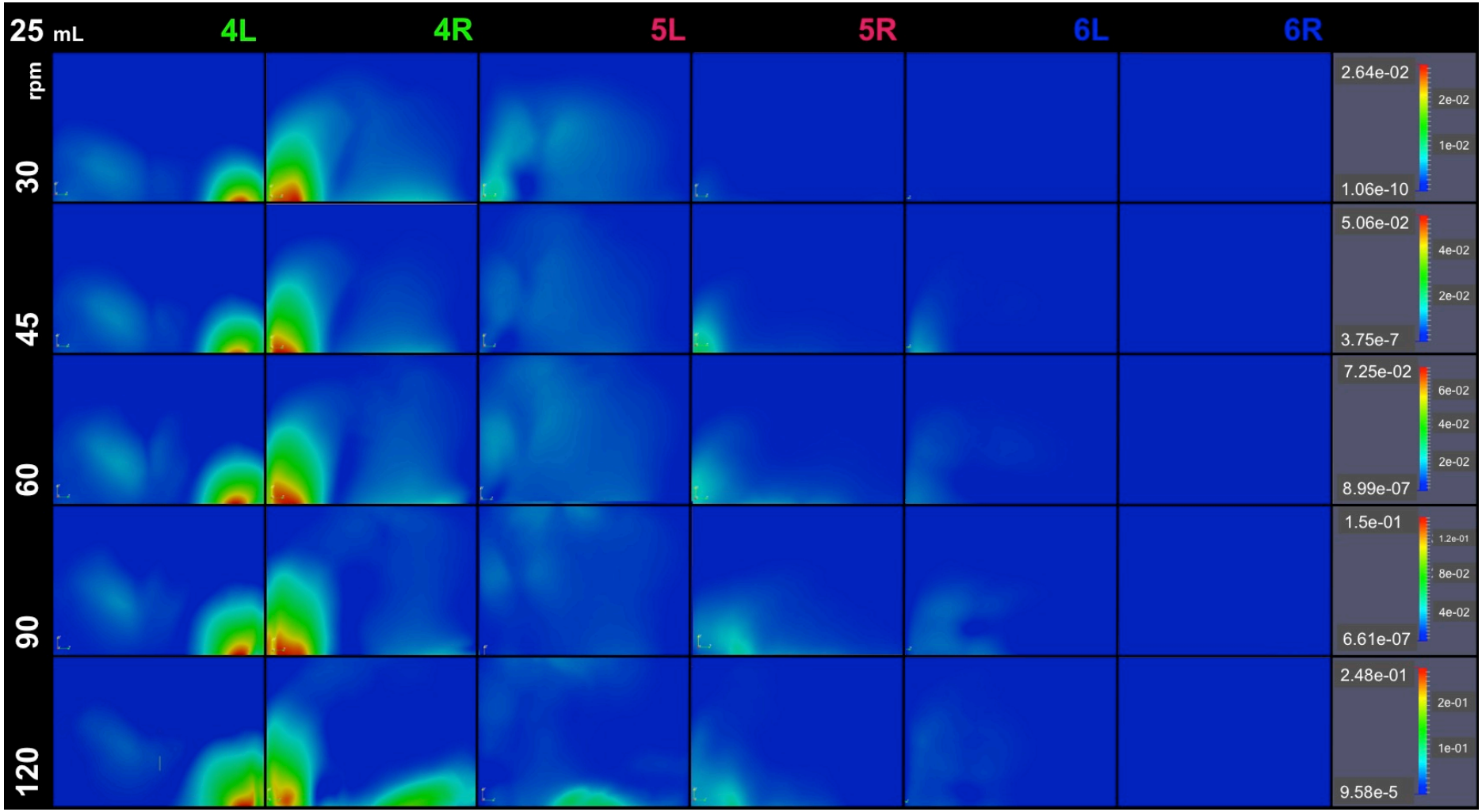

Figure IV.15 – Map of wall shear stress distribution for the 25 mL case. Scale in Pa.

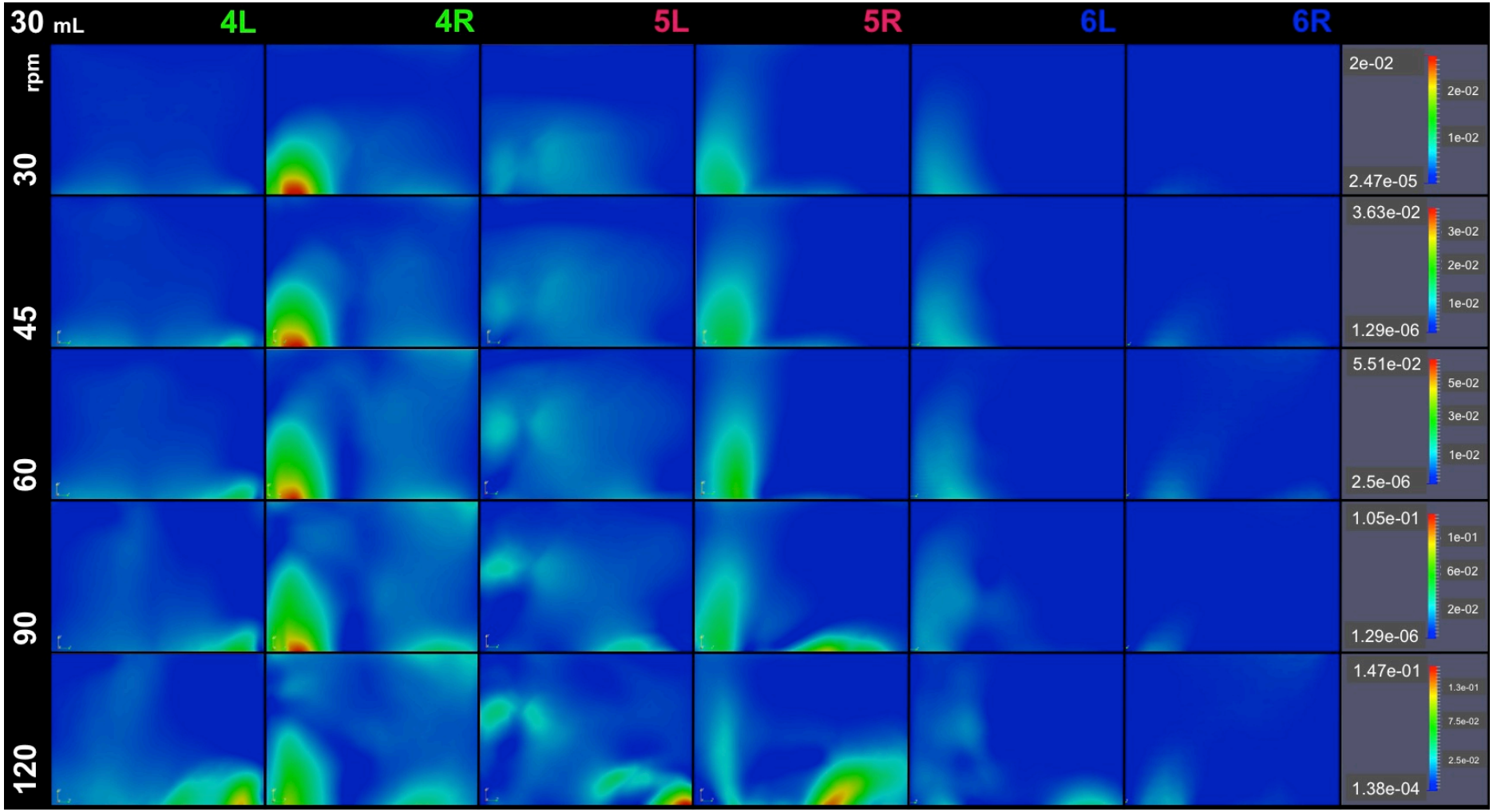

Figure IV.16 – Map of wall shear stress distribution for the 30 mL case. Scale in Pa.

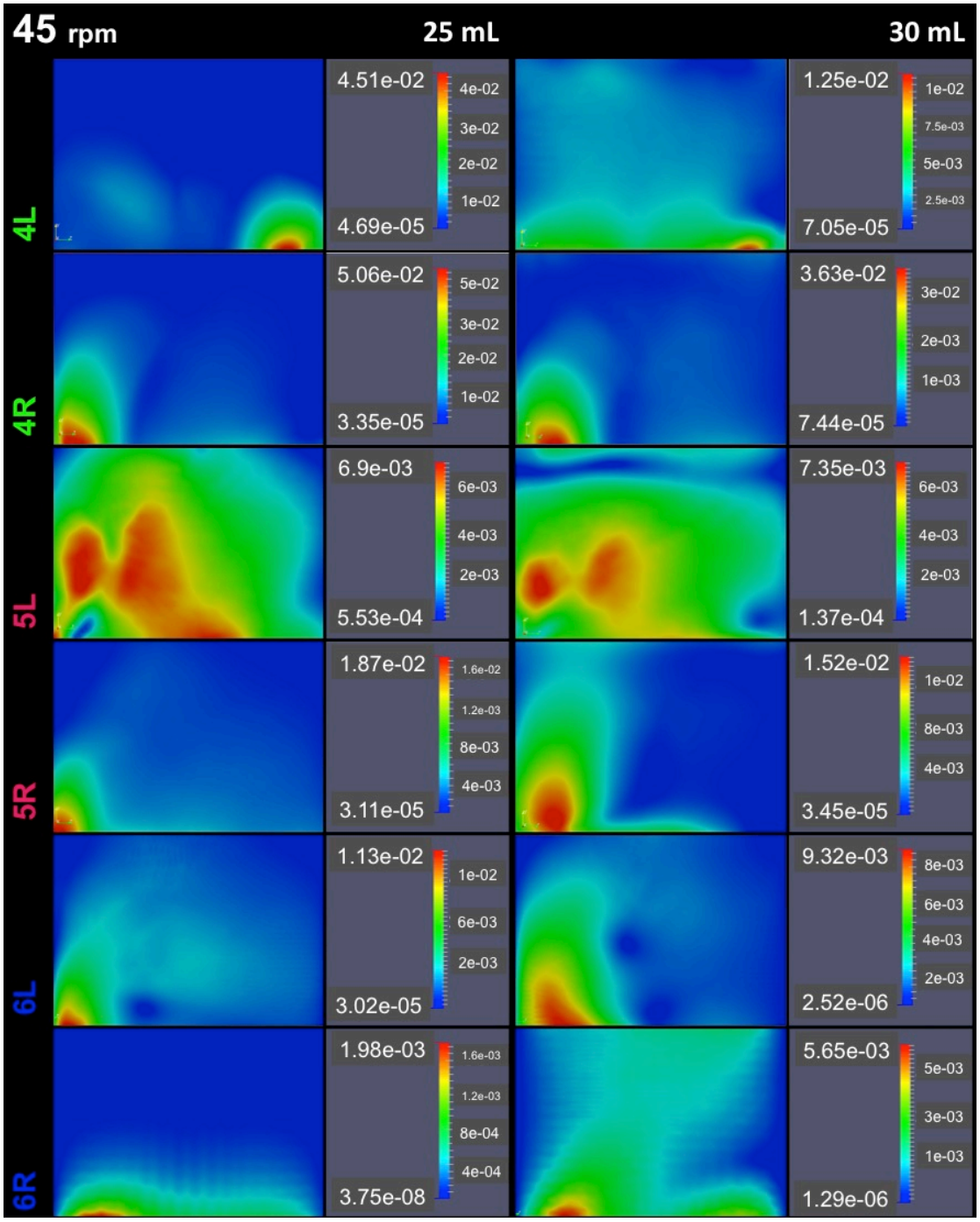

Figure IV.17 – Detail on the shear stress distribution on each interface at 45 rpm agitation velocity for 25 and 30 mL cases. Scale in Pa.

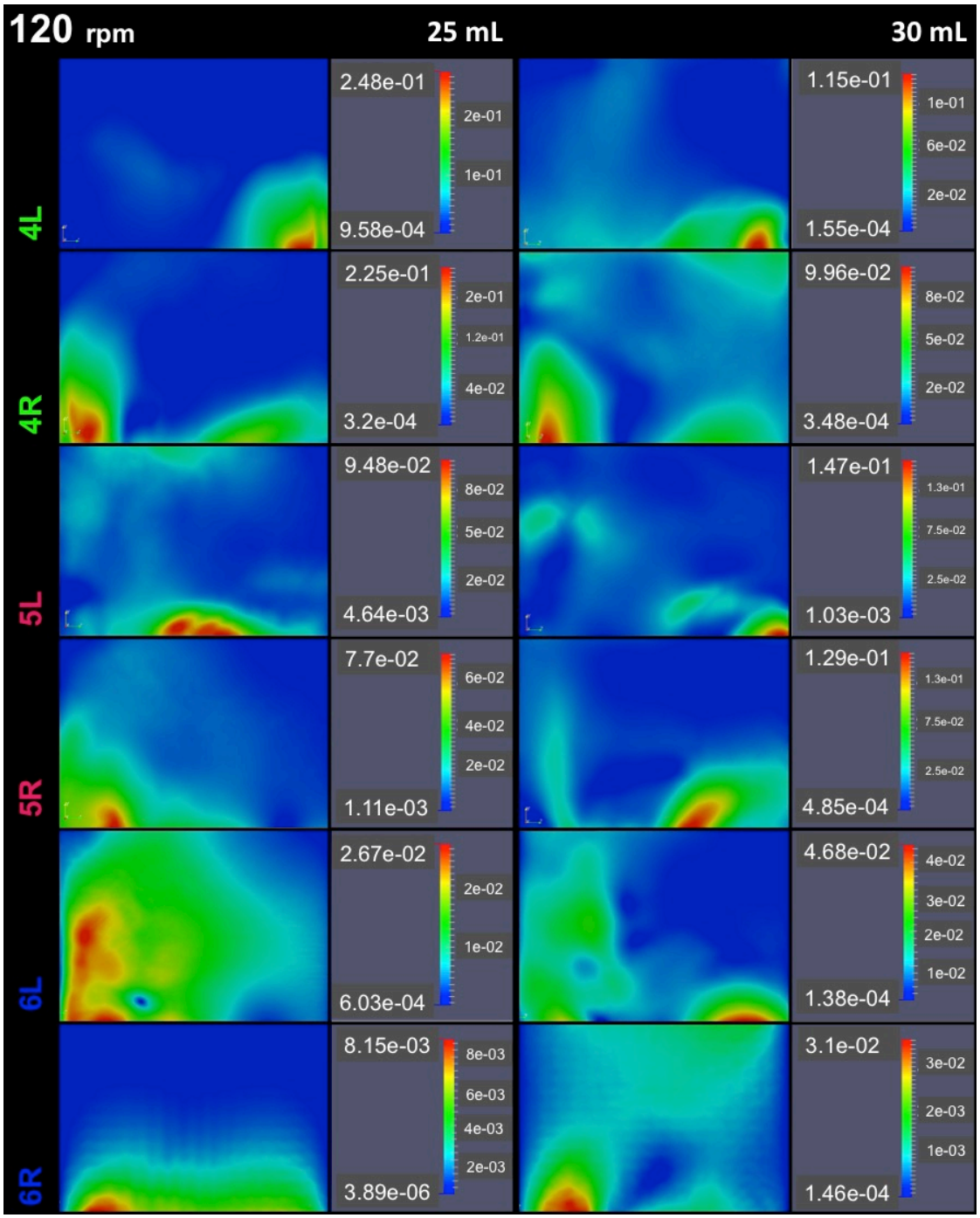

Figure IV.18 – Detail on the shear stress distribution on each interface at 120 rpm agitation velocity for 25 and 30 mL cases. Scale in Pa.

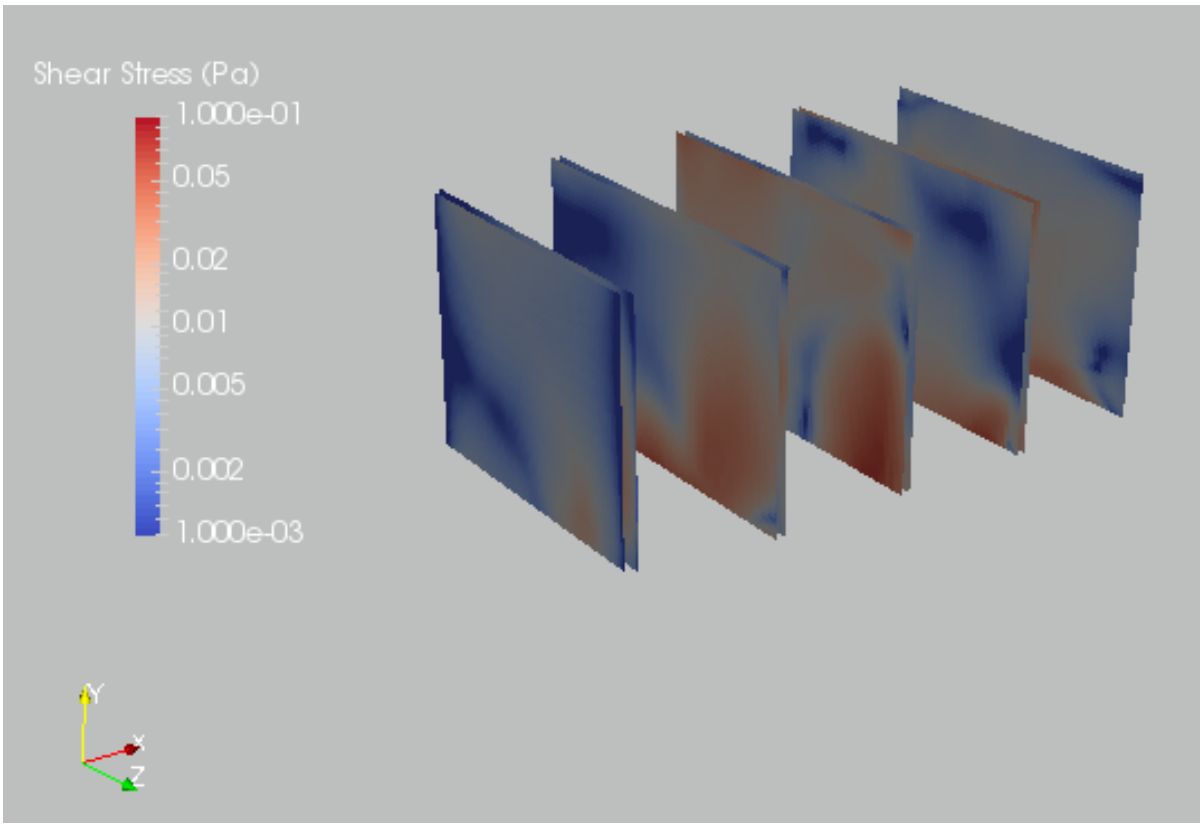

Figure IV.19 – General instantaneous distribution of shear stress (30 mL 90 rpm). Scale 0.001 – 0.1 Pa.

Considering another case of high speed rotation of 90 rpm, the superior shear stress limits predicted fall in 0.1 Pa, and the superior limits predicted for each wall individually are around 10 times higher than the average and these maximum are located on the lower zone of the wall near the stirrer. Figure IV.19 shows the instant distribution of the wall shear stress on the entire device. Since the flow oscillates, due to the rotation of the stirrer, the regions of high shear stress change from one side to the other, which is why the area with elevated shear stress extends itself along the wall. With that it can be predicted that for higher rotation velocities there are true effects of elevated shear stress in the device.

Looking at the shear stress values, as verified in the distribution maps, it increases with the rotation speed, as well as an increase from the external to the centred locations (6^{th} to 4^{th}), as verified in the average values in figures IV.14 – A, for both 25 and 30 mL laminar cases and turbulent case at 25 mL for the velocities of 60, 90 and 120 rpm.

The cell culture response to the hydrodynamic environment will depend on the cell system and on the specific culture conditions that together influence the general cell culture as mentioned in the

introduction. So, it would be safe to consider an interval of shear stress that is able to maintain a steady favorable cell culture output, without triggering important cellular alterations.

An interesting example is the increase in the proliferation of radial glia cells when exposed to laminar shear stress of 0.01 dyn/cm2 (0.001 Pa) and knowing that the physiological ventricular shear stress of the cerebrospinal fluid is in the range of 0.01 – 0.018 dyn/cm^2 (0.001 – 0.0018 Pa) (Guirao et al. 2010; Park et al. 2017). So, these values can be a first reference for safe shear stress culture conditions, and values above these ranges should be carefully monitored. With this, the conditions at 45 and 30 rpm are found closer within this range, while for 60 rpm the values are mostly above and for 90 and 120 rpm the values clearly exceed the considered reference (Table IV.4). A first prediction for favorable culture conditions can lie in the range of 30 to 60 rpm at 30 mL volume.

Table IV.4 – Average shear stress (Pa) estimated by CFD at each wall surface for different rotation velocities.

rpm	**30**		**45**		**60**		**90**		**120**	
mL	***25***	***30***	***25***	***30***	***25***	***30***	***25***	***30***	***25***	***30***
	× 10^{-4}		× 10^{-3}		× 10^{-3}		× 10^{-3}		× 10^{-3}	
4L	7.29	11.5	1.42	2.19	2.23	3.46	5.15	5.79	11.0	10.6
4R	12.4	8.63	1.79	1.55	2.59	2.16	5.95	3.64	11.5	9.90
5L	15.8	12.3	3.49	2.81	6.45	4.99	10.8	8.41	17.9	11.2
5R	2.19	10.1	1.44	2.04	2.66	3.33	5.46	5.64	8.08	8.37
6L	2.83	6.74	1.27	0.86	2.01	1.26	3.33	3.23	7.74	4.07
6R	0.09	3.35	0.11	1.09	0.20	2.17	0.85	2.77	0.72	6.41

IV.4.3.2 – Fluid Velocity Profile

Looking at the map of the fluid velocity of the designed vessel, it is possible to confirm the attributes of this system regarding the hydrodynamic performance with respect to the 25 and 30 mL working volumes and applied rotation velocities at the interface of the working frames.

In Figure IV.20 are represented the velocity magnitude distribution profiles over the entire vessel, for 25 ml and 30 ml cases. In general the fluid velocity increases with higher rotation speed, and near the magnetic stirrer the velocity is notably higher, as would be predictable. Over the entire vessel the velocity of the liquid seems more distributed in the case of 30 mL, where the dissipation of the fluid velocity is improved. In this case near the stirrer the velocity is shown as less intense green compared to the 25 mL case.

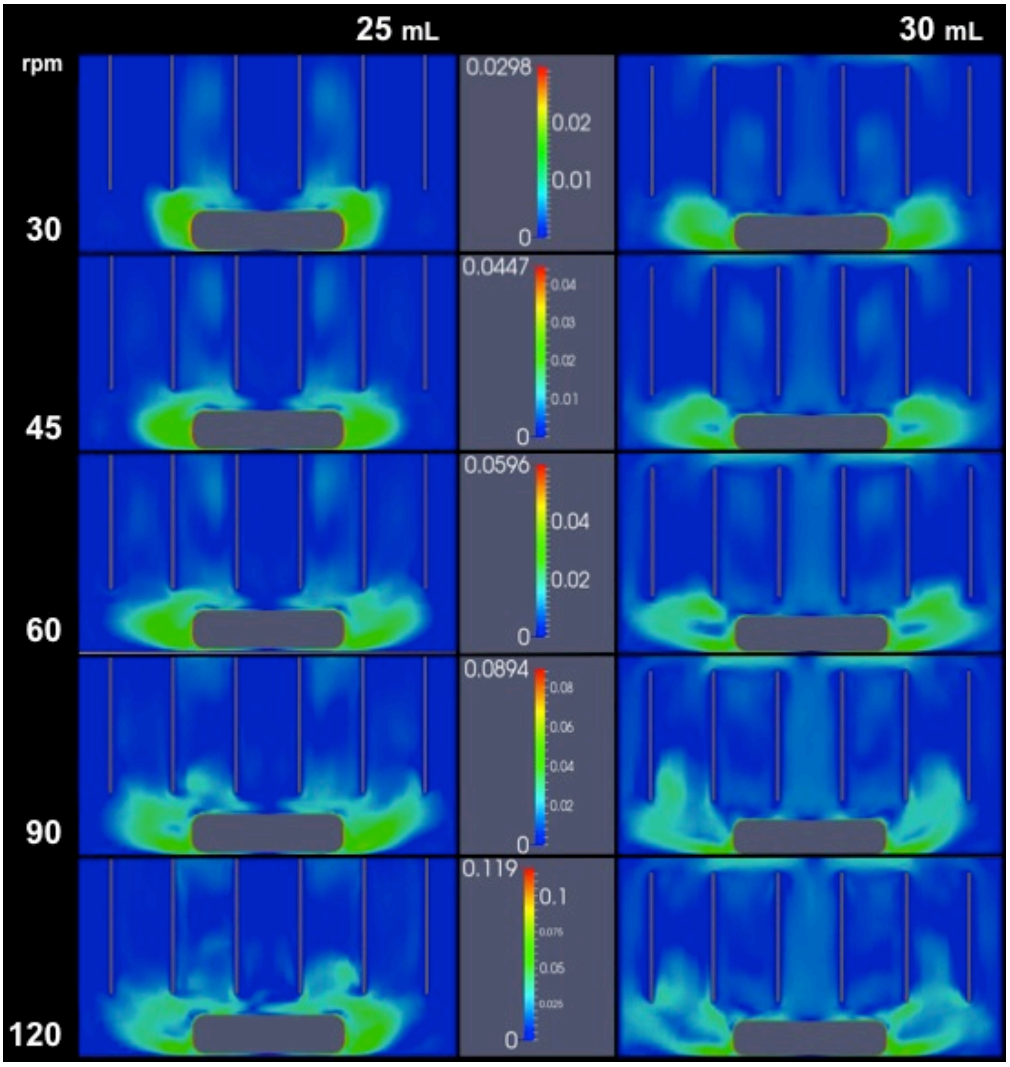

Figure IV.20 – Fluid velocity distribution on the entire vessel. Scale in ms^{-1}.

The ability of the volume of liquid to flow over the top of the frames from the inner borders of the vessel and recirculate from the centre, creates an additional flow recirculation on both extremes, improving mixing on those locations and allowing a faster liquid velocity dispersion. This effect is stronger at higher rotation speed of 120 rpm. There is a very clear barrier effect, limiting the liquid motion, caused by the frames when the liquid is only up to 25 mL.

Detailed in Figure IV.21, looking at half of the vessel at the 4th, 5th and 6th positions, interestingly the fluid velocity vectors show clearly the liquid circulation over the frames, in the 30 mL case, and the global liquid movement direction throughout the frames. Again, with a liquid volume exceeding the frames top, the fluid recirculation is such, providing a better and more homogeneous liquid flow. To

notice in the case of 25 mL the regions more external, to the right of the 6th frame, and centred, to the left of the 4th frame, appear with rather low fluid circulation.

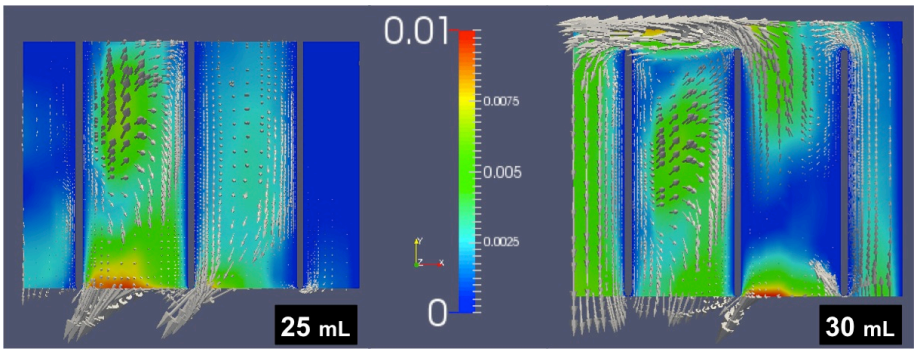

Figure IV.21 – Detail of the fluid instant velocity distribution on the 4th, 5th and 6th positions for the 25 and 30 mL cases at 90 rpm. Y-section of the right side of the vessel. Scale in ms^{-1}.

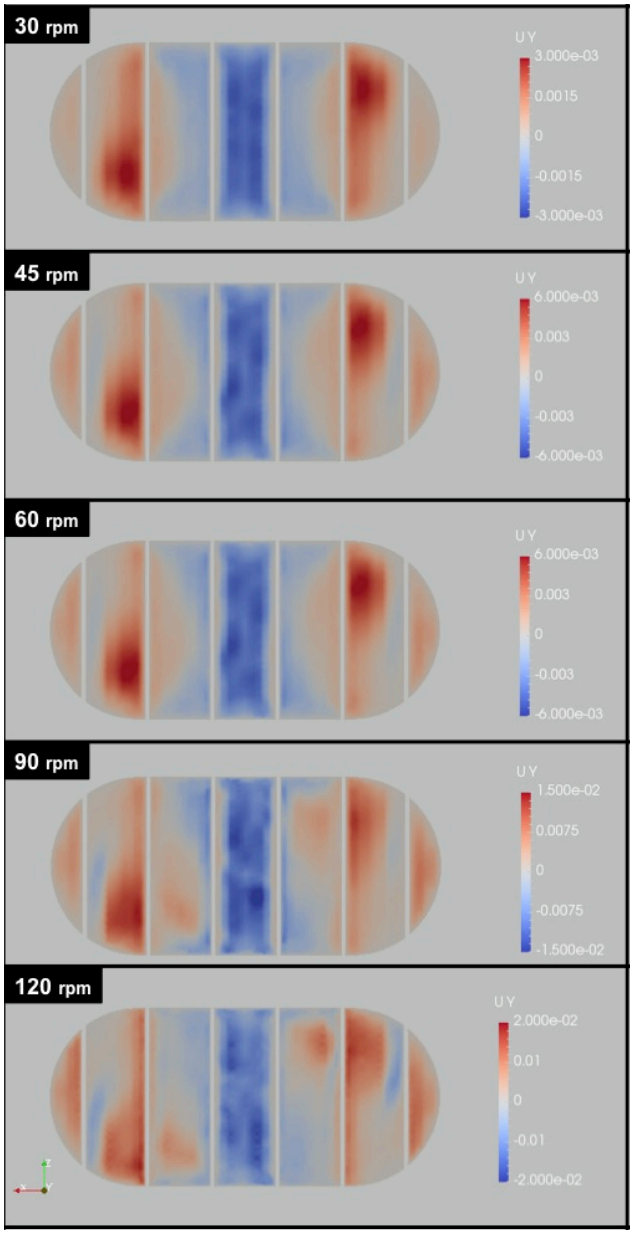

Figure IV.22 – Instant velocities (vectors) of ascending (blue) and descending (red) fluid flow for the 30 mL case. Z-section view from the top of the vessel. Scale in ms^{-1}.

In Figure IV.22 are represented the maps of the vertical component of the fluid velocity in a transversal plane of the top of the electrodes. The colour maps show that there is suction of the fluid (blue) in the central zone and emerging fluid (red) in the lateral zones. There is better fluid circulation on the device with 30 mL of volume, where the fluid is pulled by the stirrer in the central zone and pumped upwards across the lateral channels. Again is verified that with the increase of the rotation velocity there is an increase in the fluid circulation.

Therefore, it can be determined that for the 30 ml case study, increasing the rotational speed results on a higher uniformity of the liquid distribution along the vessel, which is improved compared to the 25 ml case, regarding the uniformity and the homogeneity of the nutrients and metabolites distribution and physical stimulus.

IV.5 - Conclusions

Envisaging a scalable system to cultivate neural stem cells in a set of individual nanofiber scaffolds a stirred vessel was projected. The vessel design was based on the following guidelines: simplicity, easy to build, cost effective prototype construction, easy manipulation and control (frame accommodation plate and frame based model), symmetry, small sized prototype (cost-effective cell culture experiments at the laboratory scale). A simple model suitable to be further developed in a more complex and robust system, satisfying a definitive purpose of cultivating stem cells efficiently and cost-effectively producing single nanofiber based scaffolds to serve as tissues constructs for implantation or as research model platforms/templates. The system is not exclusive for neural stem cell type, but useful as a versatile prototype for a varied of applications with different scientific approaches, biological, chemical, biochemical, research applications (immobilized molecules/peptides/enzymes, animal cells, stem cells).

The vessel physical characteristics include, full body material in Teflon, allowing easy sterilization by autoclave, durable and inert material at the working conditions (sterilization and cell culture experiments); one drilled piece for simply manipulation, easy to clean and sterilization; symmetric elliptical shape able to accommodate 6 frames of scaffolds and a magnetic stirrer in the bottom to provide agitation – a single compact vessel without requiring extra support pieces.

The hydrodynamic attributes of the designed prototype were evaluated experimentally, by the electrochemical technique based on the limiting current measurements, mixing time and by theoretical simulation by CFD. It was determined that by an increase of 5 ml in the working volume in the stirred vessel, up to a total of 30 ml, the fluid dynamic in the vessel changes consistently, the frames are completely submerged, the fluid recirculates more extensively, improving the mixing effectiveness of the system. With this small change, the mass transport is improved for the critic positions more external; the CFD simulation confirm this homogenization in terms of stimulus and from the fluid dynamic studies is also possible to understand the importance of having the scaffold frames completely covered with fluid media.

While the CFD analysis was used to estimate the shear stress and the instant velocities, the limiting current technique was applied to measure the liquid mass transfer coefficient. The later it is an adequate method to provide an average mass transfer resistance in stationary state due to bi-dimensional stagnant liquid films formed at the frames interface. However, the measurement of the wall shear stress based on the limiting current technique would be inadequate for our case. Previous studies, applied a model (Biomechanical Systems 2000 Dec 26) that assumes that the mass boundary layer is very thin and is contained in the laminar boundary layer of movement of the fluid. So, for such case the velocity gradient inside the concentration boundary layer need to be uniform. This model considers that the mechanism of mass transfer relies in the shear stress effect on the boundary layer; that is, the higher the shear stress is, the thinnest the mass boundary layer is, and a relation is established between the two. In our case there are instabilities and the fluid moves and mixes more chaotically. The limiting current method considers that the velocities field is bi-dimensional and stationary and so using such values, as input for the model, will overestimate shear stress. Actually, the shear stress is in fact low and the mass transfer coefficient is high due to the oscillation of the velocity field by the wall. This can be clearly observed in the simulation where the oscillating velocity generates an atypical increase in the mass transfer. With this, it is more adequate and accurate to estimate the shear stress values by CFD, since it accounts for the actual instability and tri-dimensionality of the velocities field, which yield, in our case study, a relatively low shear stress.

The reactor design suggested is able to provide good mixing once operated with the volume that overflows the frame top at 45 rpm. For this operation mode we forecast average shear stresses below 2.8 mPa with Sh on the range of 103 – 186 which implies a fairly good mixing at relatively low shear stresses, as also illustrated by our analysis concerning low lactate accumulation in the boundary layer and the values of shear stress below others reported in the introduction as thresholds for limiting animal cell culture. Unfortunately further comparison with other reports is difficult, as most studies on cultivation of NSC supported in scaffolds under dynamic conditions do not report fluid dynamic conditions.

In the following chapter the cell culture of a human model of NSC will be addressed, performed under the dynamic conditions predicted.

Appendix

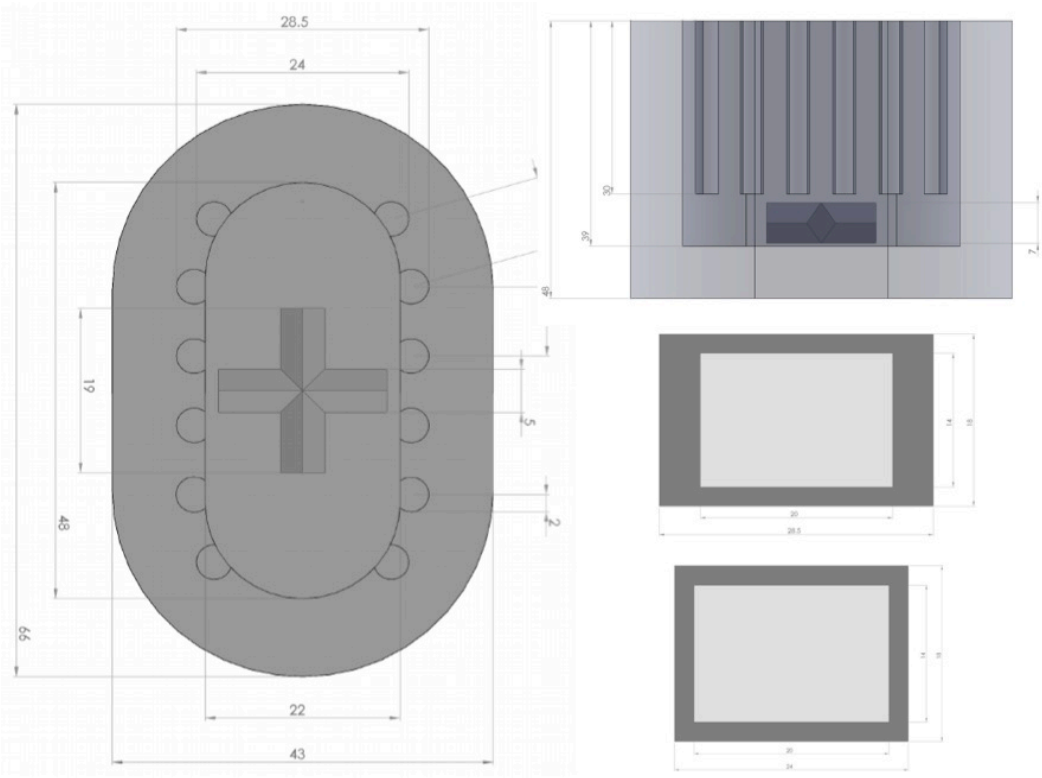

Figure IVA.1 –Model of the vessel and respective frames of scaffolds. Measure units in millimetres.

- **Testing the electrochemical system**

A preliminary experiment was performed to confirm that the fixed electrodes yield results with sensibility enough to determine the mass transfer coefficient of the electrochemical system. Four electrodes with 2.85 × 3.5 cm (base × height) and two narrower, with 2.4 × 3.5 cm to fit the first and the sixth positions, were used with 25 ml of solution (Figure IVA.2).

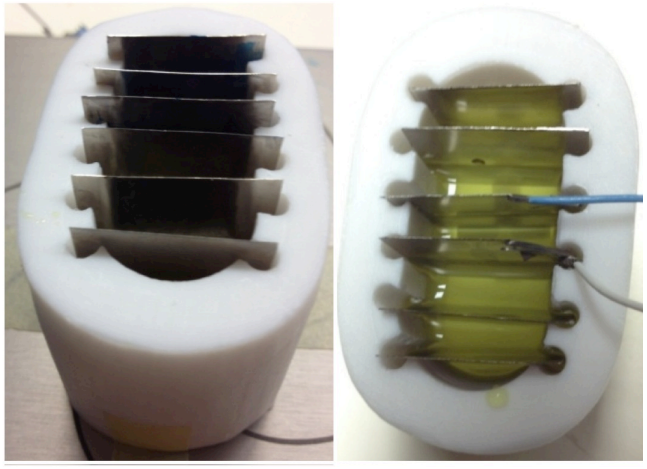

Figure IVA.2 – Experimental setting for a preliminary evaluation of the electrochemical system; one working electrode and one regenerating electrode were used.

The scanning potential applied was set from -1.3 V to 0 V, at a rate of 0.01 V/s for each scan. Different velocities were tested: 0, 10, 20, 30, 40, 45, 50, 60, 90 and 120 rotations per minute. The height of the liquid volume reaches up to 0.0175 m at the electrode surface.

A well-defined limiting current plateau is obtained, defined, approximately, in the range of -1.0 to -0.4 V (Figure IVA.3) for all the surfaces of the electrodes, in all agitation conditions tested.

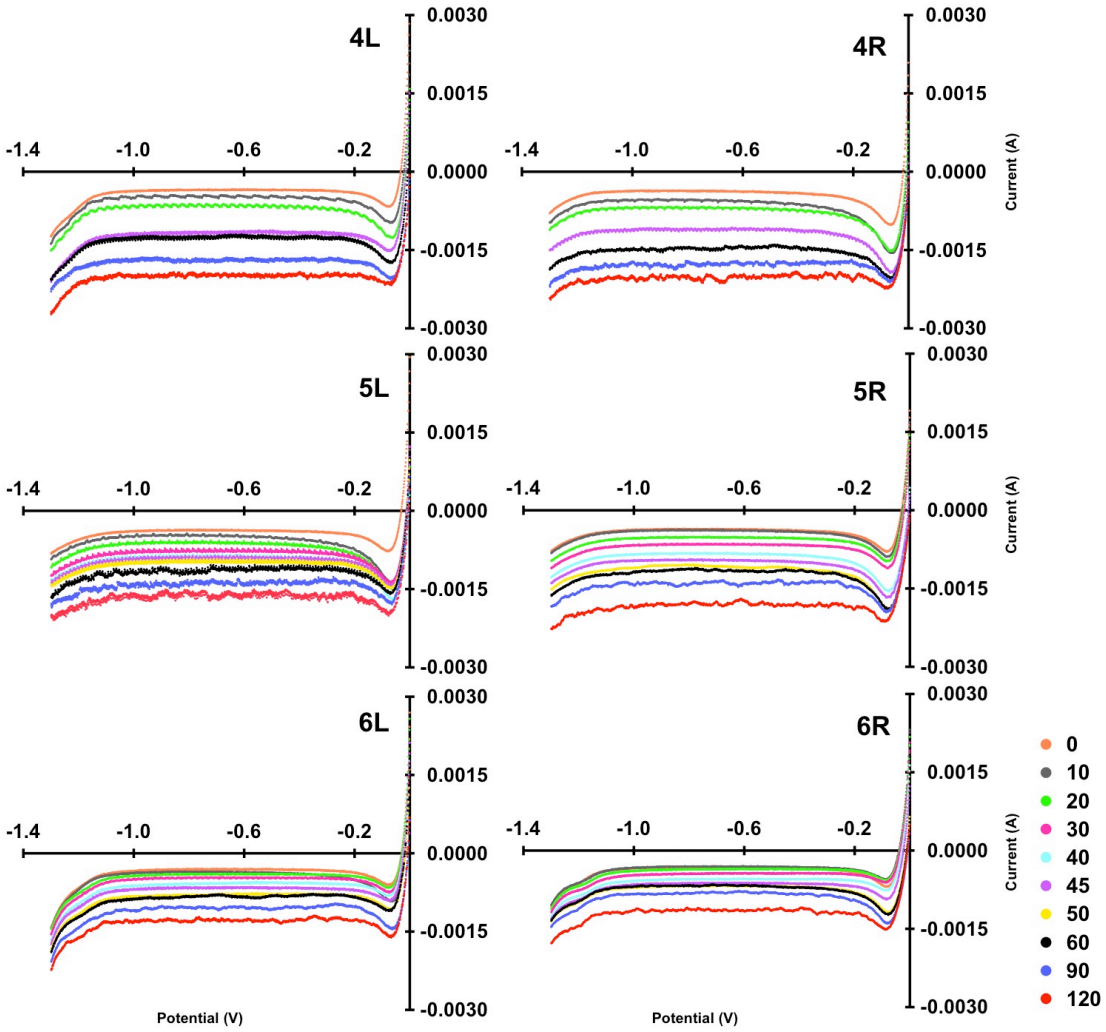

Figure IVA.3 – Limiting current preliminary experiment - Current intensity vs potential recorded at the 4th, 5th and 6th electrode surfaces for left (L) and right (R) active sides, with 25 mL of solution. A limiting current plateau can be taken, in the range of -1.0 to -0.4 V, approximately. Active surfaces of the electrodes with 0.0285 × 0.0175 m for positions 4 and 5 and 0.024 × 0.0175 m for position 6.

- **Validation of the mesh model**

Mesh validation was performed at 45 rpm for the 25 mL using a more refined 80 × 53 × 35 block mesh (*blockMesh* dictionary) resulting a mesh of 1.500.735 cells (*snappyHexMesh)*. The utility *MapFields* was used to map the results of the normal case at 4 seconds into the refined mesh and then the case was run further for 4 seconds. Comparing the results allows assessing if the mesh density refinement affects the reliability of the convergence of the model.

The refined computational domain with 1.500.735 cells corresponds approximately to the double of the 25 ml case study used with 844.698 cells. Figure IVA.4 illustrates the difference in refinement of the defined models. The absolute shear stress values determined with the refined model (Table IVA.1) show some error (value of the applied model/absolute difference between models x 100) relative to the applied case study model, however in general the refined values are lower to those determined for the 45 rpm 25 mL model except for the 4R and 6R positions. The map distribution of the shear stress in theses positions shows slight differences (Figure IVA.5) but considering that the table values correspond to average values, so no apparent significant difference is considered and the overall distribution follows the same profile applying the two mesh models. Moreover the applied model case generated slightly overestimated working values providing a safer approach for the vessel characterization.

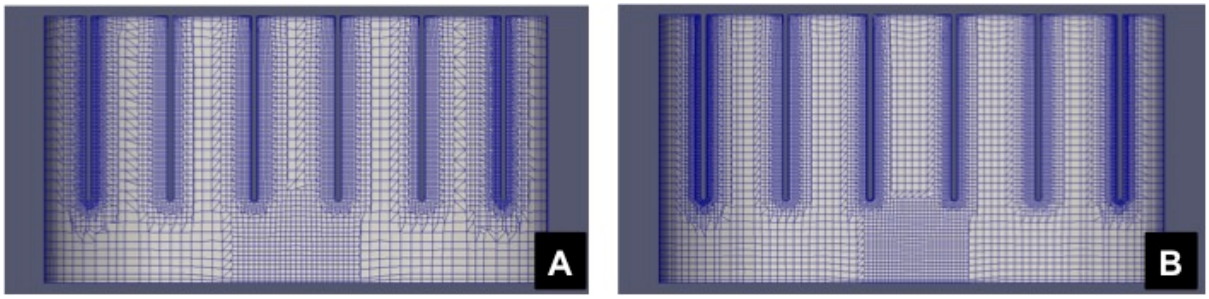

Figure IVA.4 – 45 rpm 25 mL case study mesh (A) and same case with increased mesh refinement (B).

Table IVA.1 – Average wall shear stress for the 45 rpm 25 mL laminar model with increased refined mesh and difference relative to the applied mesh case study mesh.

Position	Shear stress (Pa) $\times 10^{-3}$	Shear stress (Pa) Refined $\times 10^{-3}$	Absolute difference $\times 10^{-3}$	Error %
4L	1.42	↓ 1.33	0.09	6
4R	1.79	1.82 ↑	0.03	1
5L	3.49	↓ 1.84	1.65	47
5R	1.44	↓ 1.03	0.41	28
6L	1.27	↓ 0.91	0.36	28
6R	0.11	0.16 ↑	0.06	53

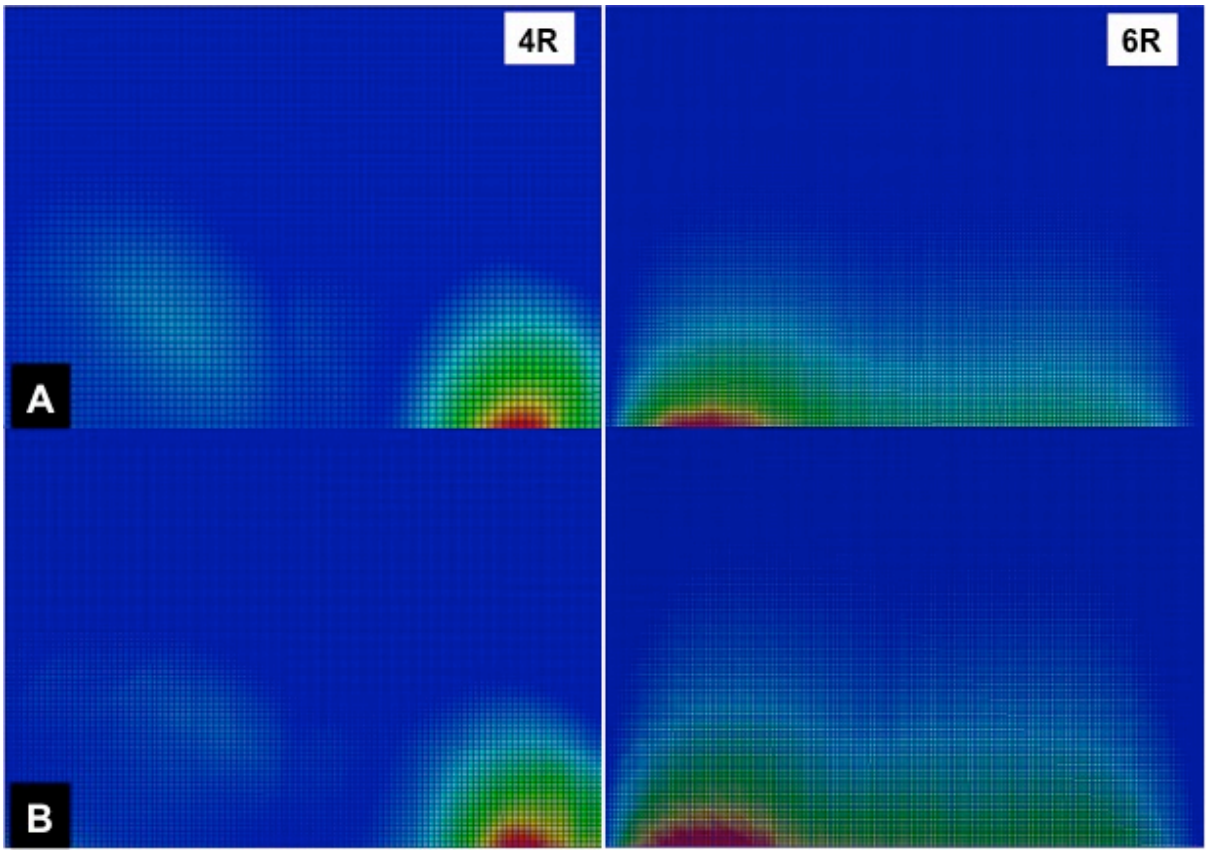

Figure IVA.5 – Shear stress distribution in 4R and 6R positions for 45 rpm 25 mL for the applied mesh model (A) and refined mesh model (B).

Table IVA.2 – 30 rpm 25 mL case: estimation of the concentration at the interface for three different cell numbers with respective lactate flux production for different bulk concentrations, to determine the limit of $C_{lac\,b}$ below toxic values, SD is lower than 3%. Estimated specific lactate production coefficient: 1.15 ×10^{-14} mol.m^{-1}.s^{-1}.

Total cells ×10^6	Cells / frame ×10^5	Flux ×10^{-5} mol/m^2.s	C_b mol.m^3	10	%	4	%	2	%	1	%	0.5	%	0.2	%	0.05	% ×10^3	0.025	% ×10^3	1.0 ×10^{-6}	% ×10^7	0
1.25	2.08	0.86	4L	10.5	5.4	4.5	13.5	2.5	27.1	1.5	54.2	1.0	108.4	0.7	271.0	0.6	1.1	0.6	2.	0.5	5.4	**0.5**
			4R	10.5	5.0	4.5	12.6	2.5	25.2	1.5	50.3	1.0	100.7	0.7	251.7	0.6	1.0	0.5	2.0	0.5	5.0	**0.5**
			5L	10.6	5.7	4.6	14.2	2.6	28.3	1.6	56.7	1.1	113.3	0.8	283.3	0.6	1.1	0.6	2.3	0.6	5.7	**0.6**
			5R	10.6	5.7	4.6	14.3	2.6	28.7	1.6	57.3	1.1	114.7	0.8	286.6	0.6	1.1	0.6	2.3	0.6	5.7	**0.6**
			6L	10.6	6.0	4.6	15.1	2.6	30.2	1.6	60.3	1.1	120.6	0.8	301.5	0.7	1.2	0.6	2.4	0.6	6.0	**0.6**
			6R	10.9	8.9	4.9	22.2	1.9	44.3	1.9	88.7	1.4	177.3	1.1	443.3	0.9	1.8	0.9	3.5	0.9	8.9	**0.9**
1.80	3.00	1.24	4L	10.8	7.8	4.8	19.5	2.8	39.0	1.8	78.0	1.3	156.1	1.0	390.2	0.8	1.6	0.8	3.1	0.8	7.8	**0.8**
			4R	10.7	7.2	4.7	18.1	2.7	36.2	1.7	72.5	1.2	145.0	0.9	362.4	0.8	1.4	0.7	2.9	0.7	7.2	**0.7**
			5L	10.8	8.2	4.8	20.4	2.8	40.8	1.8	81.6	1.3	163.2	1.0	408.0	0.9	1.6	0.8	3.3	0.8	8.2	**0.8**
			5R	10.8	8.3	4.8	20.6	2.8	41.3	1.8	82.6	1.3	165.1	1.0	412.8	0.9	1.7	0.9	3.3	0.8	8.3	**0.8**
			6L	10.9	8.7	4.9	21.7	2.9	43.4	1.9	86.8	1.4	173.7	1.1	434.2	0.9	1.7	0.9	3.5	0.9	8.7	**0.9**
			6R	11.3	12.8	5.3	31.9	3.3	63.8	2.3	127.7	1.8	255.3	1.5	638.3	1.3	2.6	1.3	5.1	1.3	13	**1.3**
2.5	4.17	1.72	4L	11.1	10.8	5.1	27.1	3.1	54.2	2.1	108.4	1.6	216.8	1.3	541.9	1.1	2.2	1.1	4.3	1.1	11	**1.1**
			4R	11.0	10.1	5.0	25.2	3.0	50.3	2.0	100.7	1.5	201.3	1.2	503.3	1.1	2.0	1.0	4.0	1.0	10	**1.0**
			5L	11.1	11.3	5.1	28.3	3.1	56.7	2.1	113.3	1.6	226.7	1.3	566.6	1.2	2.3	1.2	4.5	1.1	11	**1.1**
			5R	11.1	11.5	5.1	28.7	3.1	57.3	2.1	114.7	1.6	229.3	1.3	573.3	1.2	2.3	1.2	4.6	1.1	11	**1.1**
			6L	11.2	12.1	5.2	30.2	3.2	60.3	2.2	120.6	1.7	241.2	1.4	603.0	1.3	2.4	1.2	4.8	1.2	12	**1.2**
			6R	11.8	17.7	5.8	44.3	3.8	88.7	2.8	177.3	2.3	354.6	2.0	886.5	1.8	3.5	1.8	7.1	1.8	18	**1.8**

Table IVA.3 – 45 rpm 25 mL case: estimation of the concentration at the interface for three different cell numbers with respective lactate flux production for different bulk concentrations, to determine the limit of $C_{lac\,b}$ below toxic values, SD is lower than 3%. Estimated specific lactate production coefficient: 1.15 ×10^{-14} mol.m^{-1}.s^{-1}.

Total cells ×10^6	Cells / frame ×10^5	Flux ×10^{-5} mol/m^2.s	C_b mol.m^3	10	%	4	%	2	%	1	%	0.5	%	0.2	%	0.05	% ×10^3	0.025	% ×10^3	1.0 ×10^{-6}	% ×10^7	**0**
1.25	2.08	0.86	4L	10.4	*4.4*	4.4	*10.9*	2.4	*21.8*	1.4	*43.6*	0.9	*87.2*	0.6	*218.0*	0.5	*0.9*	0.5	*1.7*	0.4	*4.4*	**0.4**
			4R	10.4	*3.8*	4.4	*9.6*	2.4	*19.2*	1.4	*38.4*	0.9	*76.9*	0.6	*192.1*	0.4	*0.8*	0.4	*1.5*	0.4	*3.8*	**0.4**
			5L	10.5	*4.5*	4.5	*11.4*	2.5	*22.7*	1.5	*45.5*	1.0	*90.9*	0.7	*227.3*	0.5	*0.9*	0.5	*1.8*	0.5	*4.5*	**0.5**
			5R	10.4	*4.0*	4.4	*9.9*	2.4	*19.8*	1.4	*39.6*	0.9	*79.2*	0.6	*197.9*	0.4	*0.8*	0.4	*1.6*	0.4	*4.0*	**0.4**
			6L	10.5	*4.5*	4.5	*11.3*	2.5	*22.6*	1.5	*45.3*	1.0	*90.6*	0.7	*226.4*	0.5	*9.1*	0.5	*1.8*	0.5	*4.5*	**0.5**
			6R	10.9	*8.6*	4.9	*21.4*	2.9	*42.8*	1.9	*85.5*	1.4	*171.1*	1.1	*427.7*	0.9	*1.7*	0.9	*3.4*	0.9	*8.6*	**0.9**
1.80	3.00	1.24	4L	10.6	*6.3*	4.6	*15.7*	2.6	*31.4*	1.6	*62.8*	1.1	*125.5*	0.8	*313.9*	0.7	*1.3*	0.7	*2.5*	0.6	*6.3*	**0.6**
			4R	10.6	*5.5*	4.6	*13.8*	2.6	*27.7*	1.6	*55.3*	1.1	*110.7*	0.8	*276.7*	0.6	*1.1*	0.6	*2.2*	0.6	*5.5*	**0.6**
			5L	10.7	*6.5*	4.7	*16.4*	2.7	*32.7*	1.7	*65.5*	1.2	*130.9*	0.9	*327.3*	0.7	*1.3*	0.7	*2.6*	0.7	*6.5*	**0.7**
			5R	10.6	*5.7*	4.6	*14.2*	2.6	*28.5*	1.6	*57.0*	1.1	*114.0*	0.8	*285.0*	0.6	*1.1*	0.6	*2.3*	0.6	*5.7*	**0.6**
			6L	10.7	*6.5*	4.7	*16.3*	2.7	*32.6*	1.7	*65.2*	1.2	*130.4*	0.9	*326.1*	0.7	*1.3*	0.7	*2.6*	0.7	*6.5*	**0.7**
			6R	11.2	*12.3*	5.2	*30.8*	3.2	*61.6*	2.2	*123.2*	1.7	*246.3*	1.4	*615.8*	1.3	*2.5*	1.3	*4.9*	1.2	*0.1*	**1.2**
2.5	4.17	1.72	4L	10.9	*8.7*	4.9	*21.8*	2.9	*43.6*	1.9	*87.2*	1.4	*174.4*	1.1	*435.9*	0.9	*1.7*	0.9	*3.5*	0.9	*8.7*	**0.9**
			4R	10.8	*7.7*	4.8	*19.2*	2.8	*38.4*	1.8	*76.9*	1.3	*153.7*	1.0	*384.3*	0.8	*1.5*	0.8	*3.1*	0.8	*7.7*	**0.8**
			5L	10.9	*9.1*	4.9	*22.7*	2.9	*45.5*	1.9	*90.9*	1.4	*181.8*	1.1	*454.6*	1.0	*1.8*	0.9	*3.*	0.9	*9.1*	**0.9**
			5R	10.8	*7.9*	4.8	*19.8*	2.8	*39.6*	1.8	*79.2*	1.3	*158.3*	1.0	*395.8*	0.8	*1.6*	0.8	*3.2*	0.8	*7.9*	**0.8**
			6L	10.9	*9.1*	4.9	*22.6*	2.9	*45.3*	1.9	*90.6*	1.4	*181.1*	1.1	*452.9*	1.0	*1.8*	0.9	*3.*	0.9	*9.1*	**0.9**
			6R	11.7	*17.1*	5.7	*42.8*	3.7	*85.5*	2.7	*171.1*	2.2	*342.1*	1.9	*855.3*	1.8	*3.4*	1.7	*6.8*	1.7	*0.2*	**1.7**

Table IVA.4 – 60 rpm 25 mL case: estimation of the concentration at the interface for three different cell numbers with respective lactate flux production for different bulk concentrations, to determine the limit of $C_{lac\,b}$ below toxic values, SD is lower than 3%. Estimated specific lactate production coefficient: 1.15 ×10^{-14} mol.m^{-1}.s^{-1}.

Total cells ×10^6	Cells / frame ×10^5	Flux ×10^{-5} mol/m^2.s	C_b mol.m^3	10	%	4	%	2	%	1	%	0.5	%	0.2	%	0.05	% ×10^2	0.025	% ×10^3	1.0 ×10^{-6}	% ×10^7	**0**
1.25	2.08	0.86	4L	10.3	3.3	4.3	8.2	2.3	16.5	1.3	33.0	0.8	65.9	0.5	164.8	0.4	6.6	0.4	1.3	0.3	3.3	**0.3**
			4R	10.3	3.3	4.3	8.3	2.3	16.6	1.3	33.3	0.8	66.5	0.5	166.3	0.4	6.7	0.4	1.3	0.3	3.3	**0.3**
			5L	10.4	3.8	4.4	9.4	2.4	18.8	1.4	37.6	0.9	75.3	0.6	188.2	0.4	7.5	0.4	1.5	0.4	3.8	**0.4**
			5R	10.3	3.4	4.3	8.5	2.3	17.1	1.3	34.2	0.8	68.3	0.5	170.8	0.4	6.8	0.4	1.4	0.3	3.4	**0.3**
			6L	10.4	3.6	4.4	9.0	2.4	18.0	1.4	36.0	0.9	72.0	0.6	180.1	0.4	7.2	0.4	1.4	0.4	3.6	**0.4**
			6R	10.7	7.0	4.7	17.4	2.7	34.8	1.7	69.6	1.2	139.2	0.9	348.1	0.7	1.	0.7	2.8	0.7	7.0	**0.7**
1.80	3.00	1.24	4L	10.5	4.7	4.5	11.9	2.5	23.7	1.5	47.5	1.0	94.9	0.7	237.3	0.5	9.5	0.5	1.9	0.5	4.7	**0.5**
			4R	10.5	4.8	4.5	12.0	2.5	23.9	1.5	47.9	1.0	95.8	0.7	239.5	0.5	9.6	0.5	1.9	0.5	4.8	**0.5**
			5L	10.5	5.4	4.5	13.5	2.5	27.1	1.5	54.2	1.0	108.4	0.7	270.9	0.6	11	0.6	2.2	0.5	5.4	**0.5**
			5R	10.5	4.9	4.5	12.3	2.5	24.6	1.5	49.2	1.0	98.4	0.7	246.0	0.5	9.8	0.5	2.0	0.5	4.9	**0.5**
			6L	10.5	5.2	4.5	13.0	2.5	25.9	1.5	51.9	1.0	103.7	0.7	259.3	0.6	10	0.5	2.1	0.5	5.2	**0.5**
			6R	11.0	10.0	5.0	25.1	3.0	50.1	2.0	100.2	1.5	200.5	1.2	501.2	1.1	20	1.0	4.0	1.0	10	**1.0**
2.5	4.17	1.72	4L	10.7	6.6	4.7	16.5	2.7	33.0	1.7	65.9	1.2	131.8	0.9	329.6	0.7	13	0.7	2.6	0.7	6.6	**0.7**
			4R	10.7	6.7	4.7	16.6	2.7	33.3	1.7	66.5	1.2	133.0	0.9	332.6	0.7	13	0.7	2.7	0.7	6.7	**0.7**
			5L	10.8	7.5	4.8	18.8	2.8	37.6	1.8	75.3	1.3	150.5	1.0	376.3	0.8	15	0.8	3.0	0.8	7.5	**0.8**
			5R	10.7	6.8	4.7	17.1	2.7	34.2	1.7	68.3	1.2	136.7	0.9	341.6	0.7	14	0.7	2.7	0.7	6.8	**0.7**
			6L	10.7	7.2	4.7	18.0	2.7	36.0	1.7	72.0	1.2	144.1	0.9	360.2	0.8	14	0.7	2.9	0.7	7.2	**0.7**
			6R	11.4	13.9	5.4	34.8	3.4	69.6	2.4	139.2	1.9	278.5	1.6	696.1	1.4	28	1.4	5.6	1.4	14	**1.4**

Table IVA.5 – 120 rpm 25 mL case: estimation of the concentration at the interface for three different cell numbers with respective lactate flux production for different bulk concentrations, to determine the limit of $C_{lac\,b}$ below toxic values, SD is lower than 3%. Estimated specific lactate production coefficient: 1.15 ×10^{-14} mol.m^{-1}.s^{-1}.

Total cells ×10^6	Cells / frame ×10^5	Flux ×10^{-5} mol/m^2.s	C_b mol.m^3	10	%	4	%	2	%	1	%	0.5	%	0.2	%	0.05	% ×10^2	0.025	% ×10^3	1.0 ×10^{-6}	% ×10^7	**0**
1.25	2.08	0.86	4L	10.2	2.2	4.2	5.6	2.2	11.2	1.2	22.4	0.7	44.7	0.4	111.8	0.3	4.5	0.2	0.9	0.2	2.2	**0.2**
			4R	10.2	2.2	4.2	5.6	2.2	11.2	1.2	22.5	0.7	45.0	0.4	112.4	0.3	4.5	0.2	0.9	0.2	2.2	**0.2**
			5L	10.3	2.8	4.3	7.1	2.3	14.2	1.3	28.5	0.8	56.9	0.5	142.3	0.3	5.7	0.3	1.1	0.3	2.8	**0.3**
			5R	10.3	2.5	4.3	6.4	2.3	12.7	1.3	25.5	0.8	51.0	0.5	127.5	0.3	5.1	0.3	1.0	0.3	2.5	**0.3**
			6L	10.3	2.9	4.3	7.3	2.3	14.5	1.3	29.1	0.8	58.1	0.5	145.4	0.3	5.8	0.3	1.2	0.3	2.9	**0.3**
			6R	10.4	3.7	4.4	9.2	2.4	18.5	1.4	36.9	0.9	73.9	0.6	184.7	0.4	7.4	0.4	1.5	0.4	3.7	**0.4**
1.80	3.00	1.24	4L	10.3	3.2	4.3	8.0	2.3	16.1	1.3	32.2	0.8	64.4	0.5	160.9	0.4	6.4	0.3	1.3	0.3	3.2	**0.3**
			4R	10.3	3.2	4.3	8.1	2.3	16.2	1.3	32.4	0.8	64.7	0.5	161.8	0.4	6.5	0.3	1.3	0.3	3.2	**0.3**
			5L	10.4	4.1	4.4	10.2	2.4	20.5	1.4	41.0	0.9	82.0	0.6	204.9	0.5	8.2	0.4	1.6	0.4	4.1	**0.4**
			5R	10.4	3.7	4.4	9.2	2.4	18.4	1.4	36.7	0.9	73.4	0.6	183.5	0.4	7.3	0.4	1.5	0.4	3.7	**0.4**
			6L	10.4	4.2	4.4	10.5	2.4	20.9	1.4	41.9	0.9	83.7	0.6	209.3	0.5	8.4	0.4	1.7	0.4	4.2	**0.4**
			6R	10.5	5.3	4.5	13.3	2.5	26.6	1.5	53.2	1.0	106.4	0.7	265.9	0.6	11	0.6	2.1	0.5	5.3	**0.5**
2.5	4.17	1.72	4L	10.4	4.5	4.4	11.2	2.4	22.4	1.4	44.7	0.9	89.4	0.6	223.5	0.5	8.9	0.5	1.8	0.4	4.5	**0.4**
			4R	10.4	4.5	4.4	11.2	2.4	22.5	1.4	45.0	0.9	89.9	0.6	224.8	0.5	9.0	0.5	1.8	0.4	4.5	**0.4**
			5L	10.6	5.7	4.6	14.2	2.6	28.5	1.6	56.9	1.1	113.8	0.8	284.6	0.6	11	0.6	2.3	0.6	5.7	**0.6**
			5R	10.5	5.1	4.5	12.7	2.5	25.5	1.5	51.0	1.0	102.0	0.7	254.9	0.6	10	0.5	2.0	0.5	5.1	**0.5**
			6L	10.6	5.8	4.6	14.5	2.6	29.1	1.6	58.1	1.1	116.3	0.8	290.7	0.6	12	0.6	2.3	0.6	5.8	**0.6**
			6R	10.7	7.4	4.7	18.5	2.7	36.9	1.7	73.9	1.2	147.7	0.9	369.3	0.8	15	0.8	3.0	0.7	7.4	**0.7**

Table IVA.6 - Sherwood numbers estimated from the limiting current experiment for the case of 25 mL.

rpm	$Re_{tip\ stirrer}$	*4L*	*4R*	*5L*	*5R*	*6L*	*6R*
0	0	69.38	79.50	78.17	74.30	76.56	72.78
10	1.71	88.40	90.80	87.60	84.20	75.80	78.00
20	3.43	106.81	118.38	105.30	99.21	87.86	75.33
30	5.14	131.47	141.54	125.73	124.27	118.15	80.37
40	6.86	151.15	167.21	154.23	164.25	145.07	90.47
45	7.71	163.44	185.37	156.72	180.01	157.32	83.29
50	8.57	180.88	194.07	184.24	190.18	167.73	90.22
60	10.29	216.15	214.18	189.33	208.53	197.81	102.34
90	15.43	259.23	274.83	230.48	239.77	209.12	137.18
120	20.57	318.73	316.96	250.36	279.47	245.07	192.91

Table IVA.7 - Sherwood numbers estimated from the limiting current experiment for the case of 30 mL.

rpm	$Re_{tip\ stirrer}$	*4L*	*4R*	*5L*	*5R*	*6L*	*6R*
0	0	96.11	74.92	71.48	67.09	91.04	66.61
10	1.71	101.00	86.30	73.30	72.60	82.30	63.70
20	3.43	116.76	112.89	95.81	97.90	91.12	76.00
30	5.14	139.57	150.71	130.76	138.91	118.57	86.26
40	6.86	156.32	177.93	159.79	165.25	128.96	83.81
45	7.71	169.78	186.46	172.19	174.34	144.04	103.16
50	8.57	179.99	200.40	187.03	189.21	130.18	91.55
60	10.29	200.64	217.05	172.19	211.40	144.04	184.60
90	15.43	264.02	286.40	263.26	261.32	192.20	217.13
120	20.57	300.98	336.35	305.98	289.51	261.85	253.97

Table IVA.8 - Maximum instant shear stress and instant fluid velocities determined with CFD.

Volume (mL)	*rpm*	*Position*	*Shear stress (Pa)*	
25	30	4L, 4R	0.0264	
	45	4L, 4R	0.0506	
	60	4L, 4R	0.0725	
	90	4L, 4R	0.15	
	120	4L, 4R	0.248	Velocity ($m.s^{-1}$)
30	30	4R	0.02	0.003
	45	4R	0.0363	0.006
	60	4R	0.0551	0.006
	90	4R	0.105	0.015
	120	5R, 5L	0.147	0.02

References

Biomechanical Systems: Techniques and Applications, Volume IV: Biofluid Methods in Vascular and Pulmonary Systems. 2000 Dec 26. CRC Press. [accessed 2018 Jul 7]. https://www.crcpress.com/Biomechanical-Systems-Techniques-and-Applications-Volume-IV-Biofluid/Leondes/p/book/9780849390494.

Bulnes-Abundis D, Carrillo-Cocom LM, Aráiz-Hernández D, García-Ulloa A, Granados-Pastor M, Sánchez-Arreola PB, Murugappan G, Alvarez MM. 2013. A simple eccentric stirred tank mini-bioreactor: mixing characterization and mammalian cell culture experiments. Biotechnol Bioeng. 110(4):1106–1118. doi:10.1002/bit.24780.

Cabaret F, Bonnot S, Fradette L, Tanguy PA. 2007. Mixing Time Analysis Using Colorimetric Methods and Image Processing. Ind Eng Chem Res. 46(14):5032–5042. doi:10.1021/ie0613265.

Cherry RS, Kwon KY. 1990. Transient shear stresses on a suspension cell in turbulence. Biotechnol Bioeng. 36(6):563–571. doi:10.1002/bit.260360603.

Chu X-H, Shi X-L, Feng Z-Q, Gu J-Y, Xu H-Y, Zhang Y, Gu Z-Z, Ding Y-T. 2009. In vitro evaluation of a multi-layer radial-flow bioreactor based on galactosylated chitosan nanofiber scaffolds. Biomaterials. 30(27):4533–4538. doi:10.1016/j.biomaterials.2009.05.020.

Cussler EL. 1997. Diffusion. Cambridge University Press.

Doran PM. 1995. 7 - Fluid Flow and Mixing. In: Bioprocess Engineering Principles. London: Academic Press. p. 129–163. [accessed 2016 Jun 29]. http://www.sciencedirect.com/science/article/pii/B9780122208553500079.

Eroğlu E, Yapici S, Şara ON. 2011. Some Transport Properties of Potassium Ferri/Ferro-Cyanide Solutions in a Wide Range of Schmidt Numbers. J Chem Eng Data. 56(8):3312–3317. doi:10.1021/je200089b.

Ferziger JH, Peric M. 2012. Computational Methods for Fluid Dynamics. Springer Science & Business Media.

Gilbertson JA, Sen A, Behie LA, Kallos MS. 2006. Scaled-up production of mammalian neural precursor cell aggregates in computer-controlled suspension bioreactors. Biotechnol Bioeng. 94(4):783–792. doi:10.1002/bit.20900.

Grober H, Erk S, Grigull U. 1961. Fundamentals of heat transfer. New York: McGraw-Hill.

Guirao B, Meunier A, Mortaud S, Aguilar A, Corsi J-M, Strehl L, Hirota Y, Desoeuvre A, Boutin C, Han Y-G, et al. 2010. Coupling between hydrodynamic forces and planar cell polarity orients mammalian motile cilia. Nat Cell Biol. 12(4):341–350. doi:10.1038/ncb2040.

Harris CK, Roekaerts D, Rosendal FJJ, Buitendijk FGJ, Daskopoulos P, Vreenegoor AJN, Wang H. 1996. Computational fluid dynamics for chemical reactor engineering. Chem Eng Sci. 51(10):1569–1594. doi:10.1016/0009-2509(96)00021-8.

Hosseinkhani H, Hosseinkhani M, Tian F, Kobayashi H, Tabata Y. 2006. Ectopic bone formation in collagen sponge self-assembled peptide-amphiphile nanofibers hybrid scaffold in a perfusion culture bioreactor. Biomaterials. 27(29):5089–5098. doi:10.1016/j.biomaterials.2006.05.050.

Irene Sánchez Cervantes M, Lacombe J, Muzzio FJ, Álvarez MM. 2006. Novel bioreactor design for the culture of suspended mammalian cells. Part I: Mixing characterization. Chem Eng Sci. 61(24):8075–8084. doi:10.1016/j.ces.2006.09.035.

Karcz J, Cudak M, Szoplik J. 2005. Stirring of a liquid in a stirred tank with an eccentrically located impeller. Chem Eng Sci. 60(8–9):2369–2380. doi:10.1016/j.ces.2004.11.018.

King JA, Miller WM. 2007. Bioreactor development for stem cell expansion and controlled differentiation. Curr Opin Chem Biol. 11(4):394–398. doi:10.1016/j.cbpa.2007.05.034.

Li W-J, Jiang YJ, Tuan RS. 2008. Cell-nanofiber-based cartilage tissue engineering using improved cell seeding, growth factor, and bioreactor technologies. Tissue Eng Part A. 14(5):639–648. doi:10.1089/tea.2007.0136.

Lin CS, Denton EB, Gaskill HS, Putnam GL. 1951. Diffusion-Controlled Electrode Reactions. Ind Eng Chem. 43(9):2136–2143. doi:10.1021/ie50501a045.

Liu N, Ouyang A, Li Y, Yang S-T. 2013. Three-dimensional neural differentiation of embryonic stem cells with ACM induction in microfibrous matrices in bioreactors. Biotechnol Prog. 29(4):1013–1022. doi:10.1002/btpr.1742.

Lunn JS, Sakowski SA, Hur J, Feldman EL. 2011. Stem Cell Technology for Neurodegenerative Diseases. Ann Neurol. 70(3):353–361. doi:10.1002/ana.22487.

Manfredini R, Cavallera V, Marini L, Donati G. 1983. Mixing and oxygen transfer in conventional stirred fermentors. Biotechnol Bioeng. 25(12):3115–3131. doi:10.1002/bit.260251224.

Menter F. 1993. Zonal Two Equation k-w Turbulence Models For Aerodynamic Flows. In: 23rd Fluid Dynamics, Plasmadynamics, and Lasers Conference. American Institute of Aeronautics and Astronautics. (Fluid Dynamics and Co-located Conferences). [accessed 2018 Jun 25]. https://arc.aiaa.org/doi/10.2514/6.1993-2906.

Nanou A, Azzouz M. 2009. Gene therapy for neurodegenerative diseases based on lentiviral vectors. Prog Brain Res. 175:187–200. doi:10.1016/S0079-6123(09)17513-1.

Nienow AW, Langheinrich C, Stevenson NC, Emery AN, Clayton TM, Slater NKH. 1996. Homogenisation and oxygen transfer rates in large agitated and sparged animal cell bioreactors: Some implications for growth and production. Cytotechnology. 22(1–3):87–94. doi:10.1007/BF00353927.

Park MG, Jang H, Lee S-H, Lee CJ. 2017. Flow Shear Stress Enhances the Proliferative Potential of Cultured Radial Glial Cells Possibly Via an Activation of Mechanosensitive Calcium Channel. Exp Neurobiol. 26(2):71–81. doi:10.5607/en.2017.26.2.71.

Reiss LP, Hanratty TJ. 1962. Measurement of instantaneous rates of mass transfer to a small sink on a wall. AIChE J. 8(2):245–247. doi:10.1002/aic.690080223.

Rodrigues C, Geraldes V, de Pinho MN, Semião V. 2012. Mass-transfer entrance effects in narrow rectangular channels with ribbed walls or mesh-type spacers. Chem Eng Sci. 78:38–45. doi:10.1016/j.ces.2012.04.023.

Rodrigues CAV, Diogo MM, da Silva CL, Cabral JMS. 2011. Microcarrier expansion of mouse embryonic stem cell-derived neural stem cells in stirred bioreactors. Biotechnol Appl Biochem. 58(4):231–242. doi:10.1002/bab.37.

Rodrigues CAV, Fernandes TG, Diogo MM, da Silva CL, Cabral JMS. 2011. Stem cell cultivation in bioreactors. Biotechnol Adv. 29(6):815–829. doi:10.1016/j.biotechadv.2011.06.009.

Schop D, Janssen FW, van Rijn LDS, Fernandes H, Bloem RM, de Bruijn JD, van Dijkhuizen-Radersma R. 2009. Growth, metabolism, and growth inhibitors of mesenchymal stem cells. Tissue Eng Part A. 15(8):1877–1886. doi:10.1089/ten.tea.2008.0345.

Scott K, Lobato J. 2002. Determination of a Mass-Transfer Coefficient Using the Limiting-Current Technique. Chem Educ. 7(4):214–219. doi:10.1007/s00897020579a.

Sedahmed GH, Khatab MA, Mahgob FM, Al-Azzony MR. 2004. Solid-Liquid Mass Transfer at the Base of a Rectangular Agitated Vessel. Chem Eng Commun. 191(2):168–181. doi:10.1080/00986440390225242.

Selman JR, Tobias CW. 1978. Mass-Transfer Measurements by the Limiting-Current Technique. In: Thomas B. Drew GRC John W Hoopes and Theodore Vermeulen, editor. Advances in Chemical Engineering. Vol. 10. Academic Press. p. 211–318. [accessed 2016 Jul 5]. http://www.sciencedirect.com/science/article/pii/S0065237708601349.

Sen A, Kallos MS, Behie LA. 2002. Expansion of mammalian neural stem cells in bioreactors: effect of power input and medium viscosity. Dev Brain Res. 134(1):103–113. doi:10.1016/S0165-3806(01)00328-5.

Serra M, Brito C, Costa EM, Sousa MF, Alves PM. 2009. Integrating human stem cell expansion and neuronal differentiation in bioreactors. BMC Biotechnol. 9(1):82. doi:10.1186/1472-6750-9-82.

Shemesh J, Jalilian I, Shi A, Yeoh GH, Tate MLK, Warkiani ME. 2015. Flow-induced stress on adherent cells in microfluidic devices. Lab Chip. 15(21):4114–4127. doi:10.1039/C5LC00633C.

Szánto DA, Cleghorn S, Ponce-de-León C, Walsh FC. 2008. The limiting current for reduction of ferricyanide ion at nickel: The importance of experimental conditions. AIChE J. 54(3):802–810. doi:10.1002/aic.11420.

Tan R-K, Eberhard W, Büchs J. 2011. Measurement and characterization of mixing time in shake flasks. Chem Eng Sci. 66(3):440–447. doi:10.1016/j.ces.2010.11.001.

Valmikinathan CM, Hoffman J, Yu X. 2011. Impact of Scaffold Micro and Macro Architecture on Schwann Cell Proliferation under Dynamic Conditions in a Rotating Wall Vessel Bioreactor. Mater Sci Eng C Mater Biol Appl. 31(1):22–29. doi:10.1016/j.msec.2010.04.001.

Wang Y, Chou B-K, Dowey S, He C, Gerecht S, Cheng L. 2013. Scalable expansion of human induced pluripotent stem cells in the defined xeno-free E8 medium under adherent and suspension culture conditions. Stem Cell Res. 11(3):1103–1116. doi:10.1016/j.scr.2013.07.011.

Weyand B, Israelowitz M, von Schroeder HP, Vogt PM. 2009. Fluid dynamics in bioreactor design: considerations for the theoretical and practical approach. Adv Biochem Eng Biotechnol. 112:251–268. doi:10.1007/978-3-540-69357-4_11.

Zhang Q, Yong Y, Mao Z-S, Yang C, Zhao C. 2009. Experimental determination and numerical simulation of mixing time in a gas–liquid stirred tank. Chem Eng Sci. 64(12):2926–2933. doi:10.1016/j.ces.2009.03.030.

Chapter V

Dynamic Culture of Neural Stem Cells Supported in Nanofiber Scaffolds

Chapter V - Dynamic Culture of Neural Stem Cells Supported in Nanofiber Scaffolds

V.1 - Abstract

We present a simple and scalable system that couples a stirred bioreactor and nanofiber scaffold frames applied to human neural stem cells (hNSC) culture. The expansion and differentiation of hNSC cultured in dynamic conditions on the nanofiber frames in the designed stirred vessel was evaluated. Overall, the cellular growth developed homogeneously along the set of nanofiber frames positioned vertically in the ellipsoidal stirred vessel, a geometry that was not a limitation for the cellular expansion. There was effective cellular growth in all the conditions applied, 30 and 45 rpm with 25 mL and 45, 60 and 120 rpm with 30 mL working volume, with the most promising operation conditions considered at 45 – 60 rpm with 30 mL volume.

The cellular distribution was someway heterogeneous in each nanofiber frame with areas of higher cellular density than others. The obtained cell population maintained the fundamental neural multipotent properties with expression of Nestin and Sox2 specific markers and also the neural and astrocyte differentiation potential with the expression of Tuj1 and GFAP markers. The lactate concentrations at day 10 of culture obtained were between 7 – 15 $mmolL^{-1}$ and the specific lactate production rate between 8×10^{-8} – 2×10^{-7} nmol per cell per day, without reaching any cellular inhibitory concentrations.

From the hydrodynamic characterization obtained in the previous chapter it was possible to determine that with the velocity of agitation, the cellular growth increased facilitated by an increase in the mass transfer on the vessel, also the shear forces imposed in the system in general had no negative effect on the cellular expansion, except at 120 rpm condition, which could explain the lower cell numbers obtained at this condition.

These results are promising as a successful prototype system with great potential to be developed for the scale up production of tissue constructs for regenerative medicine, drug testing or cell/scaffold based platforms for research applications.

V.2 - Introduction

Therapeutic strategies based on cell therapies, in particular stem cell-based therapies, are appealing for different biomedical applications and research. However, these therapies require a large number of cells and stem cells are relatively rare in their niches in the human body. Thus, the production of cells in a scaled-up process *in-vitro*, complying with the regulatory guidelines in a cost effective way, becomes necessary. Several types of bioreactors are used for stem cell (SC) expansion at the laboratory scale, such as tissue culture flasks, well plates or gas-permeable blood bags. These static cell culture systems present some limitations regarding the restricted expansion of higher amounts of cells, oxygen, nutrient and metabolite diffusion, and the lack of agitation leading to formation of concentration gradients. Dynamic and more robust bioreactor systems are used for large cell number production, where mass transfer and diffusional problems are minimized (Rodrigues et al. 2011).

SC bioengineering coupled with biomaterials engineering has been an emergent approach to develop therapies for central nervous system (CNS) injuries (Tam et al. 2014). Regeneration of neural tissue is relevant for diseases, in particular neuro-degenerative diseases such as Parkinson's and Alzheimer's disease, and traumatic injuries such as spinal cord and cancer or stroke related brain injuries. A strategy to address these problems is the development of *ex-vivo* cultivation of SC suitable for in situ transplantation, providing the adequate soluble factors (cytokines, growth factors). Moreover processed natural and synthetic polymers are used to prepare scaffolds mimicking the extracellular matrix ECM 3D structure, recapitulating the *in-vivo* cell environment. Nanofiber scaffolds for neural regeneration are particularly attractive substrates constituting a powerful physical guidance substrate for neuronal tissue. The nanofiber mesh provides extracellular geometry at the cell scale being advantageous in terms of porosity, high surface-to-volume ratio, and permeability, contributing to cell attachment and orientation, as well as effective nutrition and oxygen diffusion (Little et al. 2008).

A scaffold platform coupled with a bioreactor is a promising approach, where materials are required to promote a specific cell response or function, such as tissue organization or cell differentiation. However only few examples of such systems (Valmikinathan et al. 2011) were designed to be scalable, thus, a scalable nanofiber-bioreactor for the production of neural tissue promoting neural stem cell (NSC) expansion and differentiation on such scaffolds seems an interesting challenge to be explored.

While better mixing can contribute to proper delivery of nutrients and removal of inhibitory compounds (metabolites, by-products) from cells vicinity, shear stress can impact cell viability and metabolism. In general, in stirred systems, the shear needed to remove animal cells adhered to surfaces is in the order of 6.5 dyn/cm^2 (0.65 Pa), and the destructive shear to cell membrane of adhered cells is in the order of 15-30 dyn/cm^2 (1.5 – 3 Pa) (Cherry and Kwon 1990; Sen et al. 2002). However the hydrodynamic shear forces necessary to detach cells will depend on the material used for scaffold/culture substrate, the degree of cellular adhesion, and the cell system (King and Miller 2007). For example, endothelial cells are subjected to physiological shear stress in the order of 20 – 40 dyn/cm^2 (0.2 – 0.4 Pa) (Whited and Rylander 2014) but also endothelial cells subjected to shear stress in the range of 0.1 – 2.5 dyn/cm^2 (0.01 – 0.25 Pa) showed morphological changes; murine NSCs expanded in aggregates with average dimension compatible without the occurrence of necrosis at 100 rpm in spinner flask and the maximum shear at which the aggregates were able to maintain integrity was at 9.76 dyn/cm^2 (0.976 Pa) (Sen et al. 2001; Sen et al. 2002) and murine ESC aggregates dislodged or disrupted at 7.8 dyn/cm^2 (0.78 Pa) in a stirred bioreactor (Cormier et al. 2006). Also mouse ESCs were found to prime differentiation under perfusion induced shear stress, in self-renewing environment. The colonies growth was attenuated at values above 1 dyn/cm^2 (0.1 Pa), with decrease in Nanog factor (self-renewal in ESC, pluripotency marker) and increase in Fgf5 epiblast (primed pluripotency marker) (Toh and Voldman 2011); mouse ESC were cultured in aggregates subjected up to ≤ 2.5 dyn/cm^2 (0.25 Pa) shear stress in rotary suspension culture showed a different profile in gene expression and also in the percentage of differentiated cells, compared to static cultures (Sargent et al. 2010), and the ectodermal and mesodermal lineage responded to a linear shear stress magnitude in the range of 1.5 to 15 dyn/cm^2 (0.15 – 1.5 Pa) in mouse ESCs cultured on a two dimensional

surface (Wolfe et al. 2012). This chapter is focused on evaluating hNSC expansion in aligned PCL nanofiber scaffolds in a designed stirred vessel, and analyse the hydrodynamic effects of the cell culture output.

V.3 - Materials and Methods

V.3.1 - Preparation of Poly(ε-caprolactone) Nanofibers by electrospinning

An electrospinner device was set consisting of a high voltage power supply (Model PS/EL40P0, Series EL 1, Glassman High Voltage Inc., High Bridge, NJ, USA), a syringe pump (Model KDS Legato 210, KDS Scientific, Holliston, MA, USA) and a tube that connected a syringe (Henke Sass Wolf, Germany) to a needle (Needle Valve Dispense Tip Kit, EFD International Inc., UK) with an inner diameter of 0.84 mm. Aligned nanofibers were prepared using 6% w/w solution of PCL (70000-90000 MW, Sigma-Aldrich, St. Louis, MO, USA,) in 1,1,1,3,3,3-hexafluoro-2-propanol (HFP, Sigma-Aldrich) at a flow rate of 1 mLh^{-1}, with an applied potential of 26 kV, at a working distance of 20 cm from the tip of the needle to the nanofiber deposition target, which consisted of two parallel steel plates. The average humidity and temperature working conditions was 30-40 % and 22-25 ºC respectively. The nanofibers were fixed to polyethylene terephthalate (PET sheet, Mylar, GoodFellow, UK) frames with biocompatible silicon glue (Sylvatic Medical Adhesive Silicone type A, Dow Corning, Midland, MI, USA).

V.3.2 - Nanofibers Surface Functionalization with GRGDSP Motif

An alkaline hydrolysis was performed to create reactive primary amine groups at the surface of the polycaprolactone nanofibers. Before the reaction the nanofibers were washed with 50 % v/v ethanol (ThermoFisher Scientific, Waltham, MA, USA) solution in water for 1 hour and rinsed with deionized water under gentle agitation at room temperature. The aminolysis reaction took place by immersing the samples in 10 % w/v solution of 1,6-hexanediamine (HDA, Fluka, Germany) in isopropanol (ThermoFisher Scientific) for 40 minutes at 37 °C, based in the method described in the literature (Zhu et al. 2002). The nanofibers were successively rinsed with deionized water, and left in gentle agitation overnight to make sure to remove traces of hexanediamine.

Crosslink of GRGDSP motif was performed using 2.5 % v/v of glutaraldehyde (GA, Sigma-Aldrich) solution in water. Closed in a desiccator the scaffolds reacted for 24 hours in GA atmosphere while immersed in 50 μgmL^{-1} of GRGDSP (Sigma-Aldrich) and 20 μgmL^{-1} laminin (Sigma-Aldrich) solutions in phosphate buffer (PBS, Life Technologies, Waltham, MA, USA) at room temperature. Following, the samples were washed with PBS and immersed in 100 $mgmL^{-1}$ of glycine (Sigma-Aldrich) solution in PBS for 1 hour, and rinsed with PBS to wash remaining products and reactants from the treatment process.

V.3.3 - Cell Culture In Standard Conditions

ReNcell®VM (Milipore, Germany) is described as an immortalized human neural progenitor cell line, derived from the ventral mesencephalon region from a 10-week fetal brain tissue. This cell line, developed by Donato and co-workers (Donato et al. 2007), is able to maintain a stable karyotype after long term culture, over 45 passages, in a proliferative undifferentiated state, with demonstrated potential to differentiate into the three neural phenotypes: neurons, astrocytes and oligodendrocytes. ReNcell®VM is thus suitable as a standardized, in vitro, human-based platform for research applications.

According to the manufacturer's protocol cryopreserved ReNcell®VM cells, upon thawing, were expanded on coated tissue culture T-flasks (Falcon, BD Biosciences, San Jose, CA, USA) with 0.5 $mg.mL^{-1}$ of poly-L-ornithine (Sigma) and 10 $mg.mL^{-1}$ of laminin (Sigma) coatings, in serum free culture medium of DMEM/F12 (Life Technologies) supplemented with 1 % v/v N2 (Invitrogen), 10 ng/mL of FGF-2 (PeproTech, Rocky Hill, NJ, USA) and 20 ng/mL EGF (PeproTech), 2 % v/v B27 (Life Technologies), 1 % v/v penicillin-streptomycin (10000 U/ml, Life Technologies), 1.6 $g.L^{-1}$ glucose (Sigma) and 20 $mg.L^{-1}$ insulin (Sigma). The cells were cultured at 37 °C under 5 % CO_2 humidified atmosphere and culture medium was changed every two days and each passage was performed at 80-90 % confluence. Cells were harvested using accutase (Life Technologies) and cell viability was evaluated using the trypan blue (Life Technologies) exclusion method.

Removing the growth factors, FGF-2 and EGF from the culture media, induces the cellular differentiation. The differentiation medium consisted on a 1:1 mixture of Neurobasal (Life Technologies), supplemented with 2% v/v B27 (Life Technologies) and 1 % v/v penicillin-streptomycin (10000 U/ml, Life Technologies), with DMEM/F12 (Life Technologies) supplemented as described previously In Chapter III. The differentiation protocol started with the substitution of the expansion culture media by the differentiation media. Following, every three days half the media were exchanged, during a total culture period of 15 days.

V.3.4 - Cell Culture On The PCL Nanofibers In The Bioreactor Vessel

The expansion of ReNcell®VM supported in the nanofibers was performed in dynamic conditions in the designed vessel, with a magnetic stir bar used as an impeller.

The culture was performed in a 5 % CO_2 incubator at 37 ºC with the bioreactor placed over a magnetic stirring plate (2 Mag) with continuous stirring. Different velocities of agitation were applied (30, 45, 60 and 120 rpm) for 25 and 30 mL culture medium volumes. Each sterilized scaffold frame comprehends an available nanofiber area of about 3 cm^2, onto which 20×10^4 cells, previously expanded in a standard tissue culture flask, were seeded. Before cell seeding the nanofibers were previously immersed in 1mL culture medium and maintained for 1h at 37ºC. After the seeding, the cells incubated on the scaffolds for at least 2 hours on a 6-well plate, allowing the cells to adhere to the nanofibers. Afterwards, each scaffold was carefully placed and fixed inside the vessel. Every two days half the medium was replaced, and cell viability on the scaffolds was monitored indirectly over time, incubating the cells for 1h with 5% (v/v) Alamar Blue® (Life Technologies) and measuring the fluorescence at excitation and emission wavelengths of 560 nm and 590 nm, respectively, using a microplate reader (Tecan, Infinite M200 Pro). A reference calibration curve (Appendix, Figure VA.1) was obtained measuring the fluorescence of various cell densities, previously quantified (trypan blue exclusion test).

The differentiation protocol applied in dynamic culture conditions was as described in the previous section, where 200.000 cells were seeded on PCL-LN functionalized nanofiber

scaffolds (scaffolds functionalization as described in section V.3.2 and as in Chapter III) and placed in culture in standard tissue culture plate for 24 hours. The differentiation culture continued on the stirred device, by moving the samples to the device and with culture media without growth factors. Fresh differentiation media was replaced every two days for 15 days.

V.3.5 – Metabolite Production Analysis

Samples of 1 mL of culture medium were collected before and after medium exchange, every two days, during the course of the cell culture. The collected samples were centrifuged (1500 rpm, 10 minutes) and the supernatant stored at -20°C, for posterior analysis.

The concentration of lactate was determined automatically (YSI 7100MBS, Yellow Springs Instruments, OH, USA), by gentle thawing and homogenization of the medium samples before the analysis. The specific lactate production rate, q_{Lac} , was estimated by the equation:

$$q_{Lac} = \frac{\Delta Lac}{\overline{X}\Delta t} \qquad \text{(Equation V.1)}$$

where ΔLac is the lactate concentration during the period Δt and $\overline{X}$ the average number of cells in the same period.

V.3.6 - Immunocytochemistry

Immunophenotype analysis was performed for Sox2, Nestin, Tuj1, and GFAP antibodies. Similar to the staining procedure, the cells were fixed in 4% PFA for 10 minutes at room temperature, washed once with PBS and permeabilized with 0.1% v/v Triton-X-100 and 10% v/v NGS in PBS for 1 hour at room temperature; porimary antibodies were incubated overnight at 4°C in 0.1% v/v Triton-X-100 and 5% v/v NGS in PBS. The following primary antibodies were used: anti-Sox2 (1:100, R&D Systems, MN, USA), anti-Nestin mouse monoclonal antibody (1:200, Millipore, Germany), anti-βIII-tubulin (1:2000, Tuj1, Covance, Princeton, NJ, USA), and anti-Glial Fibrillary Acidic Protein GFAP (1:100, GFAP, Millipore). After primary antibody incubation, the cells were washed once with PBS and incubated with

the proper secondary antibody conjugated with Alexa Fluor 546 (1:500, Life Technologies) for 1 hour at room temperature, protected from light. Next, the cells were washed with PBS and nuclei stained with DAPI (1.5 μgmL^{-1} in PBS) for 5 minutes at room temperature. Finally, the cells were washed two times in PBS and kept in PBS protected from light to be visualized under a fluorescence optical microscope. Stained samples were visualized under a fluorescence optical microscope (DMI 3000B, Leica, Germany). Digital images were taken with a digital camera (DXM 1200F, Nikon, Japan).

V.3.7 - Scanning Electron Microscopy (SEM)

The nanofibers and cell morphology were examined by scanning electron microscopy (SEM). Scaffold samples containing cells were fixed with 4% PFA for 15 minutes, washed once with PBS, and dried by immersion in graded concentrations of ethanol solutions in water (25, 50, 75 and 100% v/v). The samples were kept in an aseptic environment until complete drying. Prior to SEM visualization, the samples were coated with a 45 nm gold/palladium layer by a sputter coater (model E5100, ex-Polaron, Quorum Technologies, ON, Canada) and observed under a conventional SEM (model S2400, Hitachi, Japan) with an electron beam with 20 kV of accelerating voltage. SEM images were analyzed with image analysis software ImageJ (National Institute of Healt, USA).

V.3.8 - Statistical Analysis

The results regarding cell culture data are expressed as standard error of the mean (SEM) expressed by mean ± standard error of the mean (SEM), where SEM = standard deviation / $\sqrt{n}$, where n is the number of independent events. Statistical analysis was performed with one way ordinary ANOVA with Tukeys test for multiple comparison tests, where statistically significant results were considered for obtained p values below 0.05. Regressions were calculated by the least squares method and the correlation coefficient by the Pearson product-moment.

V.4 - Results and Discussion

V.4.1 – Evaluation of the Cellular Growth with the Hydrodynamic Properties of the Vessel

V.4.1.1 – Hydrodynamic Properties of the Stirred Device

Following the bioreactor characterization in chapter IV, in this section is analyzed the stirred vessel performance regarding the culture of a human NSC line. Taking into consideration the hydrodynamic attributes of the designed system a discussion on the previous predictions with the actual results on the cellular culture are addressed.

A summary (from the general to a more concrete view) on the variation of the shear stress and the Sherwood number of the stirred vessel, at the conditions the cellular cultures were performed, is presented in Figure V.1. The results correspond to the estimated values determined theoretically by CFD and experimentally from the limiting current technique, in Chapter IV, for shear stress and Sherwood number, respectively. Assuming the symmetry of the stirred vessel, in the image in Figure V.1, only half the vessel was experimented (frames at the positions 4 (center), 5 (middle) and 6 (exterior)), and two sets of values were obtained for each frame interface. In order to assign singular values of shear stress and Sh number to each nanofiber frame, the values determined for each interface were considered the same for the exact symmetrical positions for the 1st half of the vessel. So, for a more realistic approximation it was considered the equivalent interfaces that were facing to the same environment, to obtain an average value for each position. For example frame in position 1 will be exposed to the environment at 1 left, 1 right and 2 left, as for frame in position 2 it will be exposed to 1 right, 2 left, 2 right and 3 left, and on. The obtained values quantify the shear stress and mass transfer extent ongoing in each position to which the frame is exposed. With that, average values for the regions, from the average of the pairs of equivalent symmetrical frames, and a vessel average, were determined.

In general with the increase of the agitation velocity described by the increase in the shear stress forces the mass transfer increases (Sh number) in the entire vessel (Figure V.1 – A).

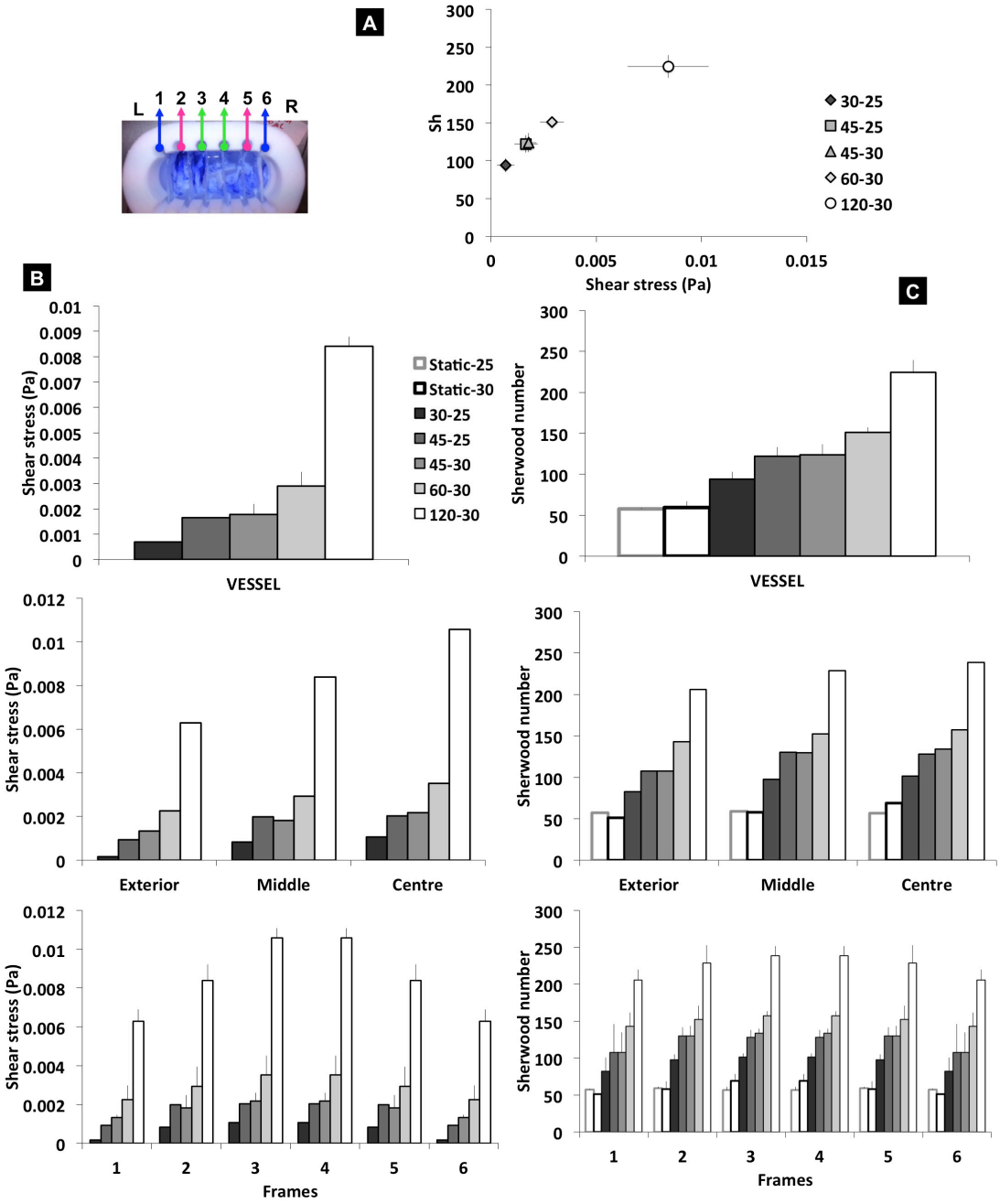

Figure V.1 – Overview of the shear stress and Sherwood number profiles of the hydrodynamic properties of the stirred vessel determined in Chapter IV: (A) Relation between the shear stress with the Sh number (global average); (B, C) Variation of the shear stress (set B) and Sh number (set C), in the overall vessel (top), in each vessel region and in each frame (bottom); error bars are SD.

Between the conditions at 45 rpm, the volume difference is hardly noticed with the values overlaid. The increase in the mass transfer seems to slow down in higher agitation velocities, and eventually a plateau, of a maximum mass transfer rate, would be attained at velocities above 120 rpm. There is a considerable mass transfer at no velocities of agitation

(convection currents) where again the 5 mL difference in volume is barely noticeable. In the fist top plots in Figure V.1 B and C, are represented individually the shear stress and Sh number, both increasing with increasing speed of agitation, as already verified. The same behavior is observed between each region, with a slight tendency to higher values when going to the external to the center of the vessel, and the same for each singular position. Next, adding the cellular growth profile, a broader overview of the system can be determined.

V.4.1.2 – Specific Growth Rates and Overview on Expansion Stage

The increase of the average cell number over time seems more noticeable for the conditions at 60 and 120 rpm, with the higher cell number attained with 60 rpm by day 10 (Figure V.2 – A). However, for both 60 and 120 rpm the initial cell number at day 1 was substantially higher than the remaining conditions, and in that way this comparison, at first, might not be straight. However, by day 10 at the end of the culture, in general the final average cell number was pretty similar in most cases, except at 60 rpm, which was higher. This observation can not be attributed to confluence and lack of space for further cell proliferation, as observations at the end of the cell culture after 10 days of cell expansion show that the cells are not evenly distributed along the total area of the nanofiber, that is, there are some zones with more dense cellular population and other zones of the scaffold that still have available area for further cell expansion. In that way, the scaffolds present still area available and eventually an improvement in the cell expansion on this conditions can lead to better yield in the obtained final cell population distribution on the scaffold.

The culture at 60 rpm results on higher number of cells but not in higher fold increase. Nevertheless, this condition represents a boundary at which further increase of mixing seems to not be any longer beneficial for cell culture. This result is in agreement to what described for the mass transfer pattern of the vessel in Figure V.1. The cellular culture was enhanced at higher speeds of agitation that provided higher mass transfer rates to the system (increased nutrient, and gases diffusion and toxic products dispersion) from 45 rpm. The low number of cells at 120 rpm could eventually be correlated to the reducing in mass transfer at higher agitations speeds, suggested in Figure V.1 – A.

Looking at the fold increase a different tendency is thus observed (Figure V.2 – B), as expected. The conditions with fewer cells at day 1 turn along the culture to fold increase values higher than the conditions starting with more quantity of cells. In this way to attain at day 10 a similar final average cell number, seems that the growth was more accentuated, with an increased slope, which can be confirmed by the estimated specific growth rates (Figure V.2 – C). In fact in the conditions starting with less cells the specific growth rate was higher which means that in those conditions of lower velocity of agitation, it was possible to verify a reasonable cell growth rate, even at 25 mL volume of culture media.

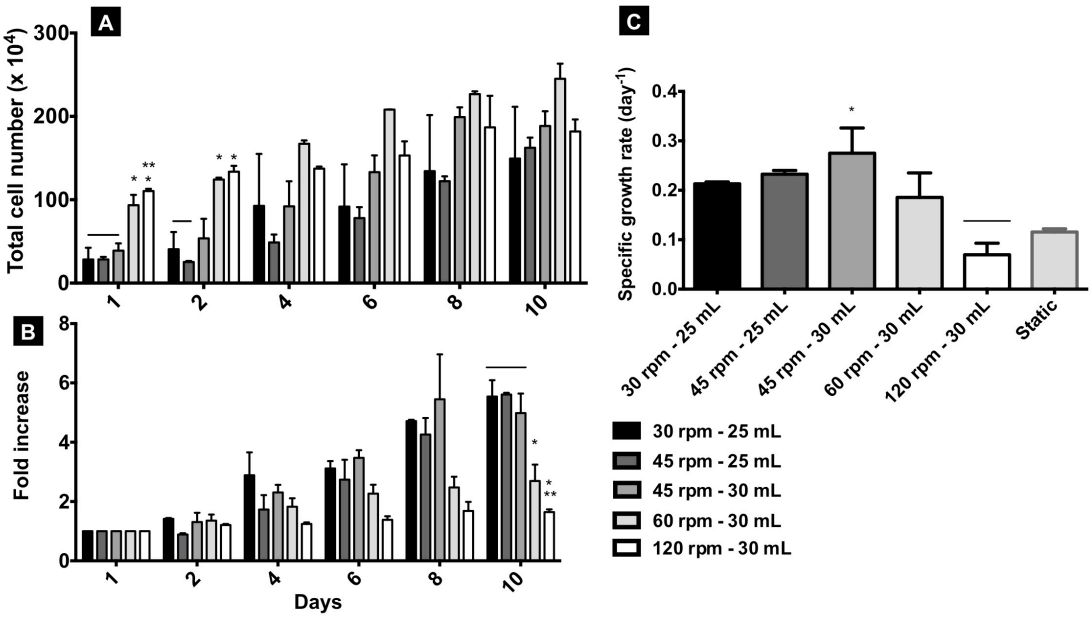

Figure V.2 – Global cell growth over 10 days at different conditions of culture: (A) Total cell number as a sum of the cells from the 6 scaffold frames; Day 1: * for 60/30 vs 30/25, 45/25, 45/30 and 120/30 vs 45/30; ** for 120/30 vs 30/25, 45/25; (B) Average fold increase, relative to the number of cells at day 1; Day 10: * for 60/30 vs 30/25, 45/25 and 120/30 vs 45/30; ** for 120/30 vs 30/25, 45/25; (C) Average specific growth rate (day-1); n=2, ** [0.001<p<0.01[, * [0.01<p<0.05[. Error bars are SEM.

After performing ordinary ANOVA tests the amount of significant differences between the dynamic culture conditions decreased considerably; in the first days of the cell culture the differences were more significant but with the progression of the cellular expansion the initial differences were apparently mitigated, although for condition 45 rpm- 30 mL it is noticeable a higher number of cells obtained and throughout the entire culture. The specific growth rates show a significant difference between 45 rpm – 30 mL and 120 rpm – 30 mL conditions,

which confirm that at 45 rpm – 30 mL the culture evolved more efficiently over time. Moreover, the fold increase shows clearly higher cell number output at the end of the culture, where an increased yield was achieved for low agitation rotation speeds (30, 45 rpm) in comparison with the high mixing rotation conditions (60, 120 rpm).

Another point of comment is the fact that the static condition represented as control, is not straightforward comparable to the dynamic conditions in study. Although the correspondent specific growth rate shown for the static is considerably lower (Figure V.2 – C), this result refers to the cell growth in the nanofibers in a 6 well plate with a total volume of 3 mL per well. To be correct, the control should be performed in the vessel with 25 and 30 mL volumes, without any agitation. So, to better associate the cellular growth in the static situation, it can be taken into consideration the ratio of total volume of media per scaffold in culture. That is, a ratio of ~4.2 mL/frame in the 25 mL case and 5 mL/frame in the 30 mL case. With that, there is an additional advantage in terms of volume available per scaffolds in the vessel culture additional to the agitation.

However, looking at 120 rpm conditions, the specific cell growth rate was found to be the lowest (Figure V.2 – C). The high rotation speed might have been too strong that pulled out cells from the scaffolds due to local shear forces, particularly in the first hours of culture in the reactor just after cell adhesion.

Another justification to consider is the fact that the initial cell number in culture could be in such a density, that the cellular expansion rate was slower, while in the case of the 30 and 45 rpm, due to possibly a lower initial cellular density the growth rate was increased.

Associating the global average of shear forces and mass transfer determined for the system, with the global specific growth rate (Figure V.3), a similar relation is observed in both plots, as expected, and would it be logical to interrogate if this relation would be likely to have an identical pattern as in Figure V.1 – A, regarding the variations in the initial cell number in culture, that affected the determination of the specific growth rate at 60 and 120 rpm. Could it be said that a lowering on the cellular growth at 120 rpm would be thus expected, but eventually not that accentuated.

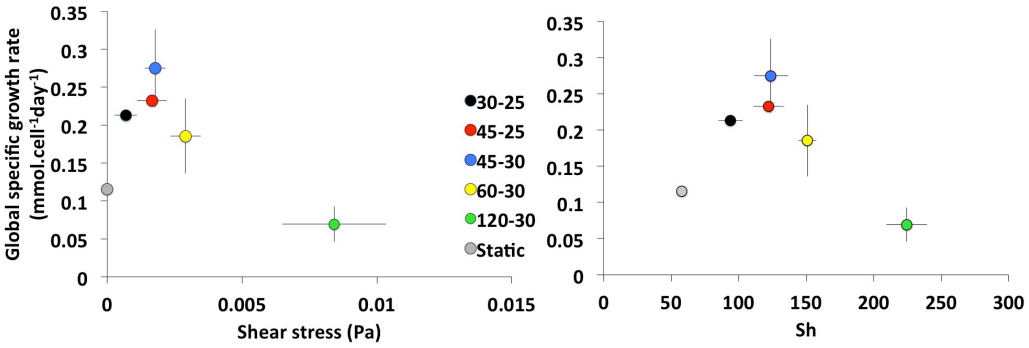

Figure V.3 – Relation of the specific cell growth rate with the average vessel shear stress and Sherwood number determined previously in Chapter IV. Error bars are SD.

Figure V.3 clearly shows an optimal condition concerning the effect of hydrodynamics on cell growth with a maximum for the specific cell growth rate corresponding to 45 rpm and 30 mL. Up to this condition there is a beneficial effect on improving mixing until a Sherwood number of 124, however above this condition the shear stress, at values higher than 1.8 mPa seems to negatively impact the cell culture. These observations are rather surprising. Indeed the improvement in mixing with the range accessed should result in marginal differences on liquid mass transfer coefficients, and our analysis on lactate profile on the boundary layer implies an increase in concentrations from the bulk to the interface of only 1.77 $mmol.L^{-1}$ in the worst case scenario. Therefore a further analysis on lactate concentration using the experimental values collected in this experiment is in section V.4.2.

On the other hand, shear stresses are considerably low when compared with thresholds previously reported (section V.2) as damaging to the cells. Our system provides an average shear stress up to 0.018 Pa while most studies only report cell damage on the range of 0.1 – 0.2 Pa. Note however that one study also reported cell damage for endothelial cells for shear stresses between 0.01 and 0.2 which lower end matches our range. Importantly we are reporting the effect of hydrodynamics and shear stress on specific cell growth rate rather than cell viability; which is actually in our view an important contribution for the scientific community.

V.4.1.3 – Specific Growth Rates on Expansion Stage Frame by Frame

Looking into detail frame by frame, the differences between the frames are not major (differences most likely due to cell seeding variations in each frame in the same culture batch), so in general it can be considered that the culture in this elliptical vessel occurred fairly uniform regarding the geometry. The statistical meaningful differences found lay on the 1st to the 4th days of the cell culture for the 30 and 45 rpm mixing velocities and on day 10 for 120 rpm condition. All compare with the static culture condition, except for frame 3 at 120 rpm at day 10 that revealed a higher cell number. Regarding the fold increase, fewer statistical meaningful differences are noticeable namely at day 8, 6 and 10 for 30 rpm, 45 rpm – 25 mL and 120 rpm conditions, respectively. It is clear the lower initial cells in the beginning of the culture in the cases at 30 and 45 rpm, which are nearly half the cells of the remaining conditions. Accordingly, the calculated fold increase values with respect to the number of cells at day 1 will reflect this difference, specially when compared to the static condition.

A more a detailed representation of the specific growth rate profiles on the stirred vessel is represented in the next set of figures.

In Figure V.5 – A the overall tendency observed previously, is confirmed looking at the values of the individual frames, each identified by the color code for the positions in the vessel (Exterior – blue, Middle – red, Center – green). In general there are no major variations amongst each frame in the set at each condition, indicating that no major fluctuations in the growth rate occurred, meaning an overall homogeneity of the culture in the different positions of the vessel. This set of figures represents various perspectives of the variation of the specific growth rate in the different positions of the vessel. In conditions 30 rpm – 25mL and 45 rpm – 25 mL, the individual frames differ statistically with the static culture condition (Figure V.5 – A), while for the remaining dynamic conditions the differences are not statistically significant.

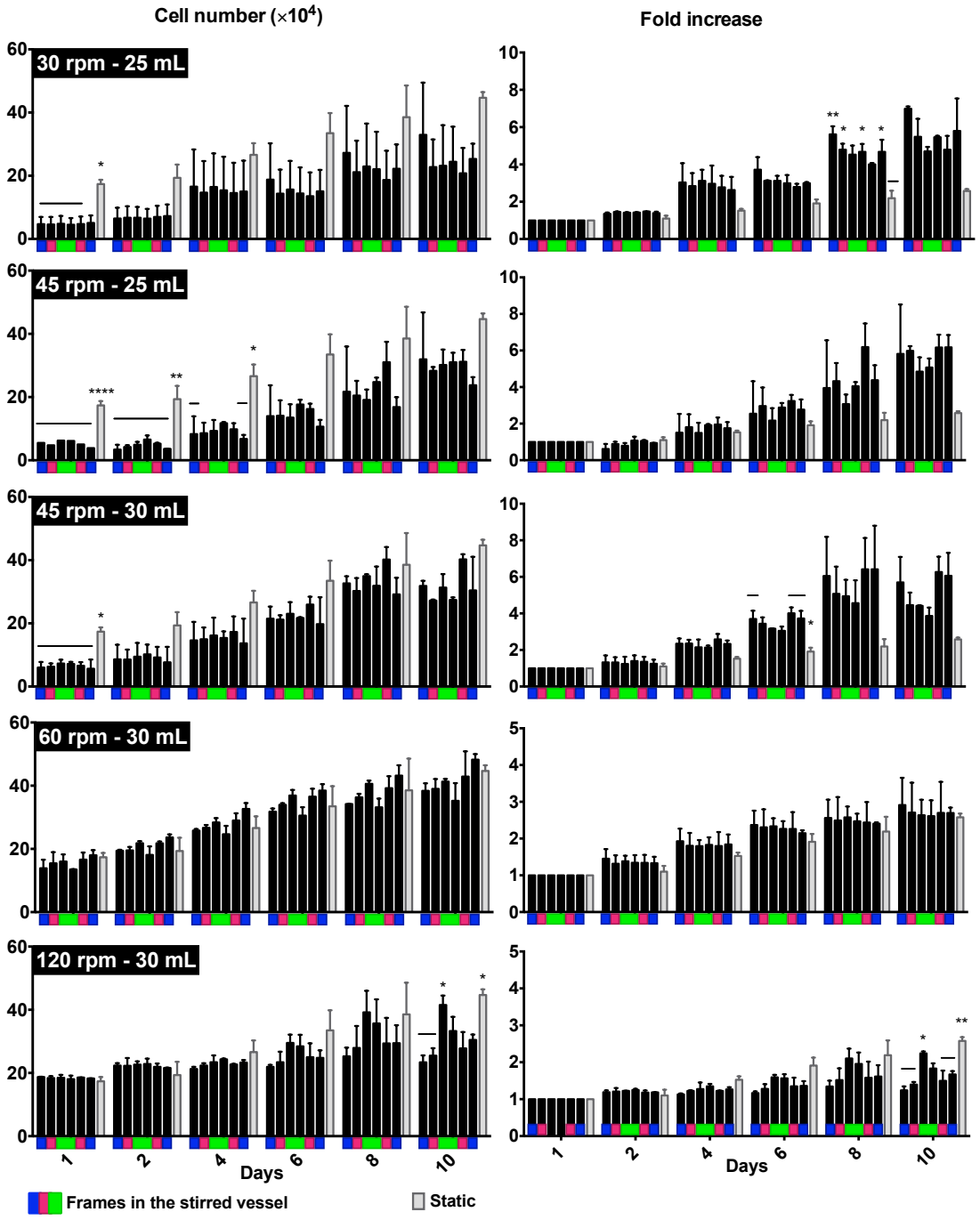

Figure V.4 – Detailed representation of the number of cells in each nanofiber frame (left) with respective fold increase (right) over 10 days of culture for each condition. The individual frames (1 to 6) are represented as black bars, and compared with identical frames cultivated in a standard tissue culture plate; n=2; **** p<0.0001, * [0.0001<p<0.001[, ** [0.001<p<0.01[, * [0.01<p<0.05[.**

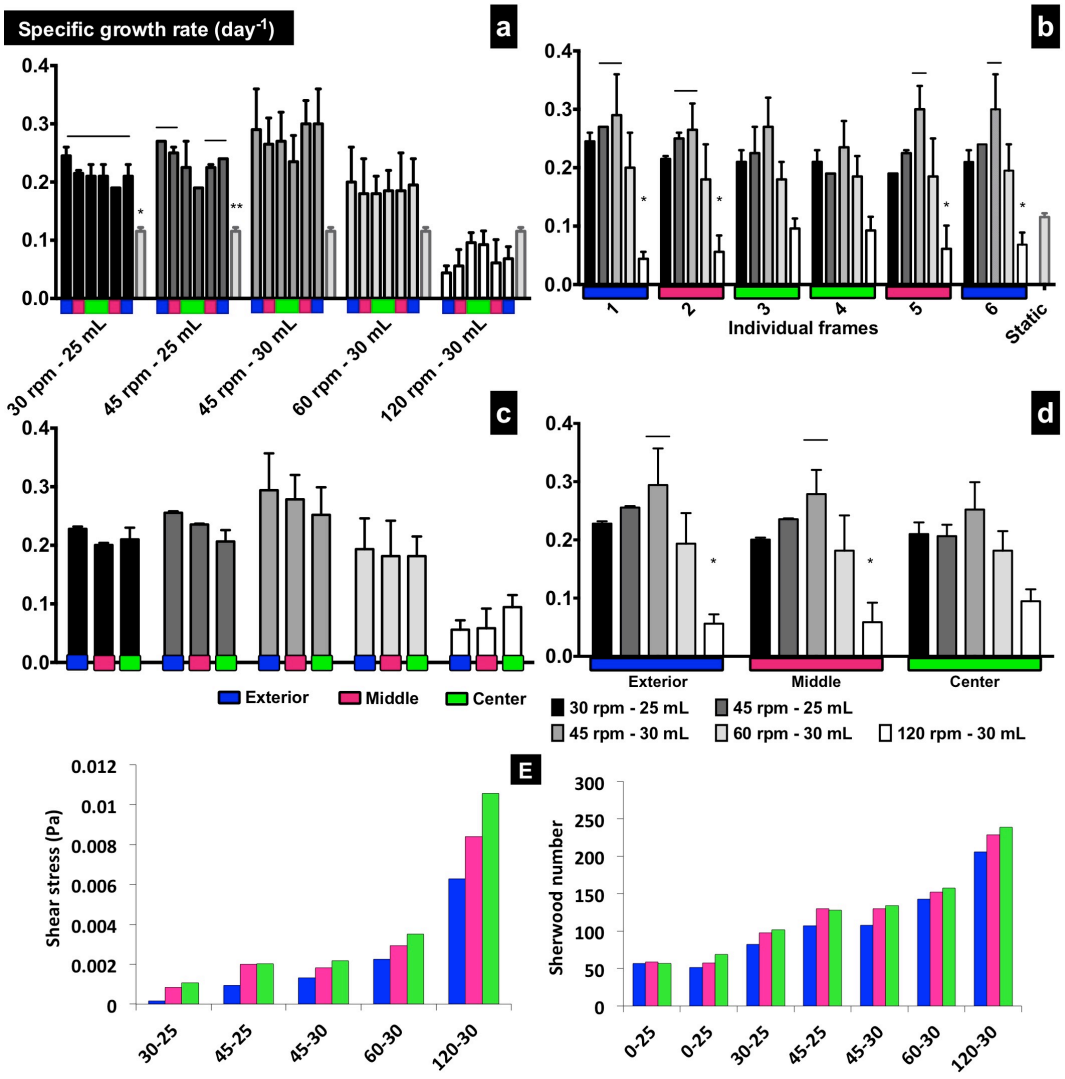

Figure V.5 – Specific growth rate profiles representations: (A) Individual frames grouped in each condition, compared with static condition represented in the grey bar at the end of the set of frames; (B) Individual frames grouped with the position (Exterior – blue, Middle – red, Centre – green); (C) Each condition distributed by the position; (D) Each position containing all conditions; n=2, ** [0.001<p<0.01[, * [0.01<p<0.05[; (E) Variation of the shear stress (left) and Sh number (right) within each region of the device.

Figures V.5 B and D represent essentially the same, what is emphasised is that in the centred position of the device, no significant differences are observed, and also the lowest specific growth rates for the higher stirring velocity (120 rpm). Also, if we look at the averages of each position independently for each condition, no significant differences are observed too. The bottom line is that the specific growth rate is higher at low rotations speeds especially at 45 rpm – 30 mL, and it decreases with the mixing velocity. Such tendency is according to the variation of shear stress, where for higher mixing rotations the shear force is higher with

possible negative impact on the cell culture. With increasing mixing velocity the rate of mass transfer increases as represented by the increase of the Sherwood number, however from a certain speed, in this case from 60 rpm, the shear stress has a negative impact on the culture. Moreover, Figure V.1 – A suggests that there is a limit in the mass transfer for higher agitation speeds.

V.4.1.4 – Characterization of the Cell Culture at the End of Expansion Stage

Figure V.6 and V.7 reports to the final time point of the expansion culture at day 10. Since this type of analysis requires sacrificing the culture it was decided to analyze only the final day, which is more relevant to understand culture characteristics before to start the differentiation stage. The cells expanded in the nanofibers not uniformly, which might have contributed to points of high cellular density, inhibiting gradually and slowing down the growth rate. As example, in Figure V.6, the immunostained samples examined at day 10 of the cellular expansion, illustrate different cellular densities found over the nanofiber frames. For example 45 rpm – 25 mL and 30 rpm – 25 mL cases reveal regions of more irregular cell spreading, compared to examples in the cases of 45 rpm – 30 mL and 60 and 120 rpm. In all the cases the cellular distribution combined both areas with aggregation and dispersion of the cellular population. The main reason for such differences in the initial cell number is due probably to the variation in the number of cells that effectively attached to the nanofibers. After two or more hours in static setting following depositing of the cells onto the nanofibers, the scaffolds were repeatedly visualized at the microscope to inspect the cell shape. With adhesion to the substrate the cells gradually appear more elongated and distorted compared when non attached (rounded sphere like shape). When the observable area with cells exhibited that morphology the nanofibers were carefully inserted into the vessel. Most likely in the cases of 60 and 120 rpm the frames were in static culture for prolonged time, enough to in fact be in equivalent cell number than in static condition. Also, it would be more cautious to increase gradually the rotation speed during the first hours of culture in the agitated vessel. Perhaps a more deep understanding of the best cell seeding conditions would be useful by determining the best cell seeding time for this system, in order to eliminate this variation.

Finally to evaluate the quality of the cells after 10 days of culture on the PCL nanofiber frames in the stirred vessel, an immunophenotype analysis for the expression of the specific antibodies Nestin, Sox2, Tuj1 and GFAP was performed (Figure V.6 and Figure V.7). The positive expression of Nestin and Sox2 antibodies (Figure V.6) validates the good quality of the cells after the expansion culture in the stirred vessel, with the NSC multipotency and self renewal primary properties conserved. Also, under these culture conditions, there was no maturation of the NSC to specific neuronal commitment, verified by the negative expression of the class III β-tubulin (Tuj1) marker. Additionally, after cellular expansion in dynamic conditions the cells were subjected to a maturation protocol (in static conditions) in order to evaluate the differentiation potential of the obtained cellular population. The presence of neurons and astrocytes in all the nanofiber frames, demonstrated by the positive expression of Tuj1 and GFAP markers, respectively (Figure V.7 - A), validates the differentiation capacity of the cell population obtained. The culture conditions at which the cellular growth was performed, at 25 and 30 mL culture media, with agitation velocities of 30, 45, 60 and 120 rpm, in nanofiber frames fixed positioned vertically, and exposed to the hydrodynamic characteristics (Chapter IV) of the designed system, maintained the cellular integrity of the NSC line ReNCellVM.

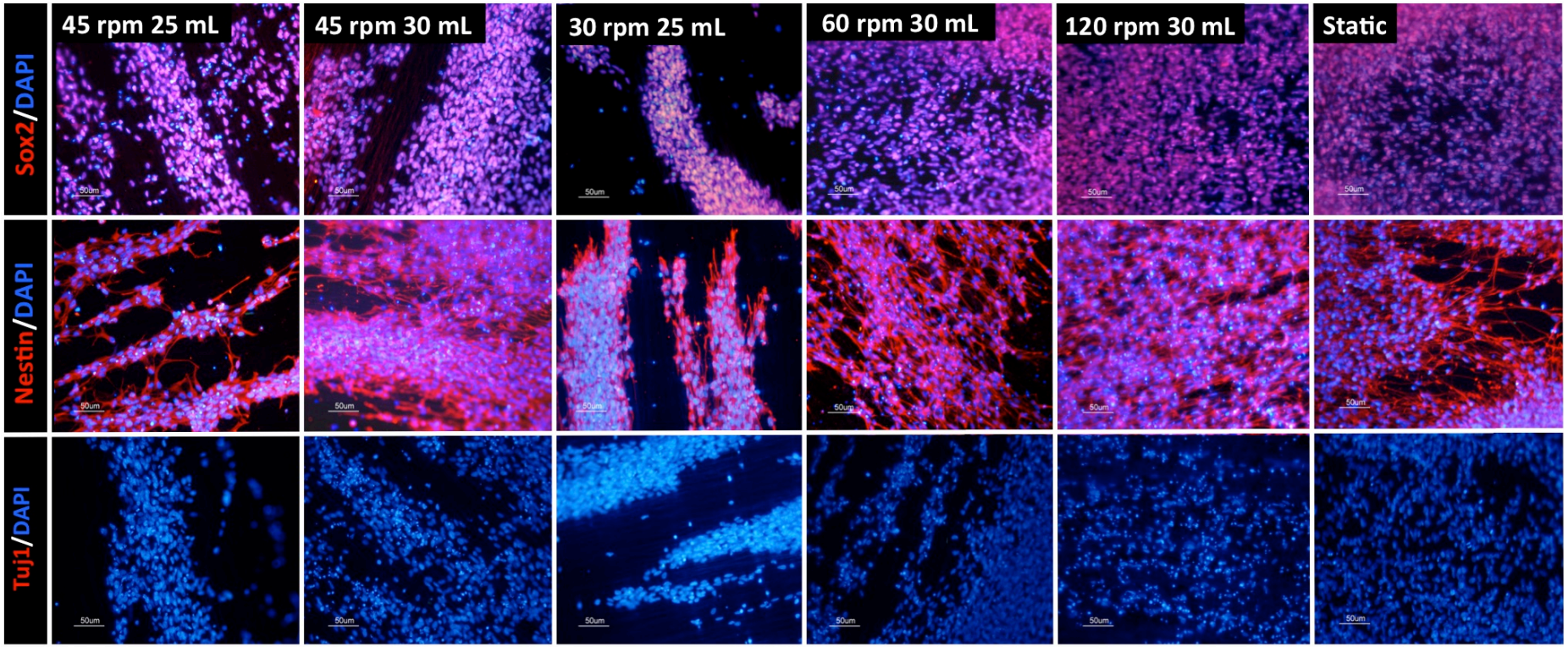

Figure V.6 – Fluorescence images for the immunophenotype analysis for Nestin and Sox2 (multipotency markers, red) and Tuj1 (neuronal marker, not observed) antibodies (red), nuclei labeled with DAPI (blue), after 10 days of culture. Scale bar 50 µm.

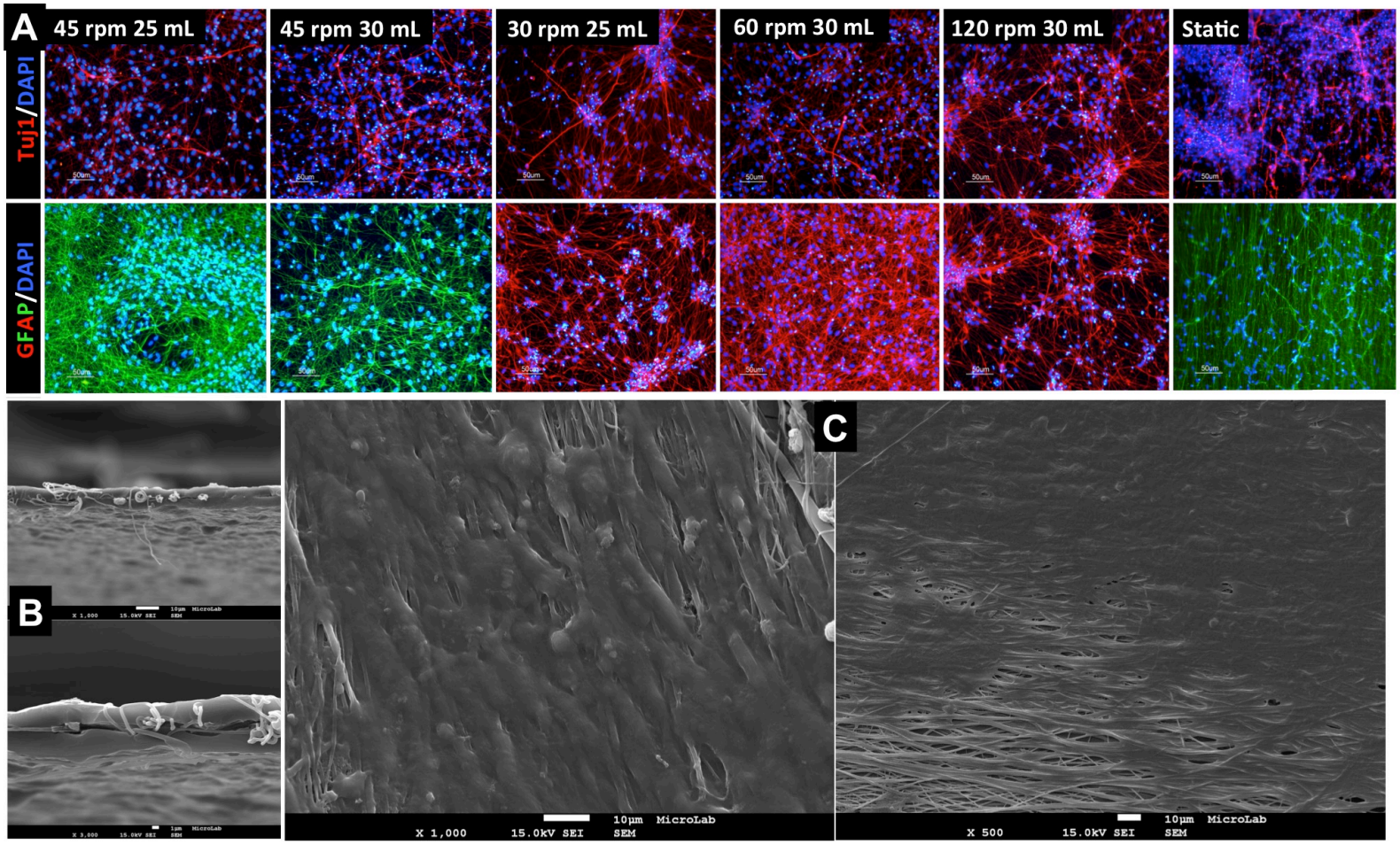

Figure V.7 – Cell characterization after the expansion culture in dynamic conditions: (A) fluorescence images for the immunophenotype analysis for Tuj1 and GFAP (glial-fibriliary precursor) antibodies (red, green), nuclei labelled with DAPI (blue), of cells expanded for 10 days in each bioreactor condition and after 15 day differentiation in standard tissue culture plates; scale bar = 50 µm. (B) SEM images illustrative of a transverse section of a scaffold with cell population; scale bars are 10 and 1 µm for 1000 × and 3000 × magnification for top and down images, respectively. (C) SEM images illustrative of the cellular population on the surface of the scaffolds after the expansion culture; magnification of 2000 × and 500 × for right and left images, respectively; scale bars = 10 µm.

The SEM images show zones of the scaffold where the cell population after the expansion period occupied extensively the surface of the nanofibers (Figure V.7 – C) and also from side to side, as shown in the scaffold transverse section images (Figure V.7 – B). That is interesting to observe, since the seeding is performed only on one side of the nanofibers, and these have a determined density to not let the cells be lost, while non adhered, during the seeding step. This means that the cells are able to migrate and proliferate surrounding the nanofibers. This is evident of the supportive role of the scaffold and an example of the 3D disposition of the cultured tissue on such support. An additional closer visualization of the 3D assembly, is represented in Figure VA.4 in Appendix. The 3D representation and respective xz and zy projections, show the general spatial arrangement of the cells-scaffold structure, while the segments along the z axis allow to visualize inside the structure (from z = 18 to z = 58).

It is in fact possible to observe that the cells migrated and proliferated populating the space inside the nanofiber mesh, reaching a depth of approximately 20.14 μm. The represented XY planes start from the bottom side to the seeding side of the scaffold, where more cells grew on the seeding side as expected, but also through the nanofibers reaching the opposite side.
It is possible to observe a thicker layer of cells occupying the scaffold, and within the nanofibers as illustrated in the xy plane images taken from z = 23 to z = 38.

The next step to explore would be to evaluate the tissue functionality in such 3D arrangement. The growth pattern was generally equivalent within the six nanofiber scaffold frames, where the cells occupied determined zones that were abundantly populated, while still a considerable area (approximately 30 – 40 %) of scaffold was available for growth at the end of the culture. This can be a consequence of the seeding procedure, where the cells attached more consistently on some points of the matrices than others. A reason might be an unevenly distribution of functionalized adhesion factor or insufficient seeding pre culture time on the tissue culture plates. Due this it is necessary to further explore new methods for the seeding and scaffold manipulation.

V.4.2 – Lactate and Glucose Variation

The analysis of the variation of the glucose consumption and lactate production allows to understand the activity of the cellular culture (Figure V.8). The gradual consumption of glucose is observed by the gradual decrease in glucose concentration in the culture medium. An irregular variation of the glucose consumption was measured, but the tendency to lower concentration along the culture is observed which means that there is metabolic activity and the culture is progressing over time. The rate of consumption for the general cases increased over time, and during the culture no inhibitor low levels of glucose were detected. Regarding lactate, over culture in all the cases this metabolite was produced gradually, with a rate of production that increased over the culture period, indicating that the cellular growth was developing regularly and no saturation of lactate was found in any case, that would led to cellular inhibition.

In Table V.1 and represented in Figure V.9, for better view, are the values obtained at day 10 for both glucose and lactate. The culture with higher metabolic activity was at the conditions of 60 rpm and 30 mL, with the lowest glucose and the highest lactate amounts at the end of the culture and respective specific rates of uptake and production. That is in agreement with the higher cell number obtained at the end of the culture at this condition (Figure V.2 – A). Also at 45 rpm - 30 mL the metabolite profile is a good indication also for the results of the cellular growth at this condition, with a behavior very similar to at 60 rpm. In contrast the lowest metabolic activity, with the lowest values regarding glucose and lactate, is in agreement with the culture at 120 rpm with the lowest cell numbers and specific growth rate.

The culture in static cell tissue culture plate (Figure VA.2 and VA.3, in Appendix), also is according with the cellular growth at this condition (Figure V.4). In this situation with only 3 mL volume of culture media per frame, the concentrations measured will be already more concentrated compared with the dynamic conditions, for both final metabolite concentrations and respective specific rates. In this cases, the lower volume in culture and with higher starting cells in culture the faster the metabolite activity is noticed due to the lower volume in culture.

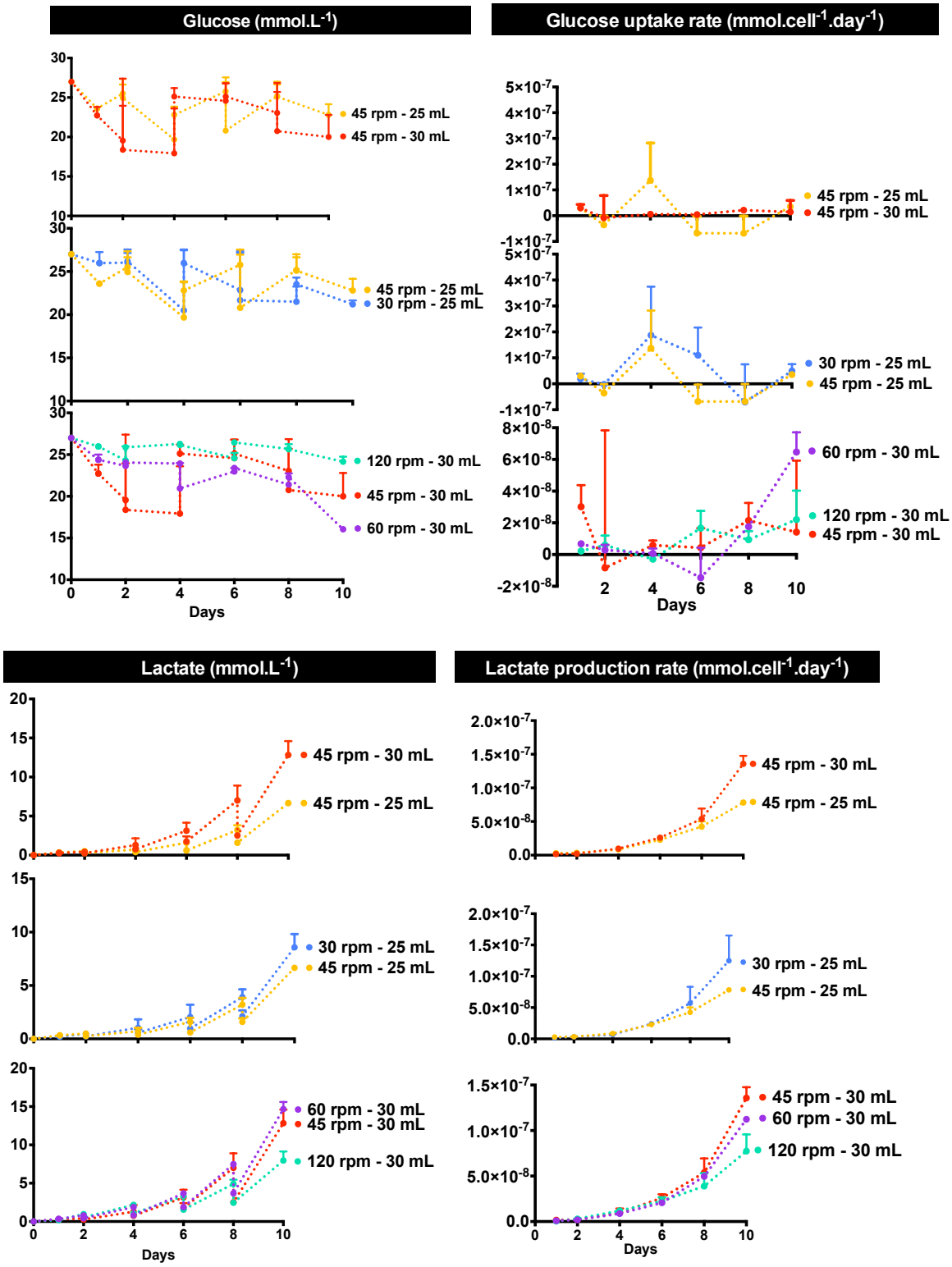

Figure V.8 – Glucose and lactate concentrations (mmol.L^{-1}) over the culture period, and specific rates (mmol.cell^{-1}.day^{-1}) of lactate production and glucose uptake over time; n=2.

Table V.1 – Lactate and glucose concentrations (mmol.L^{-1}) in culture media, lactate and glucose specific rates (mmol.cell^{-1}.day^{-1}) of production and uptake, respectively, at day 10 of cell culture.

	Lactate		Glucose	
	mmol.L^{-1}	mmol.cell^{-1}.day^{-1}	mmol.L^{-1}	mmol.cell^{-1}.day^{-1}
45 rpm – 25 mL	6.7 ± 0.2	$7.8\times10^{-8} \pm 3.7\times10^{-9}$	22.8 ± 1.4	$3.5\times10^{-8} \pm 4.3\times10^{-10}$
45rpm – 30 mL	12.8 ± 1.8	$1.6\times10^{-7} \pm 1.2\times10^{-8}$	20.0 ± 2.8	$1.4\times10^{-8} \pm 4.5\times10^{-8}$
30 rpm – 25 mL	8.6 ± 1.2	$1.2\times10^{-7} \pm 4.0\times10^{-8}$	21.2 ± 0.4	$5.0\times10^{-8} \pm 2.6\times10^{-8}$
60 rpm – 30 mL	14.7 ± 0.9	$1.1\times10^{-7} \pm 1.6\times10^{-9}$	16.1± 0.3	$6.5\times10^{-8} \pm 1.8\times10^{-8}$
120 rpm – 30 mL	8.0 ± 1.2	$7.7\times10^{-8} \pm 1.8\times10^{-8}$	24.2 ± 0.6	$1.8\times10^{-8} \pm 3.7\times10^{-8}$
Static (3 mL)	20.5 ± 2.6	$1.0\times10^{-6} \pm 2.1\times10^{-7}$	14.5 ± 2.9	$4.6\times10^{-7} \pm 7.6\times10^{-9}$

The lactate produced is dependent on the specific lactate production rate and number of cells. In spite of regular half media changes every two days, for the conditions with higher cell densities it was observed a lactate accumulation at values of 14.7 and 20.5 mM for 60 rpm at 30mL and in static culture, respectively, which are near the lower boundary for inhibitory effects (16 – 35 mM for mesenchymal stem cells). Considering that for frames ill-mixed, the difference between the lactate in the bulk and at the frame liquid interface can reach 1.77 mmol.L^{-1}, these values became of concern. Additionally one should consider that cells are not only attached to electrospun nanofiber mesh but also populate its porous structure and additional mass transfer resistances will likely exist to the diffusion of lactate inside the nanofiber mesh. For additional information on the cell population inside the nanofiber mesh see confocal image in Appendix Figure VA.4.

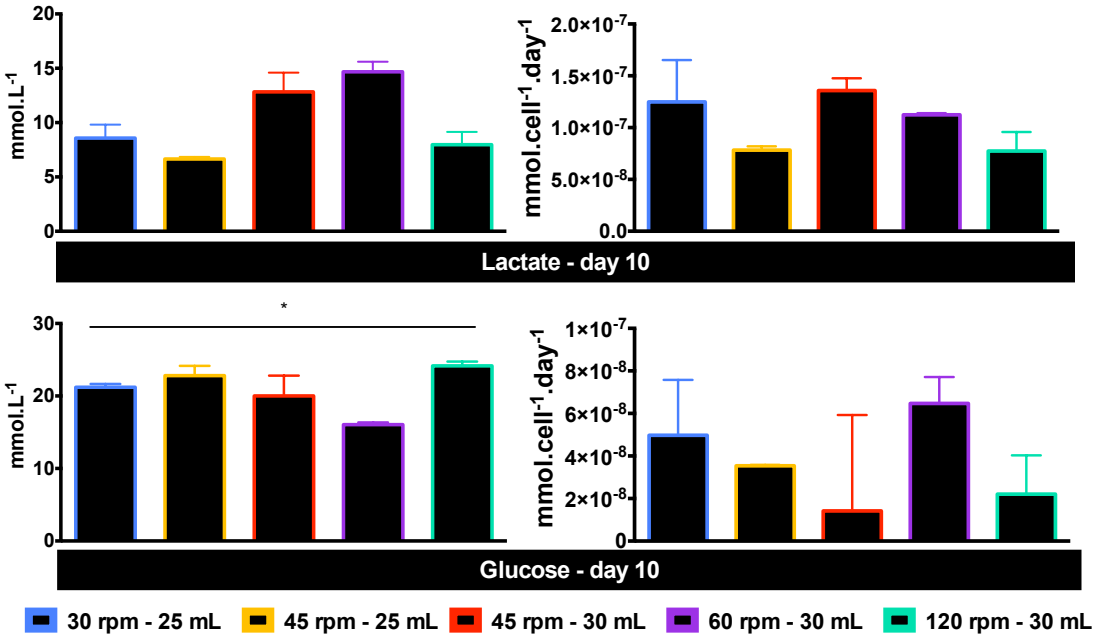

Figure V.9 - Lactate and glucose concentrations and specific rates of production and uptake, respectively, relative to day 10 (n=2). * [0.01<p<0.05[.

V.4.3 – Characterization of Differentiated NSC in Dynamic Conditions

The NSCs were seeded on the scaffolds of aligned nanofibers functionalized with laminin (PCL-LN) and after 24 hours in expansion media, the growth factors were removed to promote differentiation.

The conditions presented refer to the dynamic cell culture at 45 rpm – 30 mL compared to the static condition in standard tissue culture plate. Based on the device hydrodynamic characteristics and the results on cell culture expansion, the decision was made to evaluate the device performance on the cellular differentiation under the most promising culture condition, which was estimated to be at 45 rpm – 30 mL. The results in the dynamic culture refer to the average of the centred positions in the device. After 15 days in culture the scaffolds were analysed by immunostaining. Figure V.10 - A (on the left) shows the expressed markers identifying the differentiation of neurons and glial cells (expression of Tuj1 and GFAP markers, respectively) present in both conditions.

In Figure V.10 – A on the right is presented the quantification of each of the expressed markers. The quantification was based on the analysis of the immunofluorescence images (a minimum of 10 images

were analysed for each condition with ImageJ), by measuring the area corresponding to the each of the markers visible on the images. The measured areas were normalized for an average image area, from which the relative percentage of observed marker is represented. This method is approximated and eventually gives an overestimation of both markers. The total number of cells analysed in each case (corresponding to the DAPI stained nuclei) was also determined by the same method. Assuming an estimated average area of a cell nucleus of 65 μm^2 an average total cell number is estimated for each case. Overall the differences were found to be not statistically meaningful. A higher number of total cells were observed for the static condition, and a higher percentage of expression of GFAP marker was found for both conditions. Also, the percentage of expressed markers was higher for the dynamic culture condition. (4.33 % for Tuj1 and 7.34% for GFAP and 3.51% and 4.89 % for the static condition, respectively).

In Figure V.10 – B are represented the histograms of the angles distribution of the alignment of the neurites relative to the alignment of the nanofiber matrix. It is evident for both conditions that the cellular extensions are distributed according to an aligned pattern provided by the aligned nanofiber. Also, the degree of alignment was found to be higher for the dynamic culture, where approximately 50% of the cells are found within the same orientation, compared to 30% for static condition.

In Figure V.10 – C (on the left) is shown the general distribution of the neurites length measured, and the respective average shows a significant difference in the cell extensions, where a high length of 228.1 μm was found for the dynamic culture compared to the 111.3 μm found for the static culture.

Overall, no statistical significant differences were found on the output of differentiated cells. However the results seem promising, the stirred device performed adequately providing a higher number of differentiated cells (higher percentage of observed marker per total cells analysed), compared to the static condition, where an indication of a higher number of astrocytes was observed for both conditions. The differentiated cells followed the directive cue of the scaffold matrix, being aligned according to the nanofiber aligned pattern. Moreover the differentiated cells in dynamic culture were found to elongate more significantly compared to the static condition.

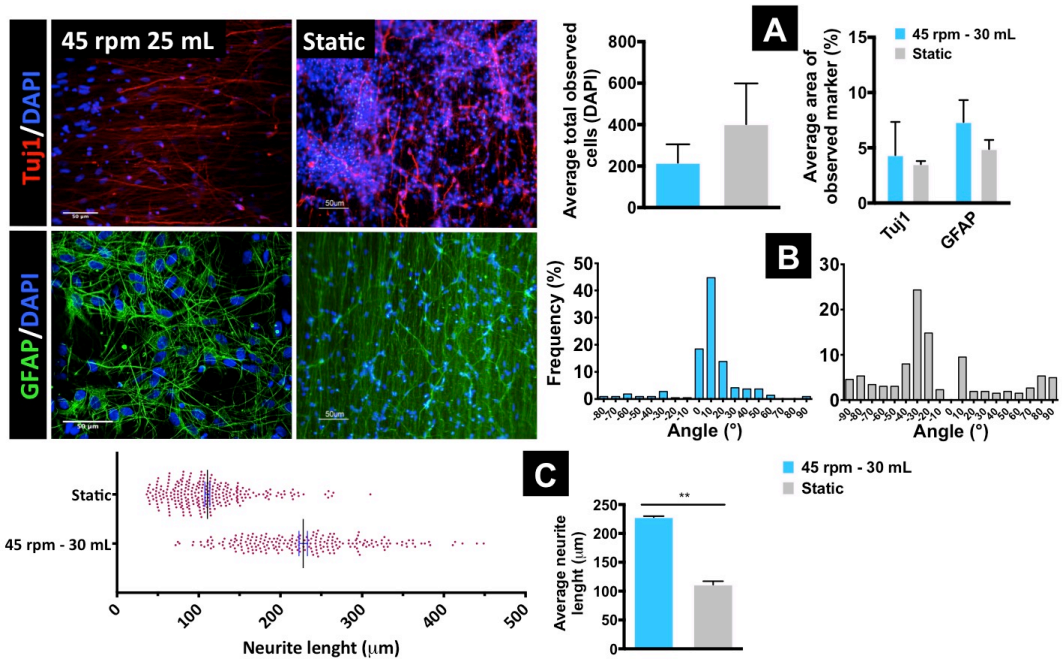

Figure V.10 – Characterization of the cell culture after differentiation in dynamic conditions (45 rpm – 30 mL) compared with static culture in a standard tissue culture plate: (A) Fluorescent images of the expression of Tuj1 and GFAP antibodies and respective quantification from the immunofluorescence images; scale bars = 50 μm; (B) Histograms for the alignment of neurites for static and dynamic culture; minimum of 100 cells measured. (C) Distribution of the measured neurite lengths (major bar is the average with SEM for small bars) and respective average; minimum of 100 cells measured. Statistical analysis was performed for average total of observed cells (DAPI) and average neurite length with an unpaired t-Test assuming a two tailed Gaussian distribution with CI of 95% where significant differences are for $p < 0.05$ and ** is $0.001 < p < 0.1$. Statistical analysis was performed to the percentage of average area of observed markers with unpaired two way ANOVA with multiple comparisons test, statistical significant differences are for $p < 0.05$. Error bars are SEM, n=2.

V.4.4 – Comparative Analysis with Systems Reported in Literature

After performing a search in Web of Science database, combining the keywords “nanofiber scaffolds stirred bioreactor fluid dynamic characterization vessel device neural stem cells expansion differentiation design model system”, no publications are found presenting a similar device. Most examples for NSCs rely on stirred suspension culture systems in cell aggregates or in microcarriers instead of other supports as scaffolds and, fewer studies present the results including the hydrodynamic characterization besides the cell culture output. With that some examples were taken

from the literature (Table V.2), in an attempt to compare the concept presented in this thesis regarding some hydrodynamic parameters.

Most of the examples shown refer to suspension culture systems except for (Bueno et al. 2004; Bilgen et al. 2006). This means that the cells in the stirred reactors are subjected to variable shear stress during the culture, due to the aggregate movement in the vessel, therefore when closer to the impeller or stirrer the cells feel higher shear than when closer to the walls (which is zero). Sen et al. and Ismadi et al. all present higher shear stress values compared to the ones for the nanofiber frames at equivalent agitation velocities, while our values are comparable for instant shear stress at 90 rpm – 25ml of 0.15 Pa (Table IVA.8) with Wang et al.

In the case of wave wall device (Bueno et al. 2004; Bilgen et al. 2006) (50 rpm, 0-0.06Pa), in this system the scaffolds are fixed at the centre of a modified spinner flask with wave walls, so the distance to the stirrer is constant, so the shear will be constant at the surface of the scaffolds constructs. In terms of average shear stress this system operates at values much higher, than the mean values for the nanofiber frames (45 rpm/25 - 30 mL, 0.00349 – 0.00219 Pa or at 60 rpm/25 - 30 mL, 0.0645 – 0.0409 Pa), which is valid to be applied to MSCs as these cells support higher values of shear stress, for example to induce osteogenesis at 1.2 Pa (Delaine-Smith and Reilly 2012).

Regarding the shear stress effect for NSCs there is some variable results reported in literature. NCS cultured under shear stress of 0.2 – 0.4 Pa in a microfluidic device in aligned laminin coated nanofibers, responded to the chemical gradients and topography of the fibers without demonstrating any alteration due to shear stress. (Wallin et al. 2012). Another study reported, an optimal shear stress of 0.004 Pa applied to maintain NSCs in culture (without expressing any alterations on proliferation and differentiation), under a steady laminar flow, in a microfluidic device (based on the shear stress range of the in vivo conditions experienced by NSCs (0.01 – 0.001 Pa)) (Wang et al. 2014). An interesting study on radial glial cells cultured under relevant physiologic shear stress (under laminar steady flow in a microfluidic device) showed a dramatic enhanced proliferation with increase in shear stress from 0.0001 to 0.001 Pa, corresponding to the minimum physiological ventricular wall shear stress of the cerebrospinal fluid in vivo, which is estimated to be in the range of 0.001~0.0018 Pa. It was reported that the increase in proliferation of the radial glial cells is due to the activation of mechanosensitive Ca^{2+} channel in response to the shear stress. (Guirao et al. 2010; Park et al. 2017).

However these values are in a very low range and report to very specific shear conditions, so not comparable to the conditions of the presented stirred systems.

Looking at the Re numbers it is clear that the numbers operating in such systems are significantly higher, as this parameter refers to the tip of the agitation device, thus depending on its geometry. The stirrer used in the nanofiber frame device is clearly smaller so the respective Re are accordingly much lower (120 rpm, 20.57).

The specific growth rate or end cell densities can point to the efficiency of mixing of the system, i.e. the higher cell outcome or growth kinetics the best the device was able to perform. From the cases presented apparently the first three cases in the Table 2 lay within the same range of initial and end cell densities performing equivalently, on the other hand the nanofiber frame stirred system best output was at 45 rpm – 30 mL with 6.3×10^5 cell.cm^{-2} , from an initial cell density of 4×10^5 cell.cm^{-2} , indicating that the system in comparison with this devices may have performed lower. Concerns regarding possible stagnant regions of the device need to be optimized, however this is a comparison between two different types of material supports for cell culture (fixed nanofiber scaffolds vs microcarriers or cells in suspension aggregates), and in these cases have fluid regimes in the laminar-turbulent range, meaning that the mixing is definitely more effective than in nanofiber stirred device which is in this case characterized as in a laminar – oscillatory regime.

Table V.2 - Table comparing the features of the bioreactor developed in this thesis with the ones of other systems reported in literature.

Type of culture	Device, experimental conditions	Cell culture output:	Hydrodynamic parameters	Shear stress (Pa)	Hydrodynamic effects	Main findings	Reference
NSC; suspension aggregates; 4 days	Spinner flask 125 mL, working volume 100 mL; magnetic stirrer; medium viscosity and agitation rate variation to control the maximum mean aggregate diameter D_{MAVG}	Seeding: 7.5 × 10^4 cells.mL^{-1} End: 8 × 10^5 cells.mL^{-1} C_{lac} = 4 mmol.L^{-1}	60, 80,90, 95, 100	0.625–0.986, maximum shear at the surface of the aggregates to dislodge the cells, without causing cell damage, limiting D_{MAVG}	Increase in agitation results in a lower D_{MAVG} , high shear experienced by the cells on the surface of the aggregate more cells are shed from the surface; increase in kinematic viscosity results in higher D_{MAVG}, mechanical forces on the cells are reduced with decrease in shear stress	D_{MAVG} occurs when the Kolmogoroff eddy η scale becomes 54–84% of the aggregate diameter: D_{MAVG} 80 μm, η147 mm, and at D_{MAVG} 160 mm, η187 μm	(Sen et al. 2002)
hiPSC; suspension aggregates; 5 days	Spinner flask 100 mL working volume 60 mL; Glass ball spinning pendulum	Seeding: 4-5× 10^5 cells.mL^{-1} End: 1-1.5 × 10^6 cells.mL^{-1}, C_{lac} = 10 mmol.L^{-1}	40-60-75 rpm, with respective maximum cell Re of 867, 1313, 1649; 40 rpm with convective vertical flow velocity of 0.018m.s^{-1}; 60 rpm with maximum instant velocity of 0.16 m.s^{-1}	0.152 maximum at 75 rpm, CFD (tip of the spinning ball), mild shear impact lower than other types of impellers	Stable flow profile without large turbulence for all rpm; highest local Re, at the small area tracking the rotating pendulum, which increased from laminar (Re < 1000) to laminar-turbulent regime (1000 < Re < 2000);	Highest cell density at 60 rpm; larger aggregates with diffusion limitation at 40 rpm; lower cell viability at 75 rpm; Steady flow in all agitation with small turbulent flow at 75 rpm according to the local Re; the resulting shear stress is considerably lower than other types of impellers.	(Wang et al. 2013)
ESCs Suspension aggregates	Suspension bioreactors 10 and 100 mL	Seeding: 3.5 × 10^4 cells.mL^{-1} End: 1.2 × 10^6 (10mL, 140 rpm)	40-60-80-100-120-140 rpm Re = 614 (10 mL, 40 rpm) Re = 8660 (100 mL, 140 rpm); maximum velocities, 0.08 ms^{-1} (100 mL), 0.03 m.s^{-1} (10 mL)	Maximum shear rate 40 times greater than the volume average shear rate for 100 and 10 mL	Laminar – turbulent regime (Re); Turbulent regime (CFD) Higher agitation rates increases the fluid velocity, the shear rate and energy dissipation rate ; volume average velocity and volume average shear rate vary linearly with the agitation; the volume average energy dissipation rate increases exponentially with the agitation.	Scale up from 10 to 100 mL by prediction of required agitation rates based on fixed volume-average hydrodynamic variables; 3.5 scale up factor predicted. 92 rpm best agitation for 100 mL	(Borys et al. 2018)
-	Wavy walled bioreactor 330mL (modified spinner flask with PGA scaffolds fixed at the center of the vessel)	-	50 rpm – Re=1246; maximum average fluid velocity 0.035m.s^{-1};	0 – 0.06, average at the constructs.	Turbulent fluid regime; recirculating fluid in the lobes regions promoting higher stimuli for cartilage growth.	Flow field differs from the standard spinner flask and by the position of the scaffolds: reduced tangential velocity and increase in axial velocity;	(Bueno et al. 2004; Bilgen et al. 2006)
iPSC suspension microcarriers 7 days	Spinner flask (flat impeller)	Seeding: 2 × 10^5 cells.mL^{-1} End: 1.5 fold relative to static.	20-25-30-35-40–45 rpm max. velocity 0.11m.s^{-1} 40 rpm, Re = 2670 25 rpm, Re = 1669	Max. 0.0984, mean 0.0520 (25 rpm); Max. 0.108, mean 0.0192 (28 rpm)	Turbulent flow regime; highest shear stress at downstream of the flat impeller; highest velocity at the bottom surface of the flask.	Higher rotations improved the mixing but increased shear stress affecting cell growth: 25 rpm best cell growth, 28 rpm cell growth decrease	(Ismadi et al. 2014)

V.5 - Conclusions

Overall the results obtained for the cell culture agree with the hydrodynamic profile of the vessel, except the different tendencies on the cellular growth between the regions of the vessel. The better culture conditions can be considered at 45 and 60 rpm (as a limit) at 30 mL. The highest cell numbers were obtained, and the highest metabolic activity was observed. Also at this conditions the shear stress and mass transport rates are in a satisfactory interval that allow good mixing conditions.

The current study finds that NSC (RenNcells) are very sensitive to shear stress and mass transfer limitations. However the current system is able to provide fine control conditions supporting a optimal cell culture conditions at 45 rpm 30mL. Also this condition was able to support NSCs culture differentiation under dynamic conditions. Moreover the bioreactor presents advantages such as scalability, easiness to sterilize and suitable to be used in commercial available cell culture incubators.

The designed vessel is considered a promising prototype to apply to further development for NSC culture applications. Additional culture conditions can be studied for example at more extreme conditions, and without initial cell seeding variations which affects extensively the cellular growth of the cell population over time, in order to visualize more clear the limitations and best performance of the bioreactor.

Appendix

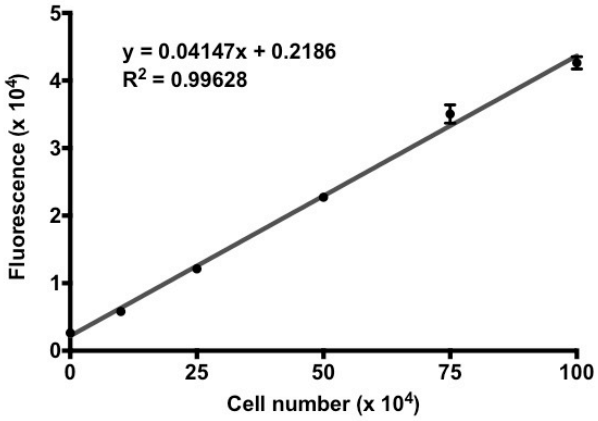

Figure VA1 – Calibration curve of the fluorescence, of the Alamar Blue® reduced product, as a function of ReNcell®VM cell number. (n=3)

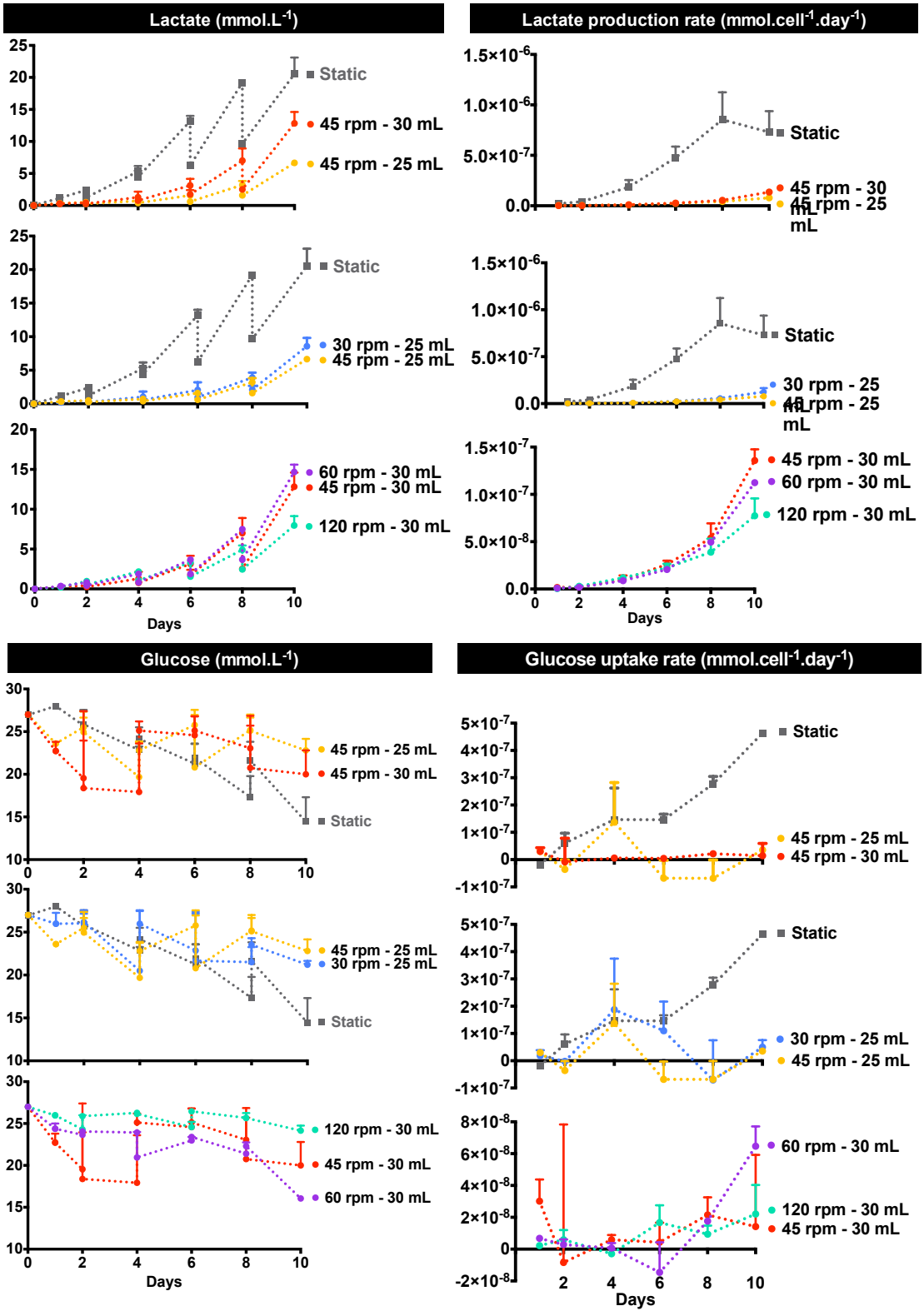

Figure VA.2 – Glucose and lactate concentrations (mmol.L^{-1}) over the culture period, and specific rates (mmol.cell^{-1}.day^{-1}) of lactate production and glucose uptake over time compared with static condition; n=2.

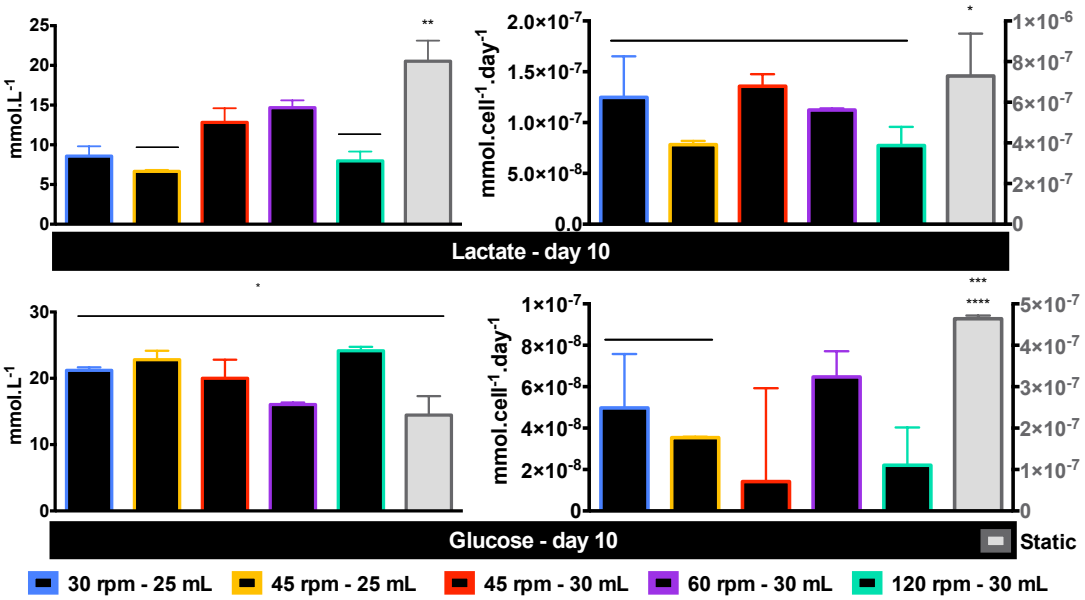

Figure VA.3 - Lactate and glucose concentrations and specific rates relative to day 10 compared with static condition (n=2). **** p<0.0001, * [0.0001<p<0.001[, ** [0.001<p<0.01[, * [0.01<p<0.05[.**

Table VA.1 – Condition 30 rpm 25 mL: final cell numbers throughout the 10 days of culture obtained in each frame and average for each vessel region and global average.

30 rpm 25 mL		Cell number (× 10^4) ± *SEM*									
Days		1		2		4		6		8		10	
Frames	1	4.68	*2.29*	6.48	*3.40*	16.56	*11.77*	18.79	*11.49*	27.25	*14.87*	32.96	*16.52*
	2	4.58	*2.39*	6.72	*3.61*	14.66	*9.98*	14.35	*7.60*	21.13	*9.99*	22.77	*8.71*
	3	4.80	*2.48*	6.73	*3.39*	16.46	*10.61*	15.65	*9.06*	22.94	*13.58*	23.16	*12.83*
	4	4.51	*2.09*	6.44	*3.06*	15.41	*10.62*	14.39	*8.26*	22.09	*11.84*	24.44	*11.10*
	5	4.71	*2.40*	6.95	*3.56*	14.54	*9.57*	13.54	*7.50*	18.66	*9.25*	20.78	*8.02*
	6	5.08	*2.36*	7.24	*3.67*	15.02	*9.77*	15.08	*6.78*	22.20	*7.73*	25.34	*4.84*
Region	E	9.76	*4.64*	13.72	*7.07*	31.58	*21.54*	33.87	*18.27*	49.45	*22.60*	58.29	*21.36*
	M	9.28	*4.79*	13.67	*7.17*	29.20	*19.55*	27.90	*15.10*	39.80	*19.24*	43.54	*16.74*
	C	9.31	*4.57*	13.17	*6.45*	31.86	*21.23*	30.04	*17.32*	45.02	*25.42*	47.60	*23.93*
Global		28.36	*14.01*	40.57	*20.70*	92.64	*62.33*	91.80	*50.68*	134.27	*67.26*	149.43	*62.02*

Table VA.2 – Condition 45 rpm 25 mL: final cell numbers throughout the 10 days of culture obtained in each frame and average for each vessel region and global average.

45 rpm 25 mL		Cell number (× 10^4) ± *SEM*									
Days		1		2		4		6		8		10	
Frames	1	5.49	*0.00*	3.38	*1.52*	8.28	*5.63*	13.98	*9.75*	21.69	*14.33*	31.95	*14.83*
	2	5.11	*0.38*	4.25	*0.65*	9.57	*4.34*	16.48	*7.24*	25.90	*10.11*	36.94	*9.84*
	3	4.73	*0.00*	4.19	*0.59*	8.56	*3.33*	14.11	*4.87*	20.47	*4.68*	28.31	*1.20*
	4	5.48	*0.75*	4.38	*0.40*	8.86	*3.02*	14.13	*4.84*	20.49	*4.65*	32.27	*2.76*
	5	6.23	*0.00*	4.91	*0.93*	9.30	*3.45*	13.50	*4.22*	19.11	*3.28*	30.16	*4.87*
	6	6.17	*0.05*	6.85	*1.01*	12.41	*0.34*	18.44	*0.72*	24.27	*1.88*	29.66	*4.37*
Region	E	9.34	*0.00*	6.99	*1.48*	15.03	*6.91*	24.62	*11.88*	38.51	*17.47*	55.70	*12.28*
	M	9.75	*0.00*	9.44	*0.31*	18.35	*5.26*	30.33	*6.55*	51.50	*1.78*	59.48	*2.55*
	C	12.35	*0.00*	11.48	*0.37*	21.02	*3.10*	31.13	*2.69*	43.88	*1.88*	61.20	*7.87*
Global		31.44	*0.00*	27.92	*1.42*	54.40	*15.27*	86.08	*21.12*	133.90	*17.57*	176.37	*1.85*

Table VA.3 – Condition 45 rpm 30 mL: final cell numbers throughout the 10 days of culture obtained in each frame and average for each vessel region and global average.

45 rpm 30 mL		Cell number (× 10^4) ± *SEM*									
Days		1		2		4		6		8		10	
Frames	1	6.02	*1.76*	8.62	*4.62*	14.63	*5.82*	21.48	*3.81*	32.66	*2.24*	31.84	*1.63*
	2	6.27	*1.04*	8.56	*3.14*	14.98	*3.72*	21.18	*1.39*	30.24	*4.09*	27.21	*0.32*
	3	7.30	*1.20*	9.46	*4.36*	16.15	*5.65*	23.03	*3.67*	34.95	*0.59*	31.33	*4.26*
	4	7.16	*0.63*	10.17	*3.12*	15.36	*2.10*	21.70	*0.25*	31.89	*6.10*	27.40	*0.83*
	5	6.57	*1.14*	9.21	*3.36*	17.28	*4.90*	25.96	*2.47*	40.19	*3.96*	40.24	*1.64*
	6	5.63	*2.91*	7.67	*4.89*	13.67	*7.84*	19.75	*8.53*	29.17	*5.27*	30.44	*10.61*
Region	E	11.66	*4.68*	16.29	*9.50*	28.29	*13.66*	41.23	*12.34*	61.83	*3.04*	62.28	*12.24*
	M	12.85	*2.18*	17.77	*6.50*	32.25	*8.62*	47.14	*3.86*	70.43	*8.05*	67.44	*1.96*
	C	14.46	*1.83*	19.63	*7.48*	31.51	*7.76*	44.73	*3.92*	66.84	*6.69*	58.72	*3.43*
Global		38.97	*8.69*	53.69	*23.48*	92.05	*30.04*	133.10	*20.12*	199.10	*11.71*	188.45	*17.64*

Table VA.4 – Condition 60 rpm 30 mL: final cell numbers throughout the 10 days of culture obtained in each frame and average for each vessel region and global average.

60 rpm 30 mL		Cell number (× 10^4) ± *SEM*											
Days		1		2		4		6		8		10	
Frames	1	13.88	*2.70*	19.43	*0.30*	25.80	*0.48*	31.79	*0.98*	34.18	*0.04*	38.39	*2.37*
	2	15.47	*3.50*	19.54	*1.07*	26.66	*0.91*	33.94	*0.51*	36.32	*1.11*	39.01	*3.10*
	3	16.02	*2.24*	21.81	*0.66*	28.39	*1.38*	36.91	*1.73*	40.61	*1.02*	41.29	*0.84*
	4	13.50	*0.08*	18.09	*2.71*	24.65	*2.66*	30.54	*2.65*	33.17	*2.77*	35.22	*5.60*
	5	16.61	*2.25*	21.77	*0.57*	29.01	*2.26*	36.54	*2.51*	39.22	*3.79*	42.90	*7.99*
	6	17.99	*1.63*	23.65	*0.95*	32.65	*1.86*	38.45	*2.04*	43.20	*3.28*	48.26	*1.76*
Region	E	31.87	*4.33*	43.08	*0.65*	58.45	*1.38*	70.24	*3.02*	77.38	*3.32*	86.64	*0.61*
	M	32.08	*5.75*	41.31	*0.50*	55.67	*1.36*	70.48	*2.00*	75.54	*4.90*	81.91	*11.09*
	C	29.52	*2.31*	39.90	*2.05*	53.04	*1.28*	67.45	*0.92*	73.77	*1.75*	76.51	*6.44*
Global		93.47	*12.39*	124.29	*2.20*	167.16	*4.01*	208.18	*0.11*	226.69	*3.33*	245.06	*18.14*

Table VA.5 – Condition 120 rpm 30 mL: final cell numbers throughout the 10 days of culture obtained in each frame and average for each vessel region and global average.

120 rpm 30 mL		Cell number (× 10^4) ± *SEM*											
Days		1		2		4		6		8		10	
Frames	1	18.73	*0.07*	22.36	*0.74*	21.27	*0.68*	21.95	*0.62*	25.26	*2.77*	23.37	*2.19*
	2	18.40	*0.61*	22.25	*2.48*	22.35	*0.72*	23.40	*3.33*	27.91	*6.95*	25.48	*2.35*
	3	18.47	*0.94*	22.65	*1.01*	23.39	*2.18*	29.51	*2.63*	39.19	*6.81*	41.53	*2.96*
	4	18.03	*1.11*	22.81	*1.71*	24.31	*0.22*	28.40	*3.65*	35.64	*7.63*	33.25	*4.48*
	5	18.55	*0.00*	21.93	*1.08*	22.70	*0.20*	25.00	*4.37*	29.34	*8.09*	27.77	*5.17*
	6	18.25	*0.05*	21.59	*0.10*	23.29	*0.80*	24.78	*2.38*	29.44	*5.67*	30.46	*1.69*
Region	E	36.98	*0.02*	43.95	*0.85*	44.56	*1.48*	46.73	*3.01*	54.70	*8.44*	53.84	*0.49*
	M	36.95	*0.61*	44.18	*3.55*	45.05	*0.92*	48.40	*7.69*	57.25	*15.04*	53.25	*7.52*
	C	36.50	*2.05*	45.46	*2.72*	47.70	*1.96*	57.90	*6.28*	74.84	*14.44*	74.77	*7.44*
Global		110.43	*2.64*	133.59	*7.12*	137.32	*2.52*	153.03	*16.98*	186.78	*37.92*	181.86	*14.46*

Table VA.6 - Average specific growth rates from the expansion culture in the stirred device, for each individual frame (1 – 6), per vessel region (E – external, M – Middle , C – Centre) and global. (day-1 ± SEM).

	45 rpm - 25 mL		45 rpm - 30 mL		30 rpm - 25 mL		60 rpm - 30 mL		120 rpm - 30 mL	
1	0.270	0.000	0.290	0.070	0.245	0.015	0.200	0.060	0.044	0.012
2	0.250	0.010	0.265	0.045	0.215	0.005	0.180	0.060	0.056	0.028
3	0.225	0.045	0.270	0.050	0.210	0.020	0.180	0.030	0.096	0.017
4	0.190	0.000	0.235	0.045	0.210	0.020	0.185	0.035	0.093	0.023
5	0.225	0.005	0.300	0.040	0.190	0.000	0.185	0.065	0.061	0.040
6	0.240	0.000	0.300	0.060	0.210	0.020	0.195	0.045	0.068	0.021
E	0.256	0.002	0.294	0.063	0.228	0.004	0.194	0.053	0.056	0.016
M	0.236	0.002	0.279	0.042	0.201	0.004	0.182	0.061	0.059	0.034
C	0.207	0.020	0.252	0.047	0.210	0.020	0.182	0.034	0.095	0.021
Global	0.233	0.008	0.275	0.051	0.213	0.004	0.186	0.050	0.070	0.024
	Static: 0.116 ± 0.007 day^{-1}									

Table VA.7 – Cell densities at the end of the expansion culture ($\times 10^4$ $cells.cm^{-2}$ ± SEM)

	45 rpm - 25 mL		45 rpm - 30 mL		30 rpm - 25 mL		60 rpm - 30 mL		120 rpm - 30 mL	
Day 10	54.11	4.05	62.82	5.88	49.81	20.67	81.69	6.05	60.62	4.82
	Initial cell density/frame = 6.7, Total cell density = 40, Nanofiber frame area = 3 cm^2									

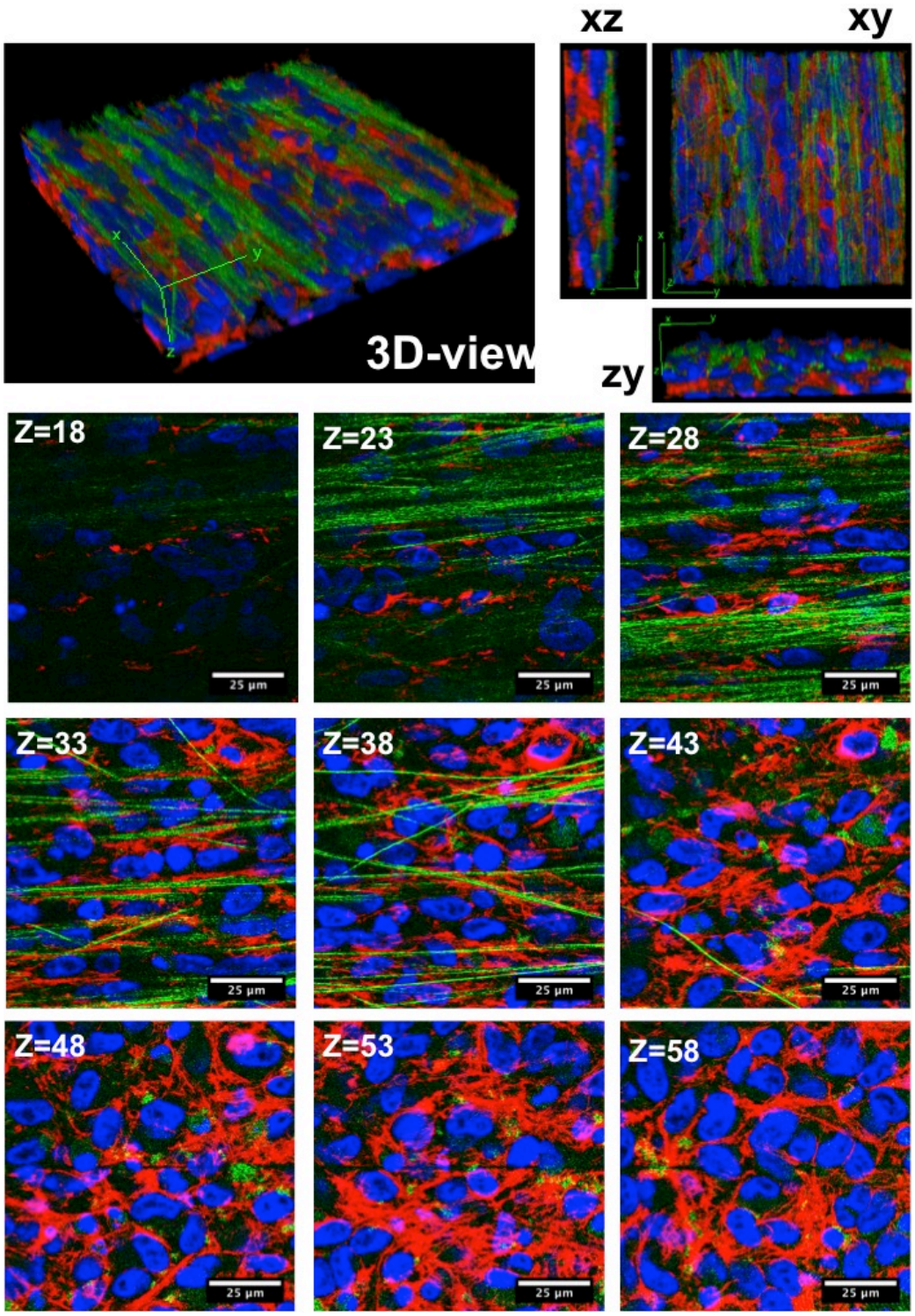

Figure VA.4 - 3D representation and respective xz, zy and xy projections of immunofluorescent images of NSC expressing Nestin (red), after dynamic expansion culture in frames of aligned nanofibers at 45 rpm - 30 mL in the stirred device. Nuclei are DAPI stained (blue) and the nanofibers are visualized in green. Δz=503.5 nm, 101.25 x 101.25 mm, 512 x 512 pixel; scale bar 25 µm. The images were acquired with confocal/multiphoton laser scanning imaging with TCS-SP5 inverted microscope (Leica), equipped with continuous Ar ion laser (458, 465, 488, 496 and 514 nm), a HeNe laser (633 nm) and a Ti:Sapphire (Spectra-Physics Mai Tai BB, 710-990 nm, 100 fs, 82 MHz). Two objectives were used, a high

numerical aperture water immersion objective (HCX PL APO CS 63.0x1.20 WATER UV, Leica) and low numerical aperture dry objective (HCX PL APO CS 10.0x0.40 DRY UV, Leica), for higher and lower magnifications, respectively. Multiphoton excitation was applied to analyze DAPI, immunolabelled dye (Alexa Fluor 546) was visualized using excitation in the visible with the Ar ion laser, and the nanofibers were observed by reflected light in the visible. Three-dimensional images of the samples were built by collecting a series of images of individual planes by scanning the samples along the z axis, with a defined step size (interval between each individual plane or frame) of 500 nm. Image J was used for image analysis, and to mount 3D images.

References

Bilgen B, Sucosky P, Neitzel GP, Barabino GA. 2006. Flow characterization of a wavy-walled bioreactor for cartilage tissue engineering. Biotechnol Bioeng. 95(6):1009–1022. doi:10.1002/bit.20775.

Borys BS, Roberts EL, Le A, Kallos MS. 2018. Scale-up of embryonic stem cell aggregate stirred suspension bioreactor culture enabled by computational fluid dynamics modeling. Biochem Eng J. 133:157–167. doi:10.1016/j.bej.2018.02.005.

Bueno EM, Bilgen B, Carrier RL, Barabino GA. 2004. Increased rate of chondrocyte aggregation in a wavy-walled bioreactor. Biotechnol Bioeng. 88(6):767–777. doi:10.1002/bit.20261.

Cherry RS, Kwon KY. 1990. Transient shear stresses on a suspension cell in turbulence. Biotechnol Bioeng. 36(6):563–571. doi:10.1002/bit.260360603.

Cormier JT, zur Nieden NI, Rancourt DE, Kallos MS. 2006. Expansion of undifferentiated murine embryonic stem cells as aggregates in suspension culture bioreactors. Tissue Eng. 12(11):3233–3245. doi:10.1089/ten.2006.12.3233.

Delaine-Smith RM, Reilly GC. 2012. Mesenchymal stem cell responses to mechanical stimuli. Muscles Ligaments Tendons J. 2(3):169–180.

Donato R, Miljan EA, Hines SJ, Aouabdi S, Pollock K, Patel S, Edwards FA, Sinden JD. 2007. Differential development of neuronal physiological responsiveness in two human neural stem cell lines. BMC Neurosci. 8:36. doi:10.1186/1471-2202-8-36.

Guirao B, Meunier A, Mortaud S, Aguilar A, Corsi J-M, Strehl L, Hirota Y, Desoeuvre A, Boutin C, Han Y-G, et al. 2010. Coupling between hydrodynamic forces and planar cell polarity orients mammalian motile cilia. Nat Cell Biol. 12(4):341–350. doi:10.1038/ncb2040.

Ismadi M-Z, Gupta P, Fouras A, Verma P, Jadhav S, Bellare J, Hourigan K. 2014. Flow Characterization of a Spinner Flask for Induced Pluripotent Stem Cell Culture Application. PLOS ONE. 9(10):e106493. doi:10.1371/journal.pone.0106493.

King JA, Miller WM. 2007. Bioreactor development for stem cell expansion and controlled differentiation. Curr Opin Chem Biol. 11(4):394–398. doi:10.1016/j.cbpa.2007.05.034.

Little L, Healy KE, Schaffer D. 2008. Engineering biomaterials for synthetic neural stem cell microenvironments. Chem Rev. 108(5):1787–1796. doi:10.1021/cr078228t.

Park MG, Jang H, Lee S-H, Lee CJ. 2017. Flow Shear Stress Enhances the Proliferative Potential of Cultured Radial Glial Cells Possibly Via an Activation of Mechanosensitive Calcium Channel. Exp Neurobiol. 26(2):71–81. doi:10.5607/en.2017.26.2.71.

Rodrigues CAV, Fernandes TG, Diogo MM, da Silva CL, Cabral JMS. 2011. Stem cell cultivation in bioreactors. Biotechnol Adv. 29(6):815–829. doi:10.1016/j.biotechadv.2011.06.009.

Sargent CY, Berguig GY, Kinney MA, Hiatt LA, Carpenedo RL, Berson RE, McDevitt TC. 2010. Hydrodynamic modulation of embryonic stem cell differentiation by rotary orbital suspension culture. Biotechnol Bioeng. 105(3):611–626. doi:10.1002/bit.22578.

Sen A, Kallos MS, Behie LA. 2001. Effects of Hydrodynamics on Cultures of Mammalian Neural Stem Cell Aggregates in Suspension Bioreactors. Ind Eng Chem Res. 40(23):5350–5357. doi:10.1021/ie001107y.

Sen A, Kallos MS, Behie LA. 2002. Expansion of mammalian neural stem cells in bioreactors: effect of power input and medium viscosity. Dev Brain Res. 134(1–2):103–113. doi:10.1016/S0165-3806(01)00328-5.

Tam RY, Fuehrmann T, Mitrousis N, Shoichet MS. 2014. Regenerative Therapies for Central Nervous System Diseases: a Biomaterials Approach. Neuropsychopharmacology. 39(1):169–188. doi:10.1038/npp.2013.237.

Toh Y-C, Voldman J. 2011. Fluid shear stress primes mouse embryonic stem cells for differentiation in a self-renewing environment via heparan sulfate proteoglycans transduction. FASEB J. 25(4):1208–1217. doi:10.1096/fj.10-168971.

Valmikinathan CM, Hoffman J, Yu X. 2011. Impact of Scaffold Micro and Macro Architecture on Schwann Cell Proliferation under Dynamic Conditions in a Rotating Wall Vessel Bioreactor. Mater Sci Eng C Mater Biol Appl. 31(1):22–29. doi:10.1016/j.msec.2010.04.001.

Wallin P, Zandén C, Carlberg B, Hellström Erkenstam N, Liu J, Gold J. 2012. A method to integrate patterned electrospun fibers with microfluidic systems to generate complex microenvironments for cell culture applications. Biomicrofluidics. 6(2):24131. doi:10.1063/1.4729747.

Wang B, Jedlicka S, Cheng X. 2014. Maintenance and Neuronal Cell Differentiation of Neural Stem Cells C17.2 Correlated to Medium Availability Sets Design Criteria in Microfluidic Systems. PLoS ONE. 9(10). doi:10.1371/journal.pone.0109815. [accessed 2018 Jul 18]. https://www.ncbi.nlm.nih.gov/pmc/articles/PMC4195690/.

Wang Y, Chou B-K, Dowey S, He C, Gerecht S, Cheng L. 2013. Scalable expansion of human induced pluripotent stem cells in the defined xeno-free E8 medium under adherent and suspension culture conditions. Stem Cell Res. 11(3):1103–1116. doi:10.1016/j.scr.2013.07.011.

Whited BM, Rylander MN. 2014. The influence of electrospun scaffold topography on endothelial cell morphology, alignment, and adhesion in response to fluid flow. Biotechnol Bioeng. 111(1):184–195. doi:10.1002/bit.24995.

Wolfe RP, Leleux J, Nerem RM, Ahsan T. 2012. Effects of shear stress on germ lineage specification of embryonic stem cells. Integr Biol. 4(10):1263–1273. doi:10.1039/C2IB20040F.

Zhu Y, Gao C, Liu X, Shen J. 2002. Surface Modification of Polycaprolactone Membrane via Aminolysis and Biomacromolecule Immobilization for Promoting Cytocompatibility of Human Endothelial Cells. Biomacromolecules. 3(6):1312–1319. doi:10.1021/bm020074y.

Chapter VI

General Conclusions and Future Perspective

Chapter VI – General Conclusions and Future Perspective

Extensive research has been conducted in order to develop effective therapeutic solutions for CNS injuries and diseases, and also to comprehend the underlying mechanisms of CNS diseases, especially the neurodegenerative such as Parkinson or Alzheimer's diseases. The therapeutic strategies are based on the stimulation of endogenous stem cells or on the transplantation of exogenous stem cells previously expanded in bioreactors. The use of biomaterials working as scaffolds transplanted into the damaged tissue can both stimulate the endogenous regeneration by providing biochemical factors or drugs, and also provide exogenous stem cells, functioning as tissue grafts transplanted into the damaged tissue.

A number of strategies are used to process biodegradable and biocompatible, natural or synthetic materials, in order to reproduce the mechanical and chemical properties of the *in vivo* environment. The electrospinning is a material processing technique that allows producing nanofibers with various topographic characteristics (variable mesh densities, aligned or random oriented fibers), mimicking the structure of the natural ECM. Polycaprolactone is an example of synthetic polyester vastly used in tissue engineering technology. Electrospun polycaprolactone nanofibers can be easily functionalized with biochemical cues such as adhesion proteins or biological factors, enhancing stem cell adhesion and organization within scaffold structure.

In this work, the studies were focused on the effect of the nanofiber scaffolds on neural stem cells. In a first case nanofiber scaffolds functionalized with an adhesion motif were successfully applied to a mouse model of NSC of embryonic origin (CGR8-NS). The focus was to determine how this cellular model would behave in terms of expansion and differentiation on the nanofibers. A special attention was given to the morphology and general cellular organization on the nanofibers. It was possible to direct cellular morphology and the cellular distribution, with positive results on the neuronal differentiation. This system of nanofiber scaffolds was suitable to be applied to NSC growth and differentiation where the obtained differentiated neurons exhibited an elongated morphology and aligned distribution. This is important regarding nervous tissue demanding highly organized cellular organization and direction and especially relevant for neuron elongation with direct implications on neuron cellular function.

This thesis highlights the use of electrospinning as a simple technique to provide aligned fibers which can be functionalized with biological motifs using robust methods. Importantly the results presented show for the first time, in a comparative manner, that contrary to other cells types, neural stem cells are very dependent of the biological motifs for cell attachment and actually the cell alignment and the quality of the differentiated cells is sensitive to the biological motif. Namely, LN and GRGDSP, are crucial adhesion factors when functionalized in aligned nanofibers to direct NSC elongation and distribution; in particular LN is able to promote in situ differentiation, resulting in relative higher cells expressing Tuj1 and longer neurite development. The highest astrocyte percentage was obtained for cultures on PCL-RGD random fibers. This comparative study is presented here for the first time, highlighting that in spite of the use of small peptide motifs being more economical attractive, NSC differentiation requires the use of the full protein or other specific motifs contained in such protein. For practical use of electrospun meshes, the current work also presents for the first time a five rank scale for fiber density, in which it was suggested and a 3.5 - 4 level, corresponding to 70 - 80% fiber density, as adequate for NSC ex-vivo culture.

The nanofibers were then upgraded to a set of scaffold frames to serve as supports for the cellular growth of a human NSC line in dynamic conditions, in a designed prototype stirred vessel. The system was characterized to its hydrodynamic properties and evaluated in terms of the cellular culture performance. The results were promising where the cellular expansion on the nanofibers was quite effective. A range of the best and worst conditions to the vessel operation was identified, and in general the overall system performance behaved according to the most predictions.

Considering the literature review, it is identified the need to build scalable systems that allow NSC culture in nanofiber scaffolds. We developed a stirred device, specially designed to accommodate nanofiber scaffold frames. The prototype is composed of 3 parts: a vessel carved in its interior walls with a set of grooves able to adjust six parallel frames of nanofiber scaffolds, a magnetic stirrer which occupies the space defined below the base of the grooves and a cap. This system was characterized regarding the hydrodynamic properties, namely the mixing time, the mass transfer coefficient and Sherwood number (both estimated experimentally by the limiting current technique), the instantly and average wall shear stress and the instantly velocity vectors of the fluid (both computed by CFD). The operating features of the device were predicted namely: the liquid film mass transfer coefficients at the interface of the liquid and frames were estimated at values from 9.7 to 38.3 $\mu m.s^{-1}$; It was also verified

that there is effective mass transfer, with low concentration polarization in the stationary boundary layer (maximum ratio of lactate flux per liquid mass transfer coefficient c_i - c_b = 1.77 mol.m^{-3}). Also, CFD predicted an average low shear stress of 2 - 3 mPa acting on the frames walls, and showed that for effective mixing along the bioreactor is required recirculation through the top of the frames.

Interestingly higher minimum shear stress values are observed, indicating less stagnant regions. In previous studies (Wang et al. 2013) it was reported local maximum shear stress of 0.152 Pa very close to our case for 75 rpm of mixing velocity for convective flow fluid in a spinner flask for adherent and suspension culture of human induced pluripotent stem cells, very similar to our case of 0.147 Pa at 125 rpm and 25 mL for the interface 4R. Another study on the other hand, reports maximum shear stress in the range of 0.625 – 0.986 Pa in a aggregate culture system for the expansion of NSC, and report no damage to the cells in spite of the higher value (Sen et al. 2002).

The stirred device was effective in the cell culture of adherent NSC on the nanofiber scaffolds with better performance at 45 rpm at 30mL. The specific growth rate obtained was in the order of 0.28 day^{-1}, with concentration of lactate at the end of the culture of 12.8 mmol.L^{-1} resulting in specific lactate rate production of 1.6×10^{-7} mmol.cell^{-1}.day^{-1}. The values of the metabolite in solution are below the minimum limit of toxicity and are comparable to other studies reported (Rodrigues et al. 2011).

A very interesting observation of the current study is the existence of an optimal cell growth with intensity of mixing, even if low shear stress have been applied and Sherwood numbers vary within a narrow range. This observation points out that NSC are more sensitive to accumulation of inhibitory metabolites and shear stress that previously reported on the literature. This result is, most probably, obtained because our study focused in growth rate rate rather than cell viability. Still, the important message that when NSC are cultured in dynamic conditions, it is important to control fluid dynamics considering its effect on cell growth (self renewable) and differentiation (cell fate). In the current version of this work, only a very preliminary and qualitative analysis of NSC differentiation under dynamic conditions was carried out. However the results are promising and deserve further research to obtain quantitative information. Note that until date very few works report NSC expansion and differentiation in aligned and functionalized nanofibers scaffold, in dynamic conditions.

We believe that this plate and frame bioreactor configuration brings novelty to the field as previous works are based either in perfusion systems using pumps or rotary bioreactors. The current system

provides a better matching with the geometry of the electrospun fibers, facilitates sterilization and avoids contamination and while providing low shear stress and acceptable Sherwood number. A limitation to the current system concerns automatization of the seeding of the cells on the nanofibers that needs to be implemented for the next generation of this device.

In this work specifically, frames of nanofibers, are the base scaffolds that will be seeded and cultivated in a custom designed nanofiber scalable bioreactor. These frames after cultivation are thus envisioned, able to be a support of a tissue transplant or a graft vehicle for cell, drug or biochemical delivery to promote in situ regeneration. It can also be intended as a systematic production of natural tissue or cell niches replicates, working as valuable platforms for high screening drug testing or disease modelling.

Each nanofiber construct, as referred in previous sections, can be tailored and assembled with smart materials or combined with drug delivery chemical strategies according to the type of graft intend to be produced and type of cell system to be applied on. A scalable nanofiber-bioreactor,, for the systematic production of scaffolds is in fact a strategy that needs to be further explored. The attractiveness of this approach lies also on the simplicity of the designed systems, both the bioreactor vessel and the nanofiber supports.

In summary the overall project delivered quite promising results, and also new questions arise from the developed work. For example regarding the nanofiber scaffolds per se. The neural tissue is essentially constituted by very soft tissue, and the polycaprolactone material, is to stiff regarding the neural tissue. Another type of scaffolds would be interesting to develop, using softer polymers as the basic architecture combined with hydrogel-based materials ideally with stimulus sensitive properties. The idea would be to develop systems to allow cellular separation by extracellular stimulus to which the material is responsive, which can be useful to in situ cellular delivery for example.

As for the bioreactor system, this presented prototype is indeed a very good starting point to a more robust system. For example the introduction of a system to allow a more accurate culture control and performance of the cellular culture (metabolite and gases delivery more efficiently, automatic medium supply minimizing scaffold manipulation, more control of the shear forces acting on the system), and introducing automatic systems of O_2 and CO_2 control, in order to get an operational closed system.

References

Rodrigues CAV, Diogo MM, da Silva CL, Cabral JMS. 2011. Microcarrier expansion of mouse embryonic stem cell-derived neural stem cells in stirred bioreactors. Biotechnol Appl Biochem. 58:231–242. doi:10.1002/bab.37.

Sen A, Kallos MS, Behie LA. 2002. Expansion of mammalian neural stem cells in bioreactors: effect of power input and medium viscosity. Dev Brain Res. 134:103–113. doi:10.1016/S0165-3806(01)00328-5.

Wang Y, Chou B-K, Dowey S, He C, Gerecht S, Cheng L. 2013. Scalable expansion of human induced pluripotent stem cells in the defined xeno-free E8 medium under adherent and suspension culture conditions. Stem Cell Res. 11:1103–1116. doi:10.1016/j.scr.2013.07.011.